

Atmospheric oxidation precursors in the marine boundary layer around the Arabian Peninsula



JOHANNES GUTENBERG
UNIVERSITÄT MAINZ



MAX-PLANCK-INSTITUT
FÜR CHEMIE

Dissertation

zur Erlangung des Grades

„Doktor der Naturwissenschaften – Dr. rer. nat.“

im Promotionsfach Chemie

am Fachbereich Chemie, Pharmazie, Geographie und Geowissenschaften
der Johannes Gutenberg-Universität Mainz

Dirk Dienhart

geb. in Wittlich

Mainz, 2022

Für meine Familie.

‘If I have seen further, it is by standing
on the shoulders of giants.’

Isaac Newton

Formal Declaration

I hereby formally declare that I wrote this dissertation independently and without any unauthorized external assistance. I did only use the acknowledged literature and other sources in this thesis, which were marked and listed separately in the supplement.

Mainz, November 2022

A handwritten signature in black ink, consisting of a stylized 'D.' followed by a flourish.

Abstract

The Arabian Gulf and the Suez Canal are famous for their Oil and Gas industry which brought wealth but also intensive ship traffic and severe amounts of air pollution to the region. Precise specification and quantification of these trace gases and pollutants is necessary to derive not only the accompanied regional impact on air quality, but also the global effects with respect to climate change. The Air Quality and Climate Change around the Arabian Basin ship expedition AQABA characterized the air quality around the Arabian Peninsula during summer 2017 covering a variety of meteorological, particulate matter and trace gas measurements in the marine boundary layer (MBL). Formaldehyde (HCHO), hydrogen peroxide (H₂O₂) and organic hydroperoxides (ROOH) reflect the photochemical activity of an air mass, as they are reservoir species for the primary oxidizing reagent of the troposphere, the hydroxyl radical (OH). Furthermore, HCHO is the most important intermediate during the oxidation of volatile organic compounds (VOCs). Measurements of HCHO, H₂O₂ and ROOH were performed with three different instruments based on fluorescence spectroscopy during AQABA onboard the *Kommandor Iona* and are presented and discussed in this doctoral thesis.

The first section gives an introduction on the topic of atmospheric chemistry, oxidation precursors and the main gas phase reactions in the MBL. Characterization of the involved instrumentation and analytical methods is presented in chapter two. HCHO measurements are based on the AL4021 (Aero-Laser GmbH) which utilizes the Hantzsch reaction to convert dissolved HCHO into a fluorescent dye. During AQABA, this technique achieved a detection limit of 128 ppt_v HCHO. H₂O₂ and ROOH were measured with a similar detection principle based on the dual-enzyme method with detection limits of 13 ppt_v H₂O₂ and 8 ppt_v ROOH (AL2021). Furthermore, hydroperoxide samples were analyzed with high-performance liquid chromatography (HPLC) which verified the abundance of methyl hydroperoxide (MHP), peracetic acid (PAA) and ethyl hydroperoxide (EHP) over the Arabian Gulf. Ship exhaust plumes were excluded from the final HCHO dataset with a filter based on nitrogen oxides (NO_x = NO + NO₂), carbon monoxide (CO), sulphur dioxide (SO₂) and wind direction data, while no significant influences on the mixing ratios of H₂O₂ and ROOH were identified.

Extreme anthropogenic air pollution events were encountered over the Arabian Gulf with a considerably increased mean ($\pm 1\sigma$) of tropospheric ozone (O₃) with 74.1 ± 9.2 ppb_v, reaching a maximum of 167 ppb_v during a pollution event on the first leg. This event also contained the largest amounts of HCHO (12.4 ppb_v) and ROOH (2.32 ppb_v), but only slightly elevated H₂O₂ (0.421 ppb_v). Highest mean values of HCHO (3.77 ± 2.44 ppb_v) and ROOH (0.357 ± 0.283 ppb_v) were determined over the Arabian Gulf, while H₂O₂ reached its highest mean of 0.273 ± 0.113 ppb_v over the Suez Canal. Cleaner air masses were detected over the Arabian Sea, the Mediterranean Sea and the southern Red Sea, where we also encountered a dust storm. The in situ observations were used to evaluate results of the general circulation model EMAC (ECHAM/MESSy Atmospheric Chemistry). Both HCHO datasets agree mostly within a factor of 2, while H₂O₂ was overestimated drastically by at least a factor of 5. Calculation of the photochemical budget of H₂O₂ revealed the overestimation of OH and hydroperoxyl (HO₂) radicals, and a slight underestimation of the dry deposition velocity. The high resolution model WRF-Chem did not improve results of HCHO over the polluted Arabian Gulf and the Suez Canal, but more accurate results were achieved for HCHO, H₂O₂ and O₃ for less polluted MBL conditions like the Arabian Sea, even though both models overestimated HO_x.

HCHO production rates were calculated based on the photochemical steady-state assumption (PSS) and were used for a regression analysis with OH reactivity and OH radical observations to estimate the HCHO yield factor α_{eff} , which represents the theoretical yield of HCHO per OH radical consumed. Largest α_{eff} were derived for the Arabian Gulf (0.315), followed by the Suez Canal (0.115) and the Gulf of Oman (0.077). According to the speciated OH reactivity, largest α_{eff} were accompanied by elevated reactivity towards alkanes, alkenes and OVOCs, while a decrease of α_{eff} over the southern Red Sea (0.013) was accompanied by reduced NO_x. The study thus successfully established a new method to estimate HCHO production efficiencies without the need for a calculation of the HCHO production budget and was published as a measurement report in ACP.

Further analysis of the Arabian Gulf with HYSPLIT trajectories showed that air pollution was mainly transported from Iraq, Kuwait and the northwestern coastline of Iran. According to satellite-based flare emission data there are many gas flaring sites located in these areas, which are strong sources of HCHO and other VOCs. Analysis of the cleaner regions during AQABA revealed enhanced HCHO compared to measurements in pristine MBL conditions, with ship emissions as a major cause even though the

Arabian Sea is known as a strong source of biogenic emissions. Furthermore, heterogeneous loss of H_2O_2 and to a lesser extent HCHO and ROOH was detected during a sand storm over the southern Red Sea. The AQABA expedition successfully analyzed the complex and highly variable air quality around the Arabian Peninsula and achieved the first measurements of HCHO, H_2O_2 and ROOH in the MBL over the Arabian Gulf, where enhanced levels of air pollution are a threat for human health and the environment. Atmospheric chemistry models were evaluated with the measurements and demonstrated missing sources of HCHO while they simultaneously overestimated HO_x . Further studies over the Arabian Gulf are necessary to increase the accuracy of anthropogenic emission databases, a local trace gas measurement network in the region would thus be highly valuable.

Zusammenfassung

Der Arabische Golf und der Suezkanal sind berühmt für ihre Öl- und Gas-Industrie, die Wohlstand, jedoch auch den damit verbundenen intensiven Schiffstransport und enorme Luftverschmutzung mit sich brachte. Eine präzise Charakterisierung und Quantifizierung der vorhandenen Spurengase and weiteren Schadstoffen ist notwendig um deren Einfluss auf die lokale Luftqualität zu bestimmen und globale Effekte auf den Klimawandel abzuleiten. Die Schiffsexpedition AQABA (Air Quality and Climate Change around the Arabian Basin) charakterisierte die Luftqualität um die Arabische Halbinsel während des Sommers 2017 und deckte dabei eine Vielzahl an meteorologischen, Partikel- und Spurengasmessungen in der marinen Grenzschicht ab. Formaldehyd (HCHO), Wasserstoffperoxid (H_2O_2) und organische Hydroperoxide (ROOH) sind dabei ein Indiz für die photochemische Aktivität einer Luftmasse, da sie Reservoirspezies für das wichtigste Oxidationsmittel der Atmosphäre darstellen, das Hydroxyl-Radikal (OH). Außerdem ist HCHO das häufigste Zwischenprodukt bei der Oxidation von volatilen organischen Verbindungen (VOCs). Messungen von HCHO, H_2O_2 und ROOH wurden mit drei verschiedenen Instrumenten basierend auf Fluoreszenz-Spektroskopie während AQABA an Board der *Kommandor Iona* durchgeführt, die in dieser Doktorarbeit vorgestellt und diskutiert werden. Das erste Kapitel präsentiert eine kurze Einführung zum Thema Atmosphärenchemie, Vorläuferspezies von atmosphärischen Oxidationsmitteln, sowie den wichtigsten Gasphasenreaktionen in der marinen Grenzschicht. Die Charakterisierung der verwendeten Messinstrumente und analytischer Methoden wird im zweiten Kapitel dargestellt. HCHO Messungen wurden mit dem AL4021 durchgeführt (Aero-Laser GmbH), welcher auf der Hantzsch'schen Dihydropyridinsynthese basiert. Bei dieser Reaktion wird aus der Umgebungsluft gelöstes HCHO in einen fluoreszenzaktiven Farbstoff überführt. Während AQABA wurde mit dieser Messmethode eine Nachweisgrenze von 128 ppt_v erhalten. H_2O_2 und ROOH wurden mit ähnlichen Messinstrumenten basierend auf der Dual-Enzym-Methode detektiert, mit welcher Nachweisgrenzen von 13 ppt_v H_2O_2 und 8 ppt_v ROOH erhalten wurden (AL2021). Außerdem wurden die organischen Hydroperoxide chromatographisch analysiert (HPLC, Hochleistungsflüssigkeitschromatographie), wodurch Methylhydroperoxid (MHP), Peressigsäure (PAA) und Ethylhydroperoxid (EHP) nachgewiesen wurden. Schiffsabgase wurden anhand von Stickoxiden (NO_x), Kohlenmonoxid (CO), Schwefeldioxid (SO_2) und der Windrichtung identifiziert und aus dem finalen HCHO Datensatz entfernt, wobei keine signifikanten Einflüsse auf die Mischungsverhältnisse von H_2O_2 und ROOH festgestellt wurden.

Extreme Schadstoffbelastung wurde über dem Arabischen Golf detektiert mit einem Ozon (O_3) Mittelwert ($\pm 1\sigma$) von 74.1 ± 9.2 ppb_v, welches Maximalwerte von 167 ppb_v während eines stark verschmutzten Events im Zentrum des Arabischen Golfs erreichte. Während dieses Events wurden außerdem die höchsten Messwerte für HCHO (12.4 ppb_v) und ROOH (2.32 ppb_v), jedoch nur leicht erhöhtes H_2O_2 (0.421 ppb_v) detektiert. Höchste Mittelwerte für HCHO (3.77 ± 2.44 ppb_v) und ROOH (0.357 ± 0.283 ppb_v) wurden über dem Arabischen Golf bestimmt, während diese für H_2O_2 über dem Suezkanal nachgewiesen wurden (0.273 ± 0.113 ppb_v). Sauberere Luftmassen wurden über der Arabischen See, dem Mittelmeer und dem südlichen Roten Meer detektiert, wo wir außerdem einen Sandsturm antrafen. Diese Messdaten wurden anschließend genutzt um Modelldaten des chemischen Transportmodells EMAC (ECHAM/MESSy Atmospheric Chemistry) zu bewerten, was in Kapitel 4.2 dargelegt ist. Die HCHO Datensätze stimmten großteils mit einer Abweichung kleiner als Faktor 2 überein, jedoch wurde H_2O_2 drastisch durch EMAC überschätzt mit einer Abweichung von mindestens Faktor 5. Anschließende Berechnung des photochemischen Budgets von H_2O_2 zeigte, dass diese Abweichung vor allem auf überschätzten OH und Hydroperoxyl-Radikalen (HO_2) beruhte. Außerdem wurden Depositionsgeschwindigkeiten berechnet, welche EMAC unterschätzte. Der Vergleich mit dem

höher auflösenden Modell WRF-Chem zeigte, dass die höhere Auflösung von WRF-Chem keine genaueren Ergebnisse für HCHO über dem Arabischen Golf und dem Suezkanal lieferte. Jedoch lieferte das hochauflösende WRF-Chem genauere Ergebnisse als EMAC für HCHO, H₂O₂ und O₃ in weniger verschmutzten Regionen wie der Arabischen See, jedoch überschätzten beide Modelle HO_x.

HCHO Produktionsraten wurden basierend auf der Näherung des photochemischen Gleichgewichtszustands (PSS) bestimmt und in einer Regressionsanalyse mit OH Reaktivitäts- und Radikalmessungen verwendet um die theoretische Ausbeute an HCHO pro abgereagtes OH Radikal abzuschätzen. Dieser Ausbeutefaktor α_{eff} ermöglicht es die Effizienz der HCHO Produktion basierend auf Reaktionen von OH für die unterschiedlichen Regionen während AQABA miteinander zu vergleichen. Höchste α_{eff} wurden für den Arabischen Golf (0.315), den Suezkanal (0.115) und den Golf von Oman (0.077) erhalten, in welchen auch erhöhte Reaktivität von gesättigten und ungesättigten Kohlenwasserstoffen nachgewiesen wurde. Das niedrigste α_{eff} (0.013) wurde für das südliche Rote Meer bestimmt während stark reduziertem NO_x. Die Studie etablierte ein neues Verfahren zur Abschätzung der HCHO Produktionseffizienz ohne das photochemische Budget bestimmen zu müssen und wurde als ‘Measurement Report‘ in ACP publiziert.

Weitere Analyse der Luftmassen des Arabischen Golfs mit HYSPLIT Trajektorien zeigte, dass die Verschmutzung hauptsächlich von der Küste Kuwaits, dem Irak und dem Nordwesten Irans transportiert wurde. Satellitenmessungen haben dort signifikante Gasfackel-Emissionen durch das Verbrennen von Erdgas detektiert, wodurch die erhöhten Mischungsverhältnisse von HCHO und weiteren VOCs erklärt werden können. Die AQABA Schiffskampagne erzielte die ersten Messungen von HCHO, H₂O₂ und ROOH in der marinen Grenzschicht des Arabischen Golfs. Die dort vorhandene Luftverschmutzung stellt eine Gefahr für die menschliche Gesundheit dar und hat Auswirkungen auf die Umwelt und den Klimawandel. Weitere Studien in der Region wären hilfreich um die Genauigkeit von Emissionsdatenbanken zu verbessern welche in Transportmodellen verwendet werden, ein lokales Netzwerk von Spurengasmessungen wäre dafür sehr hilfreich.

Table of Contents

1. Introduction	1
1.1 The structure of Earth's atmosphere and basics of Atmospheric Chemistry.....	1
1.2 Spatial and Temporal Scales of Atmospheric Processes	3
1.3 Atmospheric oxidants and their role as 'cleaning reagents'	4
1.3.1 Tropospheric reservoir species of HO _x	6
1.3.2 Photochemical production and loss reactions of HCHO, H ₂ O ₂ and MHP	7
1.4 Heterogeneous chemistry and the connection to the particle phase	13
1.5 Further heterogeneous processes in the marine boundary layer.....	15
2. Methods & experimental procedures.....	16
2.1 Formaldehyde measurement techniques.....	16
2.1.1 The formaldehyde monitor AL4021	17
2.1.2 Detection principle – the Hantzsch reaction.....	17
2.1.3 Sampling technique & operation of the AL4021.....	18
2.1.4 Iodometric redox titration of HCHO	19
2.1.5 Calibration of the AL4021.....	20
2.1.6 Temporal resolution & response	21
2.1.7 Detection limit.....	22
2.1.8 Precision	23
2.1.9 Determination of the sampling efficiency	24
2.1.10 Interferences and total measurement uncertainty	25
2.2 Hydroperoxide measurement techniques	28
2.2.1 The hydroperoxide monitor AL2021.....	29
2.2.2 Detection principle – The dual-enzyme technique	29
2.2.3 Instrument calibration and characteristics of the AL2021.....	31
2.2.4 Separation of organic hydroperoxides with HPLC.....	33
2.3 Data processing	35
2.4 EMAC	35
2.5 HYSPLIT trajectories.....	36
2.6 Photochemical steady-state assumption	37
2.7 Deposition	37
3. The AQABA ship campaign	38
3.1 Air quality and anthropogenic pollution around the Arabian Peninsula	38
3.2 Measurement setup on the <i>Kommandor Iona</i>	41

3.3 Instruments used for the detection of further trace gases and particles.....	42
3.4 Data Treatment.....	46
4. Results of the AQABA ship campaign.....	48
4.1 Meteorological observations	48
4.1.1 Air mass origin – HYSPLIT trajectories.....	49
4.2 Formaldehyde and hydroperoxide observations around the Arabian Peninsula	52
4.2.1 Formaldehyde and hydroperoxide distribution around the Arabian Peninsula – evaluation of EMAC model results with ship-based measurements.....	53
4.2.2 Supplement of: Formaldehyde and hydroperoxides distribution around the Arabian Peninsula – evaluation of EMAC model results with ship-based measurements.....	78
4.3 Formaldehyde production rates and their relation to OH reactivity.....	87
4.4 Case Study: The Arabian Gulf	104
4.4.1 Simulation of the Arabian Gulf with EMAC and WRF-Chem	110
4.5 Cleaner regimes around the Arabian Peninsula.....	113
4.5.1 Diurnal variation of trace gases.....	113
4.5.2 The Arabian Sea during the South Asian Summer Monsoon.....	116
4.5.3 Dust events over the southern Red Sea and the Gulf of Aden	118
5. Summary and Conclusion	120
6. Supplement.....	123
6.1 List of Tables.....	123
6.2 List of Figures	123
6.3 Figures.....	131
6.4 Experimental Procedures.....	141
7. Literature	146

1. Introduction

1.1 The structure of Earth's atmosphere and basics of Atmospheric Chemistry

The atmospheres of Earth and the other terrestrial planets, Venus and Mars, are thought to have formed as a result of the release of trapped gaseous volatile compounds from the planet itself. On Earth, the atmosphere contains mainly gases and fine particulate matter, which are retained by gravity. It can be separated into defined layers by means of their physical and chemical properties and the associated vertical temperature profile (Fig. 1). This yet thin but immensely important layer establishes life friendly conditions at the surface based on the greenhouse gas effect, as it absorbs most of the hazardous cosmic and solar radiation enabling the availability of liquid water. Furthermore, the abundance of oxygen (O₂) and carbon dioxide (CO₂) is of crucial importance for biological processes and living organisms. Additionally, the atmosphere plays a critical role in Earth's climate system through dynamic processes like air mass transport and weather phenomena (Seinfeld and Pandis, 2016).

Most of the atmospheric mass (~80 %) is located in the troposphere, although it only accounts for a small fraction of the atmosphere's total height. The troposphere extends from the surface of the earth to the tropopause, which is located at 10 – 15 km altitude depending on the latitude and time of the year (Seinfeld and Pandis, 2016). As a result, the atmospheric pressure follows an exponential decrease with altitude. The troposphere is characterized by ceaseless turbulence and mixing and a linear decrease in temperature, because of the increasing distance from the sun-warmed surface. It contains almost all of the atmosphere's water vapor, which condenses at colder temperature to form clouds. Thus it is also called the 'weather cauldron', since weather phenomena shape the turbulent behavior of the troposphere. It can be further subdivided into the planetary boundary layer, which extends on average up to roughly 1 km, and the free troposphere.

The tropopause is defined as the top of the troposphere, where the temperature reaches a local minimum with an average temperature of ~217 K (–56 °C). Over the equator the average height of the tropopause is about 16 km and over the poles about 8 km. By the convention of the World Meteorological Organization (WMO) the tropopause is defined as the lowest level at which the decrease in temperature with height is sustained at $\leq 2 \text{ K km}^{-1}$ or less (Holton et al., 1995). For comparison, in dry tropospheric air the temperature decreases almost linearly at 9.7 K km^{-1} (Seinfeld and Pandis, 2016).

Except for the highly variable water vapor, the main components of the troposphere are homogeneously distributed due to atmospheric dynamics. It primarily consists of nitrogen (78.1 %), oxygen (20.9 %), argon (0.9 %) and particulate matter. The remaining gases are called trace gases, which are, despite their rather low abundance, responsible for most of the chemical reactivity within the troposphere. Carbon dioxide (CO₂) is the most prevalent of these trace gases with a current mixing ratio of 419 ppm_v (0.04 %; <https://climate.nasa.gov/vital-signs/carbon-dioxide/>; September 2022), which increased by about 50 % since the pre-industrialized levels of ~280 ppm_v (Seinfeld and Pandis, 2006). It is one of the main contributors to the natural greenhouse effect besides the other primary greenhouse gases (GHG) water vapor (H₂O), methane (CH₄), nitrous oxide (N₂O) and ozone (O₃). Based on their chemical structure, these gases are able to absorb radiation within the thermal infrared and other wavelengths. This radiation is in turn emitted into all directions within the atmosphere and thus partly towards the surface, warming it up. GHG therefore have a net warming effect on the Earth's climate and without them no liquid water nor life-friendly conditions would be available at the surface. Besides gases, airborne particles strongly influence the radiation budget of the atmosphere. They are often described as aerosol, which is the suspension of fine solid or liquid particles in air or another gas. The effect of aerosols on the radiation budget in the atmosphere is quite complex, as it strongly depends on their physical (i.e. their size) and

chemical properties (i.e. sulfate, black carbon). There is a wide variety of natural and anthropogenic sources of airborne particles i.e. biomass burning, sea spray, secondary organic aerosol and black carbon, just to name a few. Diameters of airborne particles are in the range from as small as $1 \cdot 10^{-9}$ m (1 nm) to $10 \cdot 10^{-6}$ m (10 μ m) and play an important role on the lifetime of an aerosol. It is estimated that the total surface area of all particles in the atmosphere is $\sim 1 \cdot 10^{14}$ m²; this is roughly equivalent to the total surface of Earth (Seinfeld and Pandis, 2016). Recent reports of the Intergovernmental Panel on Climate Change (IPCC) highlight the importance of anthropogenic emissions and the related influence on radiative forcing. The reduction of CO₂ emissions remains one of the main challenges to fight global threat of climate change.

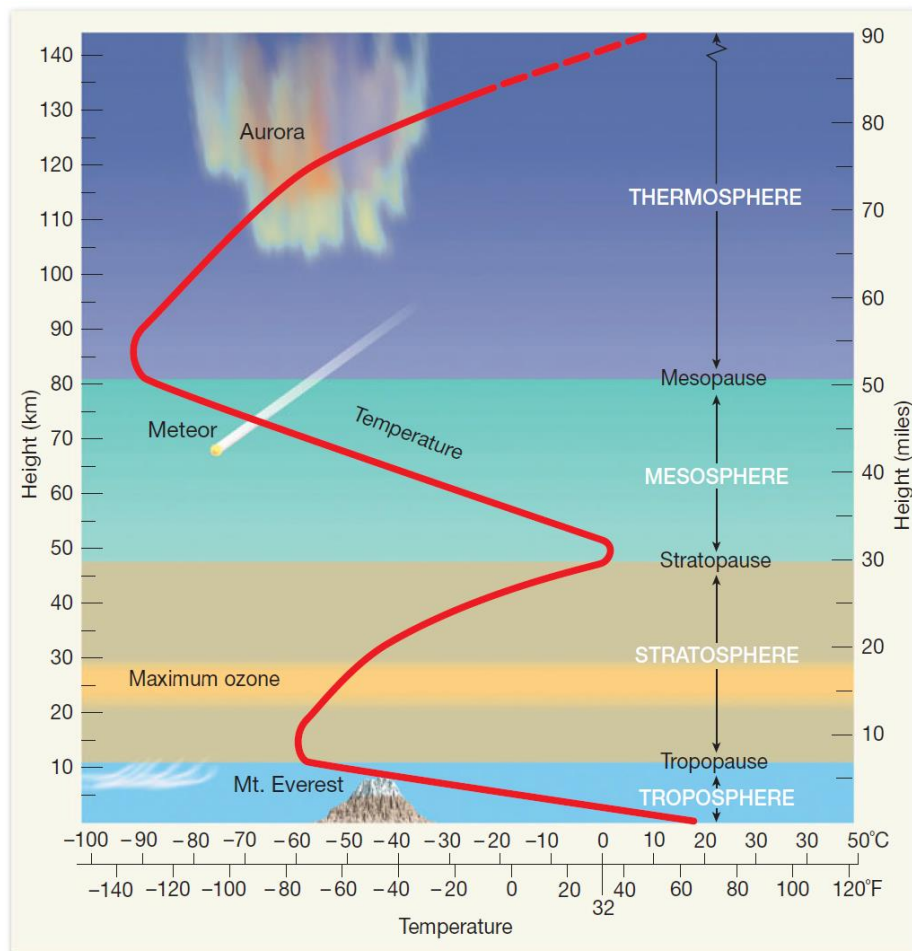


Figure 1: Vertical structure of the earth's atmosphere with its temperature profile.

Leaving behind the troposphere, the following layer is called stratosphere, where ~90 % of the atmospheric O₃ is located whereby it is often referred to as ozone layer. It extends up to 55 km and is characterized by a temperature inversion, it reaches a local maximum at the stratopause (~271 K). Highest amounts of O₃ are located in the lower third, where it locally reaches up to ~12 ppm_v. This layer is of great importance for life on Earth, as it shields the surface from harmful short-wave ultraviolet radiation. Sydney Chapman discovered the photochemical balance between O₂ and O₃ in 1930, which was named as the Chapman cycle. It describes the continuous production and loss of O₃ in the stratosphere. Production occurs through photo dissociation of O₂ by absorption of solar radiation in the UV-C region (≤ 240 nm). The released oxygen atoms react rapidly with O₂ and produce O₃. Ozone in turn absorbs less energetic solar radiation (≤ 360 nm, Hartley and Huggins bands), where the solar emission is more intense. As a next step photolysis of O₃ regenerates O₂ and excited singlet oxygen atoms (O(¹D)), which can either be lost via reaction with O₃ or start a new cycle via reaction with O₂ to

produce O₃. Further steps in stratospheric chemistry were done by Paul J. Crutzen, Mario J. Molina and F. Sherwood Rowland, who won the noble prize in chemistry (1995) for their pioneering contributions on the photochemical budget of stratospheric ozone. Paul J. Crutzen discovered that nitrogen oxides (NO_x = NO + NO₂) react catalytically with stratospheric O₃ (Crutzen et al., 1970). Together with the studies of Mario J. Molina and F. Sherwood Rowland, who elucidated the photochemistry of chlorofluorocarbons (CFCs) in the stratosphere (Molina and Rowland, 1974), they explained the destructive potential of certain anthropogenic emissions on the thickness of the ozone layer. Consequently, they contributed to our salvation from a global environmental problem, which could have had catastrophic consequences (<https://www.nobelprize.org/prizes/chemistry/1995/press-release/>; July 2022). This research breakthrough had major impact with the bans of critical emissions under the Montreal protocol and the growth of atmospheric chemistry as a research field.

The following layers of the mesosphere and the thermosphere are less distinctive, since they cover just a tiny amount of the total atmospheric mass. The mesosphere starts again with a temperature inversion after the stratopause, which enables fast vertical transport within this layer. It ends at the mesopause at ~80 km height, the coldest spot of Earth's atmosphere. The main feature in this layer are strong winds, atmospheric gravity waves and noctilucent clouds. As shown in Fig. 1 an increase in temperature is occurring again in altitudes above ~90 km, in the thermosphere, where short-wavelength radiation is absorbed by N₂ and O₂ and vertical mixing is fast. The outermost layer is called exosphere, it starts at altitudes ≥ 500 km where molecules with sufficiently large kinetic energy can escape from Earth's gravitational attraction (Seinfeld and Pandis, 2016).

1.2 Spatial and Temporal Scales of Atmospheric Processes

The atmosphere is a complex dynamic system, with its constituents continuously being exchanged with the oceans, the soil, the vegetation and organisms. Therefore, atmospheric processes are classified into homogenous and heterogeneous processes. Homogeneous processes describe phenomena within same conditions, e.g. the chemical reaction of two gases with each other. A heterogeneous process thereby describes the interaction by means of various conditions, e.g. the uptake of a gas by the oceans or soil. This can be quite complex as some gases in the atmosphere are soluble and stable, other species are highly reactive and thus have short lifetimes of just a few seconds. The lifetime thereby describes the time that surpasses until the species is lost from the atmosphere, e.g. by reaction with another gas or other removal processes. The average lifetime of a molecule introduced into the atmosphere can range from seconds to several years, depending on the effectiveness of the removal process. Trace gases are classified by means of their lifetimes, which determine their temporal and spatial scales. During transport through the atmosphere, all except the most inert species participate in some form of chemical reactions. This process can transform a species from its original physical and chemical state to another state that may have either similar or very different characteristics. The product may then also be removed from the atmosphere much more fast than the species itself in its original physical and chemical condition. For example, when a species that was originally emitted as a gas is transformed into a particle, the overall removal is usually accelerated since particles tend to be removed from the air much more rapidly than gases.

Most of the species considered as air pollutants have natural as well as anthropogenic sources. Therefore, in order to assess the potential effect of anthropogenic emissions on the atmosphere as a whole, it is essential to understand the atmospheric cycle of trace gases by means of their spatial and temporal scales. This includes both their natural and anthropogenic sources as well as the predominant removal mechanisms (Seinfeld and Pandis, 2016). Including the effect of atmospheric dynamics (e.g. vertical and horizontal transport), a species can be distributed over certain ranges. This allows the classification

of spatial scales for certain trace gases (Fig. 2): microscale (0 to 100 m), local scale (~100 m to tens of km), mesoscale (tens to hundreds of km) and global scale (hundreds to thousands of km).

One of the most important radical families are the hydrogen radicals (HO_x), which represent the sum of hydroxyl (OH) and hydroperoxyl (HO_2) radicals. OH radicals are one of the most reactive species within the atmosphere and determine its oxidizing potential. For short-lived species like OH transport is insignificant. Although one of its precursor species, hydrogen peroxide (H_2O_2), is a moderately long-lived species and thus dynamic transport, such as vertical motion and advection, become relevant. Carbon monoxide (CO) is even more stable with its lifetime of a few months and thus it achieves intra-hemispheric dispersion. It is a byproduct of combustion and other oxidation processes of organic compounds. The intra-hemispheric dispersion is reflected by global measurements of CO (Anderson et al., 2021; Yin et al., 2015), this effect is caused by the separation of the northern and southern hemisphere by the Hadley cell and the resulting Intertropical Convergence Zone (ITCZ) (Nussbaumer et al., 2021a). Even longer-lived species like CH_4 and N_2O are distributed on a global scale.

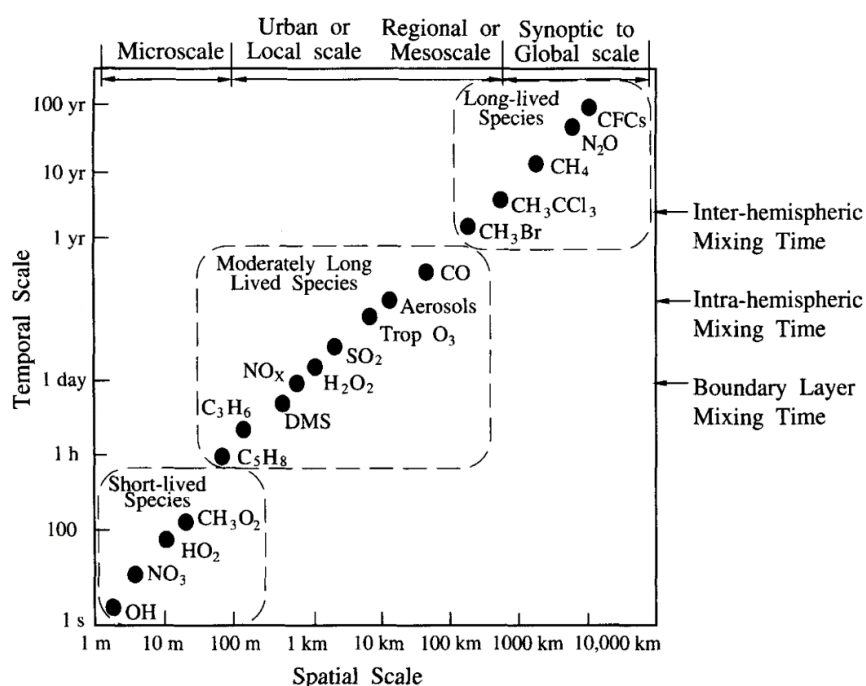


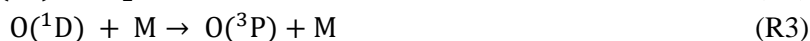
Figure 2: Temporal and spatial scales of variability for atmospheric constituents (Seinfeld and Pandis, 2016).

1.3 Atmospheric oxidants and their role as ‘cleaning reagents’

The atmosphere is an oxidizing medium and thus species, once emitted, are generally converted into substances characterized by higher chemical oxidation states than their precursor. This oxidative transformation often increases the polarity of a substance and hence its water solubility. Additionally, it often decreases the volatility of a substance. A prominent example is the conversion of sulfur dioxide (SO_2) into sulfuric acid (H_2SO_4). SO_2 itself is moderately soluble in water, but its oxidation product H_2SO_4 is even hygroscopic and thus it rapidly transitions into the particle phase. This reaction got prominent in the late 1970’s with the acidification of cloud droplets and led to a major environmental issue (Penkett et al. 1979; Seinfeld and Pandis, 2016).

Oxidation processes within the troposphere are mainly driven by OH radicals, which are produced e.g. by the photolysis of ozone (≤ 330 nm) in the presence of water vapor (Lelieveld et al., 2016). Photolysis of O_3 produces both ground-state ($\text{O}(^3\text{P})$) and excited ($\text{O}(^1\text{D})$) oxygen atoms. Since the spontaneous transition of $\text{O}(^1\text{D})$ to $\text{O}(^3\text{P})$ is forbidden, it must react with another atmospheric species. $\text{O}(^1\text{D})$ then principally collides with N_2 or O_2 (mediator species, M), which removes its excess energy, quenching

O(¹D) to its ground state. However, occasionally O(¹D) also collide with H₂O molecules and thereby produce two OH radicals. Therefore, the yield of OH is determined by the fate of O(¹D) and the abundance of H₂O. In fact, reaction 2 is the only gas-phase reaction to cleave the H–O bond of H₂O within the troposphere (Seinfeld and Pandis, 2016).



Once released, OH reacts with atmospheric pollutants and trace gases, e.g. CH₄, CO and other volatile organic compounds (VOCs). However, it does not react with the major constituents like N₂, O₂, CO₂ or H₂O. The key is that, when reacting with other trace gases, OH is generated in catalytic cycles and thus its abundance is surprisingly high despite its high reactivity. These radical reactions chains are summed up together as secondary sources of OH and are its major source besides the photolysis of O₃. Additionally, the abundance of OH is strongly coupled to hydroperoxyl radicals (HO₂) and together they form the hydrogen radical family HO_x (= OH + HO₂). During daylight hours, catalytic cycles are able to sustain concentrations of approximately 10⁶ molecules cm³ of OH within the troposphere (Seinfeld and Pandis, 2016; Anderson et al., 2021). OH thereby determines the self-cleaning or oxidation capacity of the atmosphere and thus it is often referred to as the ‘atmosphere’s detergent’. Recent model results suggest that secondary sources of OH are larger than previously assumed, mostly due to OH recycling in the free troposphere (Lelieveld et al., 2016). Despite its central role in atmospheric chemistry, the spatiotemporal distributions of OH concentrations are poorly constrained, often confounding the interpretation of observed variations and trends of important atmospheric constituents (Anderson et al., 2021).

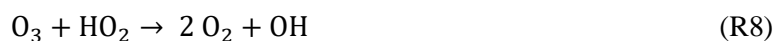
Its main losses (globally) are the reaction with CO (39 %), C₁ VOCs (15 %), C₂₊ VOCs (14 %) and CH₄ (12 %) (Fig. 3). Thereby, the most common oxidation chain is the reaction of OH with VOCs from which OH can abstract the hydrogen to form water and an alkyl radical (e.g. the methyl radical, ·CH₃). The alkyl radical then reacts fast with O₂ to form a peroxy radical (RO₂), e.g. its most essential species: hydroperoxyl (HO₂) and methyl peroxy (CH₃O₂) radicals.



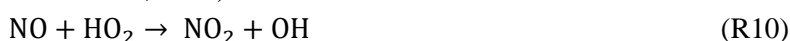
These peroxy radicals can combine and undergo peroxide formation (Lelieveld et al., 2016):



Propagation of the oxidation chain leads to higher-generation products and secondary OH formation, which can be understood as OH recycling, e.g. in clean environments via photolysis of peroxides or odd oxygen (O_x) recycling:



In more polluted air masses, several reactions are controlled by the abundance of nitrogen oxides (NO + NO₂ = NO_x). Nitric oxide (NO) is oxidized efficiently by HO₂ and thus converted into nitrogen dioxide (NO₂). This became of the most important reactions due to the strong growth of air pollution since the industrialization and is referred to as the NO_x recycling mechanism of OH. It also leads to O₃ production via photolysis of NO₂, one of the main sources of tropospheric O₃. However, in strongly polluted air masses, NO₂ can locally be a large sink of OH and the net effect of NO_x is self-limiting by formation of nitric acid (HNO₃) (Lelieveld et al., 2016).



Hence the tropospheric budget of OH is quite complex, but with a recycling probability of ~67 %, global OH is buffered and not sensitive to perturbations by natural or anthropogenic emission changes (Lelieveld et al, 2016). This thesis mainly focuses on the photochemistry of moderately long lived reservoir species of HO_x in the marine boundary layer (MBL) and the comparison of in situ measurements with the general circulation model EMAC (ECHAM/MESSy Atmospheric Chemistry).

1.3.1 Tropospheric reservoir species of HO_x

The term reservoir species demonstrates the fact that a molecule can act both as a source and as a sink for a certain molecule. Therefore, knowledge of the HO_x reservoirs aids in constraining the budget of HO_x and to understand the cycling between both OH and HO₂ with respect to the background conditions. Additionally, HO_x reservoirs typically have longer lifetimes than the radicals themselves, and thus they can be transported further than HO_x (e.g. by deep convection or sea breeze). Based on this effect, deep convective transport can significantly enhance HO_x concentrations in the UT (Anderson et al., 2017). The following sections focus mainly on the distribution of formaldehyde (HCHO) and hydroperoxides, which are moderately long lived species with lifetimes of several hours (Stickler et al., 2006; Nussbaumer et al., 2021a; Hamryszczak et al., 2022a).

Formaldehyde is a pervasive trace gas that provides insight into VOC oxidation and it acts as a source for HO₂ radicals in urban and remote regions. HCHO is also a precursor for OH in the upper troposphere. Highest concentrations are found close to the surface, where it can reach mixing ratios up to several ppb_v (parts per billion by volume), values in the UT are about an order of magnitude smaller. With its rather short lifetime (minimum of about 2 h during noontime in the tropics), formaldehyde can be an efficient tracer for recent convection (Anderson et al., 2017; Stickler et al., 2006). HCHO is mainly an intermediate during the atmospheric oxidation of VOCs, but it is also released into the atmosphere by several other primary sources. Main contributors are biomass burning (Liao et al., 2021; Akagi et al., 2011; Andreae and Merlet, 2001), industry emissions (Parrish et al., 2012), agriculture (Kaiser et al., 2015), vegetation (DiGangi et al., 2011) and exhaust emissions from vehicles (Celik et al., 2020; Marbach et al., 2009). Globally, the HCHO budget is dominated by in situ production through the oxidation of CH₄ (~970 TG yr⁻¹) and other VOCs (~250 TG yr⁻¹), while primary emissions only account for ~10 TG yr⁻¹ (Fortems-Cheiney et al., 2012). In the remote marine environment, atmospheric HCHO is mainly produced by the oxidation of CH₄, with minor contributions from methanol, acetaldehyde, glyoxal and acetone (Anderson et al., 2017), while oceanic emissions have also been suggested as a primary source of HCHO (Zhou & Mopper, 1997). In the remote marine boundary layer, this results typically in mixing ratios of several hundred ppt_v near the surface, decreasing with altitude (Fried et al., 2011; Stickler et al., 2006; Wagner et al., 2001; Heikes et al., 2001). Isoprene and other unsaturated hydrocarbons become more relevant for HCHO production in areas with large biogenic or anthropogenic emissions (Tripathi et al., 2020). The recent study of Dovrou et al. (2022) also suggests that HCHO plays a significant catalytic role in particle formation.

The production of peroxides in the troposphere is less diverse than that of HCHO, the main production pathways are the combination of peroxy radicals as shown in R6 and R7, although additional primary emissions can dominate photochemical production (e.g. biomass burning). The most crucial peroxides in the troposphere are hydrogen peroxide (H₂O₂), methyl hydroperoxide (MHP, CH₃OOH) and peracetic acid (PAA).

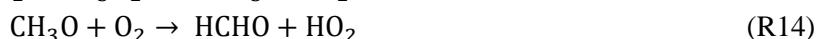
They are highly reactive and efficient oxidants in the gas, but more importantly in the liquid phase. Most prominent is the reaction of H₂O₂ to oxidize SO₂, which leads to acidification of cloud droplets. Peroxides are quite polar molecules and thus highly soluble in water, and other polar substrates. Organic peroxides like peracetic acid can decompose in water to form H₂O₂ and the corresponding acid, e.g. acetic acid. Recurrent peroxides besides H₂O₂, MHP and PAA are e.g. hydroxyl methyl hydroperoxide

(HMHP) and isoprene hydroperoxide (ISOPOOH), which is formed in rather clean regions with high isoprene emissions like forests. Biomass burning is a known primary source of H₂O₂ and MHP (Lee et al., 2000, Lee et al., 1997), although not all combustion processes lead to peroxide formation. Additionally, aqueous phase production of H₂O₂ and other peroxides has been proposed in cloud droplets (Marinoni et al., 2011). And thus release of H₂O₂ from cloud droplets could be an important source of HO_x in the FT. Organic peroxides like ISOPOOH are also recently discussed to play a significant role in the missing oxidative potential in sulfate formation in the FT (Dovrou et al., 2021).

Besides being a source via photolysis, they also act as a net sink for HO_x, since peroxides are highly soluble, and thus, they are efficiently washed out by wet deposition (e.g. by rain out or fog). Dry deposition towards the surface is another important loss process, whereby gases are deposited into the soil or the oceans. In order to evaluate the regional abundance of HCHO and peroxides and their relevance for HO_x, in situ measurement results and knowledge of their main sources and loss reactions is necessary.

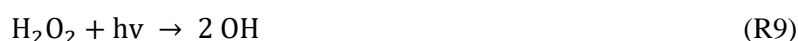
1.3.2 Photochemical production and loss reactions of HCHO, H₂O₂ and MHP

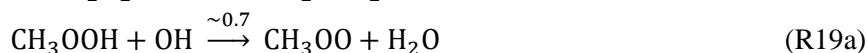
Clean conditions are nowadays rare to be found, as most air masses are influenced at least to some extent by anthropogenic emissions. Nevertheless, aged air masses with least amounts of air pollution can be found e.g. in remote marine boundary layer conditions, where NO_x concentrations are minimal (NO_x ≤ 50 ppt_v). Therefore, most trace gases represent natural background concentrations with the exception of long-lived species which are influenced by anthropogenic emissions. The marine boundary layer is thus perfectly suited for understanding key reactions of the atmospheric oxidation chain. The following reaction pathways thereby represent the simplest main production and loss processes of HCHO and peroxides on the basis of the methane oxidation (Fig. 3). For simplicity NO_x and halogen chemistry was excluded. After H-abstraction by OH, the methyl radical reacts with oxygen to the methyl peroxy radical (CH₃O₂; R4). The fate of this peroxy radical then determines if this reaction cycle produces HCHO, methanol (CH₃OH) or MHP: the combination of two methyl peroxy radicals produces HCHO and CH₃OH (R10 – R12), while the reaction with HO₂ yields MHP (R13).



Since methane concentrations are quite stable in the remote MBL due to its low reactivity, the production of HCHO or MHP is determined by OH and the reaction pathway of CH₃O₂, while photochemical production of H₂O₂ is only determined by the combination of HO₂ radicals (R6).

The main photochemical losses of both HCHO and the peroxides in clean conditions are the reaction with OH and their photolysis. For both hydroperoxides the photolysis recycles OH, while only the radical channel of HCHO leads to formation of HO₂ (R15a, R19). Therefore, net loss of HO_x only occurs through the molecular channel of the HCHO photolysis (R15b). In contrast, the reactions with OH are mostly net oxidant consuming (R16, R17a, R18). Note that loss of MHP via reaction with OH can lead to either production of HCHO or CH₃OO radicals. The branching ratio of this reaction varies between 0.65 and 0.83 in favor of the H-abstraction at the hydroperoxide leading to CH₃OO formation, with a recommended average of 0.70 (Allen et al., 2022b). The less favored reaction to release HCHO (R17b) also produces OH, so that it is irrelevant for the net change of HO_x, but a precursor of OH is converted into a precursor of HO₂.





Additionally, H_2O_2 , MHP and HCHO are subject to loss through deposition that removes these HO_x precursors from the atmosphere. Deposition is divided into two distinct processes, dry deposition, which is the removal of gases or particles from the atmosphere due to impaction onto land and ocean surfaces following turbulent transfer; and wet deposition, which occurs when gases are incorporated into suspended liquid water either by in-cloud scavenging or by washout from falling precipitation (Allen et al., 2022a). Therefore, dry deposition not only depends on the chemical properties (e.g. pH value, hydrophilic or lipophilic interactions), but also upon a variety of factors including surface properties (e.g. area, composition, moisture content) and other meteorological parameters like the vertical wind speed and the ambient temperature (Allen et al., 2022b; Fischer et al., 2019; Nguyen et al., 2015; Chang et al., 2004).

The solubility of gases is determined by the Henry's law, it states that the amount of dissolved gas in a liquid is proportional to its partial pressure above the liquid, in the so-called headspace. The determined proportionality factor is called Henry's law coefficient (or Henry's constant, k_H). H_2O_2 is highly soluble in water due to its high Henry's law coefficient of $8.3 \cdot 10^4 \text{ mol L}^{-1} \text{ atm}^{-1}$ (25 °C, O'Sullivan et al., 1996), and thus, the most sensitive to deposition out of all three compounds. Nonetheless, deposition is also a major loss for organic hydroperoxides and HCHO (Dienhart et al., 2022; Nussbaumer et al., 2021b; Fischer et al., 2019; Klippel et al., 2011). The most important production and loss processes for H_2O_2 , MHP and HCHO and the cycling of HO_x in clean conditions (without the contribution of NO_x) are shown in Fig. 3.

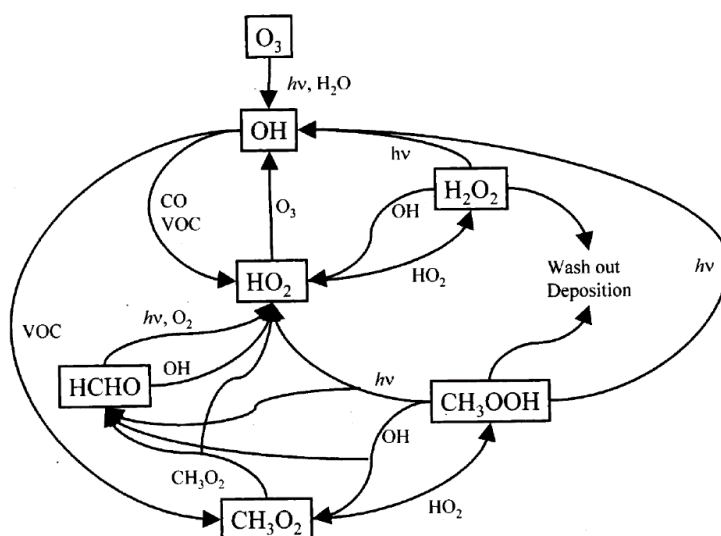
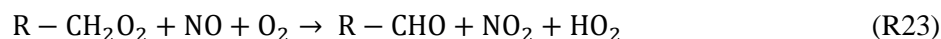
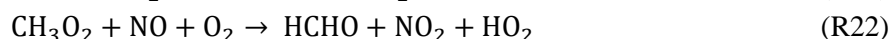


Figure 3: HO_x cycling and the thereby involved reservoir species on the basis of the methane oxidation in clean conditions, i.e. simplified by exclusion of NO_x and halogen chemistry (adopted from Reeves and Penkett, 2003).

Such clean conditions, so that NO_x chemistry can be excluded, only occur under the most remote conditions in the boundary layer, as nitrogen oxides are present almost everywhere nowadays. The remote marine boundary is one example where this can arguably be possible, far away from coastlines, seafaring and without the influence of continental air masses. Continental air masses represent

anthropogenic influenced conditions (i.e. $\text{NO}_x \geq 100$ ppt_v), so that peroxy radicals predominately oxidize NO to NO_2 , and thus peroxide formation is suppressed. As previously mentioned, this reaction is referred to as the NO_x enhanced OH recycling mechanism (Lelieveld et al., 2016). Organic peroxy radicals thereby enhance the production of HCHO and other aldehydes. Note that the oxidation of NO by organic peroxy radicals involves two steps: first the formation of a methoxy radical, followed by the addition of O_2 to yield the corresponding aldehyde and HO_2 .



But elevated concentrations of NO_x also add additional OH loss reactions, e.g. the formation of nitric acid (HNO_3) and nitrous acid (HONO).



The formation of HNO_3 is an important sink for NO_2 during the day and HNO_3 deposition rates are fast, as it is a highly soluble species. The formation of HONO during the day is less relevant, as the photolysis of HONO recycles OH and NO quite fast during daytime, although uptake on particles and loss via deposition is a relevant net sink for HO_x . The main changes of the HO_x recycling by the inclusion of NO_x are shown in Fig. 4. Generally, elevated mixing ratios of NO_x accelerate OH recycling and thereby simultaneously the oxidation of VOCs, while peroxide formation is suppressed.

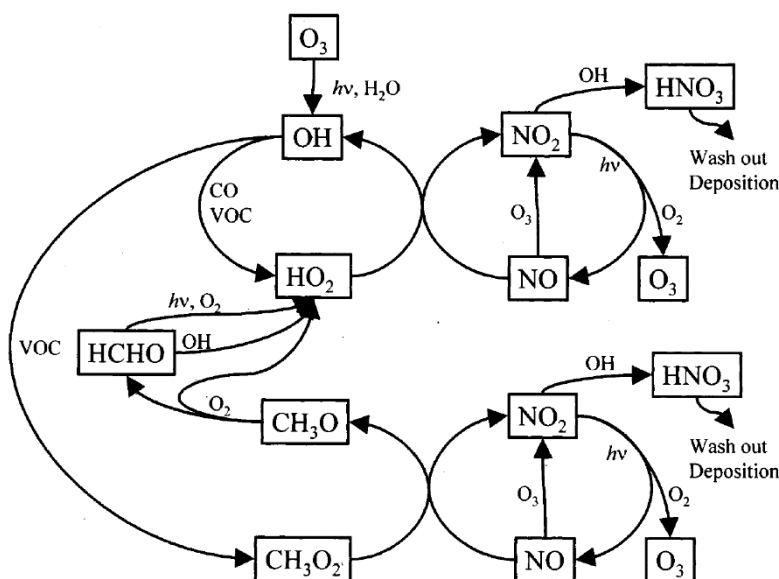


Figure 4: VOC oxidation in on the basis of the methane oxidation, simplified by exclusion halogen chemistry (adopted from Reeves and Penkett, 2003).

When considering the entire oxidation pathways of natural and anthropogenic VOCs, the production pathways of HCHO are very diverse as an intermediate during the oxidation chain of VOCs. Both oxidative additions, but also photolysis steps and some intramolecular reactions release formaldehyde. As the shortest chained carbonyl compound, it is highly reactive but generally less soluble in water than H_2O_2 , with a Henry's law coefficient of $\sim 5.4 \cdot 10^3 \text{ mol L}^{-1} \text{ atm}^{-1}$ (25 °C, Seyfioglu et al., 2007) an order of magnitude smaller than that of H_2O_2 with $\sim 8.3 \cdot 10^4 \text{ mol L}^{-1} \text{ atm}^{-1}$ at 25 °C (O'Sullivan et al., 1996). Main sources besides the oxidation of methane are the photochemical degradation of alkenes (e.g. oxidation of isoprene and ethene), methanol, acetaldehyde and MHP (Nussbaumer et al., 2021b; Axinte, 2017).

Degradation of alkenes not only includes oxidation by OH radicals, since unsaturated hydrocarbons are also oxidizable by reaction with O₃. This reaction is called ozonolysis, and it is characterized by the cycloaddition of the O₃ molecule to the double bond of the unsaturated hydrocarbon, thus forming the corresponding 1,2,3-trioxolane (molozone). Molozone is an unstable molecule, and thus they rearrange rapidly which causes the split into a Criegee intermediate and the corresponding carbonyl compound. The released Criegee intermediates are unique molecules as their chemical structure is characterized by two rather separated charge centers with biradical character. They are involved in new particle formation, OH production and various other reactions (Stone et al., 2012, Wennberg et al., 2018). Unimolecular decay of the Criegee intermediate releases OH and the corresponding alkoxy radical, which can then react to alcohols, carboxylic acids or peroxides. If the Criegee intermediate does not undergo unimolecular decay, it can react with various species in the atmosphere, e.g. with the initially released carbonyl compound in a second cycloaddition. Further reactions and photolysis steps then lead to a variety of products, e.g. peroxy radicals, aldehydes, ketones, peroxides and epoxides. These peroxy radicals are important precursor molecules for HCHO and hydroxyl methyl hydroperoxide (HMHP), e.g. by reactions with water or SO₂. Altogether, the ozonolysis of isoprene is a good example for the complexity and the variety of possible products (Fig. 5 & 6; Wennberg et al., 2018).

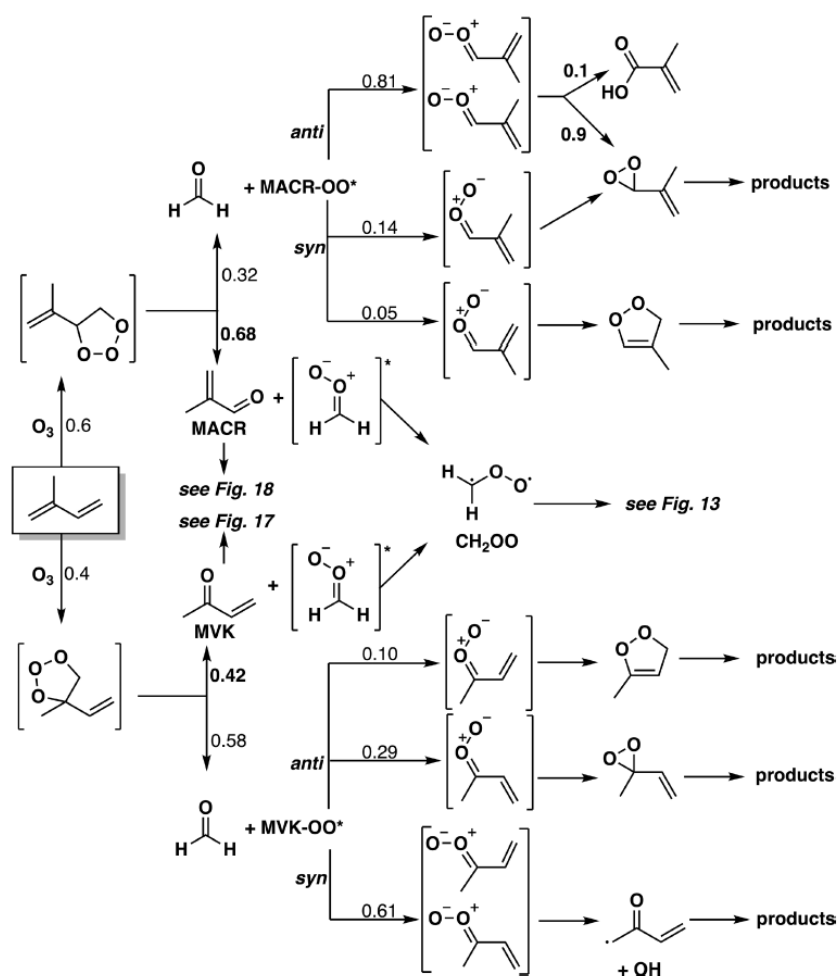


Figure 5: Reactions and products following the ozonolysis of isoprene. Many of the Criegee decomposition products remain unidentified (adopted from Wennberg et al., 2018).

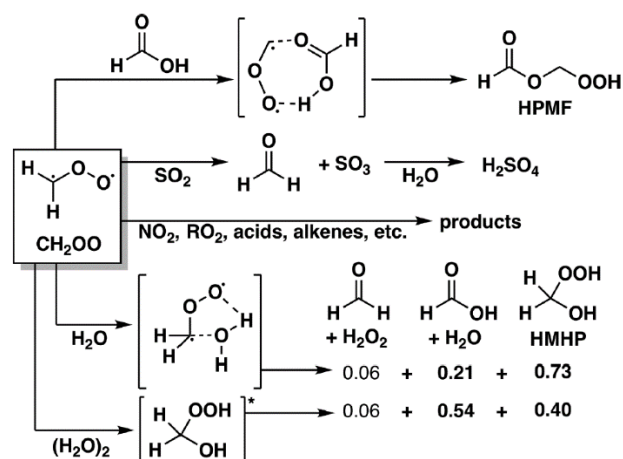
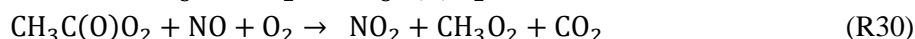


Figure 6: Reactions and products following the ozonolysis of isoprene. Many of the Criegee decomposition products remain unidentified (adopted from Wennberg et al., 2018).

Nonetheless, not only the oxidation of saturated and unsaturated hydrocarbons leads to production of HCHO. Photochemical degradation of oxidized volatile organic compounds (OVOCs) is another prominent example for its secondary production. The oxidation of CH_3OH is thereby representative for oxidation of aliphatic alcohols, which occurs in significant amounts in both clean and polluted conditions. Oxidation of CH_3OH contributed significantly to the total production of HCHO with ~14 % during the CYPHEX campaign in Cyprus (Nussbaumer et al., 2021b) and between 25 and 30 % during HUMPPA in the boreal forest of Finland (Axinte, 2017). The initial step is the abstraction of hydrogen atom, whereby two reaction pathways are possible (R26). Both reaction pathways lead to production of HCHO via the rapid reaction with oxygen (R27).



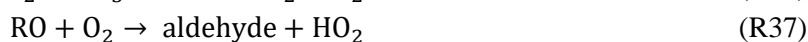
Further OVOCs like aldehydes and ketones are contributing to the secondary production of HCHO, e.g. acetaldehyde (CH_3CHO) and acetone (CH_3COCH_3). Especially the oxidation of acetaldehyde by OH can be a major local source of HCHO, Nussbaumer et al. (2021b) determined that it was responsible for up to ~15 % of total HCHO production during CYPHEX. After H-abstraction by OH (R28), the acetyl radical (CH_3CO) reacts with oxygen to the acetylperoxy radical ($\text{CH}_3\text{C}(\text{O})\text{O}_2$, R29), which subsequently oxidizes NO, followed by its degradation to CH_3 and CO_2 . The methyl radical then reacts fast with O_2 (analogously to R4) to the methyl peroxy radical (R30), which itself then produces HCHO by reaction with NO or MHP via reaction with HO_2 .



Oxidation processes by OH, HO_2 and O_3 dominate the photochemical degradation of VOCs in the troposphere, although further oxidants like the nitrate radical (NO_3) become the dominating oxidant of VOCs during nighttime (Liebmann et al., 2018b). NO_3 is a highly reactive radical which can react with several VOCs, although its reactions with saturated hydrocarbons are very slow compared to OH. However, production of NO_3 is less dependent on sunlight, as it is released by the reaction of O_3 with NO_2 (R31). Its rapid photolysis (R32) and reaction with NO (R33) limit the lifetime of NO_3 to a few seconds during the day. During night, the reaction with NO_2 results in a thermal equilibrium between NO_3 and dinitrogen pentoxide (N_2O_5) (Liebmann et al., 2018a).



These reactions play an important role for the cycling of NO_x , although they do not result in a net loss of nitrogen oxides from the gas phase. However, heterogeneous uptake of N_2O_5 on particles and the reaction of NO_3 with VOCs results in a net loss of NO_x , as the released nitric acid (HNO_3) or organic nitrates transition into the particulate phase (Liebmann et al., 2018a). NO_3 thereby reacts analogously to OH with saturated VOCs: the first and limiting step is the H-abstraction to release the respective alkyl radical, which then rapidly reacts with O_2 to the corresponding peroxy radical (R35). During night, NO is converted into NO_2 by O_3 , so that the peroxy radical reacts with further NO_3 to the alkoxy radical (R36), which rapidly reacts with O_2 to an aldehyde (R37).



Formaldehyde production through CH_4 oxidation by NO_3 is only marginal, as the reaction constant is more than three orders of magnitude smaller than for the reaction of CH_4 with OH with $k_{\text{NO}_3+\text{CH}_4} = 1.0 \cdot 10^{-18} \text{ cm}^3 \text{ molecule}^{-1} \text{ s}^{-1}$ and $k_{\text{OH}+\text{CH}_4} = 6.4 \cdot 10^{-15} \text{ cm}^3 \text{ molecule}^{-1} \text{ s}^{-1}$ (<https://iupac-aeris.ipsl.fr/htdocs/datasheets/>; July 2022). Furthermore, unlike OH, NO_3 is only the initiator of the oxidation and it is not recycled within this mechanism.

The more relevant oxidation pathways which can lead to significant HCHO production are the oxidation of unsaturated hydrocarbons (e.g. isoprene, ethene, α -pinene) by NO_3 . Similar to the daytime oxidation by OH, the initiative step is the addition of NO_3 into the double bond of the VOC forming the nitrooxy alkyl radical as shown in Fig. 7 on the example of the isoprene oxidation (R36). The resulting radical then reacts rapidly by addition of O_2 to the corresponding nitrooxy peroxy radical (R37). The following reaction with HO_2 , NO_3 or NO yields a variety of products like HCHO, peroxides, nitrates, ketones (e.g. methyl vinyl ketone (MVK)) and aldehydes (e.g. methacrolein (MACR)). Note that the photochemical degradation of MVK and MACR is a further source of HCHO (Wennberg et al., 2018).

Although the reaction with NO_3 only represents a minor sink for isoprene (5 – 6 %), a considerable proportion of isoprene-derived nitrates (40 – 50 %) are ascribed to NO_3 oxidation (Wennberg et al., 2018). This again highlights the relevance of NO_3 for the nighttime oxidation of unsaturated VOCs. Further important gaseous oxidants in the marine boundary layer, especially close to urban areas, are the halogen radicals.

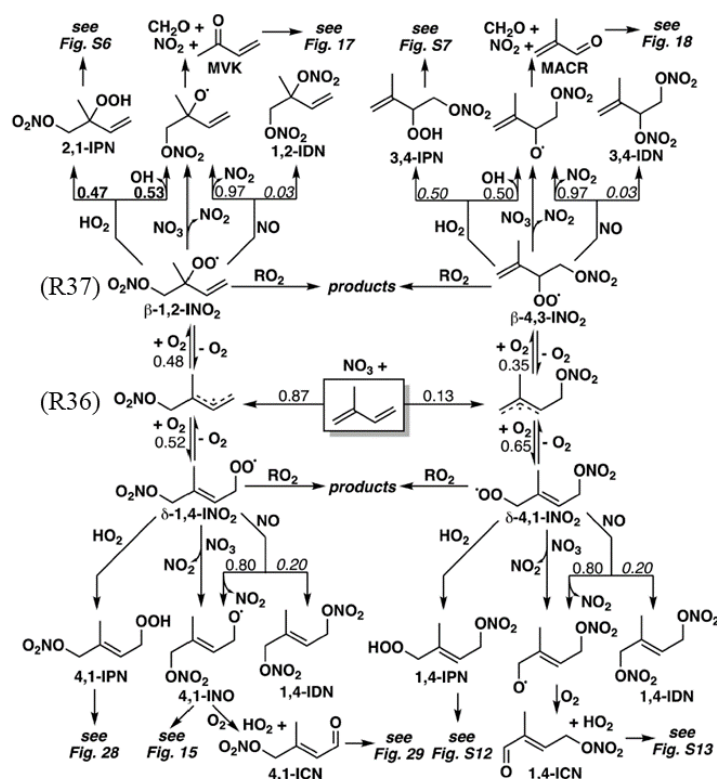


Figure 7: Reactions and products following the oxidation of isoprene by the nitrate radical (adopted from Wennberg et al., 2018).

Chlorine (Cl) radicals are known to accumulate in the urban influenced marine boundary layer, e.g. by photolysis of ClNO₂, which can enhance VOC oxidation rates in the early morning (Eger et al., 2019). Cl thereby reacts faster with CH₄ than OH and NO₃ ($k_{\text{Cl}+\text{CH}_4} = 1.0 \cdot 10^{-13} \text{ cm}^3 \text{ molecule}^{-1} \text{ s}^{-1}$; <https://iupac-aeris.ipsl.fr/htdocs/datasheets/>; July 2022). Wennberg et al. (2018) also highlight, that the reaction of Cl with isoprene is about four times faster than that with OH, and with peaking concentrations of up to $10^5 \text{ atoms cm}^{-3}$ in the urban influenced marine boundary layer, chlorine chemistry can reach comparable reaction rates to that of OH. Globally, Cl concentrations are expected to only reach an upper limit of $10^3 \text{ atoms cm}^{-3}$ (Wennberg et al., 2018), and thus the impact of chlorine chemistry is expected to be mainly important on a local scale.

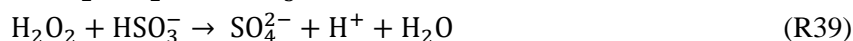
1.4 Heterogeneous chemistry and the connection to the particle phase

Heterogeneous chemistry describes the interaction and reaction of species which are in different phases, e.g. the interaction of trace gases with solid particles. Atmospheric aerosols are liquid or solid particles in air, which can vary widely in their shape, size and composition. Aerosols are divided into primary particles, which are released directly into the atmosphere, e.g. by biomass burning, volcanic eruptions, combustion of fossil fuels, wind-driven suspension of dust or sea salt and further processes. In contrast, secondary aerosols are formed by chemical and physical processes within the atmosphere (gas to particle conversion). The most prominent examples are the secondary organic aerosols (SOA), which can be classified as particles which result from atmospheric oxidation of biogenic VOCs (e.g. oxidation of isoprene, mono- and sesquiterpenes). The resulting oxidation products are highly polar substances so that they tend to nucleate and thereby form new particles, or they undergo a transition into the particle phase (heterogeneous growth of particles).

Depending on their composition, aerosols have a net cooling or warming effect on the global radiative forcing of the Earth by scattering and absorbing light of certain wavelengths (IPCC report 2021). Health effects of particulate matter are being studied extensively as they are a known source of oxidative stress

in human bodies and to cause irritation and severe damage to lung cells (Lelieveld et al., 2019). Oxidative stress of aerosols is often related to inhalation of particles, which then release or react in situ to reactive oxygen species (ROS, e.g. OH, H₂O₂) in lung fluid (S. Lelieveld et al. 2021). However, the key role of atmospheric aerosols discussed in this thesis is their relation to trace gases via heterogeneous chemistry and the formation of clouds. Once these aerosol particles reach a certain size and composition, mainly the hydrophilic sulfate aerosols, they become cloud condensation nuclei (CCN), so that water can condense on their surface. Without these particles, nucleation of water vapor is inhibited, so that CCN play a major role for cloud formation and the radiation budget of the atmosphere.

This heterogeneous interaction between the gas and the liquid or solid phase impacts also the abundance of HO_x radicals and their respective reservoirs. H₂O₂ and HMHP are highly soluble molecules so that they transition fast onto liquid particles. MHP, PAA and EHP are less sensitive to wet scavenging due to their smaller Henry coefficients (O'Sullivan et al., 1996). Vertical transport of H₂O₂ through clouds is thus less effective than that of MHP due to its high solubility, still, measurements of deep convective outflow show enhanced mixing ratios of H₂O₂ (Nussbaumer et al., 2021a; Hamryczak et al., 2022). Depending on the chemical composition of these particles, the peroxides undergo certain reactions (e.g. oxidation), or, if the particle does not contain reactive molecules, the peroxides can theoretically be transferred back to the gas phase, e.g. if the particle consisted mostly out of water. Globally, H₂O₂ acts as a major oxidant in the liquid phase for the oxidation of sulphur dioxide (SO₂) to sulfate ions (SO₄²⁻). This reaction got prominent in the late 1970's as the main contributor to acidic rain (Seinfeld and Pandis, 2016).



Organic peroxides, e.g. MHP, PAA and ISOPOOH, are also known to be able to oxidize SO₂ and are recently being discussed as missing oxidants to close the oxidative gap of atmospheric chemistry models for the formation of sulfate aerosols. Dovrou et al. (2019 & 2021) discuss the role of ISOPOOH as oxidant for the formation of sulfate in cloud droplets, and highlight that the oxidative potential of ISOPOOH in high-isoprene and low-NO_x conditions (e.g. the Amazon) is even higher than that of H₂O₂. They find that ISOPOOH contributes with ~55 % under modern conditions over the Amazon compared to ~34 % for H₂O₂. Globally, H₂O₂ oxidation dominates the sulfate production with more than 50 %, based on the global 3-D atmospheric chemistry model GEOS-Chem (NASA Goddard Earth Observing System, Dovrou et al., 2019).

Oxidation of formaldehyde in cloud droplets is expected to be the main source for formic acid, with a sink of HCHO mixing ratios of at least 0.1 ppbv h⁻¹ (Seinfeld and Pandis, 2016). Formic acid can then be further oxidized to CO₂ as the termination of the oxidation chain, analogously to gas phase oxidations of OVOCs. The oxidation pathway towards formic acid occurs additionally in the gas phase, as the hydrated HCHO, methanediol, transitions partially back from the liquid phase to the gas phase, where oxidation with OH is more efficient due to the higher concentrations of OH. In sum, the role of HCHO for the acidification of cloud droplets is more important than previously assumed (Franco et al., 2021). Formaldehyde is also discussed as a major contributor to new particle formation via its heterogeneous reactions in cloud droplets. Dovrou et al. (2022) demonstrate two reaction pathways which oxidize SO₂ to SO₄²⁻, once the direct oxidation by reaction with HCHO to hydroxy methyl sulfonate (HMS) and also the oxidation via reaction with hydroxyl methyl hydroperoxide (HMHP), which is a product of HCHO and H₂O₂. Oxidation of SO₂ by HMHP thereby recycles HCHO, which acts as a catalyst. Implementation of the ISOPOOH and HMHP chemistry in GEOS-Chem eliminated the underprediction of sulfate in some cases. Formaldehyde is thus affecting not only the gas-phase chemistry of the atmosphere, but also PM sulfate and carbon and thus it affects, in an unexpected way, both climate and human health (Dovrou et al., 2022).

1.5 Further heterogeneous processes in the marine boundary layer

As already mentioned before, the mixing ratio of a certain trace gas increases due to production processes (e.g. photochemical production, primary emissions), while it decreases via several loss processes (e.g. photochemical loss, wet and dry deposition). In the marine boundary layer, further production and loss pathways become relevant of both physical and meteorological nature. The complexity of this system makes studies of trace gas distributions in the MBL even more valuable, since some processes, e.g. the transition of trace gases between air and sea remain to some extent uncertain and underrepresented in current atmospheric chemistry models (Wang et al., 2020).

Despite the dry and wet deposition, sea spray enables the bidirectional transition of atmospheric species between surrounding air masses and the ocean. It is mainly caused by bursting air bubbles due to movement and break down of waves, so that miniscule aqueous droplets are released from the ocean which are then transported within the MBL. The movement of the ocean thereby establishes a permanent source of aqueous sea salt aerosol (SSA), which contains both sea salt and organic matter. These organic compounds can then be subsequently released into the MBL, so that SSA can act as a source of VOCs depending on its chemical composition and the surrounding conditions. Transport and ageing of these particles establishes a global source of CCN. Additionally, the ocean is a known source of gaseous dimethylsulfide (DMS), e.g. by the emissions of algae close to the coastline. Oxidation of DMS then leads to formation of sulfate and often also partitioning into the particle phase. Sulfate aerosols and SSA often develop into CCN due to their high hygroscopicity, and play an important role in cloud formation and for the cleansing air pollution from the atmosphere (Rosenfeld et al., 2002; Liss and Johnson, 2014). Despite the release of DMS, the sea surface microlayer (SML) is a known source for further organic compounds, which are mainly released from phytoplankton. Tripathi et al. (2020) measured VOCs in the MBL of the Arabian Sea and determined 20 – 40 % elevated mixing ratios of alkenes during daytime compared to their nighttime values. Highest mixing ratios of ethene (8.9 ± 3.5 ppb_v) and propene (3.4 ± 1.3 ppb_v) were detected. Such high values of unsaturated hydrocarbons can lead to significant production of HCHO and affect the local oxidation budget.

Brüggemann et al. (2018) highlight the potential of interfacial photochemistry at the ocean surface as an abiotic source of VOCs and aerosols, which, on a global scale, could compete with emissions from marine biology and for up to more than 60 % of the aerosol mass over remote oceans.

It remains difficult to quantify the net effect of air-sea exchange on a global scale, as the release of VOCs via sea spray, the SML and interfacial photochemistry strongly depends on the local conditions e.g. biological productivity, temperature, wind speed and the chemical composition of the sea water. Further research is necessary to better understand the global effects of air-sea exchange; as recent studies highlight its potential to strongly affect atmospheric chemistry in the MBL.

2. Methods & experimental procedures

This section covers a description of analytical methods for the quantification of trace gases (mainly HCHO, H₂O₂ and organic hydroperoxides), a short comparison with other well-established techniques in atmospheric sciences, as well as the application during the Air Quality and Climate Change around the Arabian Basin (AQABA) expedition during summer 2017.

The development of analytical techniques includes both scientific and technical knowledge, since the applied method must provide reliable and reproducible results. Application of a certain method for trace gas analysis involves several analytical criteria, such as the precision (P), the accuracy (A), the limit of detection (LOD) and the total measurement uncertainty (TMU). Furthermore, the applied method should enable selective and continuous detection with a preferably high temporal resolution to resolve rapid changes of the trace gas mixing ratio. This work is based on wet-chemical spectrophotometric detection techniques, which have the advantages of a high sensitivity (and thus a low detection limit), marginal chemical interferences and only minimal cross sensitivities (e.g. HCHO measurements to other aldehydes and ketones (Glowania et al., 2021; Hladová et al., 2019)). On the negative side, these methods demand frequent calibrations and zero gas measurements and their temporal resolution is limited by the transport of liquids within the instrument.

2.1 Formaldehyde measurement techniques

Formaldehyde got prominent as an indoor air pollutant, as it was previously released in hazardous amounts from e.g. chipboard panels, furniture and other processes of the furniture industry. Since environmental control policies exerted pressure to determine the effects of HCHO to better understand VOC oxidation processes and their relation for human health, new measurement techniques have been developed (Salthammer, 2013). There are several methods available to detect HCHO with typical LODs in the range of tens to several hundred ppt_v (Table 1). Formaldehyde measurement techniques can be roughly separated into wet-chemical techniques, which mostly rely on in situ derivatization and following fluorescence detection (Hantzsch, HPLC–DNPH), mass spectrometry (GC–MS, PTR–MS) and spectroscopy (FTIR, TDLAS, DOAS, LIF, CRDS).

The development of laser induced fluorescence (LIF) instruments achieved the lowest detection limits out of all HCHO measurement techniques combined with the highest temporal resolution (18 ppt_v at 1 s resolution, Cazorla et al., 2015), but this technique demands the highest instrument and personal costs. The Hantzsch method, on which the HCHO measurements in this thesis are based on, also utilizes the fluorescence principle, although initiated by in situ derivatization of HCHO instead of excitation of the HCHO molecule itself. The method is less cost intensive and reliable, and has a sufficient LOD for measurements in the boundary layer. Glowania et al. (2021) compared three different HCHO measurement techniques in the SAPHIR chamber, the Hantzsch method, CRDS and DOAS. CRDS and DOAS showed good linear correlation coefficients with the Hantzsch dataset ($R^2 \geq 0.96$). The Hantzsch method provided the lowest mixing ratios, followed by on average 2 % higher values based on the DOAS and 8 % higher values based on the CRDS technique with an intercept of -0.13 ppb_v. Additionally, CRDS and Hantzsch are both in need of regular zero measurements to correct background signal drifts. Wisthaler et al. (2008) also compared different HCHO measurement techniques and the Hantzsch method provided the lowest mixing ratios as well. The known O₃ interference is discussed as a possible reason for the offset, the manufacturer provides an interference of 1 ppb_v HCHO per 800 ppb_v of O₃ (AL4021 manual v2.2, Aero-Laser GmbH, 2019) so that under normal tropospheric conditions the interference is only marginal. Altogether, the Hantzsch method provided the best sensitivity and temporal resolution of all three instruments used in this study (Glowania et al., 2021). Altogether,

various analytical techniques are available for quantification of HCHO in the range of hundreds of ppt_v, which is sufficient for measurements in the continental boundary layer. Airborne measurements are more challenging and demand more specialized techniques with the LODs in the low ppt_v range and highest possible temporal resolution.

Recently developed satellite instruments (e.g. the TROPOspheric Monitoring Instrument, TROPOMI) enable global mapping of HCHO and other major air pollutants, with increasing resolution over the last decades (De Smedt et al., 2008; De Smedt et al., 2018; Zhu et al., 2020). These techniques thereby enable the identification of biomass burning and anthropogenic air pollution hotspots; and also to observe regional and seasonal trends.

Table 1: Brief comparison of analytical techniques for the detection of gaseous HCHO.

Method	Detection principle	LOD / ppt _v	Resolution / s	Reference
Hantzsch reaction	Fluorescence	80 – 128	180	Dienhart et al., 2022
HPLC-DNPH	Fluorescence	500	7200	Vairavamurthy et al., 1992
GC-MS	Mass spectrometry	300	900	Yokouchi et al., 1979
PTR-MS	Mass spectrometry	–	60	Lindinger and Jordan, 1998
FTIR	Infrared absorption	400	300	Hak et al., 2005
TDLAS	Infrared absorption	50	60	Harris et al., 1992
DOAS	Differential absorption spectroscopy	900	130	Glowania et al., 2021; Kluge et al., 2020
Satellite-measurements	Differential absorption spectroscopy	–	–	De Smedt et al., 2021; Zhu et al., 2020
LIF	Laser-induced-fluorescence	18	1	Cazorla et al., 2015
CRDS	Cavity ring-down spectroscopy	200	180	Glowania et al., 2021

2.1.1 The formaldehyde monitor AL4021

HCHO measurements were performed with a modified version of the commercially available AL4021 (Aero-Laser GmbH, Garmisch-Partenkirchen, Germany). The AL4021 is a completely automated and continuously sampling analyzer for gaseous and liquid detection of HCHO based on the Hantzsch reaction. As already mentioned, this reaction is highly sensitive to low concentrations of HCHO (low ppb_v mixing ratios and µg/L for liquid samples) and has only marginal chemical interferences and cross-sensitivities (Glowania et al., 2021; Hladová et al., 2019). Main advantage of the AL4021 is its low detection limit and the possibility of continuous and automated measurements with a rather compact instrument design. In contrast, its main disadvantage is the necessity of several chemicals and large amounts of purified water, for which the transport can be challenging and costly in order to operate the instrument on measurement expeditions. The AL4021 logs in 3 second intervals, although its sensitivity is limited to the liquid transport within the instrument and thus higher integration times are necessary. The detailed characterization of the instrument is described in the following sections.

2.1.2 Detection principle – the Hantzsch reaction

The one-channel technique (Fig. 8) allows quantification of HCHO via in situ derivatization by use of the Hantzsch reaction (Kelly and Fortune, 1994). To dissolve gaseous HCHO, ambient air is sampled at 1 L/min through a glass coil, which is flushed simultaneously with sulfuric acid at 0.45 mL/min. HCHO is thereby quantitatively dissolved in the sulfuric acid (at temperatures below 10 °C), which in turn is

transported to the reaction coil by a peristaltic pump. The consecutive addition of acetylacetone (acac) and ammonium acetate (NH₄OAc) in a buffered solution (Hantzsch reagent) to the sample solution starts the Hantzsch reaction (Fig. 8). It yields the fluorescent dye DDL (3,5-diacetyl-1,4-dihydrolutidine) in equimolar fraction with respect to HCHO (Kelly and Fortune, 1994). To enable a preferably fast reaction, the reaction coil is tempered to 68 °C. The excitation of DDL is performed in a flow cell at 410 nm (Hg-lamp), followed by fluorescence detection at 510 nm by a photomultiplier (H957-01, Hamamatsu Photonics GmbH, Herrsching, Germany). The quantification of HCHO is ensured by liquid and gas phase calibrations during the operation of the instrument.

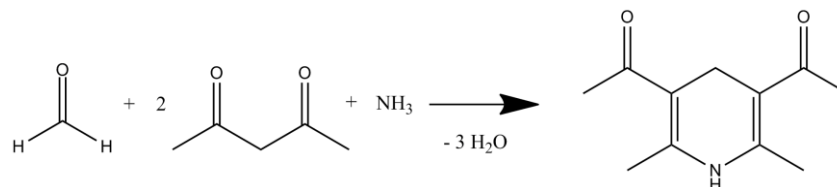


Figure 8: Hantzsch reaction of formaldehyde and acetylacetone in ammoniac solution, the product DDL (3,5-diacetyl-1,4-dihydrolutidine) is a fluorescent dye which is excited at 410 nm followed by fluorescence detection at 510 nm.

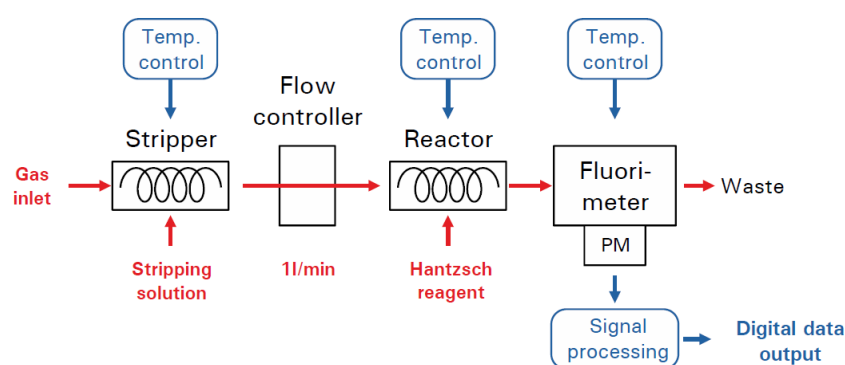


Figure 9: Scheme of the AL4021 instrumental design.

2.1.3 Sampling technique & operation of the AL4021

This work is based on liquid analysis and therefore all gaseous analysts have to be transferred quantitatively into the liquid phase. Several techniques have been proven suitable for heterogeneous sampling of HCHO and H₂O₂, e.g. impinger (Tanner et al., 1990), cryogenic traps (Campos and Kok, 1996), diffusion scrubbers (Dasgupta et al., 1988), nebulizer (Sauer, 1997) and the here used sampling coils (Lee et al., 1995).

Sampling coils are in comparison to the other sampling techniques one of the most ideal to use, as they can be used easily with peristaltic pumps for continuous and automated design, combined with a high sampling efficiency. The efficiency thereby strongly depends on the Henry's law coefficient of the target molecule. HCHO and H₂O₂ are ideal candidates as they can be quantitatively dissolved into cold and buffered aqueous solutions. Organic peroxides are less soluble in aqueous solutions and thus not ideal. These negative artifacts have to be considered in data processing. The transition of a species between the gas and liquid phase is described by the Henry's law (Eq. 1) based on its partial pressure (p , atm) and its concentration in the liquid phase (c , mol L⁻¹) at a certain temperature (T , K). It is valid for diluted concentrations and describes the equilibrium between gas and liquid depending on the temperature. The Henry coefficient K_H (mol L⁻¹ atm⁻¹) is expressed by the van't Hoff equation (Eq. 2) with the empirical constants a and b (O'Sullivan et al., 1996).

$$(K_H)_T = \left(\frac{c}{p}\right)_T \quad (1)$$

$$K_H(T) = \exp\left(\frac{a}{T} - b\right) \quad (2)$$

Based on the results of Kelly and Fortune (1994), scrubbing of HCHO is achieved with an efficiency of 100 % by using a sulphuric acid buffer (0.1 mol L⁻¹). HCHO thereby reacts to the corresponding hemiacetal in acidic solution (R14).

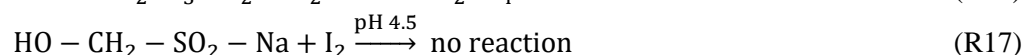
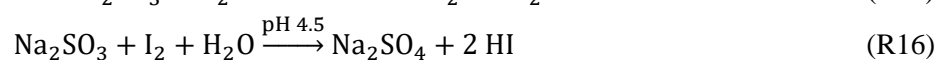
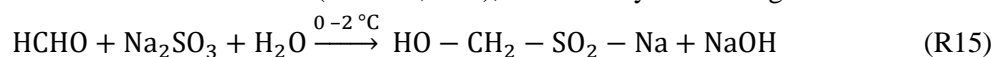


Lazrus et al. (1986) show that the stripping efficiency of H₂O₂ is ≥ 99.9 %, however, for MHP and EHP, stripping efficiencies are only in the range of ~60 % and dependent on the pH of the buffered sampling solution (O'Sullivan et al., 1996).

Linearity of this method has already been reported by Kelly and Fortune (1994), which is necessary to enable external calibration of the instrument by injection of liquid and gaseous standards of HCHO. Liquid samples are prepared freshly before injection by diluting a cooled (~4 °C) HCHO stock solution. These liquid standards are then injected through a separated inlet into the sampling coil (instead of the sampling solution). The HCHO stock solution is prepared by dilution of 3 mL 37 % HCHO with ultrapure water in a 1000 mL brown glass flask. The stock solution is ready to use after mixing and can be stored for several weeks in the fridge. HCHO standard solutions were prepared by diluting 1 mL HCHO stock in a 250 mL volumetric flask, followed by another dilution of 1 mL in to 250 mL in an additional volumetric flask (twice 1:250). These standards were prepared freshly before analysis and were used to calculate the precision of the instrument. The concentration of the HCHO stock solution was determined by weekly iodometric redox titrations.

2.1.4 Iodometric redox titration of HCHO

The iodometric redox titration is based on the reaction of iodine (I₂) and starch, which form an intense blue-black complex in aqueous solvents, which is ideal to be used as an indicator for miniscule amounts of I₂. HCHO concentrations are determined with the principle of the back titration, whereby HCHO is initially masked via reaction with bisulfate ions (SO₃²⁻, R15) in boric acid buffer (H₃BO₃). Excess bisulfate is removed by titration with I₂, which oxidizes bisulfate to sulfate (SO₄²⁻, R16) although excess I₂ does not react with the masked HCHO in acidic conditions (R17). HCHO is subsequently released by the addition of sodium carbonate (Na₂CO₃, R18), followed by titration against I₂.



Experimental procedure:

4 mL sodium bisulfate (Na₂SO₃) are added to a cooled mixture (0 – 2 °C) of 10 mL HCHO stock, 25 mL H₃BO₃ and 25 ml H₂O in an Erlenmeyer flask. Let the HCHO react for 7 minutes at 0 – 2 °C, then add 5 mL acetic acid (1 mol L⁻¹) and 1 mL of the starch solution. Excess SO₃²⁻ is removed by titration with I₂ (0.025 mol L⁻¹). The masked HCHO is then released by the addition of 30 mL Na₂CO₃ (1 mol L⁻¹). Titration of the SO₃²⁻ ions with I₂ corresponds to the volume of HCHO (1:1, R18) in the sample:

$$c_{HCHO} = \frac{c_{I_2} \cdot V_{I_2}}{V_{HCHO}} \quad (3)$$

The concentration of the HCHO stock solution has to be checked at least once a week during field campaigns, as it is one of the most important variables to achieve accurate results for the ambient HCHO mixing ratio, the formaldehyde stock solution is usually stable for a few weeks when stored in a brown glass flask in a refrigerator.

2.1.5 Calibration of the AL4021

Determination of the HCHO mixing ratio is performed by calculation of the AL4021 sensitivity via external calibration with liquid standards as described above. Each calibration cycle starts with injection of zero gas, meaning ambient air which has been dried and cleaned from interfering species. The zero gas cartridge (Infiltec GmbH, Speyer, Germany) contains silica gel (SiO₂) and Hopcalite® (MnO₂ / CuO; IAC-330, Infiltec GmbH, Speyer, Germany) as a catalyst to remove VOCs and O₃. Both substances are exchanged twice a week and can be regenerated in an oven. After removal of VOCs the clean air is injected through the sampling valve. The next step of the calibration is the injection of the freshly prepared HCHO standard solution into the sampling coil. To ensure a stable signal this step is performed for 5 – 10 minutes. The instrument then switches the three-way valve and initiates injection of the sampling solution, but still with zero gas, for another 5 – 10 minutes. Both signals are averaged in post to calculate the sensitivity of the instrument, represented by U_{standard} and $U_{\text{zero gas}}$ in Eq. 4. The expected mixing ratio of the liquid standard (μ , ppb_v) is then calculated via Eq. 5 with the sampling gas flow ($V_{\text{sampling,g}}$), the molar volume of an ideal gas (V_{mol}) and the flow of the sampling solution ($V_{\text{sampling,l}}$), which have to be controlled regularly.

$$S_{\text{HCHO}} = \frac{U_{\text{standard}} - U_{\text{zero gas}}}{\mu} \quad (4)$$

$$\mu = \frac{c_{\text{stock}}}{250 \cdot 250} \cdot \frac{V_{\text{mol}} \cdot V_{\text{sampling,l}}}{V_{\text{sampling,g}}} \cdot 10^9 \quad (5)$$

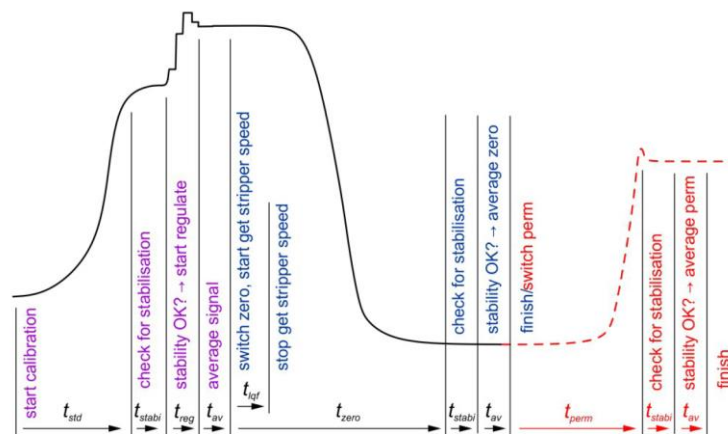


Figure 10: Schematic for the injection of liquid HCHO standards (AL4021 manual v2.2, Aero-Laser GmbH, 2019).

In addition to the liquid standards, zero gas measurements are performed every 3.5 hours for 30 minutes to identify drifts of the instrumental background signal and to calculate the detection limit (LOD) of the AL4021. Instrumental drifts can occur e.g. by changing the Hantzsch reagent solution and varying temperatures, and are corrected in post-processing by linear interpolation between the zero gas measurements, which represent the background signal of the AL4021.

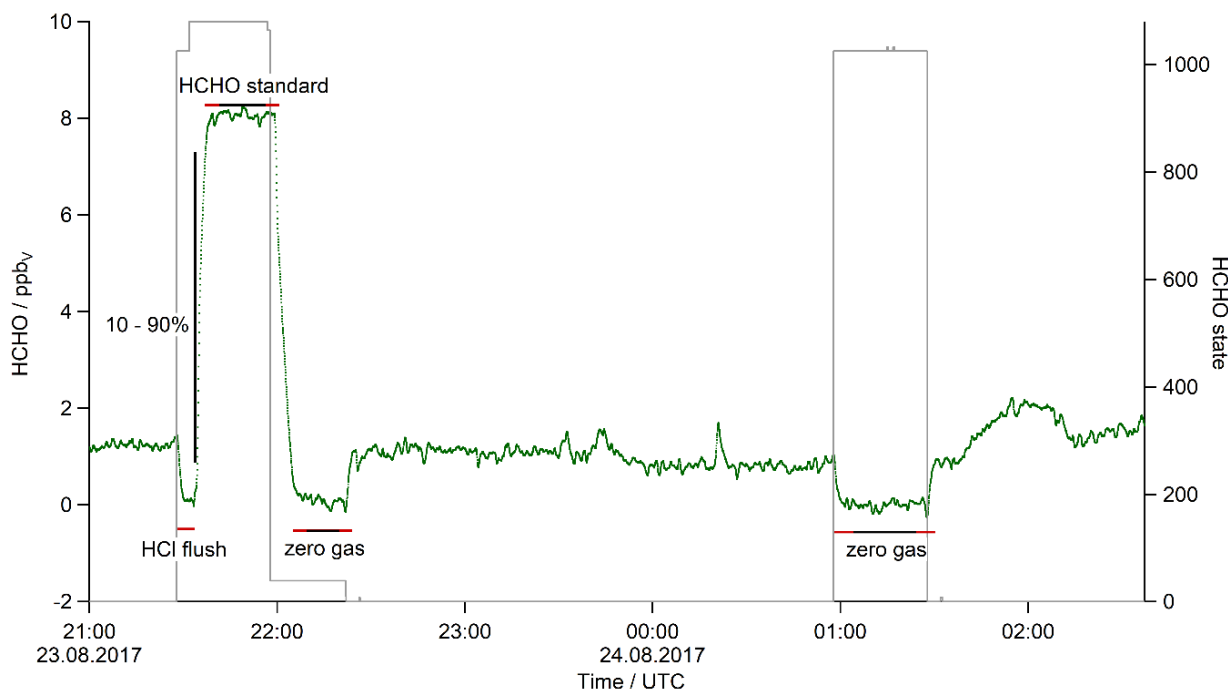


Figure 11: Example of ambient HCHO measurements during AQABA including the calibration of the instrument. The calibration includes the injection of 0.1 M HCl (4 min), followed by injection of a HCHO standard solution (26 min) and zero gas (24 min), the lines in black are used for the determination of the sensitivity, LOD and temporal resolution while the red parts were excluded from the dataset.

2.1.6 Temporal resolution & response

The AL4021 logs data points in 3 second intervals, but the response of the instrument is mainly limited by the transport of the sample with the peristaltic pump. An increase of the pump speed thus results in a higher temporal resolution, but simultaneously decreases the detection limit of the instrument. The optimal sampling solution flow of 0.45 mL min^{-1} was determined to give the highest temporal resolution and the lowest LOD, respectively. Additionally, the detection of HCHO via fluorescence causes a time delay, as the transport from the sampling coil, reaction to DDL followed by excitation in the flow cell accounts for an offset of ~ 5 min.

The effective temporal resolution was then calculated as the response of the instrument towards rapid changes of the HCHO mixing ratio. Therefore, the injection of liquid HCHO standards is perfectly suited, as it's reproducible and the HCHO signal increases fast. The signal increase from 10 % to 90 % of the standard injection then yielded the effective temporal resolution. As shown in Table 2, the liquid calibrations during the AQABA campaign demonstrate a mean value of 169 seconds. The effective temporal resolution of the AL4021 was therefore set so 180 seconds, which is not in agreement with the findings by Aero-Laser, who indicate a temporal resolution of ~ 90 seconds (AL4021 manual v2.2, Aero-Laser GmbH, 2019).

Table 2: Determination of the AL4021 temporal resolution by the signal increase of the liquid HCHO standards.

Date	Signal / ppbv	10 % / ppbv	90 % / ppbv	Δt / s
02.07.	8.759	0.876	7.883	144
04.07.	8.688	0.869	7.819	204
07.07.	8.823	0.882	7.941	168
10.07.	9.406	0.941	8.465	189
15.07.	9.016	0.902	8.114	78
17.07.	8.528	0.853	7.675	183
19.07.	8.793	0.879	7.914	177
24.07.	9.374	0.937	8.437	93
26.07.	10.122	1.012	9.110	243
31.07.	9.777	0.978	8.799	177
03.08.	8.236	0.824	7.412	198
06.08.	7.844	0.784	7.060	159
10.08.	9.061	0.906	8.155	216
15.08.	9.085	0.909	8.177	321
18.08.	8.821	0.882	7.939	120
21.08.	8.014	0.801	7.213	132
23.08.	8.065	0.807	7.259	156
25.08.	8.119	0.812	7.307	183
27.08.	8.152	0.815	7.337	171
29.08.	8.101	0.810	7.291	162
31.08.	7.969	0.797	7.172	165
31.08.	7.909	0.791	7.118	90
Mean	8.666	0.867	7.780	169

2.1.7 Detection limit

The limit of detection (LOD) is defined as the lowest signal, which can still be differentiated from the instrumental background noise. The LOD of the AL4021 was calculated with data of the zero gas measurements during the AQABA ship campaign. The timeline of the zero gas measurements presented in Fig. 12 indicates higher noise levels from the 08.08. till the 14.08.2017, which represent the data acquired in the Arabian Sea and the Gulf of Aden during high wave conditions. It seems likely, that the strong movement of the ship influenced the background signal of the AL4021 by affecting the transport of the solvents within the instrument. In a dataset which follows a normal distribution (Gauss distribution), the mean value represents the base value and the 2σ standard deviation represents 95 % of the measured data. And thus, with a signal to noise ratio of 2σ , only 5 % of the data would not be differentiable from noise.

$$\text{LOD}_{\text{HCHO}} = 2\sigma_{\text{zero gas}} \quad (6)$$

In the histogram presented in Fig. 13, the Gauss fit of the zero gas measurements (180 second averages) confirms normal distributed data with a mean value of -0.005 ppbv and the 2σ standard deviation covering 95 % of the data points (1599/1684). Therefore, the LOD was determined as the 2σ standard deviation as the signal to noise ratio, which results in a detection limit of 0.128 ppbv for atmospheric HCHO with a temporal resolution of 180 seconds. Exclusion of the wavy conditions improves the

detection limit by about 48 ppt_v, so that the achieved LOD would be below the manufacturer specification of 100 ppt_v (AL4021 manual v2.2, Aero-Laser GmbH, 2019).

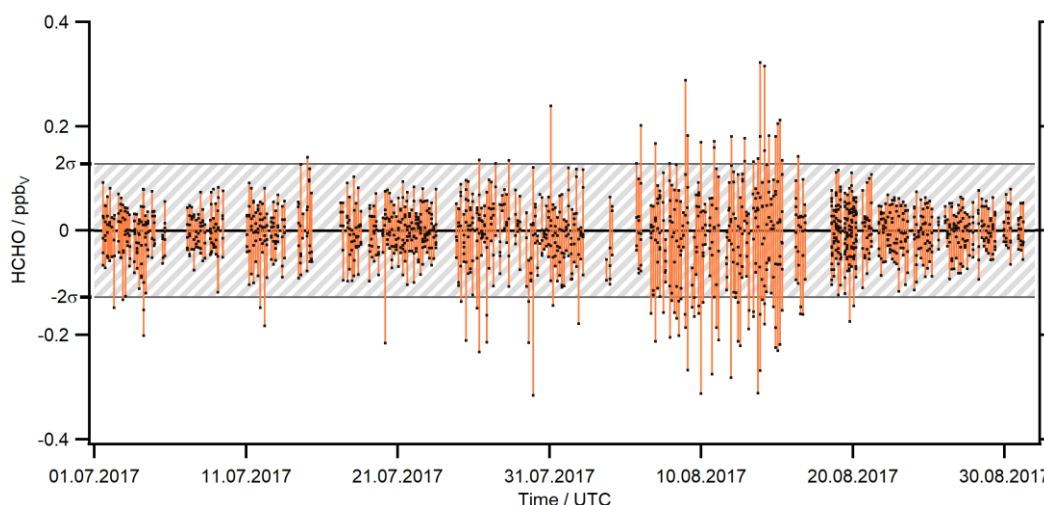


Figure 12: Timeline of the zero gas measurements during the AQABA ship campaign, elevated noise levels were detected between the 08.08. to 14.08.2017 during wavy conditions in the Arabian Sea and the Gulf of Aden.

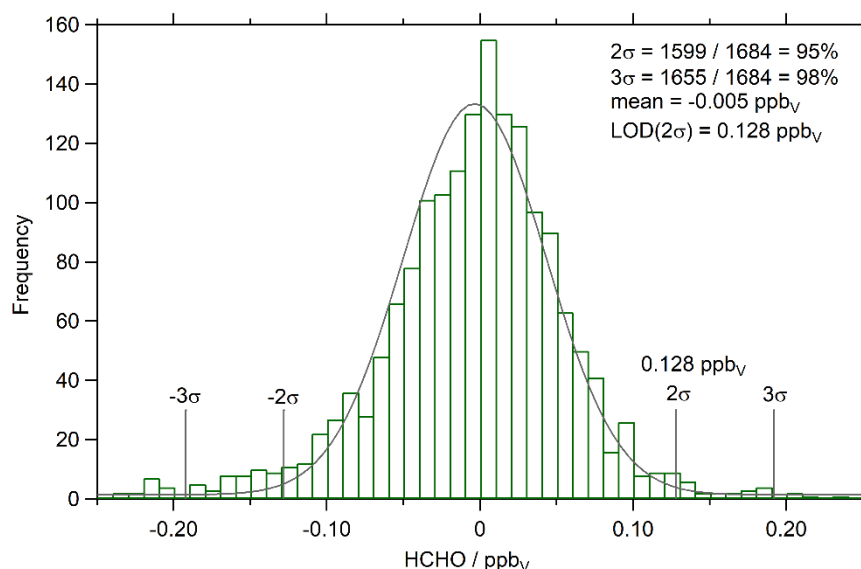


Figure 13: Frequency distribution and Gauss fit of the zero gas measurements AQABA, the Gauss fit confirms normal distribution of the measured background noise, so that the 2σ deviation represents 95 % of the data. The detection limit of the AL4021 was determined as 128 ppt_v.

2.1.8 Precision

The precision (P) is a measure for observational error. It describes how dispersed the observations are to a certain value as a measure of the reproducibility of the method due to statistical variability (random errors). Whereby the accuracy describes how close or far off the observed values are to their true value. The precision of the AL4021 (P_{HCHO}) was calculated as the reproducibility of calibrations, i.e. as the ratio of the mean value (Δ_{Std}) and the corresponding standard deviation (σ_{Std}) of the liquid standard injections during AQABA.

$$P_{\text{HCHO}} = \Delta_{\text{Std}} / \sigma_{\text{Std}} \quad (7)$$

As shown in Fig. 14, HCHO calibrations during AQABA show a rather strong variation, with highest values during the measurements over the highly polluted Arabian Gulf and the wavy conditions of the Arabian Sea (20.07. – 23.07. & 09.08. – 14.08.2017). No clear explanation for the elevated values in

these regions was found, although as mentioned before, the zero gas measurements indicate an interference of the measurements with high wave conditions.

For the whole dataset P_{HCHO} was determined as 6.8 %, while the calibrations during the calmer conditions of the second leg constitute a better reproducibility. Exclusion of the values for the Arabian Gulf and the Arabian Sea yields a significantly higher precision, with a deviation of only 1.5 % from the HCHO standard mean value (8.046 ppb_v). It remains uncertain why elevated signals were detected during the calibrations in these regions.

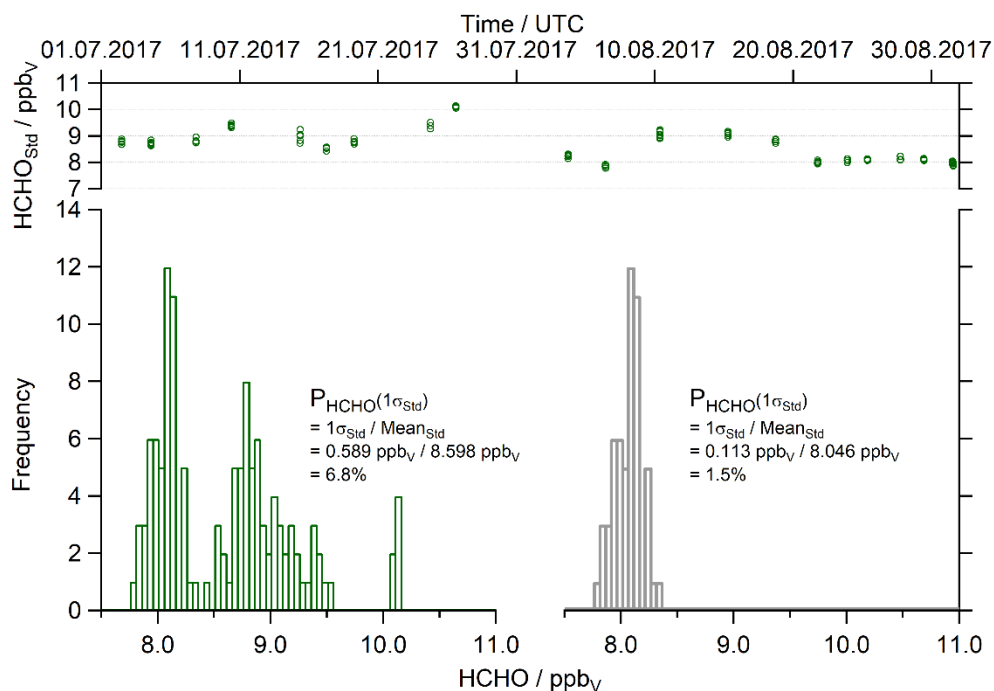


Figure 14: Frequency distribution liquid standard injections during AQABA (green) and with the exclusion of the Arabian Gulf and the Arabian Sea (grey), which demonstrate higher variability compared to the rest of the dataset.

2.1.9 Determination of the sampling efficiency

The sampling efficiency was determined as the deviation of gaseous HCHO standard observations towards their expected value. These standards were generated with a commercial permeation device (VICI®), which consists out of a polyethylene tube filled with paraformaldehyde. It was situated in a glass impinger in an oven, which was constantly purged with synthetic air (80 mL min⁻¹) and tempered to 60 °C. Gaseous HCHO from this source was then injected into the sampling inlet.

The permeation rate of this source was determined with UV/Vis spectroscopy and the chromotropic acid method (Altshuller et al., 1961): gaseous HCHO is sampled into a highly concentrated sulphuric acid solution (90 % H₂SO₄, 10 % H₂O) which contains chromotropic acid (detailed procedure in the experimental section (7)). HCHO then reacts in an electrophilic substitution with chromotropic acid and attacks as a strong electrophile in ortho position of the sulfonic acid and the hydroxyl group, which both polarize the neighboring C-atom. After dehydration, a second molecule of chromotropic acid is added, and subsequently, the sulfuric acid acts as oxidizing agent so that a stable carbenium ion is released (Fig. 15). It is stable due to its large π -electron system, which additionally causes the strong, red to violet color.

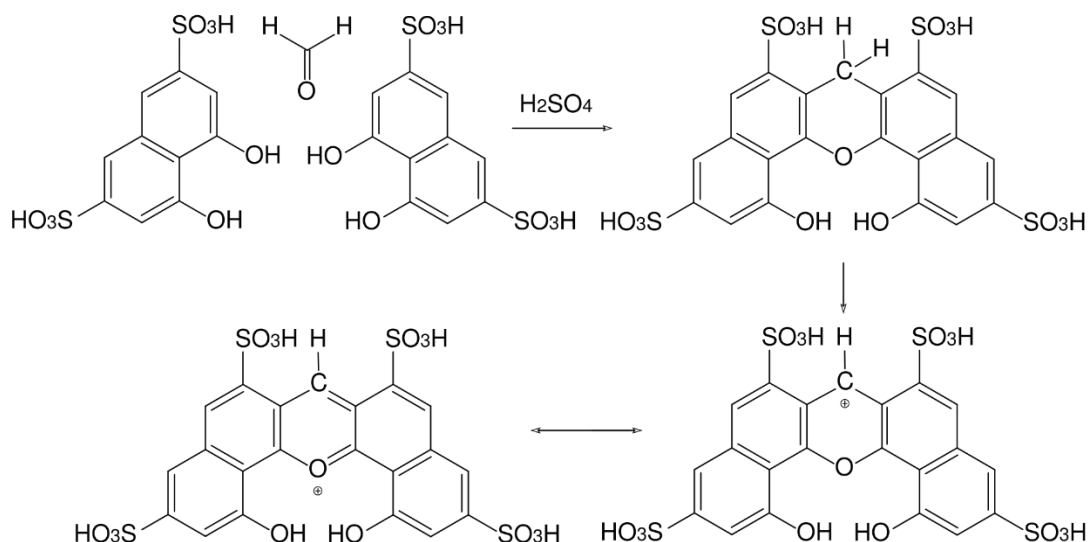


Figure 15: Reaction scheme of the detection of gaseous HCHO with chromotropic acid in sulfuric acid. The released carbenium ion is a strong chromophore and ideal for the quantification with UV/Vis spectroscopy.

To ensure quantitative results, 2 glass impingers are connected in series, so that breakthrough would be determined in the second sample. A third flask is used with the same solution to subtract the background signal. After 4 h, the sampling is stopped and all samples are cooled in a water bath and subsequently measured in a UV/Vis Spectrophotometer (Thermo Fisher, Genesys 10S UV-Vis) at 580 nm (extinction coefficient $\epsilon_{\text{Chr}} = 1.762 \cdot 10^4 \text{ L mol}^{-1} \text{ cm}^{-1}$).

The theoretical mixing ratio of gaseous HCHO (μ_{HCHO}) was calculated according to Eq. 8, with A_S as the absorption of the sample (after subtraction of the background), V_S as the volume of the sample, d as the path length of the cuvette, V_{mol} as the molar volume of an ideal gas and V_{air} as the sampling flow rate.

$$\mu_{\text{HCHO}} = \frac{A_S \cdot V_S}{\epsilon \cdot d \cdot t} \cdot \frac{V_{\text{mol}}}{V_{\text{air}}} \quad (8)$$

With the theoretical mixing ratio of HCHO, the recovery rate is determined with the corresponding signal of the AL4021 by the ratio of $\mu_{\text{HCHO, AL4021}}/\mu_{\text{HCHO}}$, which gives the sampling efficiency of the AL4021. This method resulted in a sampling efficiency of $90.2 \pm 11.9 \%$ for the AQABA expedition, which I used as a correction factor for the HCHO dataset.

Additionally, I calculated the inlet efficiency with HCHO gas standard injections close to the sampling inlet (a T-piece was connected into the bypass near to the sampling chimney) and calculated the recovery rate with injections close to the inlet of the AL4021. This method quantifies line losses in the bypass tubing (PFA, $\frac{1}{2}$ " , ~ 10 m). No significant losses were detected, with a recovery rate of $98.8 \pm 4.1 \%$.

2.1.10 Interferences and total measurement uncertainty

The AL4021 shows cross interferences with certain trace gases as they interfere with the Hantzsch technique. Known interferences were calculated based on the values of the manufacturer Aero-Laser (Table 3). There are no detectable interferences caused from NO, NO₂, SO₂ and acetone (AL4021 manual v2.2, Aero-Laser GmbH, 2019). The most significant interferences are caused by H₂O₂, glyoxal and O₃. H₂O₂ shows a rather strong interference with 1 ppt_v HCHO / 100 ppt_v H₂O₂, but as its only abundant in the lower ppb_v range in the MBL the interference yielded only an average of 2.1 ± 0.9 ppt_v HCHO during the AQABA cruise. The glyoxal interference could not be accounted for, as there were no observations available for the AQABA dataset. The O₃ interference is given to be smaller than 1:500 by the manufacturer, but was found to be almost constant with 15.0 ± 2.5 ppt_v (Axinte, 2016). For the AQABA dataset it was determined by the injection of zero gas with the addition of O₃ (in varying

concentrations) into the bypass of which the AL4021 and AL2021 were sampling from. No significant increase of HCHO with elevated O₃ was detected, with all values significantly lower than the instrumental LOD (Fig. 16). Therefore, the O₃ interference was corrected by subtraction of the constant offset of 6.8 ppt_v HCHO. In contrast to these results, the H₂O₂ measurements with the AL2021 showed a linear increase with 36 ± 1 ppt_v of H₂O₂ per 100 ppb_v of O₃ (Hottmann, 2019). Except for methanol, there are no observations for the remaining interferences available, although no significant impact of these species is expected as they all interfere with at least less than 1:10000 (Table 3).

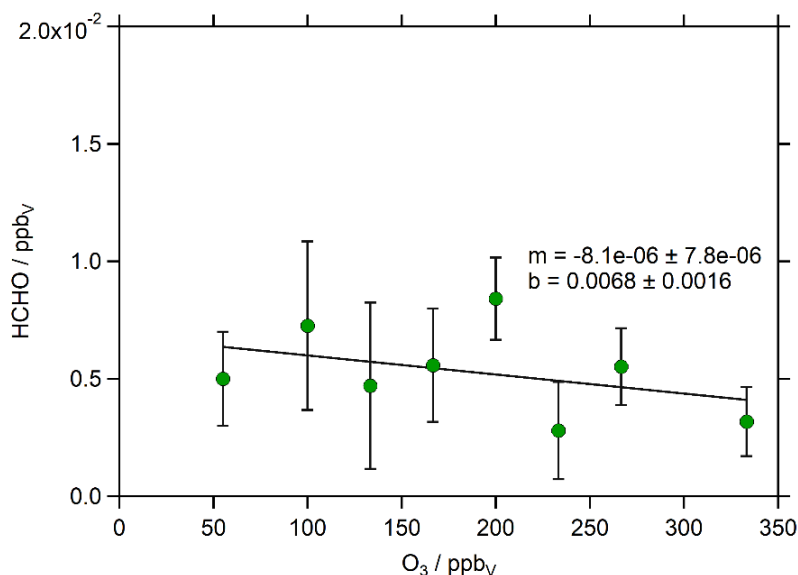


Figure 16: Determination of the O₃ interference of the AL4021 during AQABA, no significant increase of the HCHO signal was detected with increasing amounts of O₃.

Table 3: Trace gas interferences of the AL4021 measurements during AQABA.

Trace gas	Interference	Mean value AQABA (± 1σ) / ppt _v
H ₂ O ₂	< 1 : 100	2.1 ± 0.9
Glyoxal	< 1 : 123	–
O ₃	< 1 : 500	6.8 ± 1.6
Acetaldehyde	< 1 : 10000	(4.8 ± 7.5) · 10 ⁻²
NH ₃	< 1 : 10000	–
Acrolein	< 1 : 10000	–
Propanal	< 1 : 10000	–
Benzaldehyde	< 1 : 20000	–
Methanol	< 1 : 50000	(2.0 ± 2.0) · 10 ⁻²

The total measurement uncertainty (TMU) was calculated according to Gaussian error propagation. Main uncertainties of the quantification of gaseous HCHO with the AL4021 are the uncertainty of the sampling efficiency ($SE_{\text{HCHO}} = 11.9\%$) and the uncertainty of the liquid HCHO standards (S_{HCHO}), which was estimated as an upper limit of 5% (redox titration, dilution of the stock solution). Additional uncertainties for the measurements of the flow rates were added, with 2% for the air flow (V_{air} ; the maximum uncertainty of the utilized mass flow controller) and 3% for the flow rate of the sampling solution (V_{sampling}). This resulted in a total measurement uncertainty of 13.4% for the observations of the AL4021 during AQABA.

$$TMU_{\text{HCHO}} = \sqrt{(SE_{\text{HCHO}})^2 + (S_{\text{HCHO}})^2 + (V_{\text{air}})^2 + (V_{\text{sampling}})^2} = 13.4\% \quad (9)$$

The instrumental characteristics of the AQABA campaign are compared to the recent measurement expeditions in Table 4. Altogether, the AL4021 data quality is comparable to recent campaigns, while

lower detection limits were achieved when the instrument was operated on a fixed platform. As already discussed, this is most likely due to the movement of the ship, which caused elevated background signals during strong wave conditions. The precision, the total measurement uncertainty and the response time are in good agreement to previous campaigns. No major datagaps occurred due to instrumental failure, so that measurements with the AL4021 led to satisfactory results.

Table 4: Comparison of the AL4021 characteristics during AQABA with further measurement expeditions.

	AL4021	Expedition	Literature
Detection Limit / ppt _v	90 – 128	AQABA 2017	Dienhart et al., 2021; this work
	38	CYPHEX 2014	Nussbaumer et al., 2021b
	38	HOPE 2012	Nussbaumer et al., 2021b
	21	HUMPPA 2010	Axinte, 2016
	122	PARADE 2011	Axinte, 2016
	81	DOMINO 2008	Axinte, 2016
	100	–	AL4021 manual v2.2, 2019
Precision / ppt _v	589 / 113	AQABA 2017	Dienhart et al., 2021; this work
	–	CYPHEX 2014	Nussbaumer et al., 2021b
	–	HOPE 2012	Nussbaumer et al., 2021b
	194	HUMPPA 2010	Axinte, 2016
	968	PARADE 2011	Axinte, 2016
	239	DOMINO 2008	Axinte, 2016
	–	–	AL4021 manual v2.2, 2019
TMU / %	13	AQABA 2017	Dienhart et al., 2021; this work
	16	CYPHEX 2014	Nussbaumer et al., 2021b
	16	HOPE 2012	Nussbaumer et al., 2021b
	19	HUMPPA 2010	Axinte, 2016
	19	PARADE 2011	Axinte, 2016
	13	DOMINO 2008	Axinte, 2016
	–	–	AL4021 manual v2.2, 2019
Sampling efficiency / %	90.2	AQABA 2017	Dienhart et al., 2021; this work
	–	CYPHEX 2014	Nussbaumer et al., 2021b
	–	HOPE 2012	Nussbaumer et al., 2021b
	96.5	HUMPPA 2010	Axinte, 2016
	88.8	PARADE 2011	Axinte, 2016
	87.7	DOMINO 2008	Axinte, 2016
	–	–	AL4021 manual v2.2, 2019
Time Resolution / s	169	AQABA 2017	Dienhart et al., 2021; this work
	300	CYPHEX 2014	Nussbaumer et al., 2021b
	300	HOPE 2012	Nussbaumer et al., 2021b
	186	HUMPPA 2010	Axinte, 2016
	219	PARADE 2011	Axinte, 2016
	141	DOMINO 2008	Axinte, 2016
	90	–	AL4021 manual v2.2, 2019

2.2 Hydroperoxide measurement techniques

This section covers a brief overview about analytical methods to quantify gaseous hydroperoxides, mainly H₂O₂ and also the most common organic peroxides e.g. MHP and PAA. It also includes the instrumentation and its application during the AQABA expedition, although a more detailed description can be found in Hottmann (2019).

Many measurement techniques for detection of gas-phase hydroperoxides have been applied, most of them rely on aqueous sampling due to the good solubility of H₂O₂ and the smaller organic peroxides. Several collection techniques have been used such as impinger (Tanner et al., 1990), cryogenic trap (Campos and Kok, 1996) for integrative sampling and membrane diffusion scrubbers (Dasgupta et al., 1988) and scrubbing glass coil (Lazrus et al., 1986, Hottmann et al., 2020, Dienhart et al., 2022) for continuous sampling. Further detection principles are absorption spectroscopy and mass spectrometry techniques, e.g. chemical ionization mass spectrometry (CIMS). Mass spectrometry also enables detection of peroxides in the particle phase by application of online derivatization (Weloe and Hoffmann., 2020). The continuous sampling with a scrubbing glass coil is the most widely used method (Lee et al., 2000). It is based on the solubility of a certain species in a buffered sampling solution, whereby constant flows of ambient air and sampling solution are mixed in a glass coil. The gaseous hydroperoxides thereby transition from the gas phase into the liquid phase. Since the collection efficiency is temperature dependent (Henry's law), highest sampling efficiencies are achieved with pre-cooled solutions and a cooled stripping coil. This sampling technique was also applied for the separation of gaseous peroxides using high-performance liquid chromatography (HPLC) (Hafermann, 2016; Hottmann, 2019; Dienhart et al., 2022).

The most commonly used measurement techniques for the detection of H₂O₂ are compared by means of their respective temporal resolution and detection limits in Table 5. Lowest detection limits are achieved with the Fenton reagent. This detection principle does not allow for continuous sampling and thus the most commonly used method is the enzymatic fluorescence technique based on the work of Lazrus et al. (1986). Instruments that use this technique are commercially available (e.g. AL2021, Aero-Laser GmbH, Garmisch-Partenkirchen, Germany) and were used intensively on field studies (e.g. Fischer et al., 2015; Fischer et al., 2019). A modified version of the AL2021 was exclusively built for airborne measurements of hydroperoxides (Hottmann et al., 2020; Hamryszczak et al., 2022a; Hamryszczak et al., 2022b). The HYPHOP (HYdrogen Peroxide and Higher Organic Peroxides monitor) achieves similar detection limits as the commercially available AL2021, but with the addition of a pressure controlled inlet system, reduced weight and slightly higher temporal resolution of 120 s.

Table 5: Brief comparison of measurement techniques used for the detection of gaseous H₂O₂.

Method	Detection principle	LOD / ppt _v	Time Resolution / s	Reference
Dual-enzyme	Fluorescence	15	122	Hamryszczak et al., 2022b
		8 – 53	120	Hottmann et al., 2020
		25	120	Fischer et al., 2019
Dual-enzyme	Fluorescence	16	420	Hafermann, 2016
HPLC		5	900	Lee et al., 1995
Luminol	Chemiluminescence	500	–	Kok et al., 1978
Colorimetry	Fluorescence	100	–	Kok et al., 1978
Fenton	Chemiluminescence	0.1	–	Lee et al., 1990
TDLAS	Infrared absorption	300	60	Slemr et al., 1986
CIMS	Mass spectrometry	1 – 10	1	Allen et al., 2022a
		16	6	O'Sullivan et al., 2018

2.2.1 The hydroperoxide monitor AL2021

The two channel dual-enzyme technique enables quantification of H_2O_2 and qualitative results of total organic peroxides. Two channels are necessary, as one channel determines the entirety of gaseous hydroperoxides, while the second channel, by the addition of catalase, specifically removes H_2O_2 . The quantification of H_2O_2 is thus enabled by subtraction of both channel signals (ρ) with $\varepsilon(\text{H}_2\text{O}_2)$ as the catalase efficiency, which is determined by the injection of H_2O_2 standards:

$$[\text{H}_2\text{O}_2] = \rho(\text{Channel A}) - \rho(\text{Channel B}) \cdot \varepsilon(\text{H}_2\text{O}_2). \quad (10)$$

Channel B thereby gives an estimate for the abundance of organic peroxides. This signal cannot be used for quantification, as the various organic species are not separated and the solubility of organic species differs to that of H_2O_2 , depending on their respective Henry's law coefficients. O'Sullivan et al. (1996) determined k_{H} for the most abundant hydroperoxides in Earth's atmosphere (H_2O_2 , MHP, PAA, EHP, HMHP) and show that they differ by several orders of magnitude with H_2O_2 and HMHP as the most soluble species with k_{H} of $8.33 \cdot 10^4 \pm 3.80 \cdot 10^3$ and $1.67 \cdot 10^6 \pm 3.50 \cdot 10^5$, respectively (Table 6). The high solubility also implies that both species are efficiently removed from the atmosphere by precipitation or surface deposition. PAA's solubility is higher than that of MHP, most likely because PAA is the derivate of a carboxylic acid, which are highly soluble in aqueous media due to their high polarity, k_{H} of MHP and EHP are comparable. The Henry constant of hydroxyethyl peroxide could not be accurately determined due to its rapid decomposition in aqueous media at $\text{pH} > 3$; the decomposition of HMHP and PAA at neutral pH suggests, that these species can act as heterogeneous source of H_2O_2 in atmospheric water (O'Sullivan et al., 1996).

Table 6: Henry's law constants (at 25 °C) of the most abundant hydroperoxides in Earth's atmosphere based on the determinations of O'Sullivan et al. (1996).

Compound	Chemical formula	k_{H} ($\text{mol L}^{-1} \text{atm}^{-1}$)
Hydrogen peroxide	H_2O_2	$8.33 \cdot 10^4 \pm 3.80 \cdot 10^3$
Methyl hydroperoxide	CH_3OOH	311 ± 14.0
Hydroxymethyl hydroperoxide	HOCH_2OOH	$1.67 \cdot 10^6 \pm 3.50 \cdot 10^5$
Peroxyacetic acid	$\text{CH}_3\text{C}(\text{O})\text{OOH}$	837 ± 175
Ethyl hydroperoxide	$\text{CH}_3\text{CH}_2\text{OOH}$	336 ± 20.0

2.2.2 Detection principle – The dual-enzyme technique

The sampling solution is based on purified water and a phthalate buffer, which is set up by the addition of potassium hydrogen phthalate (KHP). It also contains HCHO and ethylenediaminetetraacetic acid (EDTA) to prevent negative artifacts by the reaction of H_2O_2 with solvated SO_2 and metal ions.

After solvation of the gaseous hydroperoxides in the stripping coil, the sampling solution is separated from the air flow in a gas-liquid-separator and split onto both channels. Subsequently, the fluorescent reagent (with the addition of catalase in channel B) and sodium hydroxide (NaOH) solution are added in the reagent coils. The fluorescent reagent contains horseradish peroxidase (HRP) and para-hydroxyphenylacetic acid (POPHA) in KHP buffer. The enzyme HRP thereby acts as electron donor to catalyze the reductive cleavage of H_2O_2 . HRP has a high turnover rate and thereby ensures quantitative reaction of H_2O_2 with POPHA, which yields the fluorescent POPHA dimer (6,6'-dihydroxy-3,3'-biphenyldiacetic acid).

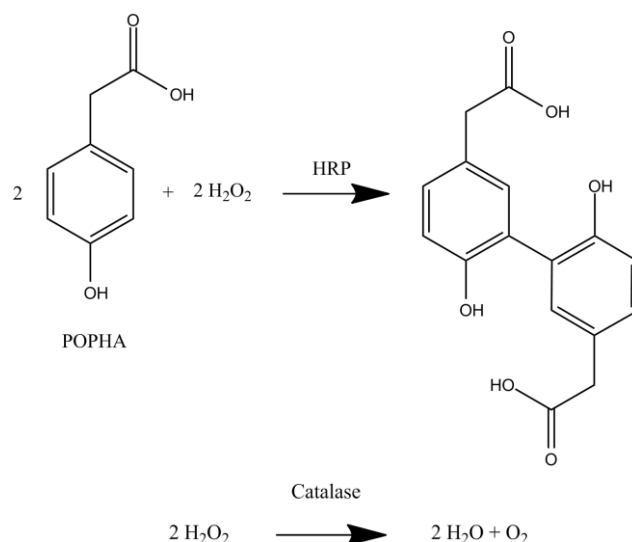


Figure 17: Reaction scheme of the dual-enzyme technique. HRP catalyzes the reaction of POPHA and H₂O₂ to the corresponding dimer. The addition of Catalase in channel B selectively breaks down H₂O₂, so that only ROOH are detected in this channel.

The method is selective for hydroperoxides due to the specific reaction of HRP, organic hydroperoxides react analogously to H₂O₂. The addition of catalase in channel B is thus necessary to determine the exact concentration of H₂O₂. Just before the flow cell, NaOH is added to increase the pH and deprotonate the POPHA dimer. Excitation of the fluorescent dye is then performed in a flow cell at 326 nm (Cadmium Pen-Ray lamp), followed by detection of the fluorescent light at 400 – 420 nm with photomultiplier tubes (H957–01, Hamamatsu Photonics GmbH, Germany).

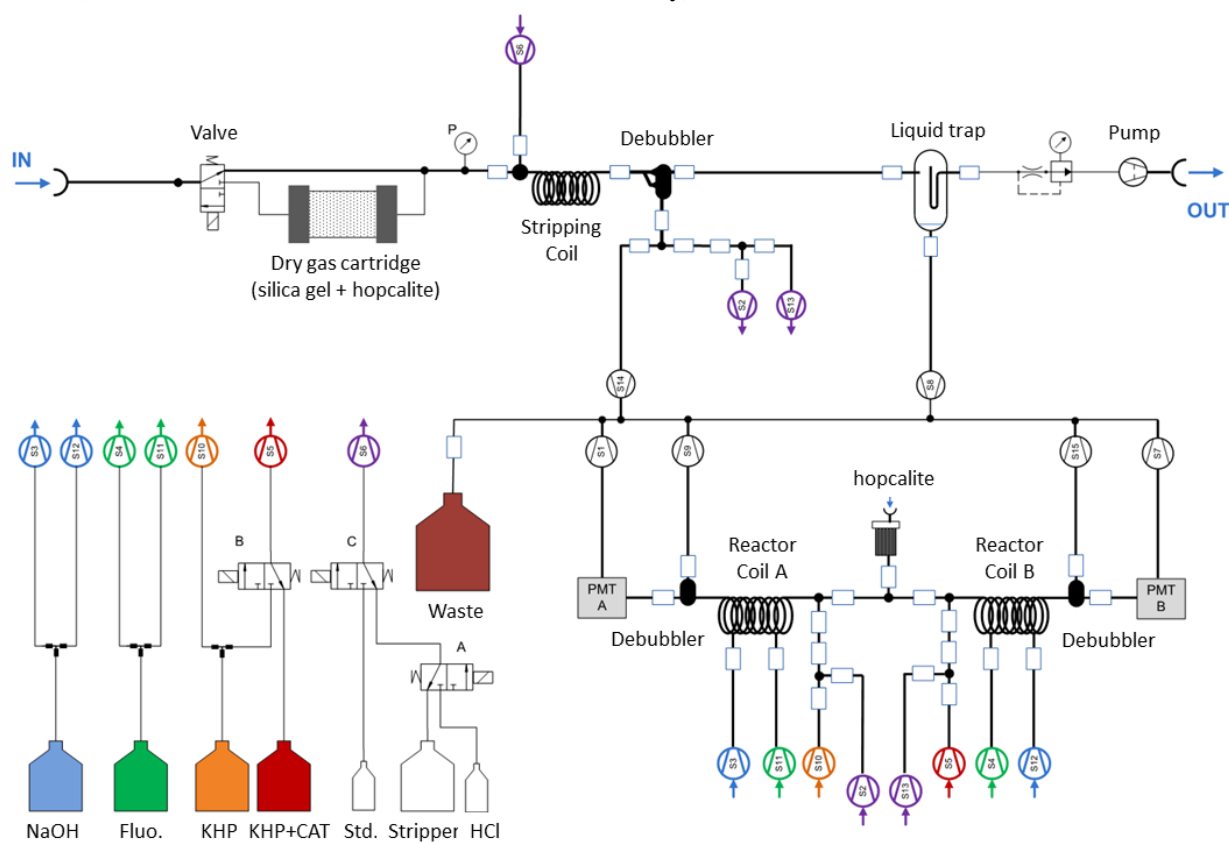


Figure 18: Flow chart of the AL2021 and the respective solutions. Please note that PMT A and B represent both the respective flow cells and photomultiplier tubes. The Cadmium lamp in the instrument is set up in 90° light angle to the corresponding photomultiplier tubes.

2.2.3 Instrument calibration and characteristics of the AL2021

Calibration of the AL2021 is performed with liquid H₂O₂ standard injections by a 4-point calibration. The first step is a short injection of hydrochloric acid (0.1 M) to clean the inlet system, followed by the liquid standard in both channels and without the addition of catalase in channel B. The next step are two zero gas measurements, the first still without the addition of catalase in channel B, to check whether both buffers show a similar background signal. The last point of the calibration is then the injection of liquid H₂O₂ standard in both channels, but with the addition of catalase in channel B.

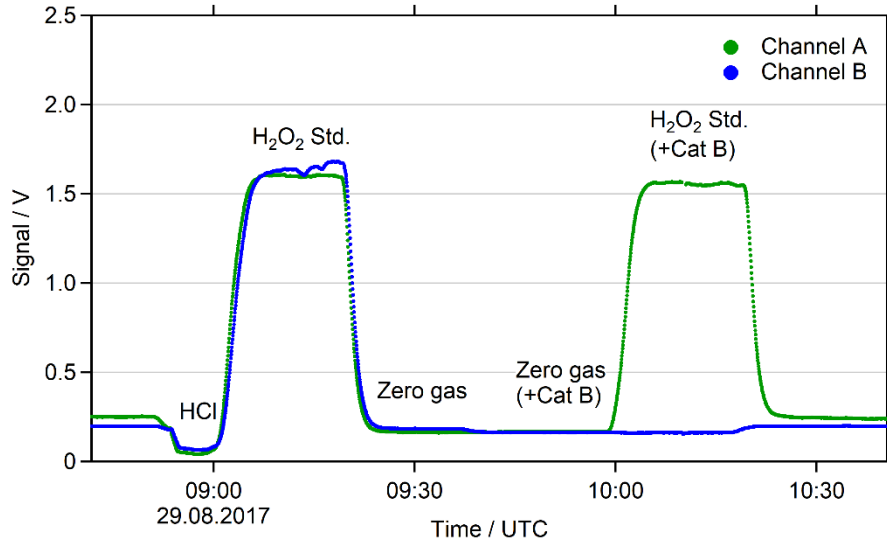


Figure 19: External calibration of the AL2021 with a 4-point calibration by the injection of liquid H₂O₂ standards.

H₂O₂ standards are prepared freshly before every calibration by a 2-step dilution of a H₂O₂ stock solution (twice 1:100) with cooled, purified water. With this 4-point calibration the sensitivity (*S*) of both channels is then calculated according to:

$$S_A = \frac{U_{A,standard} - U_{A,zero}}{\mu} \quad (11)$$

$$\mu = \frac{c_{stock}}{100 \cdot 100} \cdot \frac{V_{mol} \cdot V_{sampling,L}}{V_{sampling,G}} \cdot 10^9, \quad (12)$$

whereby $U_{standard}$ and U_{zero} represent the averaged signals of the liquid standard and the zero gas for the respective channel, c_{stock} the concentration of the H₂O₂ stock solution, $V_{sampling,L}$ as the flow rate of the sampling solution, $V_{sampling,G}$ as the flow rate of the sampled ambient air and V_{mol} as the molar volume of an ideal gas. The factor of 10⁹ then gives the molar mixing ratio in ppb_v (parts per billion by volume).

The catalase efficiency (ϵ) is then calculated according to:

$$\epsilon = 1 - \left(\frac{U_{standard+cat,B} - U_{zero+cat,B}}{U_{standard,B} - U_{zero,B}} \right) \cdot \left(\frac{U_{standard,A} - U_{zero,A}}{U_{standard+cat,A} - U_{zero+cat,A}} \right). \quad (13)$$

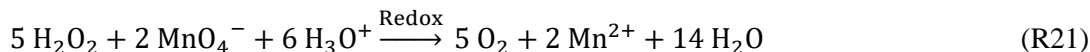
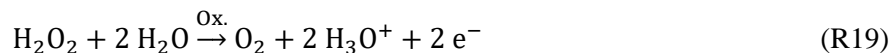
The corresponding mixing ratios of H₂O₂ and the sum of organic peroxides (ROOH) are then calculated with Eq. 14 and 15.

$$H_2O_2 = \left(\frac{U_A - U_{A,zero}}{S_A} \right) - \left(\frac{(U_B - U_{B,zero}) \cdot \epsilon}{S_B} \right) \quad (14)$$

$$ROOH = \left(\frac{U_B - U_{B,zero}}{S_B} \right) - (1 - \epsilon) \cdot H_2O_2 \quad (15)$$

The mixing ratios of ROOH thereby only represent an estimate of the majority of ROOH, as sampling efficiencies vary and thus cannot be accounted for. H₂O₂ is sampled quantitatively, while MHP, the main organic peroxide under clean tropospheric conditions, only has a sampling efficiency of 60 % (Aero-Laser, 2005). Please note that some ROOH also decompose, e.g. PAA decomposes at neutral pH (O'Sullivan et al., 1996).

The H₂O₂ stock solution needs to be kept refrigerated at all times, then its concentration is stable for several weeks. The concentration of the H₂O₂ stock is determined by redox titration with potassium permanganate (KMnO₄) according to R19 – R21, further details are described in section 6.4.



In addition to the liquid calibrations of the instrument, gaseous H₂O₂ (or ROOH) standards are useful to determine the stripping efficiency of a certain species or to calculate inlet efficiency and account for line losses. These are expected to occur if water condenses in the sampling tubes, or by chemical interactions on the tube surface. It can be quantified by injection of gaseous H₂O₂ standards (of a known concentration), e.g. with the use of a permeation source. Various permeation source materials were investigated in Hamryszczak (2020). Low-density polyethylene (LDPE) and polyvinyl chloride (PVC) qualified as the most suitable materials by means of their reliability and practicability, as they can be sealed easily with a heat gun and deliver reliable results. During AQABA, a small tube of LDPE (~15 cm, 1/8") was filled with H₂O₂ (30 %, Sigma Aldrich) and sealed with PTFE caps. This tube was placed in a glass impinger, which was purged with synthetic air (80 mL min⁻¹) and tempered to 35 °C. Gaseous H₂O₂ standards were then injected into the sampling bypass, once at the start of the sampling line, and for comparison also right in front of the inlet of the respective instrument (AL2021 & dual-enzyme HPLC).

The permeation rate of the H₂O₂ permeation source is determined based on the photometric technique of Pilz and Johann (1974), which utilizes the reaction of titanium tetrachloride with H₂O₂ to form the corresponding η²-peroxo-complex:

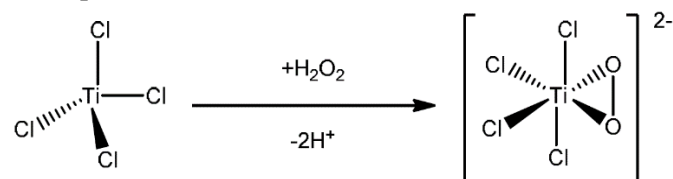
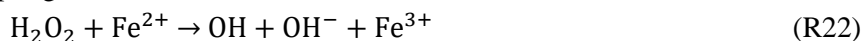


Figure 20: Reaction of titanium tetrachloride and H₂O₂ to the octahedral η²-peroxo titanium tetrachloride.

The reaction is fast and quantitative in cooled water, and the peroxo-complex shows a broad absorption maximum between 380 – 450 nm. Therefore, the reaction is ideal for fast quantification of gaseous H₂O₂ via the Lambert-Beer law (section 6.4).

Linearity of the dual-enzyme method has been proven in Hamryszczak (2020) and Christian (2019), Aero-Laser states a measuring range of 0 to 100 ppb_v (AL2021 manual v2.2, Aero-Laser GmbH, 2006). Instrumental background drifts are corrected with zero gas measurements, which can be performed together with the AL4021 (e.g. every 3.5 h for 30 minutes during AQABA) by sampling ambient air through a zero gas cartridge. Analogously to the AL4021, this cartridge is filled with silica gel and Hopcalite® (MnO, CuO), which destroys not only HCHO and peroxides, but also O₃ and additional VOCs. Further catalysts are known to destroy H₂O₂ and MHP efficiently, e.g. Carulite-300® and Carulite-200®. All three catalysts were used and compared by O’Sullivan et al. (2018), who searched for the best zero gas generation for CIMS based hydroperoxide measurements. The deployment of Carulite-300® was unsuccessful to determine MHP backgrounds, while Carulite-200® had the most consistent efficiency of all three catalysts. Another possibility to determine H₂O₂ background signals are Palladium filters (Allen et al., 2022a). It might be useful to compare these catalysts also for the determination of HCHO background signals with the AL4021, to determine the most efficient candidate for the destruction of H₂O₂, ROOH and HCHO. Zero gas measurements of the most recent campaigns

(CAFE EU, CAFE AFRICA, AQABA) were based on Hopcalite[®], which gave consistent background signals with H₂O₂ detection limits ≤ 50 ppt_v (Hamryszczak et al., 2022a; Hamryszczak et al., 2022b). The dual-enzyme method has known O₃ and NO interferences, which need to be corrected in post processing of the data. Aero-Laser states an interference of 30 ppt_v per 100 ppb_v of O₃ (AL2021 manual v2.2, Aero-Laser GmbH, 2006). Hottmann (2019) determined an O₃ interference of 36 ± 1 ppt_v per 100 ppb_v of O₃, which resulted in an average interference of 16 ppt_v H₂O₂ during AQABA. The NO interference was determined with an average of 2 ppt_v H₂O₂ and maximum values of 48 ppt_v H₂O₂ due to the highly elevated NO mixing ratios when observing ship exhausts. Other known interferences with metal ions (e.g. the Fenton reaction, R22) and the oxidation of SO₂ are suppressed by the addition of HCHO and EDTA in the sampling solution.



The instrument characteristics of the AL2021 and the HYPHOP of the most recent expeditions are listed in Table 7, further instrumental details are presented in Hottmann (2019). In sum, the detection of H₂O₂ and ROOH with the AL2021 was very successful with no major data gaps and similar data characteristics to previous campaign with detection limits and precision in the lower ppt_v range.

2.2.4 Separation of organic hydroperoxides with HPLC

The specification of solvated organic hydroperoxides can be achieved by combination of the dual-enzyme method with a separation technique. Therefore, the high-performance liquid chromatography (HPLC) is ideal, as the sampled hydroperoxides can be separated e.g. on a reversed-phase column (C18, Synergi Hydro-RP) followed by analysis via post-column derivatization. This method has been applied various times for the specification of organic peroxides (Lee et al., 1995; Kok et al., 1995; Sauer et al., 2001).

The results in this thesis are based on an HPLC-based instrument, which was developed and characterized in detail by Hafermann (2016). KHP buffer, on which the AL2021 is based, is not ideal for the detection of ROOH due to its high pH value of 5 – 6, which decreases the sampling efficiency of ROOH. Therefore, a phosphoric acid buffer is used for the HPLC. To ensure high sampling efficiencies, the stripping coil is cooled to 2 °C. Fluorescence detection is achieved with the addition of POPHA and HRP, analogously to the AL2021. The formation of the POPHA-dimer is accelerated in a heated reactor oven; 40 °C was found to be the ideal temperature for the derivatization. Excitation of the POPHA dimer is performed at 286 nm and detection of the fluorescence at 405 nm (Hafermann, 2016). The instrument achieves detection limits of 16 ppt_v for H₂O₂, 25 ppt_v for MHP and 18 ppt_v for PAA at a typical time resolution of 7 minutes for the detection of H₂O₂, MHP and PAA. Retention times of higher organics, e.g. EHP and isoprene hydroxyl hydroperoxide (ISOPOOH), are expected to be longer. During AQABA, a retention time of 8 – 10 minutes was achieved for the detection of EHP, depending on the pressure of the eluent.

Unfortunately, the instrumentation only allowed for qualitative assessment of the abundant species during AQABA due to an interference of the baseline with the movement of the ship. More comprehensive assessments of the dual-enzyme HPLC are presented in Hottmann (2019) and Hafermann (2016).

Table 7: Instrumental characteristics of the AL2021 and the HYPHOP during the recent measurement expeditions.

		H ₂ O ₂	ROOH	
Detection Limit / ppt _v	AL2021	13	8	Hottmann, 2019; Dienhart et al., 2022
		14 – 74	31 – 94	Axinte, 2016
		26	26	Klippel et al., 2011
	HYPHOP	15	6	Hamryszczak et al., 2022b
		35	13	Hamryszczak et al., 2022a
		24	24	Hottmann et al., 2020
		18 – 41	18 – 41	Christian, 2019
Precision / ppt _v	AL2021	52	76	Hottmann, 2019; Dienhart et al., 2022
		74 – 374	4 – 17	Axinte, 2016
		21	21	Klippel et al., 2011
	HYPHOP	71	45	Hamryszczak et al., 2022b
		15	11	Hamryszczak et al., 2022a
		24	24	Hottmann et al., 2020
		219 – 337	–	Christian, 2019
O ₃ Interference / ppt _v per 100 ppb _v O ₃	AL2021	36	–	Hottmann, 2019; Dienhart et al., 2022
		173	–	Axinte, 2016
		30	–	Klippel et al., 2011
	HYPHOP	57	–	Hamryszczak et al., 2022b
		16	–	Hamryszczak et al., 2022a
		52	–	Hottmann et al., 2020
		24	–	Christian, 2019
Inlet efficiency / %	AL2021	100	–	Hottmann, 2019; Dienhart et al., 2022
		100	–	Axinte, 2016
		96	–	Klippel et al., 2011
	HYPHOP	61 ± 6	–	Hamryszczak et al., 2022b
		52 ± 5	–	Hamryszczak et al., 2022a
		63 ± 1	–	Hottmann et al., 2020
		61 ± 6	93 (PAA)	Christian, 2019
TMU / %	AL2021	20	40	Hottmann, 2019; Dienhart et al., 2022
		16 – 24	51 – 54	Axinte, 2016
		12	21	Klippel et al., 2011
	HYPHOP	9	41	Hamryszczak et al., 2022b
		28	40	Hamryszczak et al., 2022a
		6	40	Hottmann et al., 2020
		7	–	Christian, 2019

2.3 Data processing

The datasets of the HCHO and peroxide measurements were recorded with the V25 data logger, an operating system constructed by the IT group of the Max Planck Institute for Chemistry. The V25 allows for synchronized operation of the AL4021 and the AL2021, so that e.g. zero gas injections can be performed simultaneously for both instruments. It records the data of both instruments in 3 s intervals in ASCII format, so that it can easily be exported into data analysis software. Data processing, analysis and image processing of long time series require software which is able to manage large data files. Therefore, WaveMetrics IGOR Pro 6 was used, which features its own C-like programming language. IGOR stores data typically in four-dimensional, sophisticated arrays called ‘waves’. For calculation of mixing ratios from the raw data, a previously developed software was utilized (Axinte, 2016).

The different instrumental operations (e.g. calibration, zero gas, ambient) are logged as a mode wave, so that they are automatically sorted with the possibility of manual adjustments. First step is to correct to time shift of the signals (in Volt), caused by the transport of the liquids in the AL2021 and AL4021 until the signal shift is detected at the photomultiplier tube. Afterwards, the liquid calibration signals are averaged, whereby the plateau length can be chosen to exclude wrong signals e.g. if a bubble entered the flow cell during liquid calibration. The same step applies for the zero gas measurements, which are afterwards used to perform background signal correction by a linear interpolation between each zero measurement once the signal is stable. The gas phase calibrations, line loss corrections and the respective interferences are then corrected manually. A short overview of the AQABA datasets used in this thesis and their respective instrumental characteristics are displayed in Table 8 in section 3.3.

2.4 EMAC

ECHAM5/MESSy2 Atmospheric Chemistry (EMAC) model is a chemistry general circulation model (CGCM), which describes tropospheric and middle atmosphere transport processes. It also includes sub-models to simulate the chemical and physical interactions with oceans and land surfaces as well as anthropogenic activities based on emission inventories. EMAC is based on ECHAM5 (ECMWF Hamburg), a GCM developed in the Max Planck Institute for Meteorology (Roeckner et al., 2006). Together with the second version of the Modular Earth Submodel System (MESSy2), several sub-models can be included into the GCM to develop a CGCM, also called chemistry transport model (CTM) (Joeckel et al., 2010). EMAC results are based on the chemistry submodel MECCA (Module Efficiently Calculating the Chemistry of the Atmosphere), implemented with the chemistry mechanism MOM (Mainz Organics Mechanism), which contains roughly 600 species and 1600 reactions. It includes the basic HO_x, NO_x and CH₄ chemistry, a variety of NMHCs, aromatics and OVOCs, including isoprene

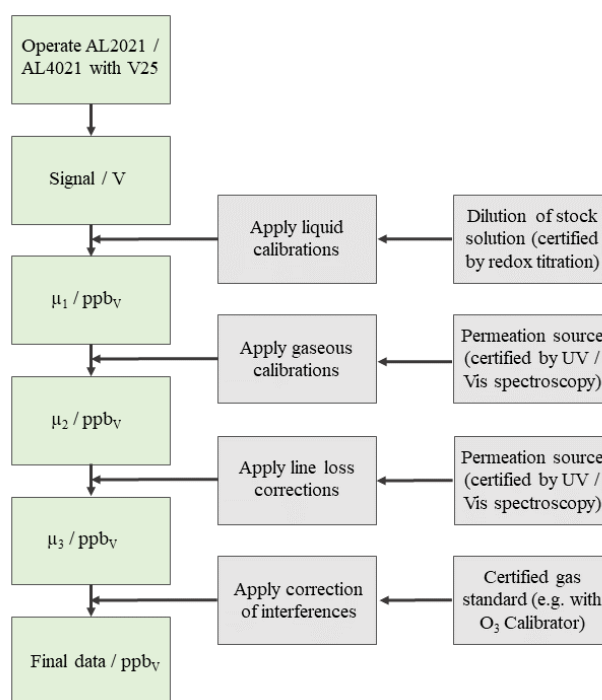


Figure 21: Flow chart of the data processing steps involved with the AL2021 and the AL4021 to convert raw signals (V) into ambient mixing ratios (ppb_V).

und terpene oxidation (Sander et al., 2019). Anthropogenic emissions are based on the Emissions Database for Global Atmospheric Research (EDGARv4.3.2) and are supplemented by biogenic emissions based on the Model of Emissions of Gases and Aerosol from Nature (MEGANv2.04) and biomass burning emissions. Oceanic emissions and deposition are calculated online with the AIRSEA submodel, which implements e.g. a net source for DMS, isoprene and acetone, as well as a net sink for methanol. Dry deposition and sedimentation are estimated by the DDep and SEDI submodels, while wet deposition is simulated by SCAV (SCAVenging submodel). Aerosol microphysics and gas-aerosol partitioning are calculated by the Global Modal-aerosol eXtension module (GMXe). EMAC has recently been evaluated in great detail with airborne trace gas measurements (Pozzer et al., 2022).

The model simulations were carried out in the T106L31 resolution, which corresponds to a grid of $1.1^\circ \cdot 1.1^\circ$ (~110 km · 110 km) with 31 vertical pressure layers up to 10 hPa, with roughly 22 levels in the troposphere. Previous results of airborne and shipborne expeditions have been compared to EMAC (Pozzer et al., 2022; Fischer et al., 2015; Klippel et al., 2011). The diverse photochemistry around the Arabian Peninsula, especially over the Arabian Gulf where a lot of oil and gas industry is operating, seems to be ideal to evaluate EMACs chemistry mechanism. NO_x , O_3 and VOCs measurements during AQABA were already compared to the EMAC results (Tadic et al., 2020; Wang et al., 2020), this thesis presents further studies on HCHO, hydroperoxides and HO_x radicals.

2.5 HYSPLIT trajectories

The National Oceanic and Atmospheric Administration (NOAA) Air Resources Laboratory's (ARL) HYbrid Single-Particle Lagrangian Integrated Trajectory (HYSPLIT) model is a complete system for computing both simple air parcel trajectories and complex dispersion and deposition simulations (Draxler and Hess, 1998). The model calculation is a hybrid between the Lagrangian approach, which uses a moving frame of reference as the air parcels move from their initial location, and the Eulerian approach, which uses a fixed three-dimensional grid as a frame of reference. Advection and diffusion calculations are made in the Lagrangian framework following the transport of the air parcel, while pollutant concentrations are calculated on a fixed grid with the Eulerian methodology. The model has evolved throughout more than 30 years, from estimating simplified single trajectories based on radiosonde observations to a system accounting for multiple interacting pollutants transported, dispersed, and deposited over local to global scales. HYSPLIT is designed to support a wide range of simulations related to the atmospheric transport and dispersion of pollutants and hazardous materials, as well as the deposition of these materials (such as mercury) to the Earth's surface. Some of the applications include tracking and forecasting the release of radioactive material, volcanic ash, wildfire smoke, and pollutants from various stationary and mobile emission sources (Stein et al., 2015). The HYSPLIT trajectories used in this thesis were calculated by David Walter (Group Schiebel, MPIC) with a starting height of 200 m and a temporal resolution of 1 h for both the position and the transport of the air parcels. Every trajectory starting point was matched to the GPS coordinates of the ship location at the sampling time and the movement of air parcels was tracked for 92 h. For an improved overview, and as most trace used in this thesis anyway have rather short lifetimes, I only used 48 h resolved trajectories for the indication of transport.

2.6 Photochemical steady-state assumption

The photochemical steady-state (PSS) of a certain species X is achieved, when its production P(X) and its losses L(X) are approximately at equilibrium, and thus, there is only negligible variability of its mixing ratio over the time period t.

$$\frac{d(X)}{dt} = P(X) - L(X) \approx 0 \quad (16)$$

The PSS assumption then allows to estimate missing observational data, such as missing loss or production pathways. One central effect is its use to determine dry deposition during the day if the photochemical budget of a species is known. Additionally, it can be used to estimate RO₂ data as shown by Tadic et al. (2020), to estimate net ozone production rates or to identify the production efficiency of organic peroxides. The PSS assumption was also used in Dienhart et al. (2021; chapter 4) to estimate HCHO production rates.

2.7 Deposition

As already mentioned in chapter 1.4.1, deposition processes are divided into wet (e.g. rain out, fog) and dry deposition, which describes the loss of a certain trace gas (or particles) on a surface based on their chemical and physical interactions. Dry deposition is a complex heterogeneous loss, which is dependent on several factors, such as the ambient temperature, turbulence and wind speed, but also on the chemical conditions such as the pH value. Calculation of the dry deposition was performed with the method of Shepson et al. (1992), which was also used in further studies (e.g. Fischer et al., 2019; Nussbaumer et al., 2021b).

During night, the photochemical production and loss reactions due to OH can be neglected, and thus the decay of H₂O₂, ROOH and HCHO is dominated by dry deposition in clean regimes. With the assumption of a constant, horizontally homogenous boundary layer, the exponential decay can be used to estimate the deposition rate k_{dep}. In this calculation, we assume that the initial mixing ratio [X]₀ (j_{NO2} < 10⁻³) represents the mixing ratio within the whole boundary layer. If species X follows exponential decay during night, the first order decay is given by Eq. 17. The first order decay plot (ln[X]_t/[X]₀ versus the time) then yields k_{dep} as the slope of the linear regression.

$$\ln \frac{[X]_t}{[X]_0} = k_{\text{dep}}(X) \cdot t \quad (17)$$

Additionally, the deposition velocity V_{dep} within the boundary layer can then be calculated with a known boundary layer height (h_{BL}) via Eq. 18, assuming that the boundary layer is well mixed and that the variation of h_{BL} is negligible during the calculated period. The boundary layer height of the marine boundary layer is expected to be reasonably stable compared to continental air masses due to the buffering effect of the ocean.

$$V_{\text{dep}}(X) = k_{\text{dep}}(X) \cdot h_{\text{BL}} \quad (18)$$

3. The AQABA ship campaign

This chapter presents the measurements performed during the Air Quality and climate change around the Arabian Basin (AQABA) measurement expedition that took place on the *Kommandor Iona* (KI) from 25th June till 3rd September 2017. An overview about the region and the expected atmospheric conditions is presented in chapter 3.1, the measurement setup for HCHO, H₂O₂ and ROOH during the expedition in 3.2 and measurements of further species used in this thesis in 3.3.

Mobilization of the ship was performed in La Seyne-sur-Mer (near Toulon, France), from where the first leg of the cruise started through the Mediterranean, the Suez Canal and the Red Sea to the first stop in Jeddah. The expedition continued two days later via the Gulf of Aden, the Arabian Sea, the Gulf of Oman and the Arabian Gulf (Persian Gulf) to Kuwait. On the second leg, the ship returned along the same route (Fig. 22) without stopping in Jeddah to end the expedition after passing the Stromboli volcano. The KI was equipped with a weather station and four laboratory containers on the front deck with instrumentation for in situ and offline monitoring of a large variety of gaseous species, particles and radicals. A short summary of the measurements used in this thesis is presented in Table 8.

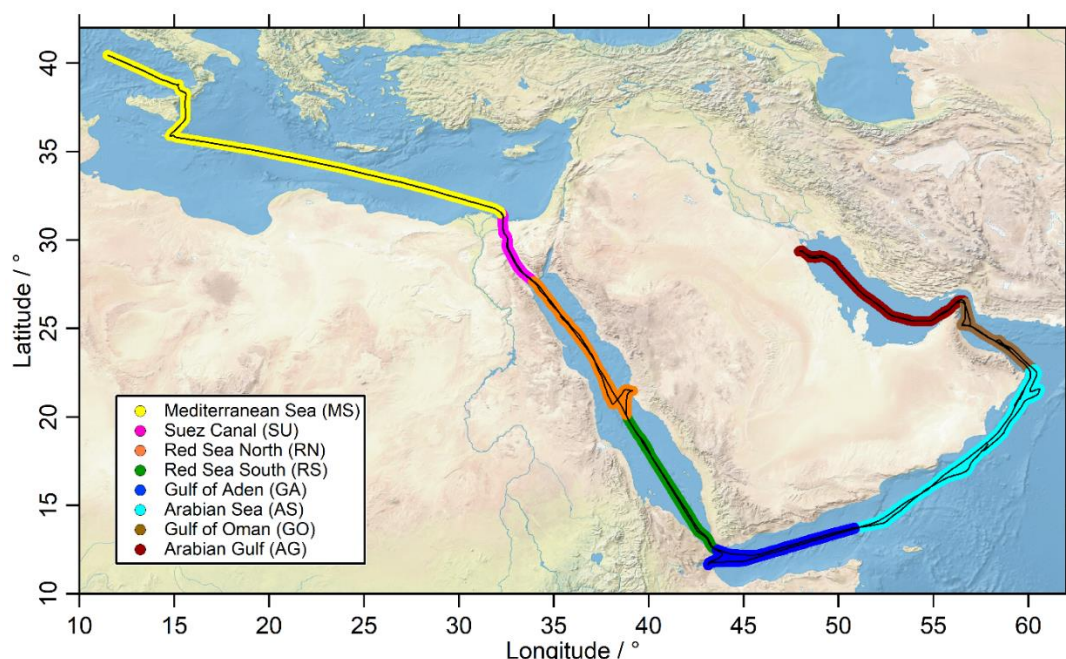


Figure 22: Overview of both legs during AQABA and color-coded regional structuring. The following acronyms are used for the different regions encountered during AQABA: MS for Mediterranean Sea (yellow), SU for Suez Canal and Gulf of Suez (magenta), RN for Red Sea North (orange), RS for Red Sea South (green), GA for Gulf of Aden (blue), AS for Arabian Sea (cyan), GO for Gulf of Oman (brown) and AG for Arabian Gulf (red).

3.1 Air quality and anthropogenic pollution around the Arabian Peninsula

The Suez region (Suez Canal, Gulf of Suez) and the Arabian Gulf (also known as the Persian Gulf) are famous for their oil and gas extraction, which brought wealth and economic growth to the region. This industry sector brings along strong effects on the regional air quality by its emissions from the oil and gas exploration sites, e.g. by flaring and venting of natural gas, but also by the transport of the extracted products through intensive ship traffic. Natural gas is often an unwanted by-product during the extraction of oil, so that developers need to either find a useful outlet for the associated gas. The possibility of delivering it to consumers and suppliers is cost-intensive, so that the gas is often pumped back for pressure supply or permanent disposal, but it can also be used as additional energy resource onsite or for the generation of electricity. If these measures fail, operators just burn the gas onsite

(flaring) or release it into the atmosphere (venting), which causes major environmental damage. If the associated gases are flared, most of this gas, which usually contains high fractions of CH₄, is converted into CO₂ (depending on the combustion efficiency). If vented, CH₄ (with its immense global warming potential ~25 times more than CO₂ in 100 years) and other air pollutants will be released to the atmosphere directly. Globally in 2011, the gas flaring was around 140 billion cubic meters, which is equivalent to 5 % of global natural gas production (Soltanieh et al., 2016). Oil and gas fields, and also the known locations of oil refineries around the Arabian Peninsula are presented in Fig. 23 and highlight the emission potential of this region.

Depending on the composition of the natural gas and the local combustion efficiency, further air pollutants like sulfur compounds (e.g. hydrogen sulfide, sulfur oxides), NO_x, CO, black carbon particles (BC), polyaromatic hydrocarbons (PAHs) and other VOCs are released to the atmosphere. When burned, the combustion efficiency strongly depends on the local meteorological conditions. Leahey et al. (2001) show, that it e.g. decreases exponentially with increasing wind speeds and stack exit velocities. They estimated combustion efficiencies of several VOCs, with that of CH₄ to be only 53 % at wind speeds of 2.5 m s⁻¹ and a stack exit velocity of 2.0 m s⁻¹, so that only half of the natural gas is actually burned when released during moderate wind speeds. Furthermore, this diverse mixture of trace gases and particles contains some amounts of toxic heavy metals such as mercury, nickel, arsenic and other inorganic salts (mainly chlorate and sulfate salts).

Lelieveld et al. (2009) demonstrate that highly elevated levels of photochemical air pollution are also predicted by the EMAC model, and mainly caused by long-distance transport of air pollution, substantial upwind natural NO_x sources, a lack of deep convective mixing and precipitation, and strong local anthropogenic emissions. Furthermore, it is expected that the region strongly contributes to net ozone transport, which leads to enhanced levels of ozone in the subtropics (Lelieveld et al., 2009). Altogether, the Arabian Gulf is prominent for its oil and gas industry emissions, which not only affect the local and regional air pollution, but are also a threat for human health and climate change.

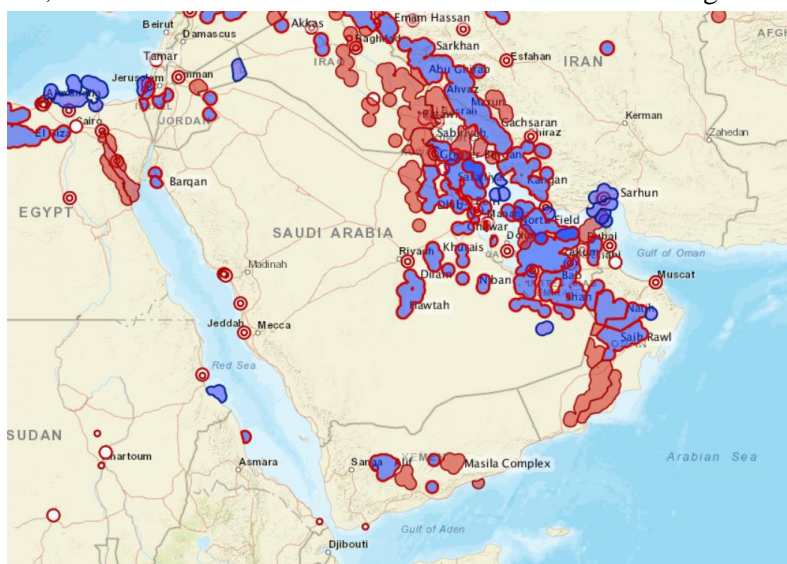


Figure 23: Oil (red) and gas field locations (blue) around the Arabian Peninsula with the oil refineries as red circles. The image was processed with Harvard WorldMap (<https://worldmap.harvard.edu/maps/6718/dJT>).

These facts highlight that further and more extensive studies in the region are necessary to evaluate the extent of primary emissions from combustion processes and further sources, and also the secondary production of air pollutants due to photochemical oxidation and transport of these emissions. The AQABA campaign reports the first ship-based measurements in the region, which are going to be highly useful to report about the air quality within the MBL of the Arabian Gulf.



Figure 24: Examples of anthropogenic emissions around the Arabian Peninsula: Oil rig with a gas flare close to the Suez Canal (photo: Steffen Dörner during the first leg) and heavy ship emissions close to Fujairah (western part of the Gulf of Oman just after leaving the Arabian Gulf during the second leg).

Moreover, ship emissions drastically affect the area, as the route through the Suez Canal is the main pathway to transport goods from Europe to Asia and Australia. Ship emissions are known sources for a variety of compounds, for the gas phase mainly NO_x , CO , SO_2 and VOCs, and also a variety of particulate matter (e.g. black carbon and sulfate aerosol). These emissions can be identified by satellite measurements (e.g. DeSmedt et al. 2021) and are implemented in the Emissions Database for Atmospheric Research (EDGAR), which is used for model simulations and to determine changes of global emissions. Tegtmeier et al. (2022) compared the values of EDGAR for emissions of CO and determined enhanced ship emissions in the whole area, with CO emissions on most ship lanes increasing by at least 4 % per year.

Celik et al. (2020) analyzed the AQABA dataset aiming on the effect of ship emissions on a local scale and to determine emission factors for the identification of ship plumes, and for parameterization of these emissions, which could be useful for the refinement of atmospheric chemistry models. They also identified that especially larger ships with more powerful engines used fuel with enhanced sulfur content compared to the KI and smaller ships. These ships were characterized by increased SO_2 emission factors, particulate sulfate and particulate organics (Celik et al. 2020).

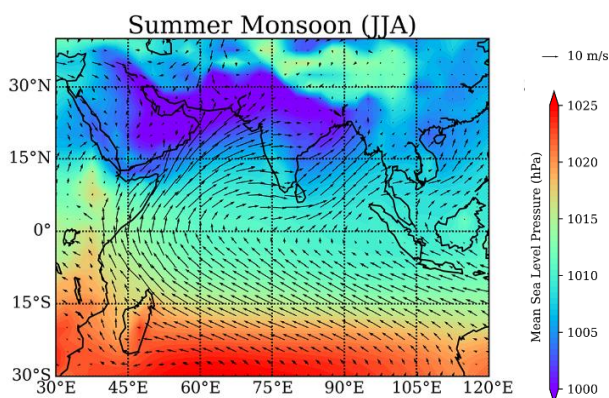


Figure 25: Mean sea(surface)-level pressure and surface wind for the summer monsoon from June – August 2018 based on Fig. 1 of Tegtmeier et al. (2022).

In contrast, air quality over the Arabian Sea is expected to represent aged and rather clean MBL conditions during the South Asian summer monsoon. Approximately from June until August, air masses are transported by steady winds in a circulation from the center of the Indian ocean towards the continent of Africa, over the Arabian Sea and then towards Pakistan and northern India, where they heat up and the warm and moist air masses rise up over the Himalayas. The resulting deep convective clouds cause the famous Indian summer monsoon rains which are responsible for roughly 80 % of India's annual rainfall (Tegtmeier et al., 2022).

This deep convective updraft of air masses was also studied by aircraft measurements during the Oxidation Mechanism Observations (OMO) campaign, which characterized the efficient cleansing mechanism over the Indian continent (Lelieveld et al., 2018; Hottmann et al., 2020).

The MBL of the Indian Ocean was already studied in detail during the Indian Ocean Experiment (INDOEX), which was an international multiplatform field campaign from January to March 1999. INDOEX had the main goal to measure long-range transport of air pollution from south and south-east Asia towards the Indian Ocean during the dry monsoon season. Air masses encountered covered both polluted and clean MBL conditions, depending on if air masses were influenced by air pollution from India or if they were transported from the clean southern hemisphere close to the Intertropical Convergence Zone (Wagner et al., 2001). Lelieveld et al. (2001) highlight that surprisingly high pollution levels were observed over the northern Indian Ocean, with elevated contributions of agricultural burning and biofuel use. These observations constitute the seasonal variation of air quality in the northern Indian Ocean and the Arabian Sea, which is dominated by rather polluted conditions transported from southern Asia during winter, while clean MBL conditions prevail during the summer monsoon (Tegtmeier et al., 2022; Lawrence and Lelieveld, 2010). The Indian Ocean and the Arabian Sea are also known for their high biological activity and the associated emissions of isoprene and ethene from phytoplankton. Tripathi et al. (2020) observed strong emissions of ethene and propene in the MBL of the eastern Arabian Sea during the pre-monsoon season 2017 with up to 8.9 ± 3.5 ppbv ethene and 3.4 ± 1.3 ppbv propene with daytime values 20 – 40 % higher than during night. These measurements revealed significantly elevated emission fluxes of unsaturated hydrocarbons compared to other oceanic regions, which would lead to enhanced HCHO production in the region. In contrast to the clean conditions over the Arabian Sea during the summer monsoon, the air masses over the Red Sea and the Mediterranean are expected to contain aged anthropogenic pollution transported from Egypt and Europe and significant amounts of fresh ship emissions, especially close to the Suez Canal.

Major scientific questions with respect to the HCHO and hydroperoxide measurements addressed during AQABA were:

- How high is the variability of HCHO, H₂O₂ and ROOH in the MBL over the Arabian Gulf and the Suez Canal compared to the rest of the dataset and how far is this air pollution transported?
- Does the Arabian Sea reflect pristine MBL conditions with least contributions of NO_x when leaving the main shipping route?
- How accurate are the emission databases and the photochemical oxidation mechanism used in EMAC?

3.2 Measurement setup on the *Kommandor Iona*

Most of the instrumentation during AQABA was placed in five lab containers on the front deck of the *Kommandor Iona* and connected to a high-flow ($10 \text{ m}^3 \text{ min}^{-1}$) cylindrical stainless steel inlet with a diameter of 0.2 m and a sampling height of 5.5 m above the deck. This sampling inlet was placed in the center of the deck in between the containers. The HO_x measurements were not connected to this inlet, as the HORUS instrument sampled from a separated inlet right on top of the container, about three meters away, in direction towards the front of the ship. The HCHO, H₂O₂ and ROOH measurements were sampled through a ½" PFA-bypass (perfluoroalkoxy alkane tubing) with a sampling flow rate of $\sim 12 \text{ l min}^{-1}$, which resulted in a residence time of ~ 9 s for both the HCHO and the hydroperoxide measurements. The 4.2 m long bypass tubing was insulated to prevent condensation within the air-conditioned lab container, it was exchanged after the first leg in Kuwait.

This setup ensured no contamination by the KI exhaust while sampling against the wind direction and least sampling artifacts by minimized residence times within the sampling. Whenever possible, the KI adjusted the route to achieve highest possible data coverage. Therefore, the ship changed the direction a couple of times in the northern part of the Red Sea during the first leg. However, about 20 % of the data obtained during the AQABA campaign was contaminated by ship exhaust plumes, mostly due unfavorable winds (e.g. while passing through the Arabian Sea during the first leg).



Figure 26: Instrumental setup on the *Kommandor Iona*. The HCHO, H₂O₂, ROOH, CO and NO_x instruments were set up in the highlighted lab container and connected to the trace gas sampling inlet via bypass tubing with high flow rates. The HO_x and aerosol instruments had separated sampling inlets, specialized with regards to the needs of the respective instrumentation.

3.3 Instruments used for the detection of further trace gases and particles

Meteorological data:

Temperature, atmospheric pressure, wind direction, wind speed and the GPS position of the KI were measured with the European Common Automatic Weather Station (EUCAWS), a weather station specifically designed for ships which was situated close to the HO_x sampling inlet.

Photolysis rates (*j*-values):

Wavelength resolved actinic flux was measured with a spectroradiometer (Metcon GmbH) to calculate photolysis frequencies. The radiometer contains a 512 pixel CCD-array and was installed about 5 m above the front deck level. It was cleaned every morning to remove sea salt and dust particles which interfere with the flux measurements. Decreases in sensitivity due to sensor contamination were corrected with a linear interpolation between the cleaning events. The *j*-values are not corrected for upwelling actinic flux from the sea surface and therefore the TMU was estimated with >10 %, depending on the reaction. More details about the setup and calibration of CCD spectroradiometers can be found in Bohn and Lohse (2017).

O₃ – Photometer

O₃ was measured with an absorption photometer (Model 202 Ozone Monitor) based on its well-established absorption maxima of the mercury line in the Hartley-band at 254 nm. Eliminating water and particle interferences during sampling was achieved by sampling through a Nafion tube and a Teflon filter (Tadic et al., 2020).

NO, NO₂ – CLD

NO and NO₂ measurements were performed with the Nitrogen Oxides Analyzer on HALO (NOAH), which is based on the commercially available two-channel chemiluminescence detector CLD 790 SR (ECO Physics AG, Switzerland), which has been optimized for field measurements over the last decade.

The detection principle is based on the addition of O₃, and the following reaction with NO to stoichiometric quantities of excited-state NO₂^{*}. These excited-state NO₂^{*} molecules emit a photon ($\lambda \geq 600$ nm), forming the detection principle of NO. The second channel is equipped with a LED solid-state photolytic converter (Droplet Measurement Techniques, USA) upstream of the addition of O₃, to selectively photolyze NO₂ to NO. The mixing ratio of NO₂ can then be calculated with a known conversion-efficiency (Tadic et al., 2020).

CH₄, CO – CRDS

Methane and carbon monoxide were measured based on Cavity Ring-Down Spectroscopy (CRDS) with the commercial instrument Picarro G2401. The air was not dried prior to analysis, so that water vapor effects were corrected in post. A filter and a peristaltic pump were installed to ensure that no dust particles or liquid water entered the analyzer. The instrument was calibrated every 15 days by injections of gaseous standards. Precision of the G2401 is typically in the range of 0.3 ppb_v for CH₄ and about 8.0 ppb_v for CO (Paris et al., 2021).

OH, HO₂ – LIF

OH and HO₂ measurements were performed with the HydrOxyl Radical measurement Unit based on fluorescence Spectroscopy (HORUS). Ambient air was sampled from a separated inlet closer to the LIF (laser-induced fluorescence) instrument, to achieve as low as possible residence times in the sampling. The instrument utilizes LIF of the OH radical at 308 nm, which is created by a Nd:YAG pumped, pulsed, tunable dye laser system (Martinez et al., 2010) operated at a pulse repetition frequency of 3 kHz. OH radicals are excited in a low pressure detection cell with a constant flow rate of 10 L min⁻¹. A White cell setup is used to maximize the fluorescence signal i.e. to improve the instrument sensitivity. The detection of HO₂ is achieved by chemical conversion with NO downstream of the OH detection. The resulting sum of remaining ambient OH plus OH originating from chemical conversion of HO₂ is measured in a second detection axis (Marno et al., 2020, Hens et al., 2014).

OVOCs – PTR-ToF-MS

OVOCs were detected with a Proton-Transfer-Reaction Time-of-Flight Mass Spectrometer (PTR-ToF-MS, Ionicon Analytik GmbH, Innsbruck, Austria) which is based on the soft ionization by primary hydronium ions (H₃O⁺). These ions are generated in the ion source and then drawn into the drift tube where they interact with the sampled ambient air. Inside this drift tube, VOCs with a proton affinity higher than that of H₂O (691 kJ mol⁻¹) are ionized via proton transfer from H₃O⁺. PTR is a soft ionization technique, so that fragmentation only occurs rarely and most ions are detected as [M+H]⁺. The resulting secondary ions are then transferred to a detector, in this case a time-of-flight detector with a mass resolution in the range of 3500 – 4500 at mass 96 amu for the AQABA campaign. Mass calibration was performed by injections of trichlorobenzene as internal standard (Wang et al., 2020).

VOCs – GC-FID

Non-methane hydrocarbons (NMHCs) were measured with two coupled Gas Chromatography–Flame Ionization Detection (GC–FID) systems (GC5000VOC and GC5000BTX; AMA Instruments GmbH, Germany). The GC5000VOC was used for the quantification of light hydrocarbons (C₂ – C₆), while the CG5000BTX was used for the heavier hydrocarbons and aromatics (C₆ – C₈). Both systems share the same collection on absorbent-filled enrichment traps, followed by thermal desorption and gas chromatographic separation. Detection of the eluting gases is performed with the flame ionization technique (Bourtsoukidis et al., 2019).

OH reactivity – PTR-MS

Total OH reactivity was measured using the comparative reactivity method (Sinha et al., 2008, Fuchs et al., 2017). The method is based on a competitive reaction of between reactive compounds from ambient air and a reagent, in this case pyrrole, which is not abundant in ambient air. OH radicals are produced by the addition of humidified nitrogen into the reactor with use of a Hg-Ar UV lamp. The instrument is then operated in three modes:

- 1) pyrrole + OH scavenger + UV light (at ambient humidity)
- 2) pyrrole + OH (at ambient humidity)
- 3) pyrrole + OH + ambient air

Variation of the pyrrole mixing ratio was monitored with a PTR-QMS, which was calibrated every week. NO, NO₂ and O₃ cause interferences in CRM as they produce OH radicals via reaction with HO₂. These interferences were quantified in the laboratory with the use of the NOAH instrument. The combined NO, NO₂ and O₃ interferences amounted to a median of 24 % of total OH reactivity over the whole campaign, which equals to 1.9 s⁻¹. Further corrections need to be applied for deviations from pseudo-first-order, e.g. for trace gases with fast reaction constants, especially if these are similar to that of pyrrole with OH, because their concentration inside the reactor decreases at a similar rate to that of pyrrole, leading to an underestimation of their reactivity. This is expected mainly for unsaturated hydrocarbons which were detected in enhanced concentrations during AQABA, e.g. enhanced contribution of a C₅H₈ alkene was identified, which was not isoprene (Pfannerstill et al. 2019).

SO₂ – CI-QMS

Sulfur dioxide (SO₂) was detected with a Chemical Ionization Quadrupole Mass Spectrometer (CI-QMS) using an electrical, radio-frequency discharge ion source through N₂/CH₃I (methyl iodide) as a source of primary ions. The ion source produces primary iodide (I⁻) ions which form iodide and water clusters which react with the targeted trace gases. The CI-QMS is sensitive to SO₂, nitryl chloride (ClNO₂), hydrogen chloride (HCl), acetic acid, peroxyacyl nitric anhydride (PAN) and peracetic acid (PAA). SO₂ was detected as ISO₃⁻ (m/z 207) (Eger et al., 2019b), further details about the instrument and the ionization method are described in (Eger et al. 2019a).

Aerosols – HR-ToF-AMS

Aerosol measurements during AQABA were performed with a High-Resolution Time-of-Flight Aerosol Mass Spectrometer (HR-ToF-AMS) with a self-built aerosol sampling inlet. This inlet contains a regenerating silica gel aerosol dryer with two parallel, switchable columns. While one of these columns is in use to dry to sampled ambient aerosol, the other one is heated and flushed with dry air. Sampling was switched between the two columns once per day. The aerosol inlet sampled ambient air at approximately 12 m above sea level. Concentrations of non-refractory submicron particle components, namely particulate sulfate (SO₄²⁻), particulate nitrate (NO₃⁻), particulate chloride (Cl⁻), particulate ammonium (NH₄⁺) and total particulate organics were calculated with the medium mass resolution mode at a temporal resolution of 30 s (Celik et al., 2020; Drewnick et al., 2012).

Particle number concentrations (PNCs) are given both by an ultrafine water-based condensation particle counter (CPC) and by the integrals of the size-resolved PNCs over the whole size range of a fast mobility particle sizer (FMPS). The FMPS also provided the particle number size distributions which were used to determine the PM₁ particle mass concentrations.

Table 8: Summary of instrumentation installed during AQABA 2017.

Species	Time resolution	Accuracy (1σ)	Precision (1σ)	Detection limit	Technique/ Instrument
HCHO	3 min	13.2 % ##	6.8 % @ 8.59 ppb _v ##	128 ppt _v ##	AL4021
H ₂ O ₂	3 min	3 % ##	1.2 % @ 4.36 ppb _v ##	8 ppt _v ##	AL2021
ROOH	3 min	3 % ##	1.8 % @ 4.49 ppb _v ##	6 ppt _v ##	AL2021
OH	14 s	17 %	0.06 – 0.26 ppt _v	0.03 – 0.15 ppt _v	IPI-LIF-FAGE
HO ₂	14 s	20 %	0.95 – 10.0 ppt _v	0.22 – 2.01 ppt _v	IPI-LIF-FAGE
NO	5 s	5.6 % #	4.4 ppt _v #	10.5 ppt _v #	CLD
NO ₂	5 s	7 % #	112.4 ppt _v #	26.1 ppt _v #	CLD
O ₃	5 s	2 % #	2 % #	3 ppb _v #	Optical absorption
SO ₂	10 s	20 % °	4 % °	38 ppt _v °	CIMS
CH ₄	1 min	0.3 ppb _v *	0.1 % *	–	CRDS
CO	1 min	8.0 ppb _v *	5 % *	–	CRDS
CO	1 s	20 %	11 – 19 %	4.2 – 8.5 ppt _v	QCL spectrometer
VOCs	50 min	–	– **	1 – 25 ppt _v **	GC-MS
OVOCs	1 min	50 % ++	6 – 17 % ++	9 – 52 ppt _v ++	PTR-TOF-MS
OH reactivity	5 min	26 – 35 % +	0.05 – 54.54 s ⁻¹ +	5.4 – 12.19 s ⁻¹ +	CRM
Photolysis frequencies	10 s	> 10 %	–	–	Spectral radiometry
Aerosols	–	–	–	–	CNC, OPC, FMPS, AMS

(Tadic et al., 2020), ## (Dienhart et al., 2022), * (Paris et al., 2021), ** (Bourtsoukidis et al., 2019), + (Pfannerstill et al., 2019), ++ (Wang et al., 2020), ° (Eger et al., 2019).

Acronyms: CLD = Chemiluminescence Detector, HPLC = High-Performance Liquid Chromatography, CIMS = Chemical Ionization Mass Spectrometry, CRDS = Cavity Ring-Down Spectroscopy, QCL = Quantum Cascade Laser, LOPAP = Long-Path Absorption Photometer, GC = Gas Chromatography, PTR-TOF MS = Proton Transfer Reaction Time-of-Flight Mass Spectrometry, CRM = Comparative reactivity method, CNC = Condensation Nuclei Counter, OPC = Optical Particle Counter, FMPS = Fast Mobility Particle Sizer, AMS = Aerosol Mass Spectrometer

3.4 Data Treatment

The HCHO, H₂O₂ and ROOH observations during AQABA were finalized according to chapter 2.3 by the application of liquid and gas calibrations, while zero gas measurements were used for background corrections of the AL4021 and the AL2021. Further known interferences of the instruments were also corrected with the in situ data of several trace gases.

The formaldehyde dataset based on the AL4021 was corrected for its O₃, H₂O₂, acetaldehyde and methanol interferences according to chapter 2.1.10, with all interferences affecting the measurements only in the low ppt_v range. The H₂O₂ interference was determined with mean value ($\pm 1\sigma$) of 2.1 ± 0.9 ppt_v for the AQABA dataset and for O₃ a constant offset of 6.8 ppt_v HCHO was subtracted. Furthermore, since maritime shipping is a major source of HCHO (Gopikrishnan et al., 2021; DeSmedt et al., 2021), ship exhaust plumes and further combustion sources were identified with the use of NO_x, CO, SO₂ and wind direction data. A filter for primary emissions was set up based on these in situ observations, to exclude influenced data points. The same filter was also applied to further datasets used in this thesis, which were expected to be impacted by combustion processes, e.g. OVOCs, OH reactivity and aerosols.

As a result, the first leg shows decreased data coverage compared to the second leg of the expedition as unfavorable winds caused sampling of the KT's ship exhaust, especially for the Arabian Sea. Additionally, as presented in Fig. 27, many other short pollution events were encountered with highly elevated NO (occasionally more than 200 ppb_v, Fig. 27). The finalized HCHO dataset (blue) still contains these events which were often accompanied by elevated HCHO (exhaust plumes, pollution close to the Jeddah and Kuwait). I only used the filtered HCHO dataset (green) for further studies in this thesis. Celik et al. (2020) identified a total of 252 emission plumes in the AQABA dataset, a qualitative overview of how they identified the ship plumes and how ship plumes are expected to chemically age with time (e.g. SO₂ is transferred into particulate SO₄²⁻) is shown in Fig. 28.

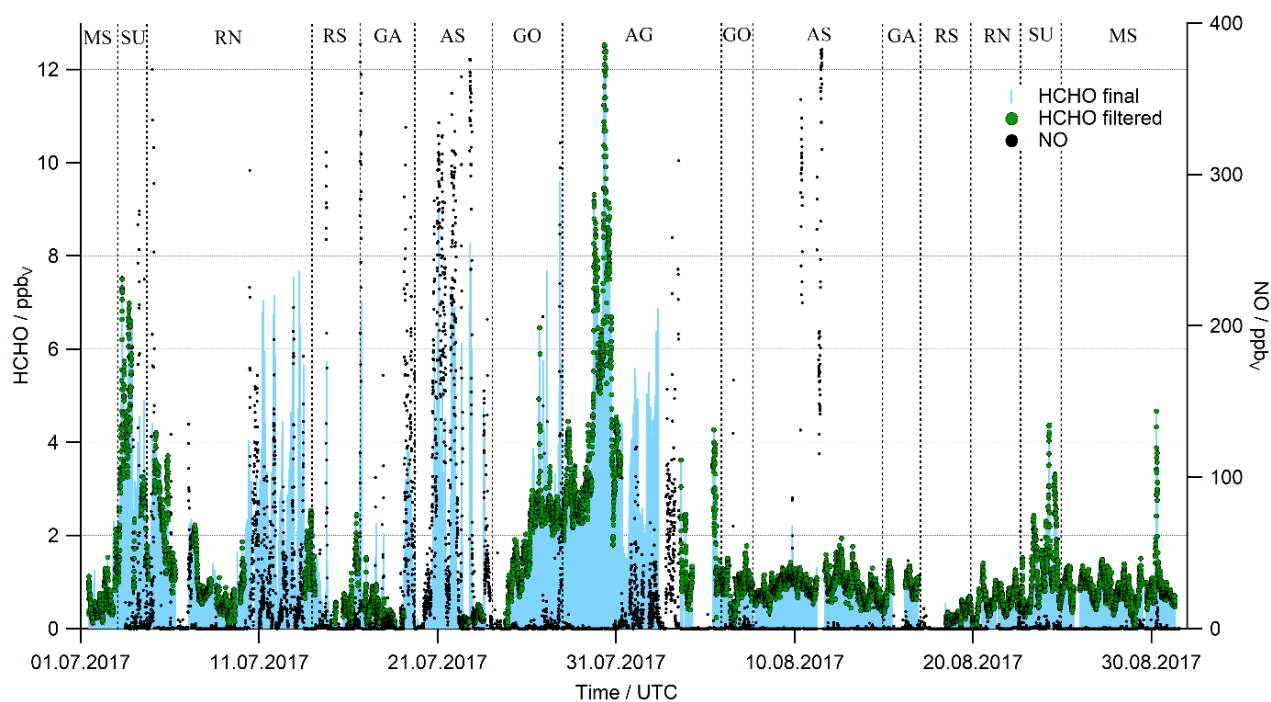


Figure 27: Timeline of the final HCHO dataset (blue) the filtered HCHO data (green) and the NO measurements (black) which were used with the addition of CO, SO₂ and wind direction data to set up a filter, mainly to remove ship exhaust emissions.

The hydroperoxide dataset was processed by Bettina Brendel (Hottmann, 2019). The AL2021 has a known O_3 and NO interference which has to be corrected in post. Hottmann (2019) determined a mean O_3 interference of 16 ppt_v per 100 ppb_v of O_3 while the manufacturer gives a value of 30 ppt_v H_2O_2 per 100 ppb_v of O_3 (AL2021 manual v2.2, Aero-Laser GmbH, 2006). The NO interference accounted for 12 ppt_v H_2O_2 per 100 ppb_v of NO , which resulted in a mean of 2 ppt_v H_2O_2 and a maximum of 48 ppt_v H_2O_2 for the AQABA dataset. Both the H_2O_2 and $ROOH$ dataset did not show significant increases due to primary emissions, and thus the emission filter was not applied to these datasets.

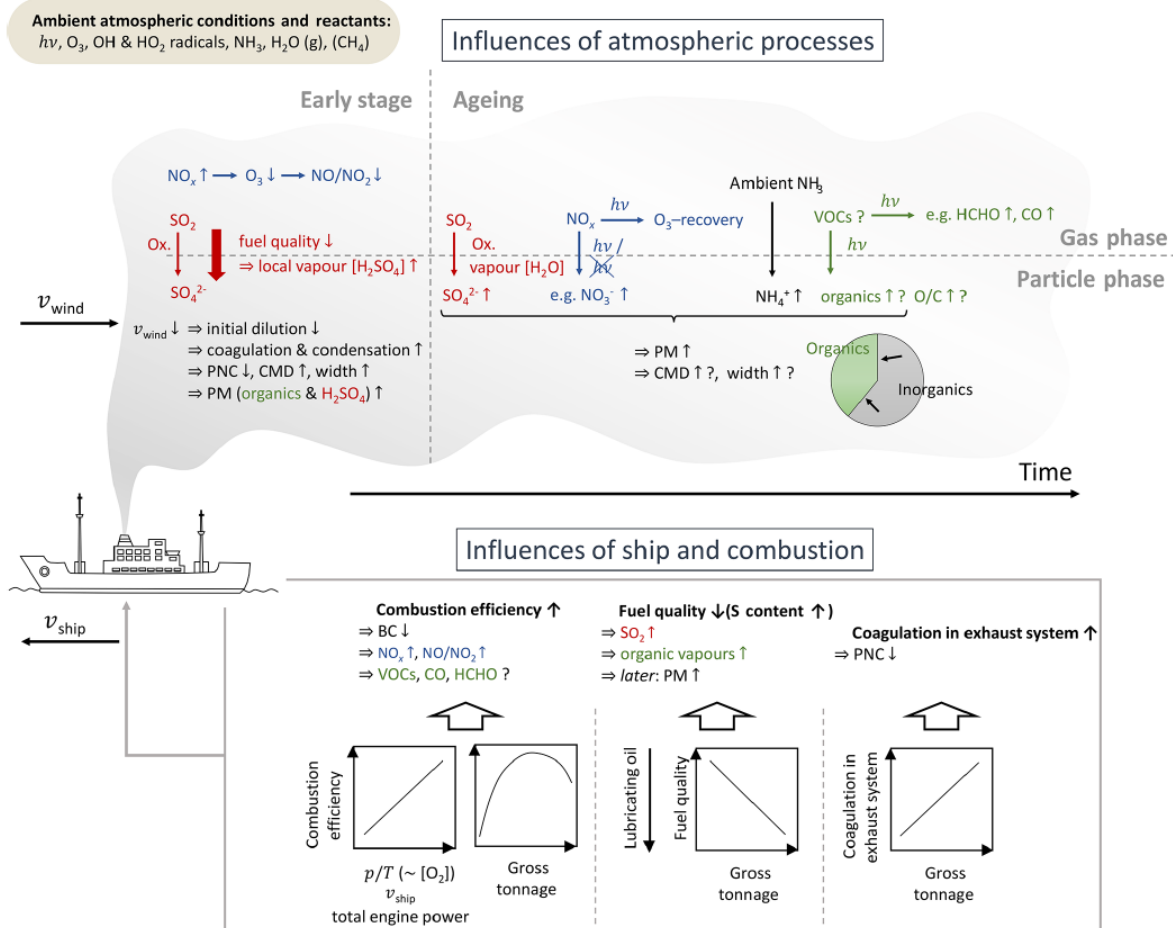


Figure 28: Qualitative overview of the observed ship exhaust plume characteristics and their dependency on ship parameters, combustion conditions and the atmospheric processing / ageing after release into the atmosphere based on Celik et al. (2020).

4. Results of the AQABA ship campaign

This chapter presents the results of the AQABA campaign starting with the meteorological observations in section 4.1, followed by the formaldehyde and hydroperoxide distribution around the Arabian Peninsula in section 4.2. The observations are presented in form of a research paper, which also includes the evaluation of HCHO, H₂O₂ and ROOH data based on the general circulation model EMAC. The next chapter contains the determination of HCHO production rates and their relation to measured OH reactivity and OH radicals, which were published in ACP as a measurement report. Chapter 4.4 presents a case study of the air pollution encountered over the Arabian Gulf, followed by the analysis of cleaner regimes (e.g. the Arabian Sea) and the encountered dust events in chapter 4.5.

4.1 Meteorological observations

The marine boundary layer is generally characterized by high humidity and rather stable temperatures due to the buffering effect of the ocean, which prevents rapid cooling of air masses in the MBL during night. During AQABA we experienced generally hot conditions with a mean temperature ($\pm 1\sigma$) of 30.7 ± 4.0 °C. Highest temperatures were detected in the harbor of Kuwait (01. – 03.08.2017) with values of up to 46.0 °C, and the lowest temperatures while sailing through the Arabian Sea with a mean of 25.6 °C. Relative humidity was mostly above 60 %, while some events with dryer air masses were encountered close to the Suez Canal and while the *Kommandor Iona* stayed in the harbors of Jeddah (10. – 12.07.2017) and Kuwait (01. – 03.08.2017). Overall, the dataset covers an average relative humidity of 70 % with the highest levels of up to 96 % over the Arabian Sea, where we observed a mean humidity of 86 % (Fig. 29).

Wind speed observations reflect a large variability during AQABA, with the highest local wind speed of 13.9 m s^{-1} over the southern Red Sea during the first leg, high speeds were also encountered over the Arabian Sea due to the South Asian summer monsoon circulation and over the northern Red Sea. The strong breeze while sailing through the Arabian Sea had an average wind speed of 8.1 m s^{-1} with local maxima up to 12.6 m s^{-1} , during which we encountered strong waves (8 – 10 m). Calmer conditions were then again experienced over the Arabian Gulf with a mean wind speed of 3.3 m s^{-1} . For the whole AQABA dataset, a mean wind speed ($\pm 1\sigma$) of $5.4 \pm 2.8 \text{ m s}^{-1}$ was observed.

We rarely encountered cloudy conditions during the AQABA expedition which is indicated by the high photolysis rates of NO₂ in Fig. 29; we detected values below $6 \cdot 10^{-3} \text{ s}^{-1}$ only on three days. The 14.07.2017 in the southern Red Sea and two days in a row while sailing through the Arabian Sea (09. – 10.08.2017). There was no rain during the whole campaign except a short rain event during the night of the 12.08.2017.

The boundary layer height is expected to be reasonably stable in the MBL, since the ocean prevents that air masses cool as fast as above the continent. Due to lack of accurate measurements, I used the BLH based on hourly ERA5 (ECMWF reanalysis, <https://www.ecmwf.int/en/forecasts/datasets/reanalysis-datasets/era5>) data in Fig. 29, which confirms a reasonably stable BLH of the MBL around the Arabian Peninsula, with a mean boundary layer height ($\pm 1\sigma$) of 691 ± 192 m. Lowest values of the BLH were documented while staying in the harbor of Kuwait, Jeddah and Djibouti, i.e. when staying close to the coastline, where strong diurnal variations of the BLH are expected, which can lead to entrainment and vertical mixing. The BLH is also used in chapter 4.2 to calculate dry deposition velocities (V_{dep}).

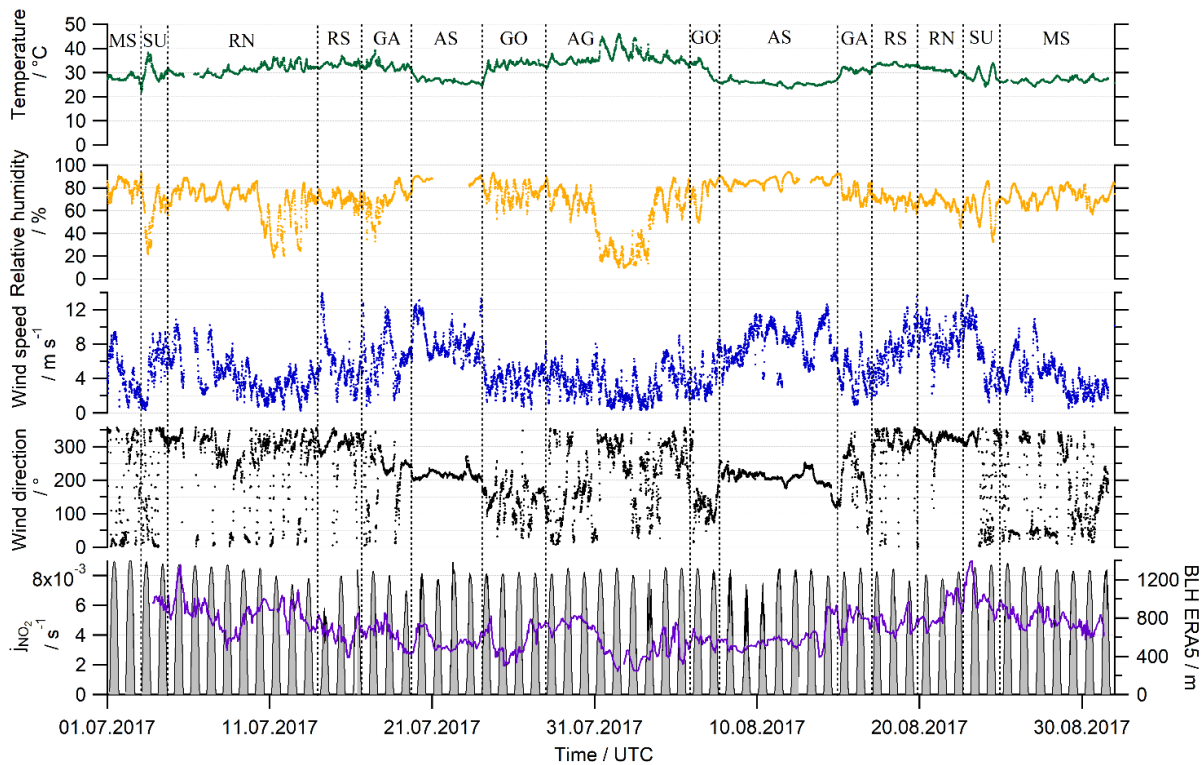


Figure 29: Meteorological observations during the AQABA campaign: Mediterranean Sea (MS), Suez Canal (SU), Red Sea North (RN), Red Sea South (RS), Gulf of Aden (GA), Arabian Sea (AS), Gulf of Oman (GO), Arabian Gulf (AG).

4.1.1 Air mass origin – HYSPLIT trajectories

Air mass origins for the first and the second leg of AQABA are shown in Fig. 30 and 31 based on HYSPLIT trajectories (section 2.5) starting with a sampling height of 200 m at the GPS location of the *Kommandor Iona*, a sampling time of 48 h and a temporal resolution of 1 h. Air masses over the Suez Canal originated for both legs mostly from the Mediterranean Sea with additional winds from Turkey during the first leg. The northern of the Red Sea was dominated by westerly winds coming from Egypt, Sudan and Eritrea, while we encountered very dusty winds from the Sahara over the southern Red Sea with a stronger dust storm during the first leg. These air masses with elevated dust were also detected over the western part of the Gulf of Aden during the first leg, while we encountered mainly winds from Ethiopia and Djibouti over center and the eastern part of the Gulf of Aden. The air mass origin changed with arrival in waters of the Arabian Sea, which was dominated by the strong and stable winds of the South Asian summer monsoon (section 3.1). These winds originated primarily from the Indian Ocean, and then followed along the eastern coastline of Somalia. In the Gulf of Oman, we encountered different conditions for the first and the second leg. During the first leg, air masses originated mostly from Oman, while we encountered primarily winds from Iran and the Arabian Sea during the second leg. A similar trend is reflected by the HYSPLIT trajectories over the Arabian Gulf, where we detected air masses originating from Iraq, Kuwait and the western coastline of the Gulf during the first leg – while the second leg was mainly influenced by winds coming from Iran and the eastern coast of the Gulf, with some short events with winds from Iraq and the western coast of the Gulf. These air masses are analyzed in more detail in a case study in chapter 4.4. Please note that there is data available for the Mediterranean Sea during the first leg, which was not included in Fig. 30. Winds had a similar air mass origin compared to the second leg with long range transport from eastern Europe.

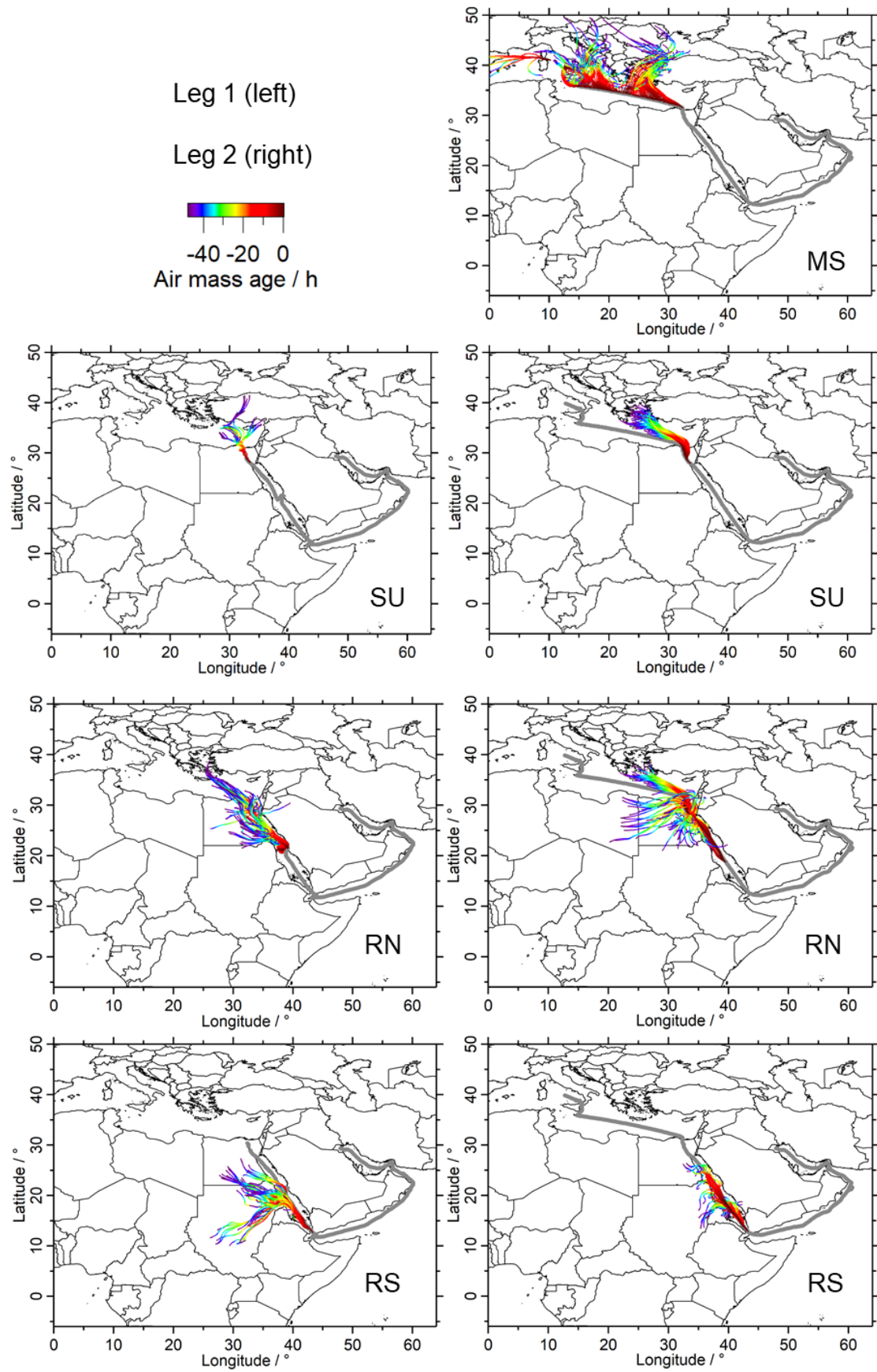


Figure 30: HYSPLIT trajectories for of the Mediterranean Sea (MS), the Suez Canal (SU), the northern Red Sea (RN) and the southern Red Sea (RS) for the first (left) and the second leg (right) of AQABA. Trajectories were calculated with a sampling time of 48 hours and a temporal resolution of one hour.

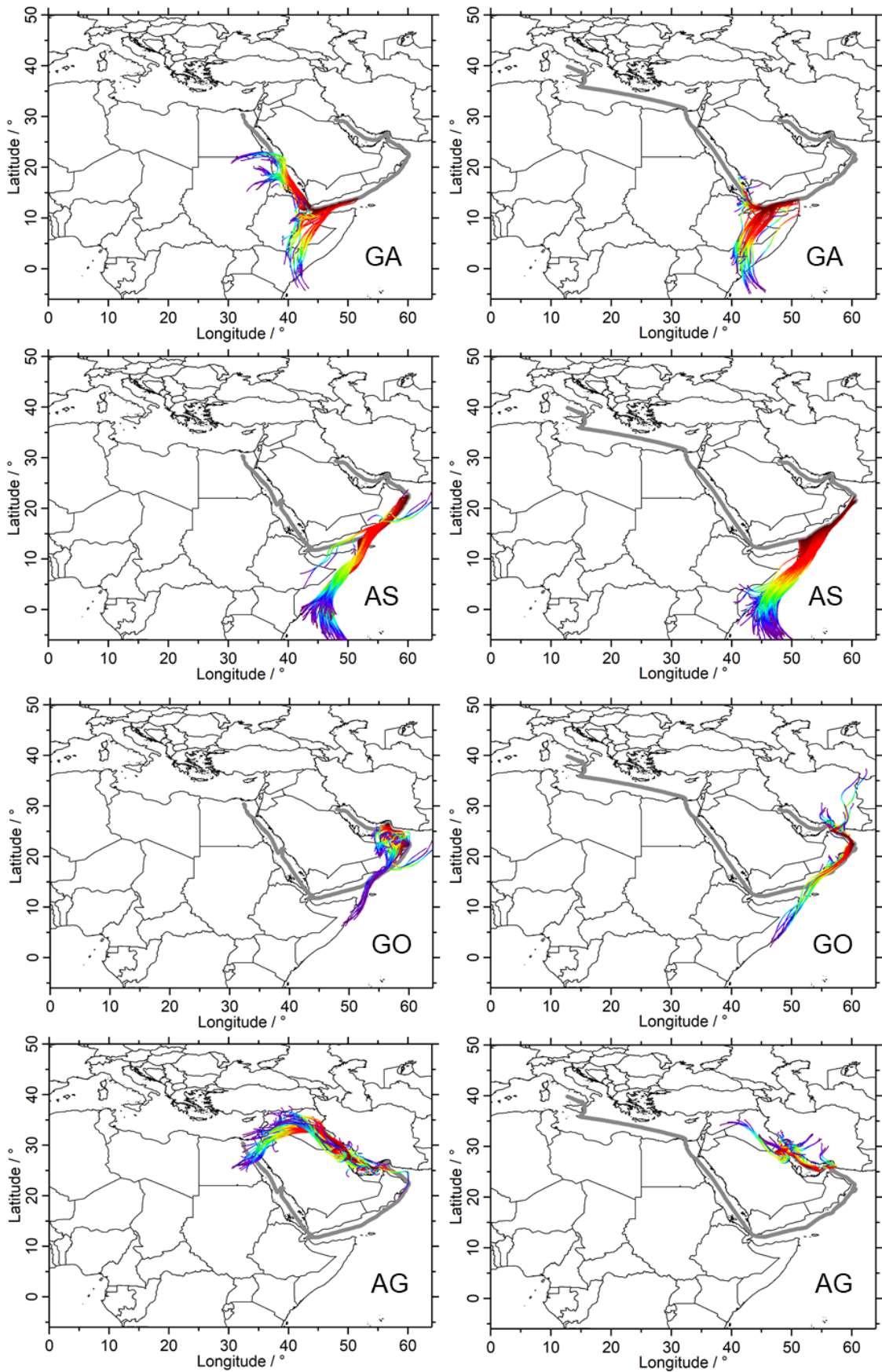


Figure 31: HYSPLIT trajectories for of the Gulf of Aden (GA), the Arabian Sea (AS), the Gulf of Oman (GO) and the Arabian Gulf (AG) for the first (left) and the second leg (right) of AQABA. Trajectories were calculated with a sampling time of 48 hours and a temporal resolution of one hour.

4.2 Formaldehyde and hydroperoxide observations around the Arabian Peninsula

The following chapter contains an overview about the observed HCHO, H₂O₂ and ROOH mixing ratios and their interpretation with respect to the different chemical regimes encountered during AQABA. These were submitted as a research paper to the journal Atmospheric Chemistry and Physics (ACP) and were recently published as a preprint in Atmospheric Chemistry and Physics Discussions (ACPD), the discussion forum of ACP. The draft is presented in its original state. Please note that I therefore did not change the identification of the figures in this chapter. I am the first author of this paper, performed the data analysis and the comparison with the general circulation model EMAC. Additionally, I was responsible for the HCHO, H₂O₂ and ROOH measurements with the AL2021, AL4021 and the dual-enzyme HPLC during the second leg of AQABA, while Bettina Brendel performed the measurements during the first leg.

The manuscript includes the presentation of observed HCHO, H₂O₂, ROOH, OH and HO₂ and their geographical distribution around the Arabian Peninsula. These were compared to EMAC model results, which revealed a strong overestimation of H₂O₂. The photochemical budget of H₂O₂ was evaluated for the observations and the model and identified overestimated HO₂ as a major reason for the offset of simulated H₂O₂. EMAC also simulated a very strong pronounced daily variation of H₂O₂ which was not observed and cannot be explained by the overestimated HO_x. This may indicate underestimated dry deposition. Dry deposition velocities of HCHO and H₂O₂ were calculated during night. EMAC matched the observations over the Arabian Sea within a factor of 2, while the model generally showed a decreased variability of V_{dep} compared to the measurements. Dry deposition over the Mediterranean Sea was underestimated by EMAC while the remaining regions were not compared due to EMACs resolution.

Furthermore, missing anthropogenic sources were identified to be a major cause for missing HCHO over the Arabian Gulf, which is in agreement with the results of Wang et al. (2020). High pollution events of HCHO and ROOH were not matched by EMAC and lead to the recommendation to increase anthropogenic VOC emissions in emission inventories. The AQABA results showed surprisingly declined mixing ratios of OH and HO₂ over the Arabian Gulf which may be related to the dominance of VOC emissions in the area. Elevated ROOH also highlights the abundance of RO₂, which is in agreement with the estimates of HO₂+RO₂ by Tadic et al. (2020).

4.2.1 Formaldehyde and hydroperoxide distribution around the Arabian Peninsula – evaluation of EMAC model results with ship-based measurements

<https://doi.org/10.5194/acp-2022-580>
Preprint. Discussion started: 24 August 2022
© Author(s) 2022. CC BY 4.0 License.



Formaldehyde and hydroperoxide distribution around the Arabian Peninsula – evaluation of EMAC model results with ship-based measurements

Dirk Dienhart¹, Bettina Brendel¹, John N. Crowley¹, Philipp G. Eger¹, Hartwig Harder¹, Monica Martinez¹, Andrea Pozzer¹, Roland Rohloff¹, Jan Schuladen¹, Sebastian Tauer¹, Jos Lelieveld^{1,2}, and Horst Fischer¹

¹Atmospheric Chemistry Department, Max Planck Institute for Chemistry, Mainz, Germany

²Energy, Environment and Water Research Center, The Cyprus Institute, Nicosia, Cyprus

Correspondence to: Dirk Dienhart (D.Dienhart@mpic.de) or Horst Fischer (Horst.Fischer@mpic.de)

Abstract. Formaldehyde (HCHO) and hydrogen peroxide (H₂O₂) play a key role in atmospheric oxidation processes. They act as sources and sinks for HO_x radicals (OH + HO₂), with OH as the primary oxidant that governs the atmospheric self-cleaning capacity. Measurements of these species allow evaluation of global chemistry-transport models which need to account for multifarious source distributions, transport and mixing, complex photochemical reaction pathways and deposition processes. HCHO is an intermediate produced during the oxidation of VOCs and is an indicator of photochemical activity and combustion related emissions. Due to its many production pathways and its rather short lifetime of only several hours at noon, accurate modelling of this species is challenging. In this study, we use in situ observations in the marine boundary layer (MBL) to evaluate results of the general circulation model EMAC (ECHAM5/MESSy2 Atmospheric Chemistry). The dataset was obtained during the AQABA ship campaign around the Arabian Peninsula in summer 2017. This region is characterized by high mixing ratios of photochemical air pollution, high humidity and strong solar irradiation, especially in the area around the Suez Canal and the Arabian Gulf. We find that EMAC fails to predict absolute mixing ratios of HCHO, especially during high pollution events, but it reproduces most of the HCHO variability seen in the different regions, while it systematically overestimates H₂O₂. This is mainly attributed to missing primary VOC emissions and the overestimation of HO_x radicals, and also related to the models coarse spatial resolution.

1 Introduction

The effects of anthropogenic emission of greenhouse gases and aerosols and their increasing impact on climate and air quality represent a global threat. Industrialization enabled the economic development to the modern society, which is characterized by urbanization and immense population growth. Large shares of the agriculture and industry are coupled to the utilization of fossil fuels and thus, emission controls and the characterization of air quality and its health impacts are of increasing importance. Globally, fossil-fuel-related emissions account for about 65 % of the excess mortality and 70 % of the climate cooling by anthropogenic aerosols (Lelieveld et al., 2019). Worldwide some of the largest oil reservoirs are being mobilized by the oil and gas industry in the Middle East, increasing also the local

ship traffic drastically. The emission of volatile organic compounds (VOCs) and nitrogen oxides ($\text{NO}_x = \text{NO} + \text{NO}_2$) by combustion processes make this region a hotspot of tropospheric air pollution in the last decade and favor the production of tropospheric ozone (O_3). The Arabian Peninsula is overall characterized by unique atmospheric conditions (e.g. high temperatures and intense solar irradiation, accompanied by aridity, low cloudiness and occasional dust storms), which classifies the region as a unique environment to study the abundance of atmospheric pollutants and their processing through photochemical oxidation.

The oxidation capacity of the atmosphere determines its self-cleaning ability and is mainly controlled by hydroxyl (OH) radicals in the gas phase. OH oxidizes methane (CH_4) and other VOCs so that these gases are efficiently removed from the atmosphere, e.g. by transition into the particle phase and subsequent wet and dry deposition. Lelieveld et al. (2016) showed that global OH concentrations are buffered with a mean recycling probability of 67 %, indicating that OH is not very sensitive to perturbations by natural or anthropogenic emission changes. This buffering mechanism is based on complementary primary and secondary production of OH, e.g. through photo dissociation of ozone (O_3), reservoir species and radical recycling mechanisms (Lelieveld et al., 2016). OH recycling is generally dominated by the reaction of peroxy radicals with NO, which is referred to as the NO_x recycling mechanism of OH.

Besides hydroxyl radicals, peroxides are a main contributor to the oxidation capacity of the atmosphere, especially in the liquid phase. Further, H_2O_2 plays a key role in atmospheric sulfate formation and acts as a temporary reservoir for OH. With its lifetime of several hours, H_2O_2 enables horizontal or vertical transport of HO_x by e.g. advection and convection of air masses (Nussbaumer et al., 2021a). However, H_2O_2 also transitions readily into the liquid phase and thus also acts as a net sink for HO_x radicals via its dry and wet deposition. To understand the H_2O_2 budget and its diurnal variability, it is necessary to consider all physical and chemical processes within the atmosphere. Besides the net photochemical production (production minus loss) and deposition, horizontal and vertical transport have to be considered. The variation of the H_2O_2 mixing ratio in the absence of clouds during the day can be described by Eq. 1 (Fischer et al., 2019):

$$\frac{d[\text{H}_2\text{O}_2]}{dt} = P_{\text{chem}} - L_{\text{chem}} + \frac{\omega_e \Delta[\text{H}_2\text{O}_2] - V_{\text{dep}}[\text{H}_2\text{O}_2]}{h_{\text{BL}}} - \nabla(v[\text{H}_2\text{O}_2]) \quad (1)$$

with P_{chem} as the sum of all photochemical production terms and L_{chem} the sum of photochemical losses. The third term describes vertical transport in the well mixed boundary layer, which is determined by entrainment and deposition. ω_e represents the entrainment velocity with $\Delta[\text{H}_2\text{O}_2]$ as the concentration difference between the boundary layer and the free troposphere. The deposition is determined by the deposition velocity (V_{dep}) and the boundary layer height (h_{BL}). The last term describes the effect of horizontal transport on the H_2O_2 budget due to a gradient in H_2O_2 mixing ratios ($-\nabla(v[\text{H}_2\text{O}_2])$).

The dominant photochemical source of H_2O_2 is the recombination of HO_2 radicals which involves a collision partner (M) usually nitrogen (N_2), oxygen (O_2) or water vapor (H_2O):



The production of H_2O_2 via R1 competes with the reaction of nitrogen monoxide (NO) and HO_2 (R2), which is one of the most important reactions in the troposphere to recycle OH radicals (Lelieveld et al., 2016).



The photochemical formation of peroxides therefore depends to a large extent on the abundance of NO_x , as elevated mixing ratios of NO ($\sim 100 \text{ ppt}_v$ and higher) substantially suppress peroxide formation (Lee et al., 2000). Photochemical loss reactions of H_2O_2 are the conversion by OH radicals to HO_2 radicals (R3) and photolysis as a source of OH (R4).



Note that R3 and R4 regenerate HO_x , and thus only physical removal of H_2O_2 from the atmosphere results in a net loss of HO_x . According to its high Henry's law coefficient ($\sim 10^5 \text{ mol L}^{-1} \text{ atm}^{-1}$), H_2O_2 is highly soluble and thus efficiently washed out by rain or fog (Klippel et al., 2011; Fischer et al., 2019). Dry deposition also contributes significantly to the removal of H_2O_2 in the boundary layer with typical deposition velocities of $0.1 - 5 \text{ cm s}^{-1}$ (Stickler et al., 2007; Nguyen et al., 2015), which leads to a local maximum of H_2O_2 mixing ratios above the boundary layer (Stickler et al., 2007; Klippel et al., 2011). In the MBL, H_2O_2 concentration gradients are small, so that horizontal transport becomes unimportant. Additionally, the MBL height is relatively constant with no significant diel variation and thus vertical transport is weak, except close to convective clouds (Nussbaumer et al. 2021a, Fischer et al., 2015). Therefore, the H_2O_2 distribution in the MBL depends largely on net photochemical tendencies and deposition processes (Fischer et al., 2015). The H_2O_2 budget in the continental boundary layer is more complex, since all terms in Eq. 1 contribute significantly to the H_2O_2 budget and the boundary layer height follows a relatively strong diel variation. In situ observations in various locations enable (together with meteorological and boundary layer height information) assessment of the role of H_2O_2 for the oxidizing capacity of the atmosphere (Fischer et al., 2019). Various measurement techniques have been developed to determine its vertical and geographical distribution, understand its budget and its response to natural and anthropogenic perturbations (Hottmann et al., 2020; Fischer et al., 2019; Bozem et al., 2017; Fischer et al., 2015; Klippel et al., 2011; Snow et al., 2007; Lee et al., 2000; Sauer et al., 1997). Similar to H_2O_2 , organic peroxides (ROOH) impact the oxidative potential of the atmosphere significantly and they also act as HO_x reservoirs (Lee et al., 2000). Methyl hydroperoxide (MHP, CH_3OOH) is generally the most abundant gaseous, organic hydroperoxide, which is produced by the reaction of HO_2 with methylperoxy radicals (CH_3O_2) formed e.g. during the photochemical oxidation of methane (CH_4) (R5, R6), or by reactions of acetyl peroxy radicals ($\text{CH}_3\text{C}(\text{O})\text{O}_2$) with HO_2 and NO , which can dominate the production of CH_3O_2 (Crowley et al. 2018). Note that the production of MHP competes with the production of formaldehyde (HCHO , R7) from the methylperoxy radical (Nussbaumer et al., 2021b). Besides the photochemical pathways, H_2O_2 and MHP have also been observed to be directly released from biomass burning (Lee et al., 1997).



The main loss reactions of MHP are its photolysis ($\sim 5 \cdot 10^{-6} \text{ s}^{-1}$ at sun peak) (R8), the reaction with OH (R9) (with a lifetime of ~ 15 hours for most regions during AQABA) and physical deposition processes, although it is roughly two orders of magnitude less soluble than H_2O_2 (O'Sullivan et al., 1996; Klippel et al., 2011).



H_2O_2 and MHP can be found in comparable concentrations in many parts of the atmosphere, with the highest variations in the boundary layer (Reeves and Penkett, 2003; Klippel et al., 2011). Besides MHP, peracetic acid (PAA) is another abundant organic hydroperoxide in the troposphere. PAA production rates depend on HO_2 and the acetyl peroxy radical ($\text{CH}_3\text{C}(\text{O})\text{O}_2$), which is considered one of the four most abundant organic peroxy radicals (Tyndall et al., 2001; Crowley et al., 2018). Acetyl peroxy radicals also react rapidly with NO_x , thus the highest concentrations of PAA are expected in regions which are impacted by biogenic emissions in which HO_2 levels are high enough to compete with NO_x

(Berasategui et al., 2020; Phillips et al., 2013). Further organic peroxides are formed in the oxidation of isoprene and other volatile organic compounds (VOCs) (Wennberg et al., 2018; St. Clair et al., 2016; Reeves and Penkett, 2003; Sauer et al., 1999; O’Sullivan et al., 1996). Recent studies also indicate the oxidative potential of isoprene hydroxyl hydroperoxides (ISOPOOH) for sulfate formation in cloud droplets, which could even surpass that of H₂O₂ in forested regions (Dovrou et al., 2021; Dovrou et al., 2019).

Another major HO_x reservoir is formaldehyde, which is a ubiquitous trace gas and the most abundant aldehyde in the troposphere. HCHO is highly reactive and acts as a major source of HO₂ via its photolysis to H and HCO radicals. It can be emitted directly from a variety of both biogenic and anthropogenic sources and is an intermediate during the oxidation of a large number of VOCs, making budget assessments highly complex. Previous studies designed to distinguish between secondary production and direct emissions of HCHO vary widely in their estimates and highlight the importance of local phenomena (Dienhart et al., 2021; Nussbaumer et al., 2021b, Luecken et al., 2018; Anderson et al., 2017; Wolfe et al., 2016; Stickler et al., 2006; Lee et al., 1997).

Remote sensing techniques on satellites platforms enable global observations of HCHO and thus identification of VOC oxidation hotspots (e.g. due to oxidation of isoprene and anthropogenic emissions) and seasonal variability (Zhu et al., 2020; De Smedt et al., 2018; De Smedt et al., 2015; De Smedt et al., 2012; Marbach et al., 2009). HCHO measurements are currently used as HCHO / NO_x ratios for O₃ sensitivity studies (i.e., NO_x or VOC limitation) and global mapping of OH variability in remote air (Nussbaumer et al., 2021a; Nussbaumer et al., 2022; Tadic et al., 2020; Wolfe et al., 2019; Schroeder et al., 2017; Wolfe et al., 2016). In very clean conditions like the remote MBL or the free troposphere, HCHO production is dominated by the photo-oxidation of methane (R5), with the bimolecular self-reaction of methyl peroxy radicals the rate limiting factor (R11) (Nussbaumer et al., 2021b; Wagner et al., 2001). The methoxy radical product (CH₃O) reacts quasi-instantaneously with oxygen to form HCHO and HO₂ (R12). In continentally influenced air masses (NO ≥ 100 ppt_v) R11 is suppressed, as methyl peroxy radicals rapidly oxidize NO, which accelerates HCHO and simultaneously limits MHP formation (Nussbaumer et al., 2021b; Klippel et al., 2011; Lee et al., 2000).



Photolysis of the NO₂ product (R2, R13) leads to tropospheric O₃ formation. Further sources of HCHO are the photochemical degradation of several VOCs, e.g. the ozonolysis of isoprene and other alkenes as well as the degradation of MHP, acetaldehyde, acetone and methanol (Nussbaumer et al., 2021b; Wennberg et al., 2018; Wolfe et al., 2016; Snow et al., 2007; Stickler et al., 2006).



Since the sources of HCHO are diverse, an alternative approach instead of calculating the HCHO budget is to derive the production rate of HCHO from measurements of OH-reactivity towards VOCs, as demonstrated for the Air Quality and climate change in the Arabian Basin (AQABA) campaign data by Dienhart et al. (2021).

Photochemical losses of HCHO are the reaction with OH and its photolysis (R15 – R17) (e.g. Heikes et al., 2001).



Anthropogenic release of HCHO by the oil and gas industry, biomass burning, and secondary production can significantly enhance local HO₂ production (Parrish et al., 2012; Klippel et al., 2011; Lee et al.,

1997). Since the atmospheric lifetime of HCHO is at least several hours and it is released during the photochemical oxidation of numerous VOCs, it is a suitable tracer for recent emissions from anthropogenic activity and combustion processes including biomass burning. The budget of HCHO can be described similarly to H₂O₂ via Eq. 1: its photochemical production pathways depend strongly on the abundance and the composition of VOCs. In the free troposphere, the main sources of HCHO are the photochemical degradation of methane, methanol and MHP (Stickler et al., 2006), whereas in the boundary layer the oxidation of alkenes (e.g. isoprene, ethene), alkanes, and the photochemical degradation of e.g. acetaldehyde, acetone, peroxyacetyl nitrate (PAN) and dimethyl sulfide (DMS) become more significant (Crowley et al., 2018; Nussbaumer et al., 2021b). Wolfe et al. (2016) showed that the link between HCHO and isoprene oxidation is a strong, nonlinear function of NO_x. Primary emissions of HCHO are dominated by combustion processes, with the combustion of fossil fuels in industrialized areas (Williams et al., 2009; Wert et al., 2003) and biomass burning as a strong local source (Kluge et al., 2020, Coggon et al., 2019). Heterogeneous losses via wet and dry deposition also significantly influence the HCHO distribution, although it is less soluble than H₂O₂. This is also reflected in the vertical profile, as maximum mixing ratios of HCHO are typically found in the boundary layer and decrease with altitude in the free troposphere (Zhu et al., 2020; Anderson et al., 2017; Stickler et al., 2007). In clean MBL conditions, HCHO mixing ratios mainly depend on the abundance of HO_x and it is therefore rather homogeneously distributed, whereby horizontal transport is not significant. In more polluted conditions, horizontal transport can significantly influence HCHO mixing ratios on a regional scale. Vertical transport of HCHO is often limited to the MBL, as the boundary layer height is almost constant, except close to convective clouds where elevated mixing ratios of HCHO can be used as an indicator for recent convection (Anderson et al., 2017).

In this study we present the first ship-based measurements in the marine boundary layer of the Arabian Gulf and around the Arabian Peninsula. H₂O₂, organic peroxides and HCHO mixing ratios were evaluated during AQABA in summer 2017 and compared to the general circulation model EMAC (ECHAM5/MESy2 Atmospheric Chemistry). Dry deposition rates of H₂O₂ and HCHO were determined during night using the method of Shepson et al. (1992). Photochemical equilibrium concentrations of H₂O₂ were evaluated with measured OH, HO₂ and actinic flux measurements.

2 Experimental

2.1 AQABA campaign

The Air Quality and Climate Change around the Arabian Basin (AQABA) measurement expedition took place from June 25 until September 3, 2017. Instrumentation of the ship (*Kommandor Iona*) was performed in La Seyne-sur-Mer (near Toulon, France), from where the first leg of the cruise started through the Mediterranean, the Suez Canal and the Red Sea to the first stop in Jeddah. The expedition continued two days later via the Gulf of Aden, the Indian Ocean, the Gulf of Oman and the Arabian Gulf (also Persian Gulf) to Kuwait. On the second leg, the ship returned with the same route (Fig. 1), without stopping in Jeddah, to end the expedition at Stromboli volcano. The *Kommandor Iona* was equipped with a weather station and five laboratory containers on the front deck with instrumentation for in situ and offline monitoring of a large variety of gaseous species, particles and radicals. Details about the measurements performed during AQABA can be found in a number of previous publications (Dienhart et al., 2021; Friedrich et al., 2021; Paris et al., 2021; Celik et al., 2020; Tadic et al., 2020; Wang et al., 2020; Bourtsoukidis et al., 2019; Pfannerstil et al., 2019; Eger et al., 2019;).

2.2 Instrumentation and sampling

HCHO and hydroperoxides were measured using modified commercial Aero-Laser instruments (AL2021, AL4021, Aero-Laser GmbH, Garmisch-Partenkirchen, Germany), which were placed in a temperature-controlled container. With the exception of the aerosol and radical measurements (OH and HO₂), air was sampled from a high-flow (10 m³ min⁻¹) cylindrical stainless steel inlet (HFI, sampling height: 5.5 m above deck, diameter: 0.2 m), placed between the containers on the front deck of the ship. Air was drawn from the center of the HFI into the air-conditioned laboratory containers using PFA (perfluoroalkoxy alkane) tubing. The 4.2 m long ½" PFA-bypass was insulated to prevent condensation and was used with a flow rate of 12 L min⁻¹, which resulted in a residence time of ~9 s for both instruments. This setup ensured no vessel contamination while sampling against the wind direction and minimized sampling artifacts e.g. by preventing condensation. The sampling bypass was exchanged in Kuwait before the second leg.

2.3 HCHO measurements

HCHO measurements were performed based on the fluorometric Hantzsch reagent method (AL4021 therefore called 'Hantzsch monitor') following the principle of (Dasgupta et al., 1988) and the design of (Kelly and Fortune, 1994). In a first step, HCHO is stripped from an airflow of 1 L min⁻¹ into 0.025 M H₂SO₄ (sulphuric acid for analysis, 96 %, Acros Organics) with a flow of 0.55 ml min⁻¹ at 10 °C in a stripping coil. The acidity of the stripping solution promotes quantitative solubility of HCHO and minimizes the dissolution of gaseous SO₂ which otherwise could interfere by formation of a sulfur adduct in the liquid phase. Subsequently, HCHO(aq) quantitatively reacts with pentane-2,4-dione (acetylacetone, EMSURE for analysis, 99 %, Merck) and ammonia (ammoniumacetate, 99 %, VWR) at low pH (acetic acid, analytical grade, 100 %, Serva) in the reactor coil, thermostatted at 65 °C, to form the Hantzsch product 3,5-diacetyl-1,4-dihydrolutidine (DDL). DDL is subsequently detected by excitation at 410 nm with a mercury Pen-Ray[®] lamp, followed by collection of the fluorescence radiation 90° off axis around 510 nm with a photomultiplier tube (Hamamatsu Photonics, model H957-01). Aqueous HCHO standards were used to calibrate the response. Line losses and sampling efficiency during the campaign were corrected by measuring gaseous standards generated using a HCHO permeation source (section 2.5).

2.4 H₂O₂ and organic hydroperoxide measurements

H₂O₂ and organic hydroperoxides (ROOH) were measured with the AL2021 based on the dual-enzyme technique described in Lazrus et al. (1985). Ambient air is collected through a bypass with 2.3 L min⁻¹ and consequently passed through a glass coil together with a buffered (potassium hydrogen phthalate for analysis, PanReac; NaOH, 1 mol/L, Fluka) stripping solution (0.55 mL min⁻¹, pH 5.8). Hydroperoxides dissolve in the stripping solution with a stripping efficiency depending on their Henry's law constant (O'Sullivan et al., 1996). Typically, H₂O₂ is dissolved quantitatively, CH₃OOH (methyl hydroperoxide, MHP) the smallest organic hydroperoxide, with a stripping efficiency of ~60 % (Hottmann et al., 2020; Klippel et al., 2011). As the instrument does not differentiate between different organic hydroperoxides and as solvation is a critical step for quantification, the AL2021 delivers a lower estimate of the total organic hydroperoxide mixing ratios. The dissolved hydroperoxides are separated into two channels and subsequently detected via reaction to a fluorescent dye with horseradish peroxidase (HRP, Sigma Aldrich) and 4-hydroxyphenylacetic acid (POPHA, Sigma Aldrich). The dimer of POPHA, 6,6'-dihydroxy-3,3'-biphenyldiacetic acid, is formed stoichiometrically and detected by fluorescence spectroscopy via excitation with a Cadmium Pen-Ray[®] lamp at 326 nm. Detection of the

fluorescence radiation 90° off axis is performed between 400 – 420 nm with a photomultiplier tube (Hamamatsu Photonics, model H957-01) for both channels. The enzyme catalase (Sigma Aldrich) is injected into the reaction coil of channel B, prior to the reaction with HRP and POPHA, to selectively destroy H₂O₂. This technique allows quantification of H₂O₂ by calculation of the difference between channel A, which delivers the total mixing ratio of ROOH and H₂O₂, and channel B, which delivers the total mixing ratio of ROOH. Since this principle is dependent on the catalase efficiency, it is determined for every liquid calibration and was in the range of 95 – 100 % during AQABA. In addition to the AL2021, we also operated an instrument for the detection of different organic peroxides separated by HPLC (high-performance liquid chromatography). Similar to the AL2021, it utilizes the selective dual-enzyme technique by post column derivatization and thus the HPLC enables quantification of separated organic hydroperoxides and H₂O₂ in low ppt_v levels. When the sea was rough, the movement of the ship interfered with the instrument, causing drifts of the baseline, which may have been caused by pressure variations within the constant-flow eluent pumps. Therefore, quantification of the organic hydroperoxides was not possible and we only used the chromatograms for qualitative identification of the more abundant species.

2.5 Calibration and instrument characteristics during AQABA

External calibration of both instruments was performed with aqueous standards (HCHO, H₂O₂) by dilution of stock solutions. The H₂O₂ stock solution was prepared with 1 mL H₂O₂ (30 %, Roth) in 999 mL H₂O (EMSURE®, Merck) and checked for stability by regular titration with potassium permanganate (KMnO₄, 0.002 mol/L, Merck). The HCHO stock solution consisted of 3 mL HCHO (37 %, Sigma Aldrich) in 997 mL H₂O and was titrated against iodine (I₂, 0.05 mol/L, Merck).

In addition, gaseous standards were measured to calculate the inlet efficiency of the PFA-bypass. Calibration gas flows were generated using permeation devices in temperature controlled glass flasks, which were flushed at a constant flow rate of 80 standard cubic centimeters (sccm) per minute with zero air (Zero Air generator CAP 60, Infiltec, Germany). HCHO calibration gas was created from a paraformaldehyde container (VICI AG, Switzerland) which was heated to 60 °C. The gaseous H₂O₂ standard was generated from a permeation source built with a 15 cm long 1/8" polyethylene (PE) tube, that was filled with the 30 % H₂O₂ solution, closed with PFA fittings (Swagelok, USA) and heated to 35 °C. The highly concentrated flow was then diluted with additional zero air. The permeation rates of both sources were measured based on the chromotropic acid reaction (Altshuller et al., 1961) and the reaction of H₂O₂ with TiCl₄ described in Pilz and Johann (1974). Note that the AL2021 has known O₃ and NO interferences, which were accounted for in the final dataset. We found an interference of 36 ppt_v H₂O₂ equivalents per 100 ppb_v O₃ and 12 ppt_v H₂O₂ per 100 ppb_v NO. We did not find a significant O₃ interference in lab experiments for the AL4021.

Zero gas measurements were performed every 3.5 h for 30 minutes to account for baseline drifts and to determine the instrument's stability. This interval was used intentional so that zero measurements are performed on a variable time stamp to ensure no data gaps for diurnal profiles. For this purpose, we used a bypass via a three-way valve with a silica gel cartridge (SiO₂ with orange indicator, Roth) to dry the sampled air followed by a scrubber cartridge containing Hopcalite® (MnO₂/CuO, IAC-330, Infiltec, Germany) and platinum (Pt/Al₂O₃, IAC-114, Infiltec, Germany) as catalysts to destroy the remaining hydroperoxides, HCHO, other OVOCs and O₃.

Both instruments log data on a custom built computing unit (V25) with a 3 second time resolution, but the data shown in this paper was at least averaged to the so-called effective time resolution, which was determined as the response time of the instrument (10 to 90 % of the signal intensity during the injection of liquid standards). The limit of detection (LOD) was calculated as the 2σ deviation of all zero air

measurements during AQABA at the effective time resolution of 180 seconds. The precision (P) was calculated by the 1σ deviation of the liquid standard calibrations throughout the whole measurement campaign, therefore it contains also the pipetting error during the preparation of the standards. The total measurement uncertainty (TMU) was calculated according to Gaussian error propagation. In this equation, S is the uncertainty of the standard, IE the inlet efficiency and OI the O₃ interference.

$$TMU = \sqrt{(P)^2 + (S)^2 + (IE)^2 + (OI)^2} \quad (2)$$

Table 1: Instrument characteristics of the HCHO and hydroperoxide measurements during the AQABA campaign.

	HCHO (AL4021)	H ₂ O ₂ (AL2021)	ROOH (AL2021)
Time Res.	180 s	180 s	180 s
LOD (2 σ)	80 – 128 ppt _v	13 ppt _v	8 ppt _v
P (1 σ)	1.5 % @ 8.1 ppb _v	1.2 % @ 4.4 ppb _v	1.7 % @ 4.5 ppb _v
TMU	13 %	20 %	≥ 40 %

Note that for the LOD of the AL4021, we found a significant change of the background noise, while operating the instrument when the sea was rough during strong wave conditions. Excluding these rough sea conditions for observations over the Arabian Sea yields a detection limit of 80 ppt_v.

2.6 Further measurements

OH and HO₂ were performed with the HydrOxyl Radical Measurement Unit based on Fluorescence Spectroscopy (HORUS) and sampled from a separated inlet closer to the LIF (laser-induced fluorescence) instrument, to achieve as low as possible residence times in the sampling. The instrument utilizes LIF of the OH radical, and by the titration of HO₂ with NO, simultaneous measurements of HO₂ are implemented (Hens et al., 2014; Marno et al., 2020).

Wavelength resolved actinic flux was measured with a spectral photometer (CCD Spectroradiometer 85237) to calculate photolysis frequencies (*j*-values). The radiometer was installed about 5 m above the front deck level and it was cleaned every morning to remove sea salt and dust particles. Decreases in sensitivity due to sensor contamination were corrected with a linear interpolation between the cleaning events. The *j*-values are not corrected for upwelling actinic flux from the sea surface and therefore the TMU was estimated with > 10 %, depending on the reaction. More details about the setup and calibration of CCD spectroradiometers can be found in Bohn and Lohse (2017). Temperature, pressure, wind direction and speed were measured with the European Common Automatic Weather Station (EUCAWS), a weather station specifically designed for ships.

2.7 Global Atmospheric Chemistry model EMAC

ECHAM5/MESy2 Atmospheric Chemistry (EMAC) model is a numerical chemistry general circulation model (CGCM), which describes tropospheric and middle atmosphere processes. EMAC is based on 5th generation of the European Center HAMburg (ECHAM5), a general circulation model (Roegner et al., 2006), and uses the second version of the Modular Earth Submodel System (MESy2) to link multi-institutional sub models (Joeckel et al., 2010). Here we use EMAC with the chemistry mechanism MOM (Mainz Organics Mechanism) implemented with the sub-model MECCA, which contains the basic HO_x, NO_x and CH₄ chemistry, but also halogens, sulfur and mercury (Sander et al., 2019; Lelieveld et al., 2016). Development of MOM also included a variety of NMHCs, aromatics and OVOCs including isoprene und terpene oxidation (Sander et al., 2019) and, recently, the model has been thoroughly evaluated with this chemical mechanism (Poizzer et al., 2022). Therefore, it is ideal to test the model with the complex photo oxidation during AQABA, especially in the Arabian Gulf, where a lot of oil and gas industry is operating and model results already identified it as a hotspot of tropospheric

O₃ (Lelieveld et al., 2009). The model simulations were carried out in the T106L31 resolution, which correspond to a grid of 1.1° · 1.1° with 31 vertical pressure layers. Previous results of airborne and shipborne expeditions have been compared to EMAC (Fischer et al., 2015; Klippel et al., 2011), also the AQABA datasets of NO_x, O₃ and VOCs during AQABA have been published (Tadic et al., 2020; Wang et al., 2020). The dynamics have been weakly nudged (Jeuken et al., 1996; Jöckel et al., 2006) towards the ERA-interim data (Berrisford et al., 2011) of the European Centre for Medium-Range Weather Forecasts (ECMWF) to reproduce the actual day-to-day meteorology in the troposphere. The anthropogenic emissions are based on the Emissions Database for Global Atmospheric Research (EDGARv4.3.2). Further details are presented in Pozzer et al. (2022).

2.8 Methods

In the MBL, the production of peroxides is dominated by the recombination of peroxy radicals, thus the in situ measurements of HO₂ enable calculation of the production rates P(H₂O₂) with Eq. 4.

$$P(\text{H}_2\text{O}_2) = k_{\text{HO}_2+\text{HO}_2} [\text{HO}_2]^2 \quad (3)$$

Photochemical loss reactions are the photolysis and the reaction with OH, besides the deposition, which is the dominant loss during night.

$$L(\text{H}_2\text{O}_2) = (j_{\text{H}_2\text{O}_2} + k_{\text{H}_2\text{O}_2+\text{OH}}[\text{OH}]) [\text{H}_2\text{O}_2] + k_{\text{Dep}(\text{H}_2\text{O}_2)}[\text{H}_2\text{O}_2] \quad (4)$$

Since the measurements were performed in the MBL, the water dependency of the HO₂ recombination becomes significant and was calculated with the relative humidity measurements (RH) via Eq. 10 - 12 (<https://iupac-aeris.ipsl.fr/test/front-office/datasheets/pdf/HOx14.pdf>, July 2022).

$$k_{\text{HO}_2+\text{HO}_2} = (k_1 + k_2) \cdot (1 + 1.4 \cdot 10^{-21} \cdot [\text{H}_2\text{O}] \cdot \exp\left(\frac{2200}{T}\right)) \quad (5)$$

$$k_1 = 2.2 \cdot 10^{-13} \cdot \exp\left(\frac{600}{T}\right) \frac{\text{cm}^3}{\text{molec s}} \quad (6)$$

$$k_2 = 1.9 \cdot 10^{-33} \cdot [\text{N}_2] \cdot \exp\left(\frac{980}{T}\right) \frac{\text{cm}^3}{\text{molec s}} \quad (7)$$

$$[\text{H}_2\text{O}] = \frac{p_{\text{H}_2\text{O}}^0 \cdot \text{RH} \cdot N_A}{R \cdot T} \quad (8)$$

$$p_{\text{H}_2\text{O}}^0(T) = 1013.25 \text{ hPa} \cdot \exp(13.3185a - 1.97a^2 - 0.6445a^3 - 0.1299a^4) \quad (9)$$

$$a = 1 - \frac{373.15 \text{ K}}{T} \quad (10)$$

During night, the photochemical production and loss reactions due to OH can be neglected, therefore, the decay of H₂O₂ and HCHO in clean air masses during night is dominated by deposition. With the assumption of a constant and horizontally homogenous boundary layer, the exponential decay can be used to estimate the deposition velocity (V_{dep}) with the method of Shepson et al. (1992). In this calculation, we assume that the initial mixing ratio [X]₀ (j_{NO2} < 10⁻³) represents the mixing ratio on top of the nocturnal boundary layer (h_{BL}). If species X is homogeneously distributed within the BL and it follows exponential decay during night, the first order decay is given by Eq. 11. Thus, the first order decay plot (ln[X]_t/[X]₀ versus the time) yields the deposition velocity of species X with a known boundary layer height.

$$\ln \frac{[\text{X}]_t}{[\text{X}]_0} = \frac{-V_{\text{dep}}(\text{X})}{h_{\text{BL}}} t \quad (11)$$

Additionally, the deposition rate can be calculated with Eq. 12, assuming that the boundary layer is well mixed.

$$V_{\text{dep}} = k_{\text{dep}} h_{\text{BL}} \quad (12)$$

3 Results

3.1 Regional distribution of HCHO, H₂O₂ and organic peroxides around the Arabian Peninsula

The cruise track of the *Kommandor Iona* is shown in Fig. 1, subdivided into eight regions identified by different colors: The Mediterranean Sea (MS), Suez Canal and the Gulf of Suez (SU), Red Sea North (RN), Red Sea South (RS), Gulf of Aden (GA), Arabian Sea (AS), Gulf of Oman (GO) and Arabian Gulf (AG). The AG (also known as the Persian Gulf) and the SU are well known for their oil and gas industry and intensive ship traffic, respectively, hence primary emissions of NO_x, CO, and to a lesser extent HCHO were expected to affect mixing ratios of these trace gases. Nearby ship plumes (including the *Kommandor Iona* exhaust) and other point sources were identified with the use of NO_x, CO, SO₂ and wind direction data and excluded from the dataset used in this study (Celik et al., 2020). The measurements were affected by aft winds in particular during the first leg, resulting in a contamination from the ships exhaust, thus limiting the amount of data available (Fig. S1). In general, we did not find elevated mixing ratios of peroxides in ship plumes (presumably a result of the high NO_x levels) and thus decided to keep the data, but corrections for known NO interferences were applied (2.4). Contrary to H₂O₂, HCHO is affected by ship exhaust plumes (Celik et al., 2020) and thus contaminated data have been filtered out.

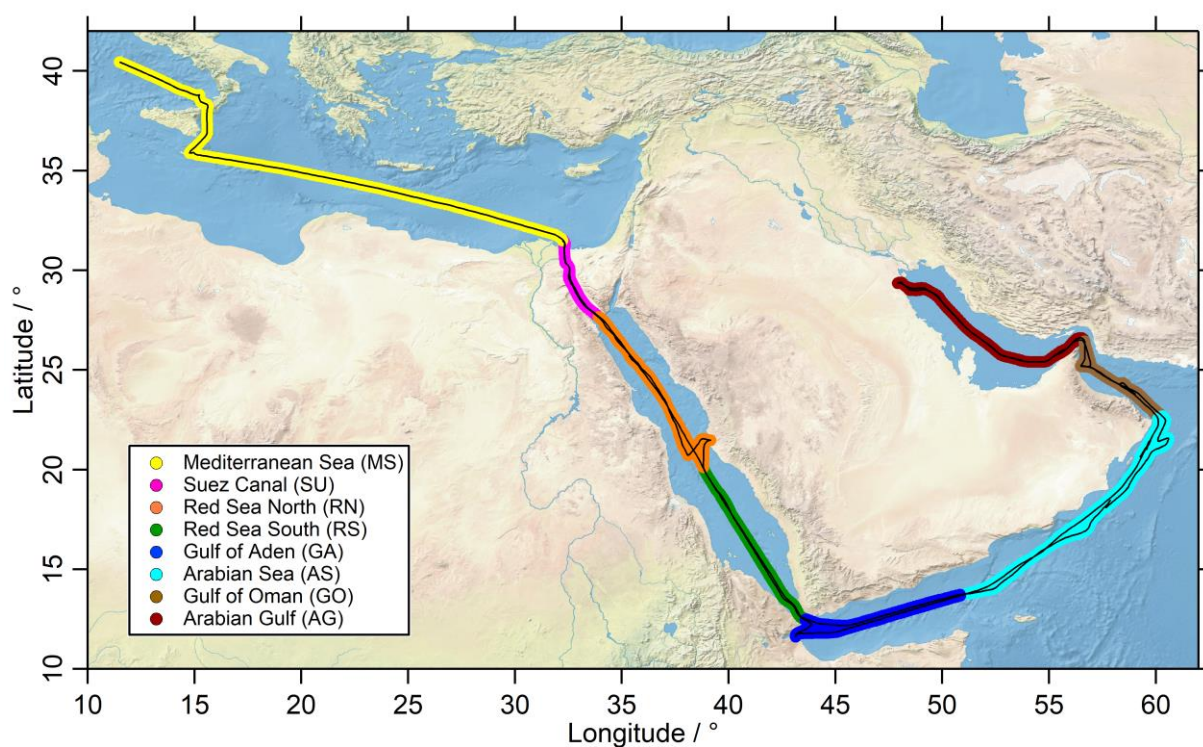


Figure 1: The shiptrack (black) of the *Kommandor Iona* during the AQABA cruise subdivided into eight regions: Mediterranean sea (MS: yellow), Suez Canal (SU: pink), Red Sea North (RN: orange), Red Sea South (RS: green), Gulf of Aden (GA: blue), Arabian Sea (AS: turquoise), Gulf of Oman (GO: brown) and Arabian Gulf (AG: red). The map was created with data provided by the Natural Earth website (<http://www.naturalearthdata.com>).

In Figure 2 we present mixing ratios of HCHO (upper panels), H₂O₂ (middle panels) and ROOH (lower panels) color-coded along the ship cruise track for the first (left panels) and second leg (right panels). Time series of these species can also be found in the supplementary information (Fig. S1, Fig. S3 and S5). Box-and-whisker plots of the mixing ratios for HCHO, H₂O₂ and ROOH for the 8 regions are shown in Fig. 3 and 4. Numerical values are listed in Tab. S1.

Mixing ratios of HCHO (upper panels of Fig. 2, Fig. S1) exhibit a large variability. The highest mixing ratios (12.62 ppb_v) were measured in the center of the Arabian Gulf with north-westerly winds originating from Iraq / Kuwait during the first leg (Fig. 2, upper left panel). Lower mixing ratios were detected in this area during the second leg, when the wind originated from the north-east, coming from Iran (Fig. 2, upper right panel). The lowest HCHO median mixing ratios were measured in the RS (0.37 ppb_v) during the second leg, in unpolluted air mass originating from Eritrea. Low HCHO was also found in the GA (0.50 ppb_v), the MS (0.77 ppb_v) and the AS (0.86 ppb_v). In general, low mixing ratios of HCHO are associated with low NO_x, low O₃ (Tadic et al., 2021), low VOCs (Bourtsoukidis et al., 2019), low OH reactivity (Pfannerstill et al., 2019) and in particular low OH reactivity towards VOCs (Dienhart et al., 2021), while high mixing ratios of HCHO are associated with elevated values for these species.

To the best of our knowledge there are no ship-borne measurements of HCHO available in the Red Sea and the Arabian Gulf to be compared to our data. In general, the measured mean mixing ratios during AQABA are generally larger compared to previous studies in the MBL. Wagner et al. (2001) performed ship-borne measurements during the INDOEX campaign in the central Indian Ocean with HCHO mixing ratios between 0.2 – 0.5 ppb_v, with the lowest mixing ratios in the clean maritime background of the southern hemisphere. Weller et al. (2000) reported ship-based HCHO measurements in the Atlantic, which reached a broad maximum with values of 1.0 – 1.2 ppb_v in the tropical Atlantic.

The lowest median mixing ratios of H₂O₂ were found in GO and GA (0.12 ppb_v), followed by AS (0.15 ppb_v), while higher mixing ratios of H₂O₂ were found in RS, SU (0.25 ppb_v) and MS (0.26 ppb_v). Altogether, the H₂O₂ measurements exhibit lower variation around the Arabian Peninsula compared to HCHO. Higher variability of H₂O₂ was found in SU and AG, although less than 25 % of the data exceeds 0.50 ppb_v, with highest H₂O₂ mixing ratios observed in AG (0.92 ppb_v) in the harbor of Kuwait. AG, SU, MS and RN also show the strongest diurnal variations of up to ~300 ppt_v (Fig. S3).

Absolute mixing ratios of H₂O₂ are in the same range as previous measurements of H₂O₂ in the MBL (Fischer et al., 2015; Stickler et al., 2007; O'Sullivan et al., 2004; Chang et al., 2004; Kieber et al., 2001; Lee et al., 2000; Weller et al., 2000; Junkermann and Stockwell, 1999). These observations indicate highest mixing ratios (> 500 ppt_v) of H₂O₂ in the tropics (O'Sullivan et al., 2004; Weller et al., 2000; O'Sullivan et al., 1999; Junkermann and Stockwell, 1999; Heikes et al., 1996; Slemr and Tremmel, 1994) and decreasing concentrations towards higher latitudes in both hemispheres, reaching 200 – 300 ppt_v in the extra-tropics (Fischer et al., 2015; O'Sullivan et al., 2004; Weller et al., 2000; Junkermann and Stockwell, 1999; O'Sullivan et al., 1999; Slemr and Tremmel, 1994). In general, higher H₂O₂ mixing ratios have been observed in continental outflow (e.g. Heikes et al., 1996).

The organic peroxides showed higher variability compared to H₂O₂ (Fig. 4), with the lowest median value in AS (0.06 ppb_v), followed by GO (0.07 ppb_v) and GA (0.10 ppb_v). We found the lowest variability (whisker-intervals) in AS, which represents the cleanest conditions and the lowest variability of O₃ and NO_x (Tadic et al., 2020). Higher levels of organic peroxides were detected in SU (0.26 ppb_v), AG (0.23 ppb_v), MS (0.22 ppb_v) and RN (0.20 ppb_v) with the highest mixing ratios in the center of the Arabian Gulf during the first leg (2.26 ppb_v).

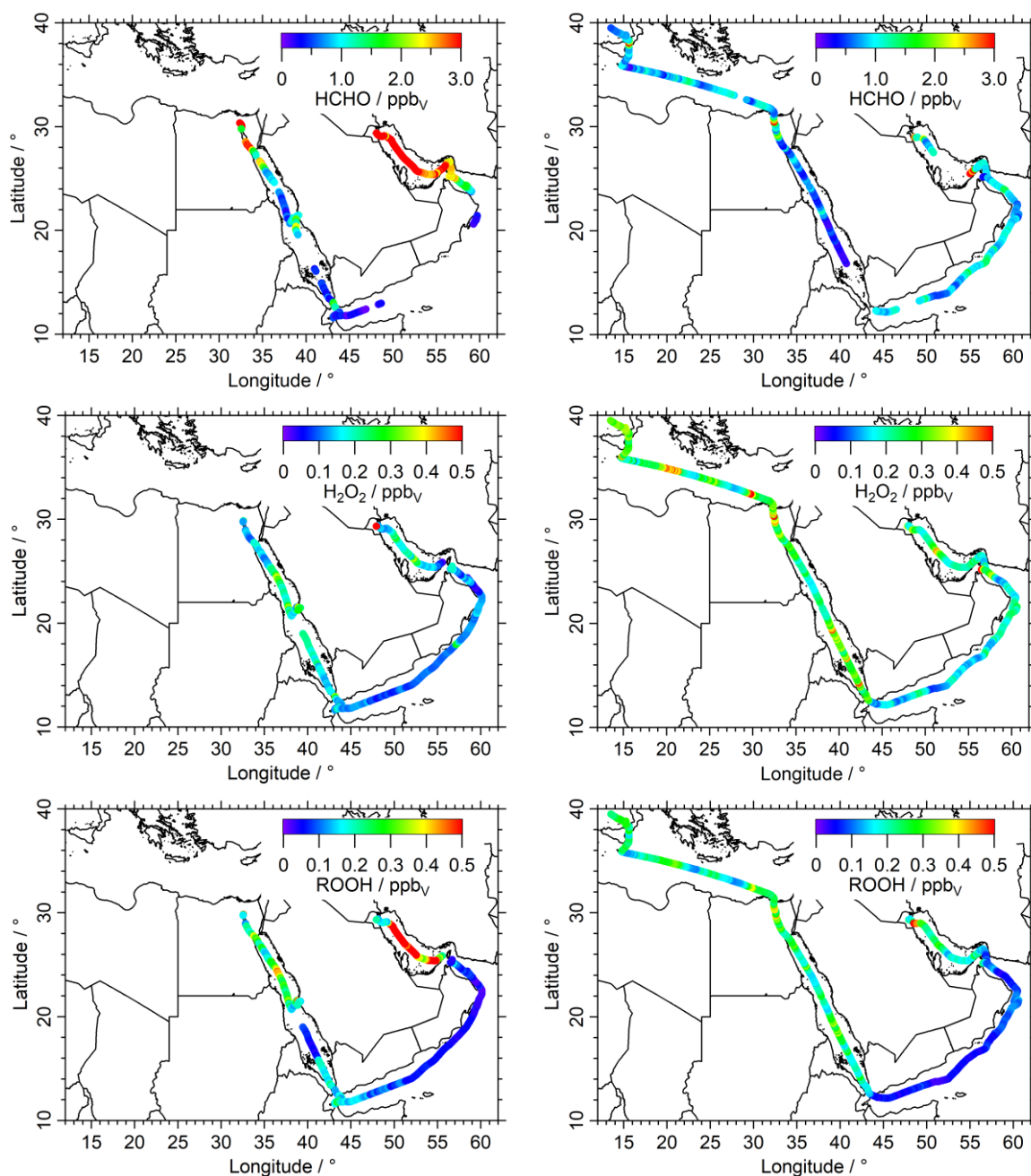


Figure 2: Overview and data coverage of HCHO, H₂O₂ and organic hydroperoxide measurements during both legs of the AQABA ship campaign (graphs on the left represent the first leg). Contaminated HCHO data (e.g. by ship exhausts) were removed from the dataset with a stack filter (based on the NO, CO and SO₂ observations), therefore there is less HCHO data coverage during the first leg in the Arabian Sea.

The chromatograms of the HPLC-based instrument indicate significant abundances of four distinct inorganic and organic hydroperoxides in AG (Fig. S10), which were identified as H₂O₂, MHP, PAA (peracetic acid) and EHP (ethyl hydroperoxide) based on their retention times and gaseous injections of PAA with a diffusion source. In addition to the continuous HPLC measurements, we also injected enriched samples with sampling times varying between 12 – 36 h during various times along the ship track. Although these samples have very limited time resolution, they were used for a qualitative assessment of the abundance of further organic hydroperoxides. Significantly enhanced amounts of EHP were only detected over the Arabian Gulf, although small amounts of EHP were also detected in the enriched samples in MS (Fig. S10).

Highest amounts of photochemical air pollution were detected over the AG, which is confirmed by the highest mixing ratios of HCHO and ROOH in this region when observing winds from the western

coastline and Kuwait. Less air pollution was observed during the second leg, when we were sampling air masses originating from Iran. In this region we also observed the strongest radiation and the highest temperatures during AQABA. SU and RN also show enhanced contributions of VOCs (Wang et al., 2020) and elevated OH reactivity (Pfanerstill et al., 2019), mainly while passing oil rigs and on the way through the Suez Canal. Tadic et al. (2020) found the cleanest conditions, from both a NO_x and O_3 perspective, in the AS and the RS. This can be confirmed by the rather decreased mixing ratios of HCHO, ROOH and H_2O_2 mixing ratios, which reflect low levels of HO_x . Air masses from Eritrea also contained suppressed mixing ratios of ROOH during the first leg.

3.2 EMAC model comparison

The observations of HCHO, H_2O_2 and ROOH were compared to numerical results of the model EMAC. The highly complex photochemistry around the Arabian Peninsula is well suited to MOM's photochemistry mechanism. The high pollution levels e.g. in the AG contrast with the rather clean regions like AS and MS, that represent mostly aged air masses with less anthropogenic influence, although clean MBL conditions ($\text{NO}_x < 50 \text{ ppt}_v$) were rarely encountered during AQABA. Here we use simulations from the lowest vertical level of EMAC (~30 m) at a temporal resolution of 10 minutes. Time series (Fig. S1, S3 and S5) and scatter plots (Fig. S2, S4 and S6) are shown in the supplement. Regional variations are highlighted in Fig. 3 and 4 by box-and-whisker plots and by the measurement to model ratio (Fig. 3 and 4), the EMAC data was adapted to the measurements with a time resolution of 10 minutes for these plots. Numerical values are listed in Table S1. Additionally, frequency distribution of mixing ratios for observations and model simulations for the individual regions are presented in the supplement (Fig. S14, S15, S16).

In general, EMAC reproduces the regional trends of HCHO quite well (Fig. 3, left panel) although the whisker intervals (10 – 90 %) demonstrate that the model computes less variability, most likely due to missing localized pollution events, which is to be expected for a global model at relatively low resolution. The median values of the measured to model ratio vary between 0.3 and 1.6 (Fig. 3, right panel). EMAC overestimates HCHO in the cleaner regions MS, RS and GA, while it underestimates HCHO in AS and the heavily polluted AG.

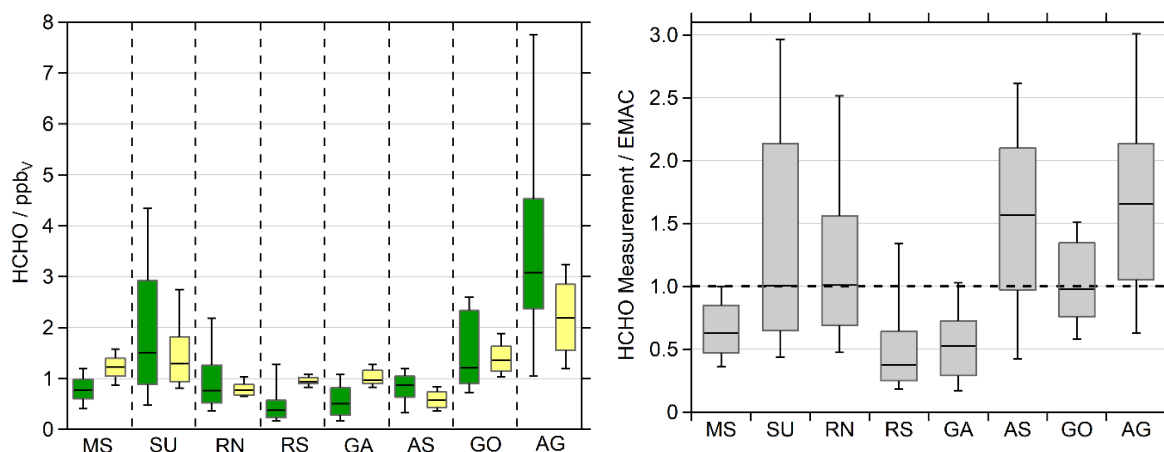


Figure 3: Formaldehyde observations (green) and EMAC simulations (yellow) divided into the eight regions during AQABA: Mediterranean sea (MS), Suez Canal (SU), Red Sea North (RN), Red Sea South (RS), Gulf of Aden (GA), Arabian Sea (AS), Gulf of Oman (GO) and Arabian Gulf (AG). We used the lowermost model results (~30 m) for the comparison in 10 min averages (left). The box represents 25 to 75 % of the data and the whiskers 10 to 90 % with the median as the black line. The right panel shows the ratio between the observations and the model simulations.

Elevated NO_x and O_3 measurements classified AG and SU as the most polluted regions, followed by RN and GO which both were influenced to a higher extent by anthropogenic pollution (Tadic et al., 2020). The elevated HCHO during the high ozone and VOC conditions on the first leg in AG was not reproduced by EMAC. Here the model clearly underestimates HCHO (Fig. S1) and ROOH (Fig. S5). Since the elevated OVOCs correlated well with CO and O_3 (Wang et al. 2020), we can assume that we probed a highly polluted and photochemically active air mass, with both effective photochemical production and primary emissions of HCHO. During this event, maximum HCHO and ROOH mixing ratios were measured during AQABA, with values up to 12.63 ppb_v HCHO and 2.26 ppb_v ROOH in the center of the Gulf (Fig. 2, Fig. S9). The event was less pronounced in EMAC with simulated values reaching up to 3.31 ppb_v HCHO leading to the model underestimating HCHO in the AG by about a factor of 4. EMAC does not simulate significantly elevated values of ROOH peaking at 0.49 ppb_v, but with elevated contribution of PAA and EHP. Even though, the model underestimates ROOH also by about a factor of 4 (Fig. S9). Wang et al. (2020) also show, that EMAC simulates enhanced acetone and methyl ethyl ketone (MEK) during this event, although the model shows no significant increase of acetaldehyde.

In the Suez Canal and the Gulf of Suez (SU), the second most polluted region, the model simulations clearly underestimate the high HCHO mixing ratios encountered during the first leg, even though EMAC also simulates a significant increase. This is most likely due to local emissions from oil rigs, the dense ship traffic and air masses influenced by biomass burning in this region (Wang et al., 2020).

EMAC overestimates HCHO in the less polluted regions of the MS, RS and GA. Tadic et al. (2020) also found that the simulations overestimate NO_x and O_3 in these areas. EMAC significantly underestimates HCHO for the AS, especially during the night (Fig. S1). Here, a well pronounced diurnal cycle is simulated, while the observations indicate only a distinct diurnal variation in the eastern part of AS, which got stronger in GA (Fig. S1). Slightly elevated mixing ratios were observed in AS, compared to clean MBL conditions e.g. during INDOEX (Wagner et al., 2001), and are most likely caused by other primary sources and oxidation of further VOCs, not by methane oxidation only. Previous observations in the remote MBL showed significantly lower HCHO in the range of 0.2 – 0.4 ppb_v (Wagner et al. 2001). Thus, we assume that the air masses encountered in the AS during AQABA were still influenced by anthropogenic pollution, which is supported by the elevated NO_x (Tadic et al., 2020) and acrolein as the main contributor to OH reactivity in AS and GA (Pfanterstill et al., 2019). An additional source for HCHO was the ozonolysis of ethene, which reached maximum values of 0.24 ppb_v with a median of 0.08 ppb_v in AS (Bourtsoukidis et al., 2019). Wang et al. (2020) also show strongly enhanced acetaldehyde in AS relative to model simulations, indicating a missing oceanic source in the model. Tripathi et al. (2020) also performed VOC and sea water measurements of phytoplankton species, which demonstrate the high biological activity in the region. They determined elevated ethene (8.92 ± 3.50 ppb_v) and propene (3.38 ± 1.30 ppb_v) in marine air originating from the Arabian Sea. Just recently, Tegmeier et al. (2022) highlighted the complexity of the air phase composition over the Indian Ocean, with the major differences between the Indian summer and winter monsoon.

Altogether, EMAC reproduces observed HCHO mixing ratios on average within a factor of two. However, the model clearly underestimates the local maxima, especially for the AG, which leads to the assumption of missing sources in EMAC. The model simulates the AS cleaner than it was observed, but the relatively clean RS (with winds from Eritrea) was overestimated.

Given the multitude of potential HCHO sources, both from direct emissions and a large variety of photochemical precursors, the agreement is satisfactory, although the observations highlight that VOC emissions in the AG need to be adjusted.

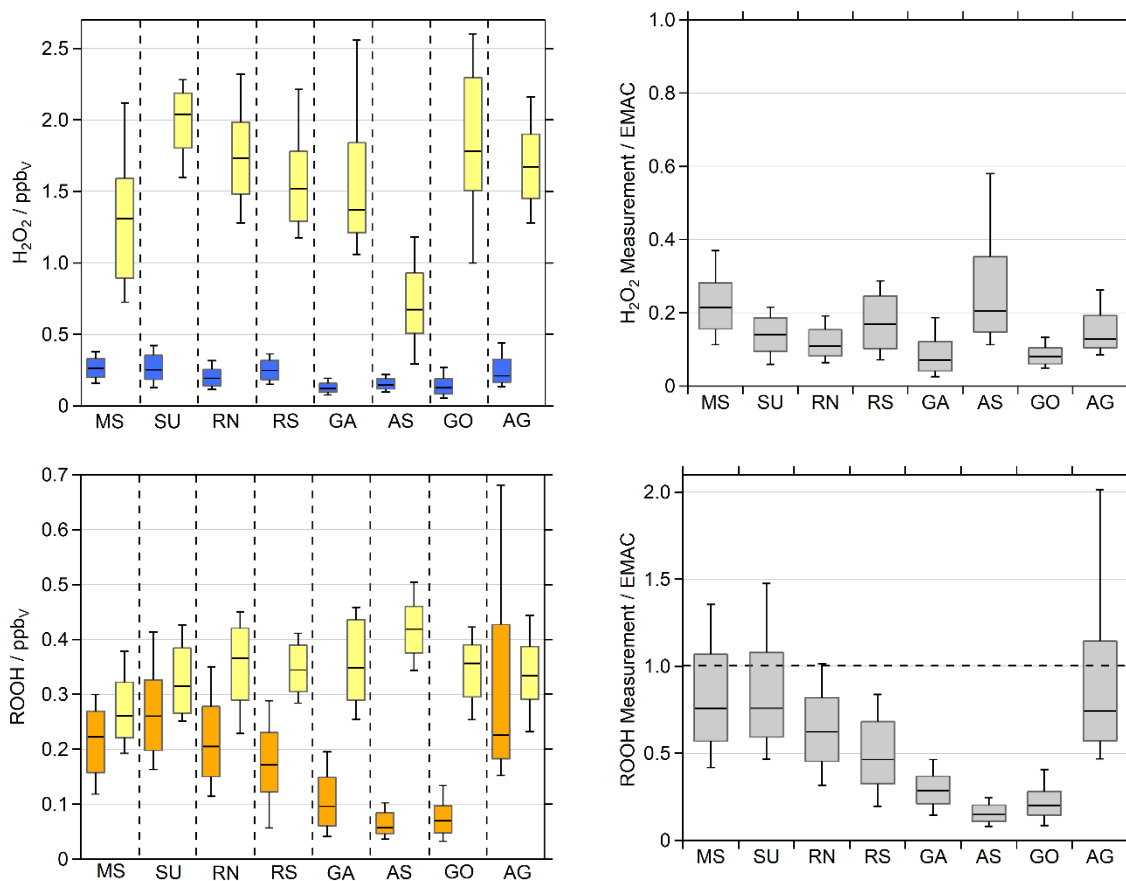


Figure 4: H_2O_2 (blue) and organic hydroperoxide (ROOH, orange) observations compared to the EMAC simulations (yellow), we used the lowermost model results (~ 30 m) for the comparison. The box represents 25 to 75 % of the data and the whiskers 10 to 90 % with the median as the black line. The right panel shows the ratio between the observations and the simulations.

The simulation of H_2O_2 is not satisfactory as EMAC systematically overestimates H_2O_2 mixing ratios by up to an order of magnitude. With the exception of the Arabian Sea (0.7 ppb_v), the model predicts H_2O_2 with median mixing ratios in excess of 1.3 ppb_v , with the highest median values of 2.0 ppb_v and 1.8 ppb_v for SU and GO, respectively. While the measurements cover a whisker range (10 to 90 % of the data) of only 0.1 to 0.4 ppb_v . This consistent overestimation by the model indicates either a significant overestimation of H_2O_2 sources or missing sinks in the model, or a combination of both.

In order to compare the observations of ROOH with model results, we summed up individual simulated organic hydroperoxide species, which were identified in the qualitative HPLC measurements (Fig. S4): methyl hydroperoxide (MHP), peracetic acid (PAA) and ethyl hydroperoxide (EHP). Please note that measured ROOH is a lower limit of the sum of organic hydroperoxides, since different sampling efficiencies for the individual species, which depend on the Henry's law constants, are not accounted for. It can be assumed, that MHP is the dominant contributor to the total organic hydroperoxides in the clean MBL, which has a sampling efficiency of only 60 % (Fischer et al., 2015). In remote areas, this would lead to an underestimation of measured ROOH by a factor 0.6. With significant contributions of higher organic hydroperoxides, which are generally more soluble, this underestimation tends to be smaller.

EMAC also tends to overestimate the organic hydroperoxides, with the lowest median value of 0.26 ppb_v in MS (observations 0.22 ppb_v), and the highest of 0.42 ppb_v in AS (observations 0.06 ppb_v) (Fig. 4 and Table S1). For the whole dataset, the simulated ROOH cover a whisker range (10 to 90 % of the data) between 0.19 to 0.50 ppb_v , while the observations yield a span of 0.04 to 0.68 ppb_v . Although the

measurements can be reproduced within the 25 to 75 % box range in some regions, median values differ between about a factor of 1 to 7 between the simulations and observations. Please note that AG was the only region where we measured four separated hydroperoxides in the in situ results of the HPLC, with the largest contribution of MHP and EHP. This enhancement was also found in the EMAC results, as EHP and PAA mixing ratios increased in AG, especially during the high pollution events of the first leg (Fig. S10). Although the simulations of ROOH match the observations better than H₂O₂, EMAC overestimates the organic peroxides, especially in the clean regions while cruising close to the coast. AG shows the highest variability of ROOH, which is to be expected due to the complex photochemistry of VOCs (Bourtsoukidis et al., 2019; Pfannerstill et al., 2019). The model simulates strong diel cycles (~300 ppt_v) throughout the whole dataset, while the observations only indicate comparable variations for the RN, SU, MS and AG. A distinct decline in ROOH mixing ratios was observed for the AS and GO, which is not reproduced by EMAC.

Possible explanations for the systematic overestimation of both H₂O₂ and organic hydroperoxides by EMAC can be an overestimation of photochemical sources or an underestimation of loss processes in the model, or due to the unknown sampling efficiencies of the organic peroxides. To investigate photochemical misrepresentations, we compared the observed and simulated OH and HO₂ daytime values ($j_{\text{NO}_2} \geq 10^{-3} \text{ s}^{-1}$; Fig. 5, S7, S8). Since the source term of H₂O₂ depends quadratically on HO₂ concentrations (Eq. 3), simulations of H₂O₂ are highly sensitive to HO₂, while its photochemical loss scales linearly with OH (Eq. 4). The model overestimates both OH and HO₂ throughout the whole campaign. Highest observed HO₂ median values were found in SU (19.3 ppt_v) and RN (16.3 ppt_v), followed by RS (14.8 ppt_v) and MS (14.4 ppt_v). The remaining regions show significantly less HO₂ with the smallest median value for GO (4.5 ppt_v). The smallest whisker ranges of the dataset in AS and GO demonstrate suppressed HO₂ in these regions. Surprisingly small mixing ratios were also detected over the polluted Arabian Gulf (6.8 ppt_v).

According to the observations, EMAC simulates the highest HO₂ median values for SU (27.9 ppt_v) and RN (26.1 ppt_v), while mixing ratios in MS (19.4 ppt_v) and RS (11.2 ppt_v) are smaller. Significant overestimation of HO₂ was found for GO (23.1 ppt_v) and AG (19.0 ppt_v) show similar enhancements of HO₂. In the rather clean regions during AQABA, e.g. GA (16.7 ppt_v) and AS (19.6 ppt_v), the model generates significantly enhanced daytime HO₂ compared to the observations, while diurnal variation of HO₂ matches the observations in RS and MS (Fig. S8). Altogether, we examined an overestimation of HO₂ by about a factor of 2 (EMAC dataset was aligned to the observations), with average daytime mixing ratios of 11.3 ppt_v for the observations and 19.7 ppt_v for the EMAC simulation, respectively.

Highest median OH values were observed for SU (0.13 ppt_v), RN (0.13 ppt_v), MS (0.12 ppt_v) and GO (0.11 ppt_v). Slightly less OH was detected in RS (0.07 ppt_v), AS (0.05 ppt_v) and AG (0.05 ppt_v). The box and whisker ranges indicate highest variations of OH in GA, where we detected the highest OH mixing ratios of 0.6 ppt_v close to Bab-el-Mandeb on the 16.08.2017 (Fig. S7). EMAC simulates the highest OH mixing ratios in SU (0.49 ppt_v), GO (0.47 ppt_v) and RN (0.44 ppt_v), while the lowest median values of OH were simulated in RS (0.13 ppt_v), followed by MS (0.26 ppt_v) and AS (0.26 ppt_v).

The EMAC results for OH follow similar regional trends compared to HO₂, although they reflect a stronger pronounced overestimation, since the measurements do not reflect a substantial increase of OH in MS, SU, RN and RS. This results in overestimated daily median values within a factor of 2 to 5.

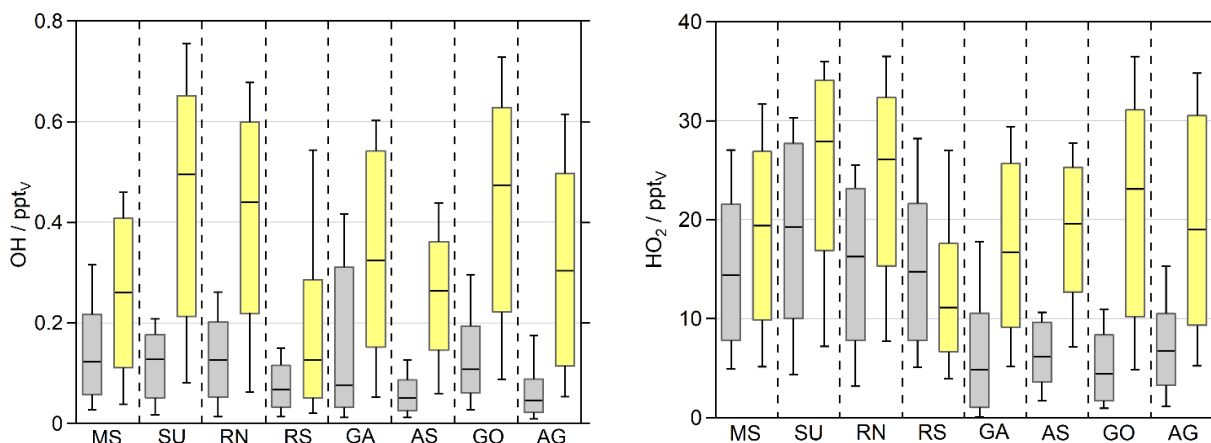


Figure 5: OH and HO₂ daytime values ($j_{\text{NO}_2} \geq 10^{-3} \text{ s}^{-1}$) of the observations (grey) and the EMAC simulations (yellow). The box represents 25 to 75 % of the data and the whiskers 10 to 90 % with the median as the black line. The EMAC data was adapted to the measurements with a time resolution of 10 minutes, so that the diurnal variations are reflected accurately.

3.3 Photochemical production and loss of H₂O₂

The comparison to EMAC in the previous section showed that overestimations of HO_x by EMAC affect simulations of HCHO, H₂O₂ and ROOH. How mis-representation of HO_x will affect HCHO is complex due to the many HCHO sources and the fact that both sources and sinks are strongly related to OH concentrations. Therefore, we will concentrate on H₂O₂ in the following calculation of its photochemical production and loss terms in order to evaluate the discrepancy between modelled and measured H₂O₂. H₂O₂ is highly sensitive towards deviations of HO_x between the observations and the model, as its production depends quadratically on HO₂ (Eq. 3), but its loss only linearly on OH (Eq. 4). Thus, H₂O₂ can be used to evaluate the discrepancy between measured and modelled HO_x.

The daytime production rates of H₂O₂ ($j_{\text{NO}_2} \geq 10^{-3} \text{ s}^{-1}$) are displayed in Fig. 6 in order to compare the results of the observations and EMAC, with the corresponding timelines presented in Fig. S11 and a scatter plot of $k_{\text{HO}_2+\text{HO}_2}$ in Fig. S12. Based on the observations, the highest production rates were found in SU with a median production of 202 ppt_v h⁻¹ and the largest whisker range of up to ~480 ppt_v h⁻¹. A similar range was obtained by EMAC, although with an increased median value of 298 ppt_v h⁻¹. MS and RN demonstrate comparable results, where the box ranges of the observations and the model agree to some extent, although the overestimated HO₂ by EMAC outweighs the slightly smaller reaction constant of $k_{\text{HO}_2+\text{HO}_2}$ (Fig. S12). Overall, EMAC tends to overestimate P(H₂O₂), except in RS, where the model correctly simulates the lowest H₂O₂ production rates of the dataset with a median value of 63 ppt_v h⁻¹ – about a factor of 5 lower than in SU. However, the observations display reduced P(H₂O₂) in the remaining regions, which resulted in a stronger pronounced discrepancy with at least a factor of 5 for GA, AS, GO and AG.

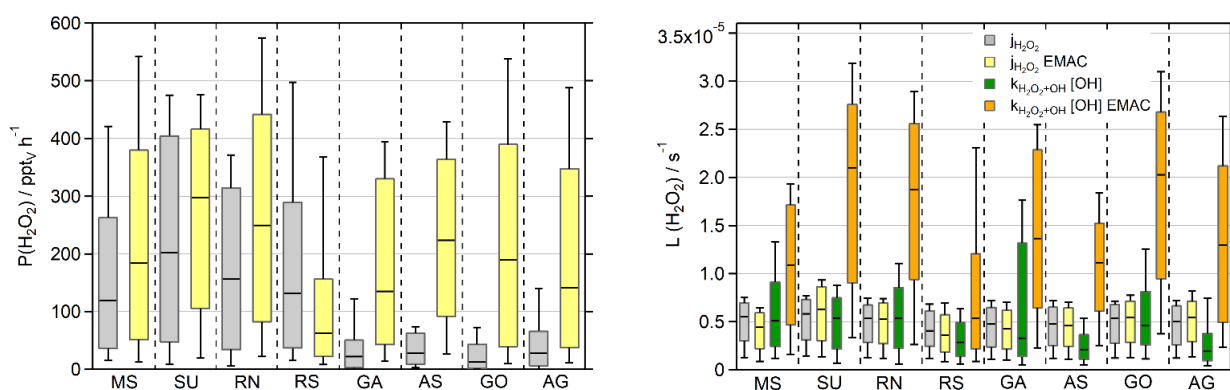


Figure 6: Box plots of H_2O_2 production rates ($\text{ppt}_v \text{ h}^{-1}$) for the observations (grey) and the EMAC model (yellow) during daytime ($j_{\text{NO}_2} \geq 10^{-3} \text{ s}^{-1}$) and the corresponding loss rate constants (s^{-1}) for photolysis (observations in grey and EMAC in yellow) and reaction with OH (green, orange). The boxes represent 25 to 75 % of the data and the whisker intervals 10 to 90 % with the median values as the black lines. The corresponding timelines are presented in Fig. S11.

Photochemical losses of H_2O_2 are the reaction with OH and photolysis, which were calculated according to Eq. 4, and displayed without multiplication of the H_2O_2 mixing ratio for the sake of comparability (Fig. 6). The simulated photolysis rate constants (j -values) demonstrate good agreement with the observations with a factor of 1.2, during the rarely cloudy conditions of AQABA. EMAC only overestimates $j_{\text{H}_2\text{O}_2}$ for air masses very close to the coastline, e.g. in SU (up to $\sim 1.5 \cdot 10^{-6} \text{ s}^{-1}$) and to a lesser extent in GO, while the photolysis rate was underestimated in RS (Fig. S11). Loss of H_2O_2 due to photolysis was less important than the reaction with OH for most regions, while photolysis prevailed for AS, RS and AG. In contrast to the observations, photochemical losses of H_2O_2 were dominated by the reaction with OH and were overestimated within a factor of $\sim 2 - 5$ by the model with the best agreement in RS.

To better put these results into perspective, Fig. 7 presents the net photochemical production of H_2O_2 ($P(\text{H}_2\text{O}_2) - L(\text{H}_2\text{O}_2)$), whereby the loss rate constants were multiplied with H_2O_2 mixing ratio. Please note that in this term neither physical processes nor transport are represented and thus it only reflects the effect of photochemistry on the H_2O_2 mixing ratio. The slightly overestimated photochemical production in MS, SU and RN by EMAC is compensated by elevated losses via reaction with OH in these regions, so that both datasets agree well in MS and RN, and demonstrate a strongly pronounced diurnal variation peaking at $\sim 580 \text{ ppt}_v \text{ h}^{-1}$ and $\sim 500 \text{ ppt}_v \text{ h}^{-1}$, respectively (Fig. 8). Net photochemical production of H_2O_2 outweighs the model results in SU and RS, especially during noon (Fig. 8). GA, AS, GO and AG remain overestimated by EMAC, so that the elevated losses in the model do not compensate for the enhanced production rates due to the quadratic dependence on the HO_2 concentration. The observations demonstrate less net photochemical production in GA, AS, GO and AG with noontime values below $200 \text{ ppt}_v \text{ h}^{-1}$ due to the decreased HO_2 . Pfannerstill et al. (2019) reported highest OH reactivity in AG (11.6 s^{-1}) and SU ($10.4 \text{ s}^{-1} - 10.8 \text{ s}^{-1}$), comparable results for GO (8.4 s^{-1}) and GA (8.0 s^{-1}); and the lowest OH reactivity for AS (4.9 s^{-1}). Air masses in AG demonstrated by far the highest contribution of reactivity towards OVOCs ($\sim 40\%$), alkanes and alkenes (together $\sim 14\%$). Air masses in GO showed slightly higher contributions of reactions with NO_x compared to AG, while AS represents the cleanest conditions during AQABA with respect to NO_x (Tadic et al., 2020). A potential explanation for the surprisingly low HO_2 mixing ratios in AG could be suppressed OH recycling by means of enhanced organic peroxy radicals (RO_2) and in general high contribution of reactions with OVOCs, alkanes, alkenes and aromatics, as OH recycling through these reactions is slower compared to NO_x recycling (via $\text{HO}_2 + \text{NO}$). Enhanced ROOH indicate a higher contribution of RO_x reactions ($= \text{OH} + \text{HO}_2 + \text{RO}_2$), which would also slow down OH recycling. There are no measurements of

organic peroxy radicals available, but Tadic et al. (2020) calculated noontime estimates of $\text{HO}_2 + \text{RO}_2$, with the highest noontime median values of $\sim 75 \text{ ppt}_v$ in AG (see Tadic et al., 2020 Fig. 7). The remaining regions of AQABA show noontime median values in the range of $\sim 10 - 35 \text{ ppt}_v$. Elevated RO_2 in AG is also supported by the enhanced mixing ratios of ROOH , the only region where we detected MHP, PAA and EHP in the in situ measurements of the HPLC (Fig. S10).

The decreased observations of net photochemical production of H_2O_2 in AS, GO and GA are generally caused by lower HO_x mixing ratios, which are not reproduced by EMAC. The box range indicates similar values of net photochemical production in MS, which agree mostly within a factor of 2. However, the H_2O_2 observations display an average diurnal variation of $\sim 0.2 \text{ ppb}_v$ with highest mean mixing ratios of $\sim 0.4 \text{ ppb}_v$ at 12 UTC, while the EMAC results indicate a variation of $\sim 1.2 \text{ ppb}_v$ with highest mixing ratios of $\sim 2.1 \text{ ppb}_v$ also at 12 UTC (Fig. S13). In general, the observations only display weak diurnal variations compared to the large diurnal variation in net photochemical production, which implies that other loss processes (e.g. deposition, wash out due to sea spray) contributed significantly to the diurnal variability of H_2O_2 in the marine boundary layer.

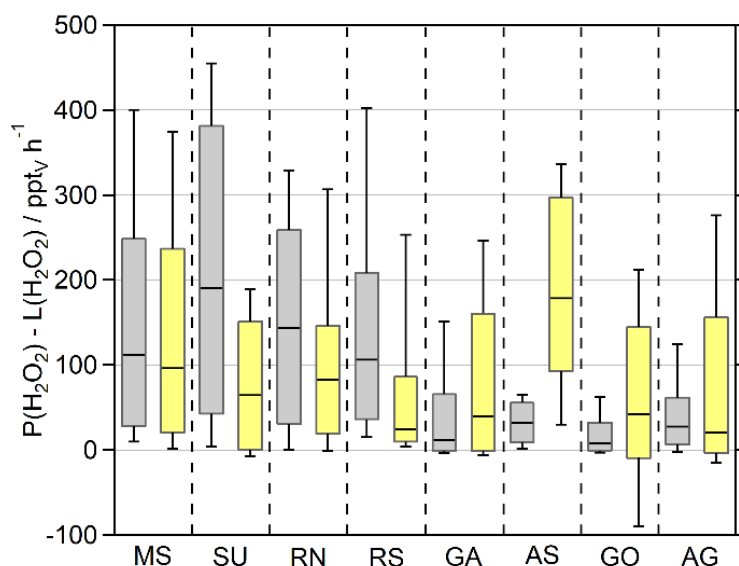


Figure 7: Box Plot of the net photochemical production of H_2O_2 ($P(\text{H}_2\text{O}_2) - L(\text{H}_2\text{O}_2)$) of the observations and the EMAC model results (yellow) during noon ($j_{\text{NO}_2} \geq 10^{-3} \text{ s}^{-1}$) without the dry deposition. The boxes represent 25 to 75 % of the data and the whisker intervals 10 to 90 % with the median values as the black lines. The corresponding timelines are presented in Fig. S11.

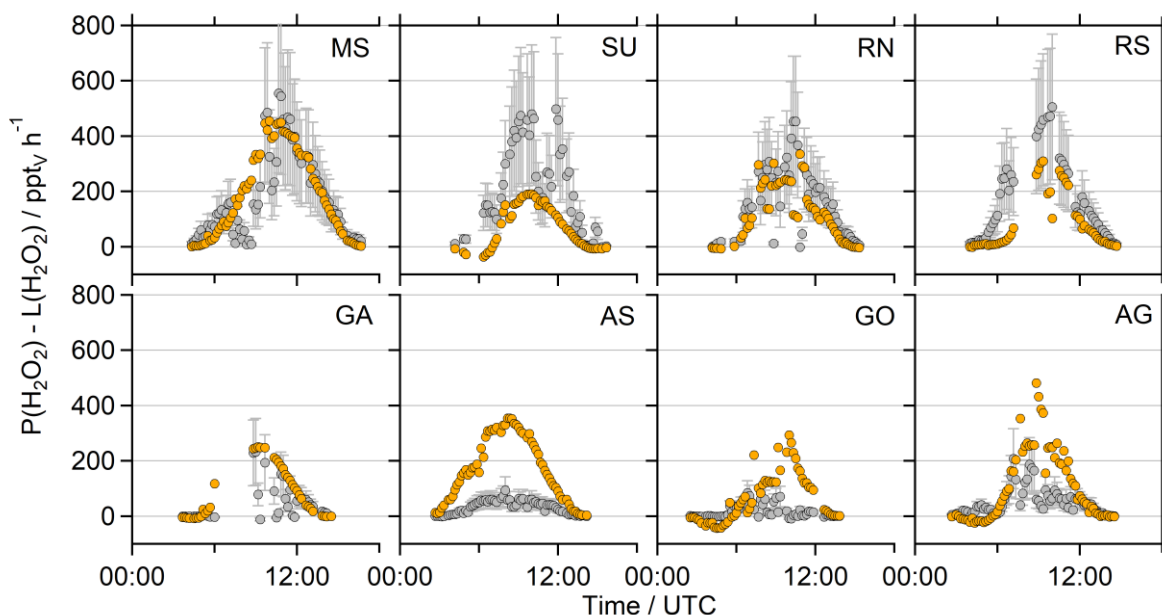


Figure 8: Diurnal variation of the net photochemical production of H_2O_2 ($P(\text{H}_2\text{O}_2) - L(\text{H}_2\text{O}_2)$) of the observations (grey) and the EMAC model results (orange) during noon ($j_{\text{NO}_2} \geq 10^{-3} \text{ s}^{-1}$) without the dry deposition. The corresponding timelines are presented in Fig. S11.

3.4 Dry deposition

An alternative reason for deviations between H_2O_2 observations and EMAC predictions could lie in the physical processes of deposition to the ocean surface and entrainment through the top of the MBL. Both processes are related to the absolute value and the diurnal variability of the boundary layer height. Due to the coarse resolution of EMAC grid cells (approx. 120 km), the BLH in the model is often affected by diurnal variation due to neighboring continental cells, especially close to the coast. Figure 9 shows EMAC simulations of BLH compared to ERA5 data (ECMWF ReAnalysis 5th generation). ERA5 resolves the global atmosphere in hourly intervals for 30 km grids at 137 vertical levels up to 0.01 hPa and thus its horizontal resolution is a factor of 4 higher than that of EMAC. The ERA5 dataset is available within the Copernicus Climate Change Service (<https://www.ecmwf.int/en/forecasts/datasets/reanalysis-datasets/era5>; last access 27.02.2021). The BL simulated by EMAC is very shallow during night and increases rapidly in height after sunrise, which may reflect continental influence in the EMAC grid-boxes. The only regions where EMAC shows no clear continental influence are the AS and the MS, even though the model clearly underestimated the BLH over the Arabian Sea and even more over the Mediterranean Sea. Local maxima on the 27th and 30th August are prominent while passing Crete and the Strait of Messina.

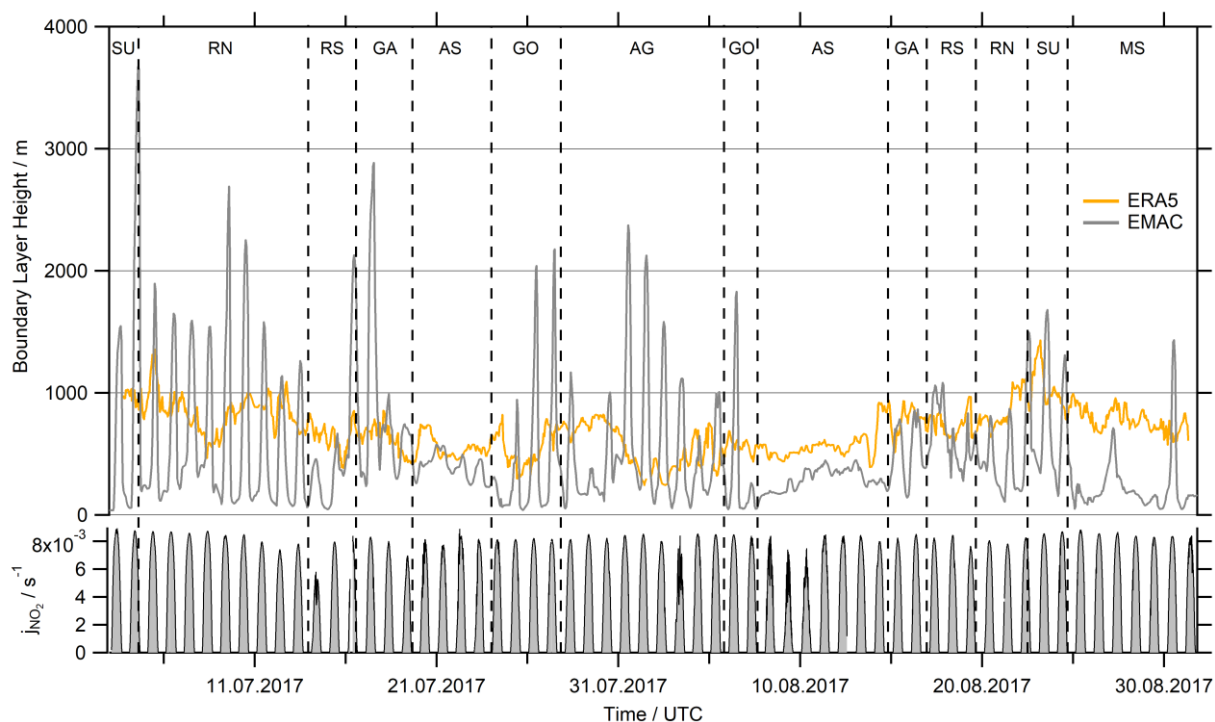


Figure 9: Comparison of the simulated BLH in EMAC with ERA5 (ECMWF ReAnalysis 5th generation) data at a four times higher resolution (31 km grid) than EMAC (~110 km grid) and hourly averaged data. EMACs BLH indicates continental influence by the strong diurnal variation while cruising close to the coast (SU, RN, GA, GO and AG, with the highest values determined for the ports of Jeddah (10. – 13.07.), Djibouti (16.07.) and Kuwait (01. – 03.08.). The measured photolysis frequency j_{NO_2} serves as a reference of sunlight intensity during AQABA.

This misrepresentation of the MBL height and its diurnal variation by EMAC has two consequences. First, according to Eq. 11, the deposition loss k_{dep} for a given deposition velocity V_{dep} is inversely proportional to the boundary layer height h_{BL} . Overestimations of h_{BL} by EMAC in particular during the day would thus lead to an underestimation of the deposition sink, while it would lead to an overestimation during the night. Additionally, diurnal variations of h_{BL} lead to entrainment of free tropospheric air into the MBL, in particular during the early morning (Fischer et al., 2015; Fischer et al., 2019). While vertical profiles of HCHO mixing ratios decrease with height (Anderson et al., 2017; Klippel et al., 2011; Heikes et al., 2001), H_2O_2 and MHP mixing ratios increase up to a local maximum above the boundary layer (Allen et al., 2022; Nussbaumer et al., 2021a; Klippel et al., 2011). Therefore, intrusion of air masses from the lower troposphere will most likely result in a decrease of HCHO in the MBL, while peroxide mixing ratios would likely increase as shown in Fischer et al. (2015).

To further evaluate the influence of deposition on H_2O_2 and HCHO levels, deposition velocities were derived from nighttime observations ($j_{\text{NO}_2} < 10^{-3} \text{ s}^{-1}$) of their loss rates following the method of Shepson et al. (1992) (Eq. 12). Here we use the exponential decays of the HCHO and H_2O_2 mixing ratios versus time to deduce nighttime loss rates in the Arabian and the Mediterranean Sea, where the EMAC simulation of h_{BL} was most accurate (Fig. 9, 10). The slope of the linear regression yields the respective deposition rate constant (k_{dep}) during night, assuming negligible nighttime chemistry, i.e. non-significant production of H_2O_2 and HCHO due to ozonolysis and nighttime oxidants (NO_3 , Cl) and their respective losses. We only used the data of the second leg in AS (less data coverage on the first leg due to contamination), which represent high humidity conditions ($87.6 \pm 3.1 \%$) and strong headwinds ($10.3 \pm 2.3 \text{ m s}^{-1}$), while winds over the Mediterranean Sea were slower ($6.1 \pm 2.2 \text{ m s}^{-1}$, $73.6 \pm 7.0 \%$). In general, deduced loss rates for H_2O_2 and HCHO show higher variability in AS than in MS, with highest values for both species on the 12.08.2017, and lowest values on the 09.08.2017 the eastern part of AS after a partly cloudy day.

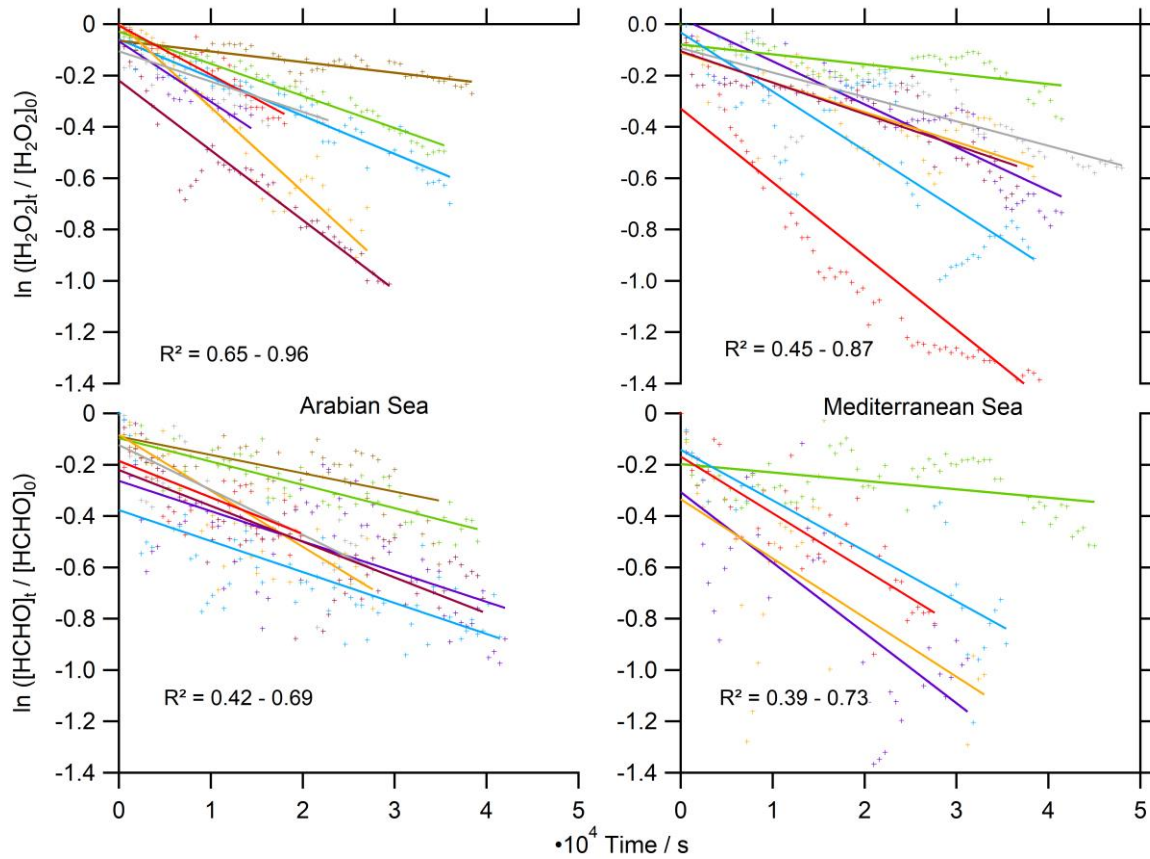


Figure 10: Determination of the deposition rates k_{dep} for H_2O_2 and $HCHO$ over the Arabian and the Mediterranean Sea in 10 min averages during night ($j_{NO_2} < 10^{-3} s^{-1}$).

A mean deposition loss $k_{\text{dep}}(H_2O_2)$ of $1.83 \pm 0.93 \cdot 10^{-5} s^{-1}$ was determined for the Arabian Sea, similar to the results in the Mediterranean Sea ($1.51 \pm 0.85 \cdot 10^{-5} s^{-1}$). We thereby determined a minimum of $0.37 \pm 0.15 \cdot 10^{-5} s^{-1}$ and a maximum deposition loss rate of $2.87 \pm 1.15 \cdot 10^{-5} s^{-1}$ for H_2O_2 with a variation of an order of magnitude. Dry deposition rates of HCHO are comparable to H_2O_2 with $k_{\text{dep}}(HCHO) = 1.34 \pm 0.46 \cdot 10^{-5} s^{-1}$ in the AS and $1.91 \pm 0.93 \cdot 10^{-5} s^{-1}$ in the MS. The deposition losses of HCHO cover a similar range of $0.33 \pm 0.13 \cdot 10^{-5} s^{-1}$ to $2.74 \pm 1.10 \cdot 10^{-5} s^{-1}$. The results for MS cover less nights, as we experienced local increases of HCHO from the 24.08. to the 26.08.17. These enhancements were associated with elevated NO_2 , indicating local pollution events and thus we excluded these nights.

Based on the deposition losses we calculated deposition velocities according to Eq. 12 using mean values of h_{BL} from ERA5 data for the corresponding timeframe. For the resulting V_{dep} we assume an uncertainty of at least 40 % (Fig. 11, Table S2). $V_{\text{dep}}(HCHO)$ cover a range of $0.23 - 2.22 \text{ cm s}^{-1}$, with the highest values during the night of the 27.08. – 28.08.17. in the Mediterranean Sea. Mean values ($\pm 1\sigma$) of 0.77 ± 0.29 and 1.49 ± 0.76 were determined for AS and MS, respectively. The deposition velocities of H_2O_2 cover a similar range of $0.26 - 2.34 \text{ cm s}^{-1}$, also with the highest values during the night of the 27.08. – 28.08.17. This resulted in mean values of $1.03 \pm 0.52 \text{ cm s}^{-1}$ for AS and $1.21 \pm 0.69 \text{ cm s}^{-1}$ for MS.

Averaged values were compared to the V_{dep} used by EMAC in Fig. 11. In general, observation based V_{dep} and model values for both species are of similar magnitude for AS (with the exception of the very low values derived during the night of the 09.08. – 10.08.17), while values of V_{dep} are underestimated by at least a factor of 2 for the Mediterranean Sea. Additionally, EMAC simulates less variability compared to the observations with mean values ($\pm 1\sigma$) of $0.78 \pm 0.16 \text{ cm s}^{-1}$ for AS and

$0.32 \pm 0.16 \text{ cm s}^{-1}$ for MS, respectively. Observed deposition velocities of H_2O_2 show enhanced values compared to EMAC, with mean values of $1.05 \pm 0.27 \text{ cm s}^{-1}$ for AS and $0.37 \pm 0.21 \text{ cm s}^{-1}$ for MS. Striking similarities were found for both species, as the calculated k_{dep} , and also the derived V_{dep} , seem to follow the same trend in the Arabian Sea. A linear correlation coefficient of $R^2=0.77$ was found for a linear fit of $V_{\text{dep}}(\text{HCHO})$ against $V_{\text{dep}}(\text{H}_2\text{O}_2)$ for the Arabian Sea. The simulated deposition velocity in EMAC depends linearly on the wind speed (Fischer et al., 2015), which explains the higher values derived during the strong head winds in the Arabian Sea. The observations confirm larger deposition velocities of H_2O_2 for the AS, while we determined enhanced values of $V_{\text{dep}}(\text{HCHO})$ for the MS. Both species show declined deposition velocities close to the coast on the 30.07.17, and in general a higher variability than the simulations by EMAC.

The observed nighttime values of $V_{\text{dep}}(\text{H}_2\text{O}_2)$ match previously derived values within the literature: Allen et al. (2022) found similar values of $V_{\text{dep}}(\text{H}_2\text{O}_2)$ in the MBL with a range of $1.00 - 1.32 \text{ cm s}^{-1}$, which corresponds to a loss of 5 – 10 % HO_x in the marine boundary layer. Stickler et al. (2007) determined a mean $V_{\text{dep}}(\text{H}_2\text{O}_2)$ of 1.3 cm s^{-1} in the MBL with a range of 0.1 to 1.8 cm s^{-1} depending on the entrainment rate. Fischer et al. (2019) calculated nighttime deposition velocities in the continental boundary layer for five different campaigns in Europe and determined values in the range of 0.16 to 0.60 cm s^{-1} during night, and 0.56 to 6.04 cm s^{-1} during the day. Nguyen et al. (2015) performed flux measurements and derived a diel cycle of $V_{\text{dep}}(\text{H}_2\text{O}_2)$ with values $\leq 1 \text{ cm s}^{-1}$ during night and a maximum of $\sim 6 \text{ cm s}^{-1}$ during noon. In sum, our observations agree with previous measurements in the continental and marine boundary layer during night.

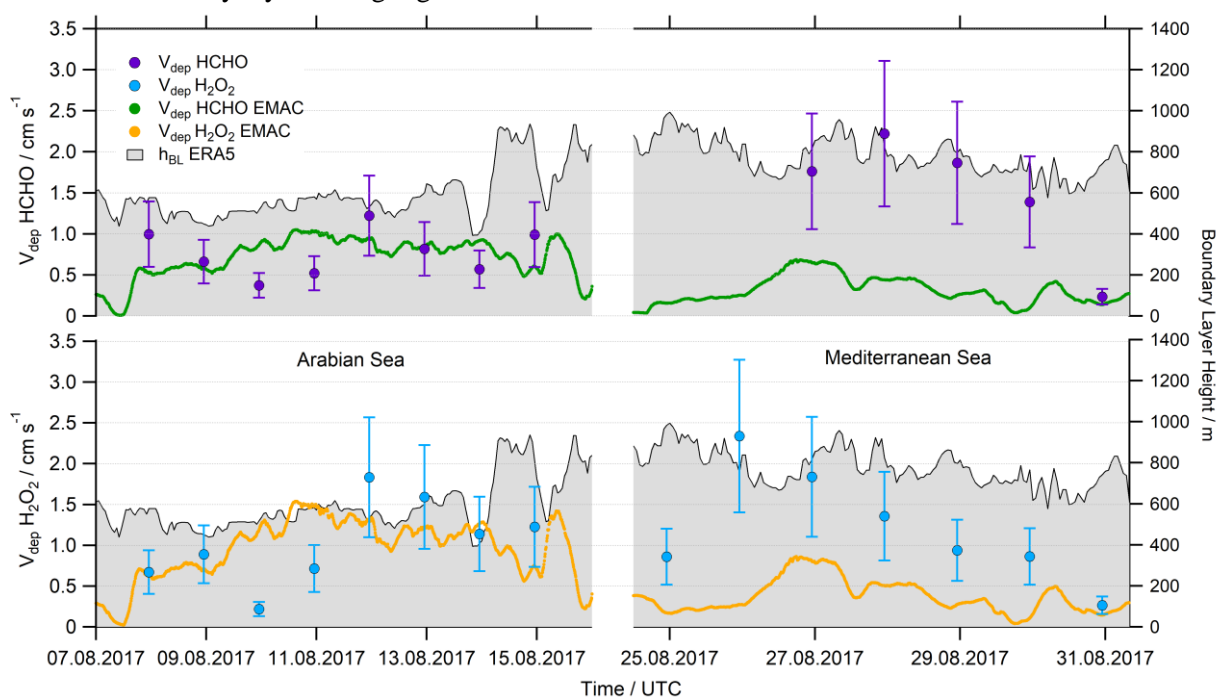


Figure 11: Comparison of the calculated deposition velocity V_{dep} for HCHO and H_2O_2 in the Arabian (AS) and the Mediterranean Sea (MS).

Deposition velocities of HCHO are generally expected to be lower than that of H_2O_2 due to its higher uptake resistance, which is related to e.g. solubility and hydrolysis of the trace gas (Stickler et al., 2007; Ganzeveld and Lelieveld, 1995). This can be confirmed with our results in AS, where $V_{\text{dep}}(\text{HCHO})$ is on average a factor of 0.8 smaller than $V_{\text{dep}}(\text{H}_2\text{O}_2)$. The results in MS do not confirm this expectation, as we determined a factor of 1.2 higher deposition velocities of HCHO. To the best of our knowledge, reports of the deposition velocity of HCHO in the MBL are sparse. Nussbaumer et al. (2021b) derived a nighttime $V_{\text{dep}}(\text{HCHO})$ of 0.47 cm s^{-1} in the continental boundary layer. Sumner et al. (2001)

calculated a $V_{\text{dep}}(\text{HCHO})$ of $0.65 \pm 0.36 \text{ cm s}^{-1}$ during night at a mixed deciduous/coniferous forest site, while Stickler et al. (2007) suggest a constant value of 0.36 cm s^{-1} over the ocean based on a single-column model. In comparison to the evaluated V_{dep} in the continental boundary layer, our measurements indicate more efficient deposition over the open ocean. This may be due to a more efficient near-surface transport, e.g. due to high wind speeds and turbulence as it is expected that high wind speeds lead to a more efficient deposition. Altogether, EMAC simulated accurate dry deposition velocities of HCHO and H_2O_2 for the AS with a deviation of less than 5 % for the derived mean values, while V_{dep} was underestimated by at least a factor of 2 for MS. Additionally, the observations demonstrate a higher variability than the model. Please note that deposition velocities for the observations were only calculated during night, and thus deposition losses of H_2O_2 and HCHO during daytime remain uncertain, although previous observations indicate a stronger pronounced deposition loss during the day (e.g. Fischer et al. 2019). Please note that our observations might be affected by additional loss processes, e.g. due to interactions with sea spray or in general heterogeneous chemistry.

4 Conclusions

In situ measurements of HCHO, H_2O_2 , ROOH, OH, HO_2 and actinic flux were carried out in the MBL around the Arabian Peninsula during the AQABA campaign in summer 2017 (01.07 – 01.09.2017). Mixing ratios of HCHO varied greatly within a range of 0.05 to 12.63 ppb_v, with the highest mixing ratios over the polluted Arabian Gulf. Elevated ROOH mixing ratios (up to 2.26 ppb_v) also reflected the high level of photochemical air pollution in AG while mixing ratios in other regions were below 0.30 ppb_v. H_2O_2 was the least abundant HO_x reservoir with mixing ratios mostly within the range of 0.10 – 0.40 ppb_v, and no significant enhancements were detected during the pollution event in the center of the AG. Highest daytime median values of HO_2 were detected for the area around the Suez Canal (15.90 ppt_v), while significantly lower values were found for the AG (4.65 ppt_v). In AG, we also encountered the lowest daytime median values of OH (0.04 ppt_v), while we determined a daytime median of 0.09 ppt_v for the whole dataset. In general, the elevated values of HCHO and ROOH in the Arabian Gulf are consistent with the increased mixing ratios of O_3 (Tadic et al., 2020), VOCs (Bourtsoukidis et al., 2019), OVOCs (Wang et al., 2020) and the high levels of OH reactivity during AQABA, where Pfannerstill et al. (2019) derived the highest median loss rate of OH with 18.8 s^{-1} . The lowest mixing ratios of HCHO, H_2O_2 and ROOH were found for air masses in the Arabian Sea and the southern Red Sea during the second leg of the campaign, where the lowest concentrations of NO_x and O_3 were present (Tadic et al., 2020), although we rarely encountered really clean MBL conditions during AQABA (Celik et al., 2020).

The comparison of measurements with results from the general circulation model EMAC indicates that the model simulates HCHO mixing ratios on average within a factor of 2, while it clearly overestimates H_2O_2 and to a lesser extent ROOH. This effect can to a large degree be explained by the overestimated mixing ratios of HO_x . Production and loss of HCHO scale linearly with OH, while the photochemical production of H_2O_2 depends quadratic on HO_2 and only linearly on OH. The calculation of net photochemical production of H_2O_2 ($P(\text{H}_2\text{O}_2) - L(\text{H}_2\text{O}_2)$) revealed an overestimation of the model, with largest deviations for the Arabian Sea, the Gulf of Oman and the Arabian Gulf. These regions were characterized by reduced mixing ratios of HO_2 , which are not reproduced by EMAC.

Loss of HCHO and H_2O_2 due to dry deposition, their predominant loss process during night, was performed for the regions far away from the coastline, so that the diurnal variation of the boundary layer height in EMAC interfered less with the derived results. The analysis revealed mean values ($\pm 1\sigma$) of $V_{\text{dep}}(\text{HCHO})$ with $0.77 \pm 0.29 \text{ cm s}^{-1}$ for the Arabian Sea and $1.49 \pm 0.76 \text{ cm s}^{-1}$ for the Mediterranean Sea. Enhanced values of $V_{\text{dep}}(\text{H}_2\text{O}_2)$ compared to $V_{\text{dep}}(\text{HCHO})$ were determined for the AS

($1.03 \pm 0.52 \text{ cm s}^{-1}$), while the deposition of H_2O_2 in the MS was on average slower than that of HCHO with $1.21 \pm 0.69 \text{ cm s}^{-1}$. EMAC simulates accurate deposition velocities of HCHO and H_2O_2 in AS, while the deposition of both species was underestimated by at least a factor 2 for the Mediterranean Sea. Additionally, the simulated V_{dep} shows less variability compared to the observations. Losses due to deposition could not be compared during the day and remain uncertain.

The analysis of the deposition velocity revealed underestimated losses due to dry deposition in the MBL, which leads to overestimated HO_x precursors in EMAC. An updated scheme for the simulation of dry deposition of land – atmosphere exchange in EMAC was developed by Emmerichs et al. (2021). They include e.g. improved stomatal uptake and dry deposition on soil moisture, which decreased HCHO mixing ratios during boreal summer by up to 25 % on ground level. We want to highlight that the ocean surface might be an additional surface where dry deposition of trace gases might need to be adjusted. This effect may be most important on a local scale, but certainly could have an effect on the HO_x budget in EMAC. Additionally, EMAC is limited by its coarse spatial resolution ($\sim 110 \text{ km}$), which leads to spurious diurnal variation of the boundary layer height when cruising close to the coast.

The overestimated HO_x in EMAC most likely results from the overall enhanced VOC oxidation. Additionally, the model was not able to reproduce the local phenomena encountered, e.g. the air pollution event in AG. This leads to the assumption that the model may reproduce HCHO within a factor of 2, but partly due to wrong reasons, i.e. overestimated HO_x which compensates for missing sources in the model. This assumption is supported by the observations of several other OVOCs which were not matched by EMAC (Wang et al., 2020).

The systematic overestimation of H_2O_2 is at least partly explained by the overrated HO_2 , although net photochemical production of H_2O_2 revealed that the model matches the observations in some regions well, as the overall overestimated OH compensates partially for too high values of HO_2 . The decreased observations of HO_2 in GA, AS, GO and AG are not matched by EMAC. The reduced HO_x encountered in air masses over the Arabian Gulf can most likely be addressed to elevated mixing ratios of RO_2 , which are reflected in the enhanced ROOH and the estimates of $\text{RO}_2 + \text{HO}_2$ by Tadic et al. (2020). Despite matching results for the net photochemical production in some regions, the observations of H_2O_2 reflect less diurnal variation and overall lower mixing ratios than simulated by EMAC. This implies that further loss processes, e.g. the deposition during daytime and in general heterogeneous chemistry remain a major uncertainty in the photochemical budget of H_2O_2 in the MBL. We therefore emphasize the importance of H_2O_2 and organic peroxide in situ measurements, which were valuable to evaluate simulated deposition velocities and the accuracy of HO_x simulations and lead to the assumption of a missing sink of HO_x in the model.

4.2.2 Supplement of: Formaldehyde and hydroperoxides distribution around the Arabian Peninsula – evaluation of EMAC model results with ship-based measurements

Supplement of:

Formaldehyde and hydroperoxide distribution around the Arabian Peninsula – Comparison of ship-based measurements with the general circulation model EMAC

Dirk Dienhart¹, Bettina Brendel¹, John N. Crowley¹, Philipp G. Eger¹, Hartwig Harder¹, Monica Martinez¹, Andrea Pozzer¹, Roland Rohloff¹, Jan Schuladen¹, Sebastian Tauer¹, Jos Lelieveld^{1,2}, and Horst Fischer¹

¹Atmospheric Chemistry Department, Max Planck Institute for Chemistry, Mainz, Germany

²Energy, Environment and Water Research Center, The Cyprus Institute, Nicosia, Cyprus

Correspondence to: Dirk Dienhart (D.Dienhart@mpic.de) or Horst Fischer (Horst.Fischer@mpic.de)

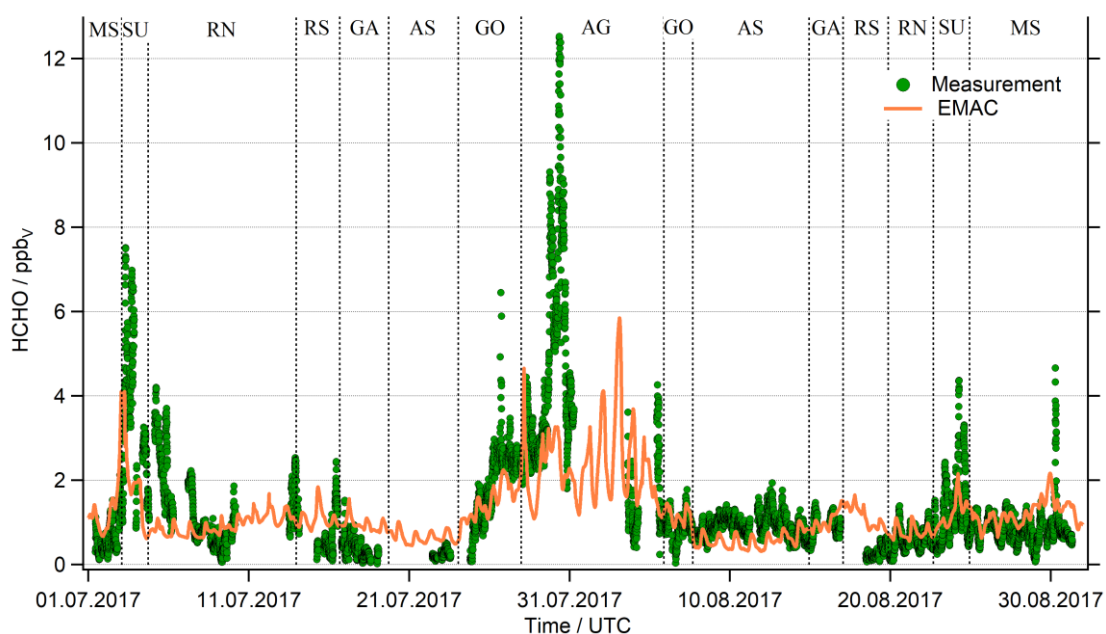


Figure S1: Timelines of the HCHO measurements and the EMAC simulation, averaged along the ship track.

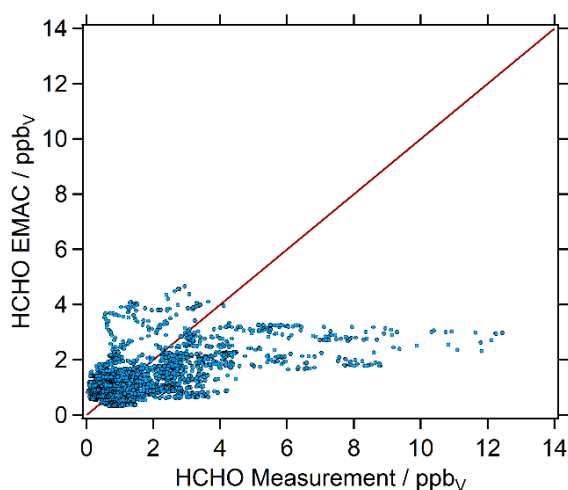


Figure S2: Scatter plot of the HCHO measurements versus the simulated data (EMAC) in hourly averages.

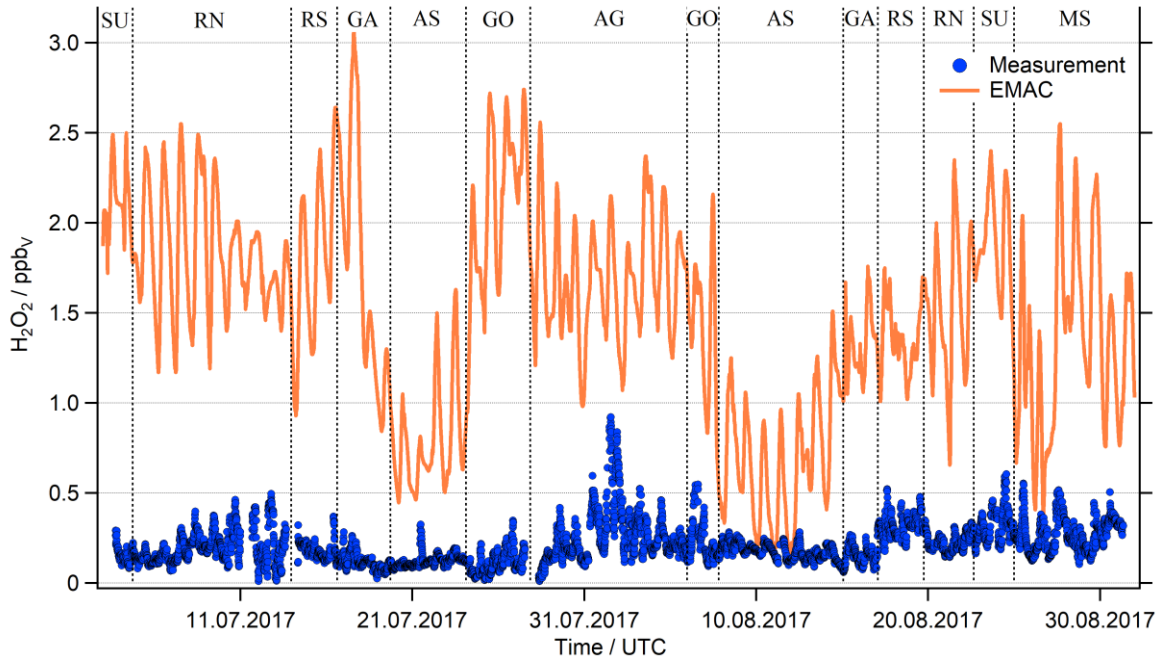


Figure S3: Timelines of the H_2O_2 measurements and the EMAC simulation, averaged along the ship track.

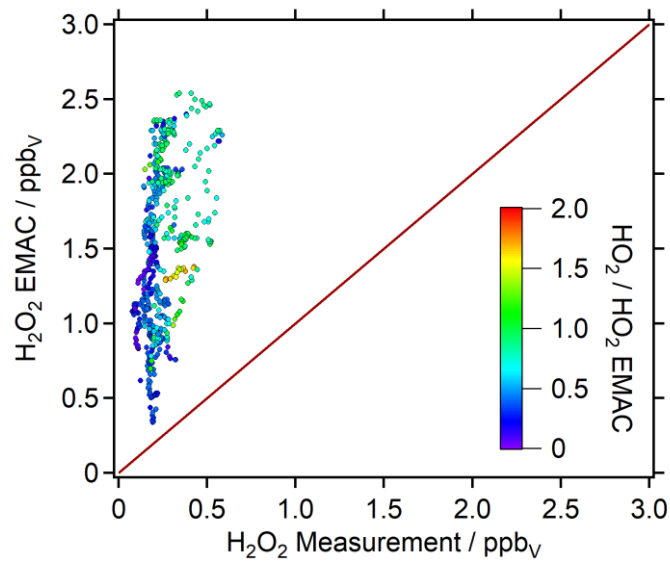


Figure S4: Scatter plot of the H_2O_2 measurements versus the simulated data (EMAC) in hourly averages.

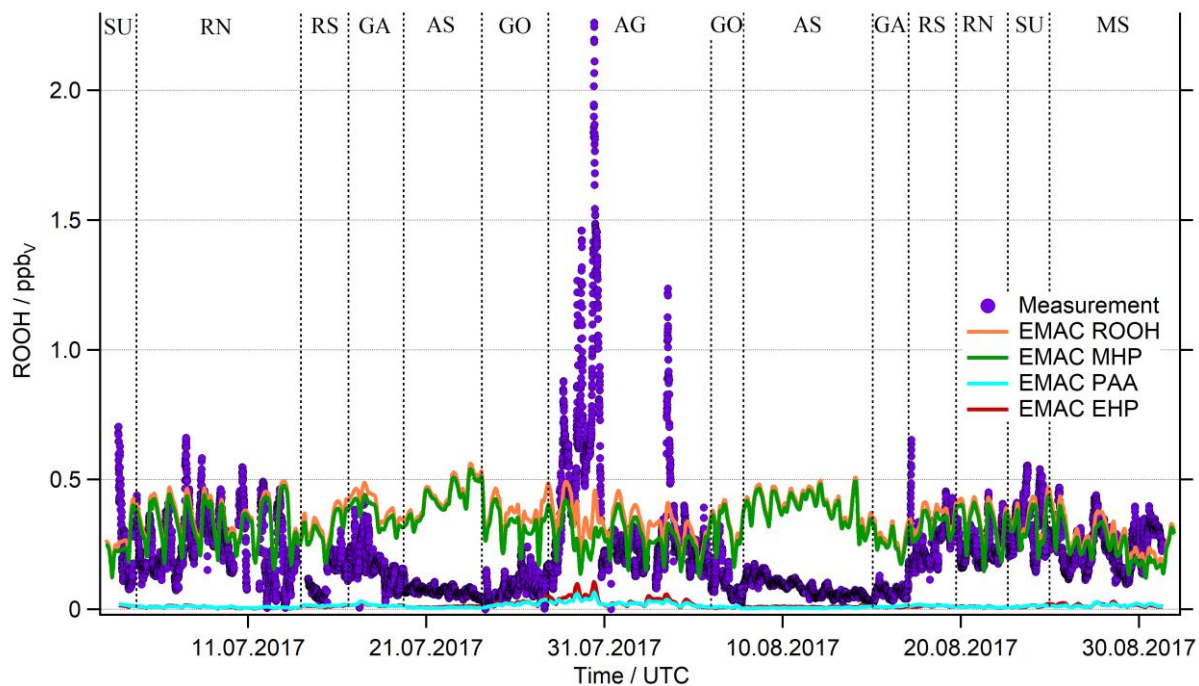


Figure S5: Timelines of the organic peroxide (ROOH) measurements and the EMAC simulations along the ship the track. The simulated dataset consists of the most prominent species methyl hydroperoxide (MHP), peracetic acid (PAA) and ethyl hydroperoxide (EHP).

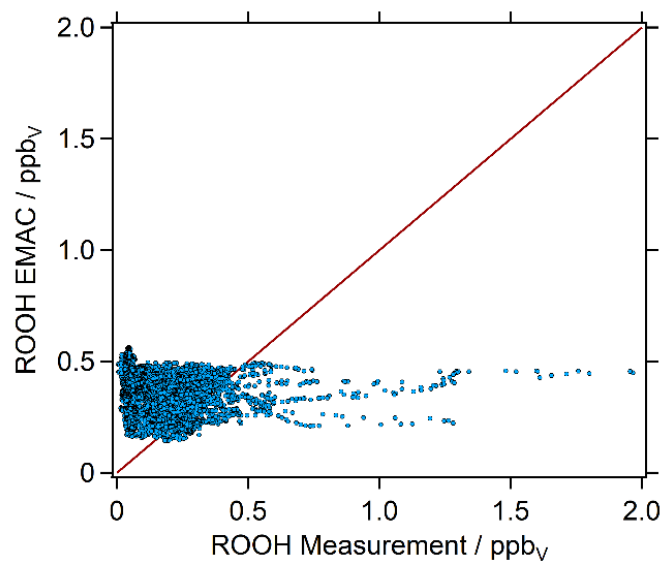


Figure S6: Scatter plot of the organic peroxide measurements versus the simulated data (EMAC) in hourly averages.

Table S1: Mean, median, 25- and 75-percentile values of the HCHO, H₂O₂ and organic peroxide measurements (black) and the corresponding EMAC simulations (orange) for the eight different regions encountered during AQABA: Mediterranean Sea (MS), Suez Canal (SU), Red Sea North (RN), Red Sea South (RS), Gulf of Aden (GA), Arabian Sea (AS), Gulf of Oman (GO) and Arabian Gulf (AG).

HCHO	MS	SU	RN	RS	GA	AS	GO	AG
Mean	0.818±0.397	2.074±1.612	1.037±0.783	0.519±0.435	0.566±0.337	0.826±0.326	1.499±0.831	3.769±2.443
± 1σ	1.260±0.389	1.535±0.837	0.799±0.145	0.986±0.192	1.019±0.169	0.588±0.178	1.410±0.331	2.259±0.765
Median	0.771	1.499	0.763	0.374	0.503	0.862	1.218	3.077
	1.220	1.290	0.775	0.942	0.966	0.572	1.360	2.190
25 %	0.602	0.888	0.520	0.232	0.286	0.633	0.897	2.368
	1.040	0.941	0.673	0.906	0.896	0.430	1.140	1.550
75 %	0.989	2.925	1.264	0.574	0.814	1.045	2.332	4.528
	1.400	1.820	0.882	1.020	1.160	0.734	1.633	2.850
H₂O₂	MS	SU	RN	RS	GA	AS	GO	AG
Mean	0.269±0.088	0.271±0.113	0.204±0.084	0.255±0.085	0.129±0.046	0.155±0.046	0.148±0.092	0.261±0.149
± 1σ	1.328±0.512	1.984±0.253	1.756±0.379	1.598±0.402	1.594±0.573	0.721±0.323	1.851±0.537	1.684±0.327
Median	0.263	0.252	0.192	0.246	0.121	0.146	0.125	0.210
	1.310	2.040	1.730	1.520	1.370	0.672	1.780	1.670
25 %	0.200	0.185	0.141	0.183	0.096	0.118	0.081	0.166
	0.892	1.803	1.480	1.290	1.210	0.506	1.505	1.450
75 %	0.329	0.352	0.253	0.318	0.155	0.189	0.188	0.327
	1.590	2.188	1.985	1.780	1.840	0.928	2.295	1.900
ROOH	MS	SU	RN	RS	GA	AS	GO	AG
Mean	0.216±0.069	0.270±0.094	0.220±0.096	0.173±0.083	0.110±0.064	0.065±0.026	0.079±0.047	0.348±0.285
± 1σ	0.276±0.074	0.325±0.066	0.351±0.082	0.345±0.051	0.355±0.077	0.419±0.059	0.347±0.066	0.335±0.075
Median	0.223	0.260	0.205	0.171	0.096	0.057	0.070	0.226
	0.261	0.315	0.366	0.344	0.349	0.419	0.357	0.335
25 %	0.158	0.198	0.150	0.122	0.061	0.046	0.048	0.183
	0.221	0.266	0.290	0.305	0.289	0.375	0.295	0.291
75 %	0.269	0.326	0.278	0.230	0.149	0.084	0.097	0.427
	0.322	0.384	0.420	0.390	0.436	0.460	0.390	0.387

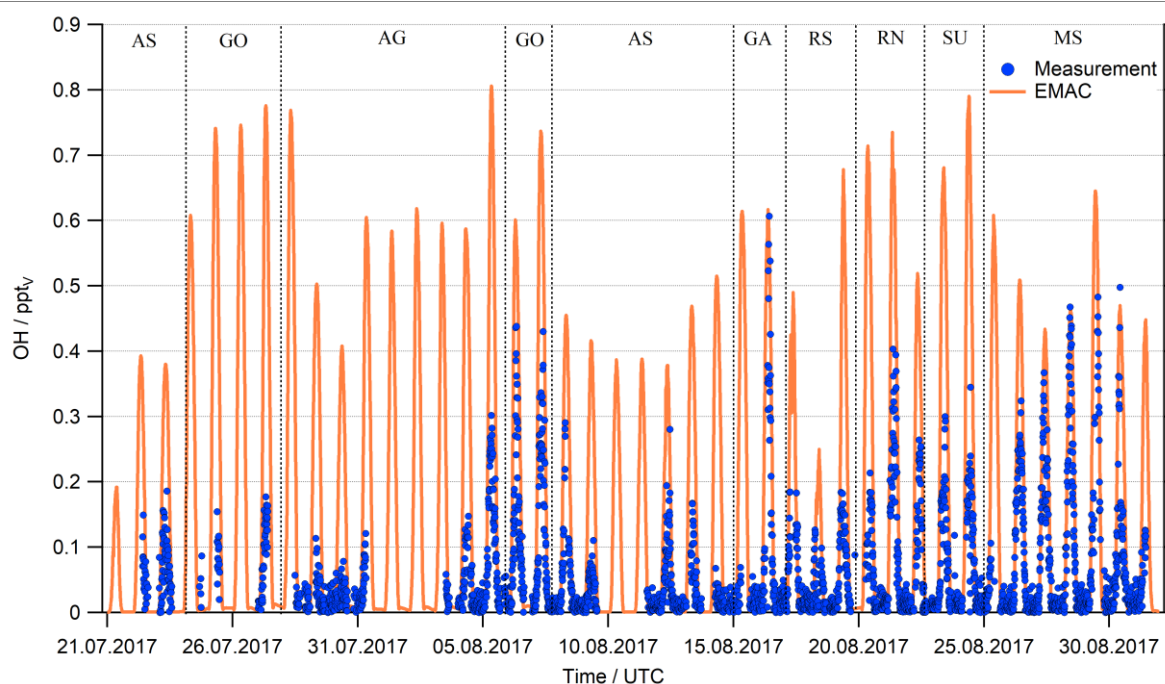


Figure S7: Timelines of the OH measurements and the EMAC simulation, averaged along the ship track.

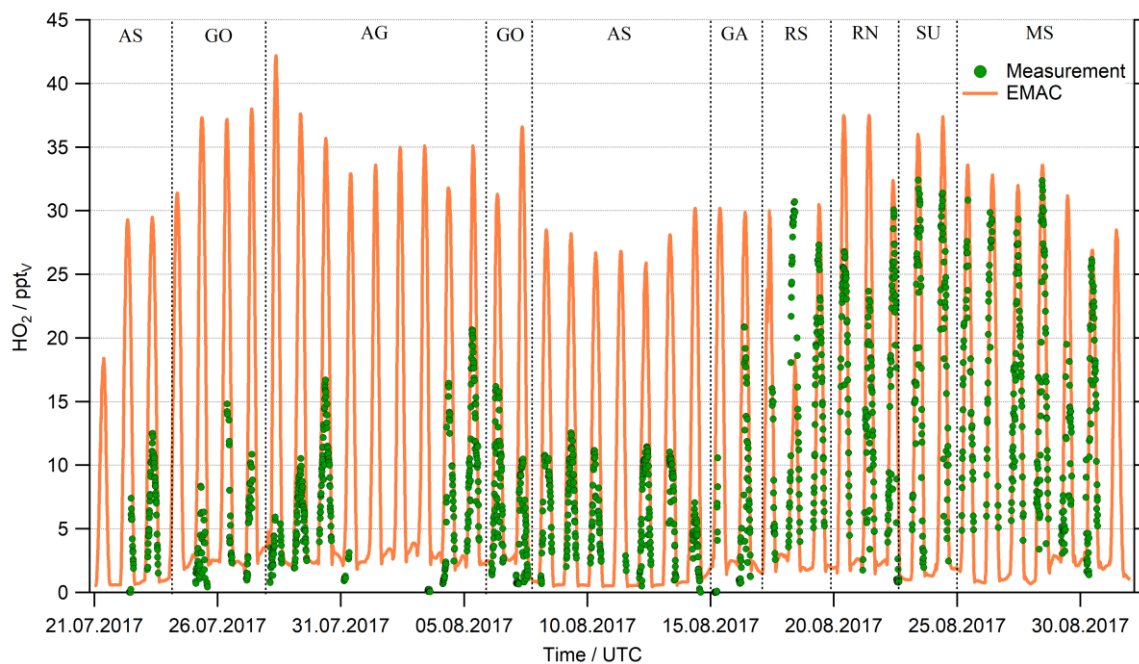


Figure S8: Timelines of the HO₂ measurements and the EMAC simulation, averaged along the ship track.

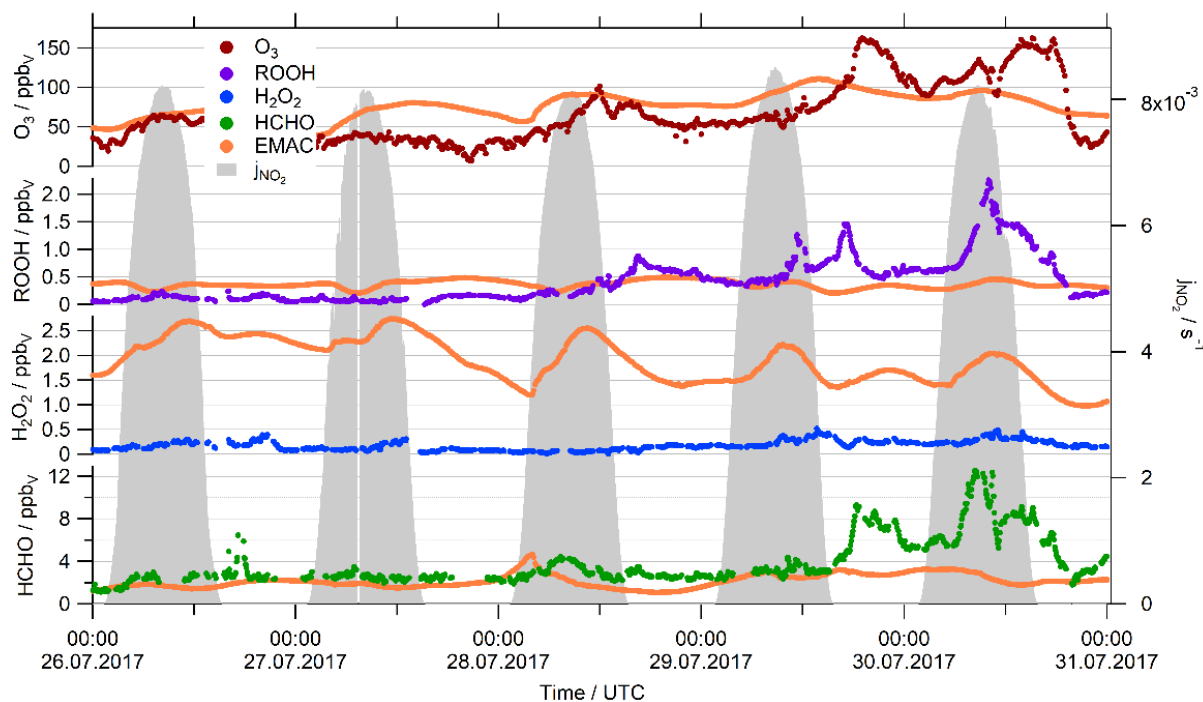


Figure S9: Case study of the Arabian Gulf during the first leg for the observations and the corresponding EMAC simulations. Highly polluted air masses were detected during the night of the 29.07.17, when we measured 170 ppbv of O₃ in the center of the Arabian Gulf.

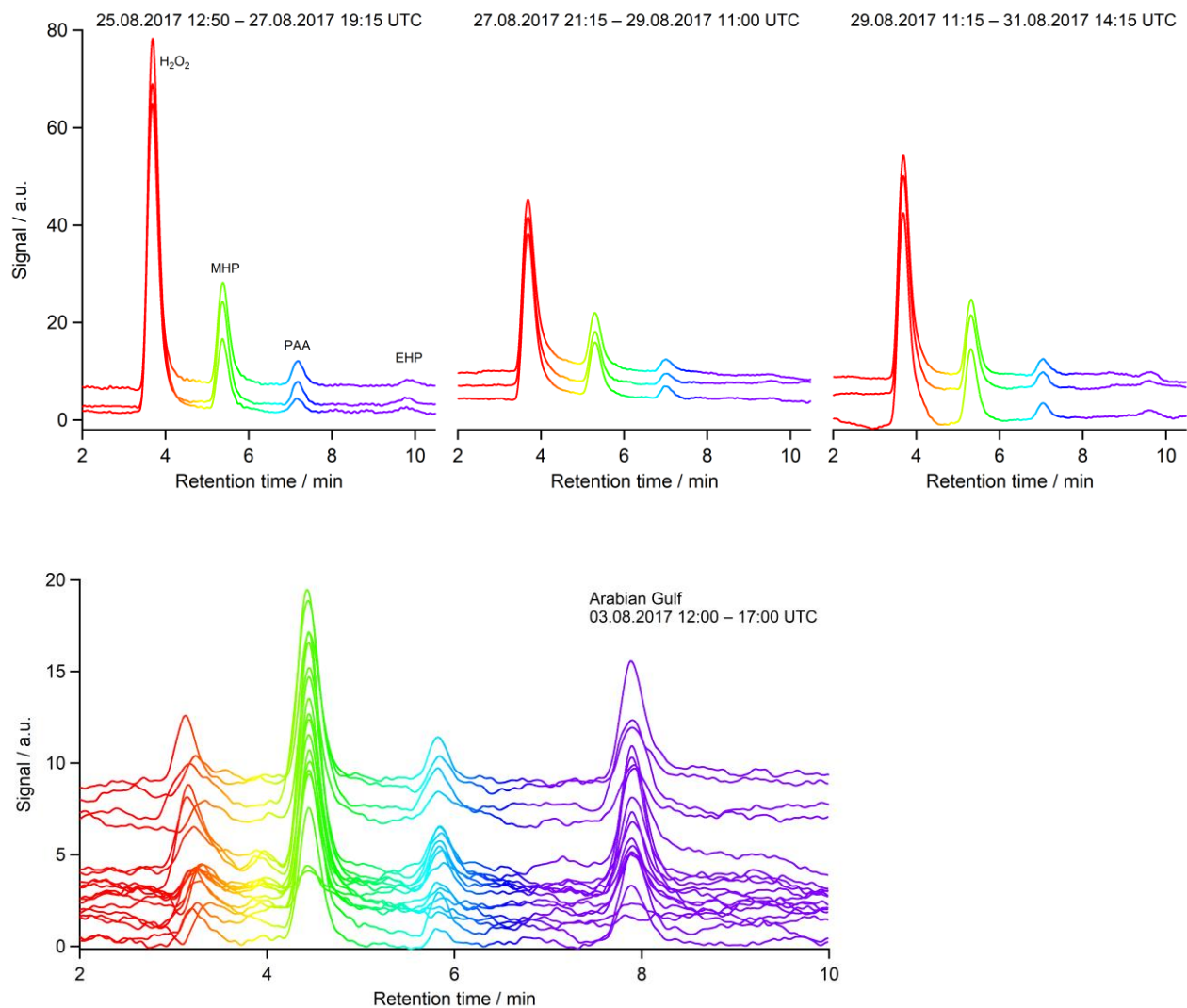


Figure S10: Identification of H₂O₂ and three separated organic peroxides based on the qualitative HPLC measurements. MHP (methyl hydroperoxide), PAA (peracetic acid) and EHP (ethyl hydroperoxide) were identified with their respective retention times and gaseous injections of PAA with a diffusion source. The lower panel shows the continuous results in AG, the upper panel the injection of enriched samples in MS.

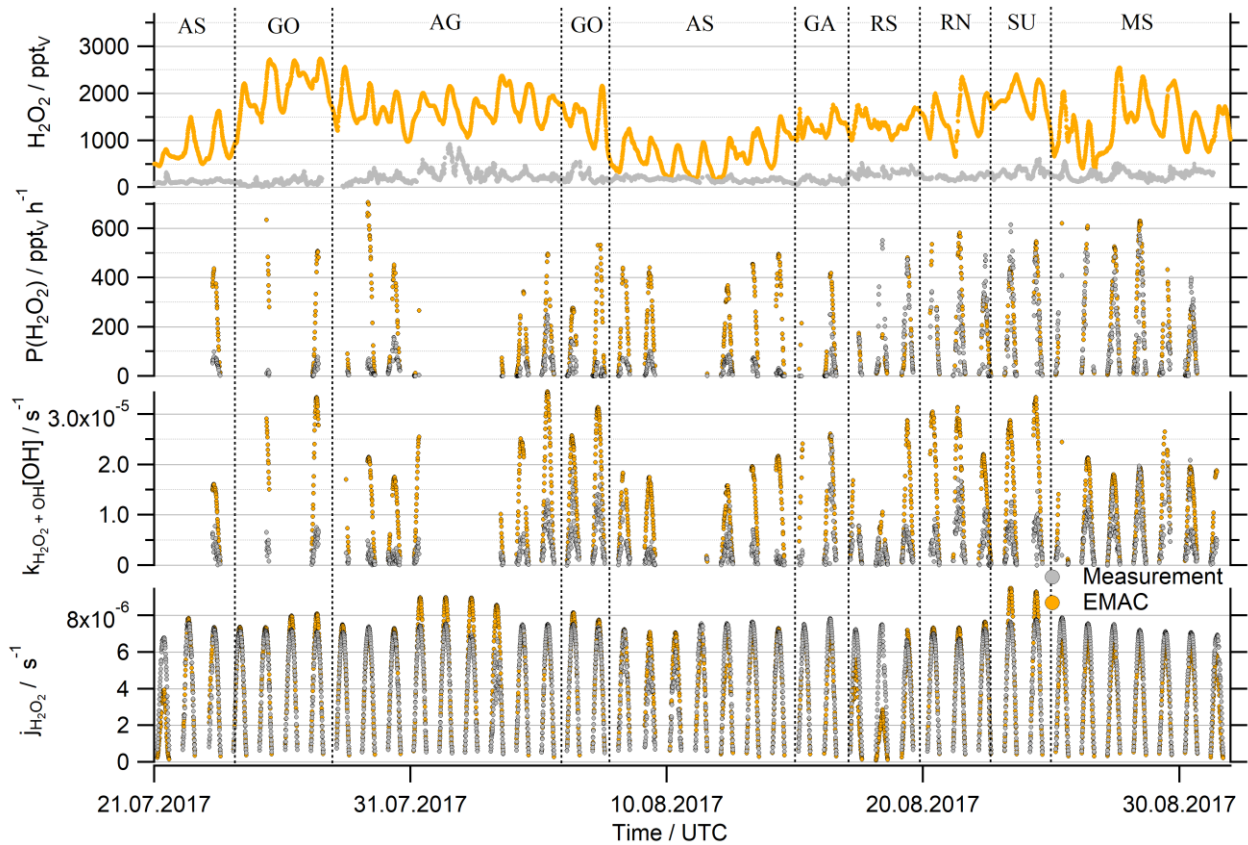


Figure S11: Timelines of the production and loss terms of H_2O_2 for the observations (black) and the EMAC model results (orange). Note that the loss terms were not multiplied with the H_2O_2 mixing ratio.

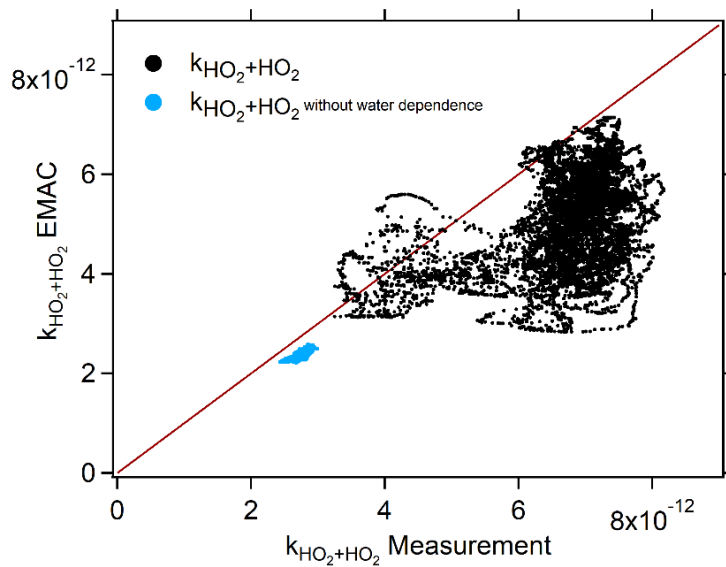


Figure S12: Scatter plot of $k_{\text{HO}_2+\text{HO}_2}$ for the measurements and EMAC. The water dependence causes a maximum deviation of about factor 2, as EMAC slightly underestimated water vapor.

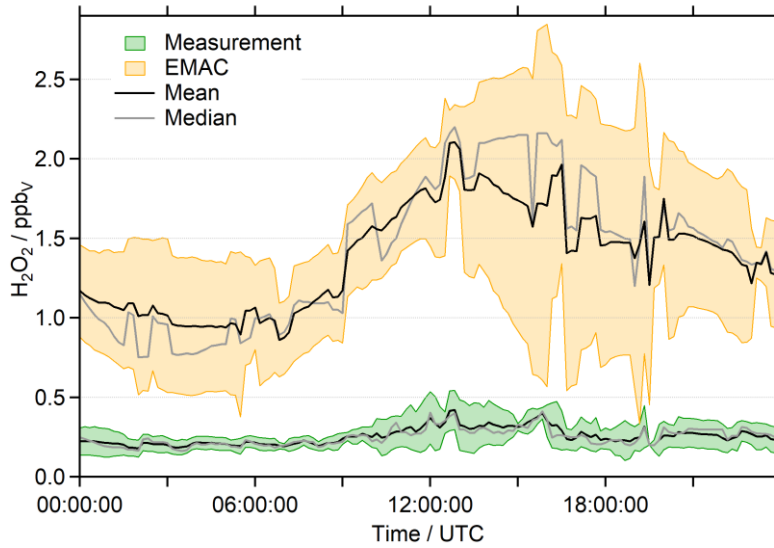


Figure S13: Diurnal variation of H_2O_2 ($\pm 1\sigma$) over the Mediterranean Sea (MS) for the observations (green) and EMAC (orange).

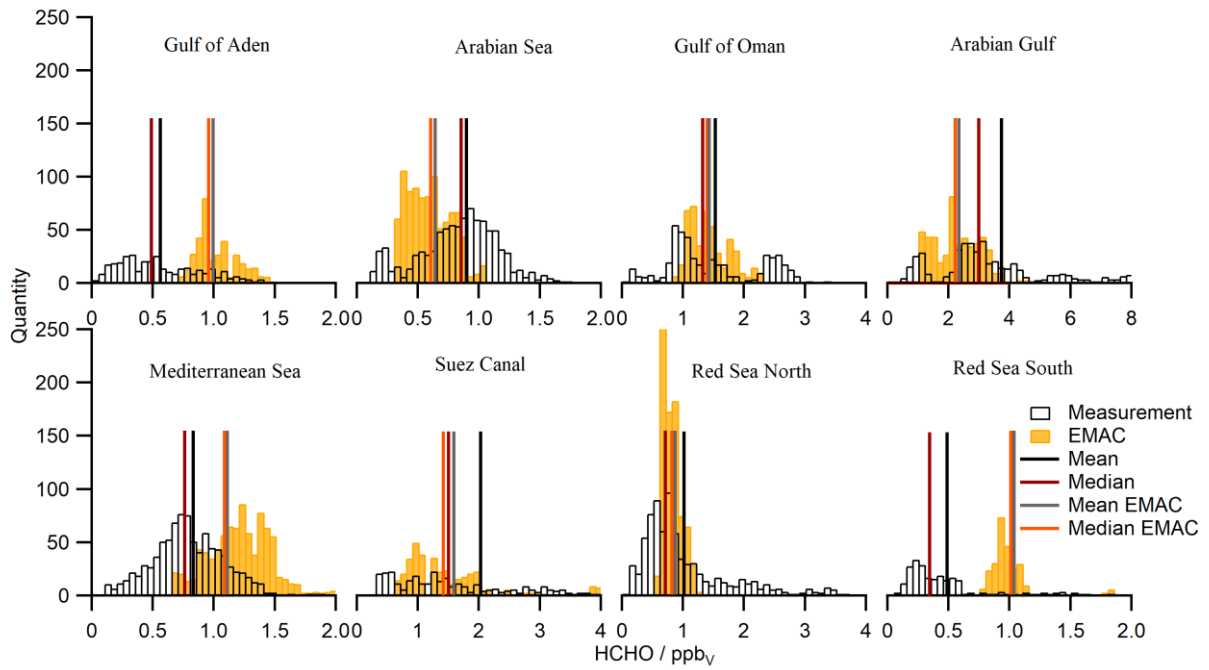


Figure S14: Frequency distributions of the HCHO observations (black) and the EMAC model results (orange) for the eight regions encountered during AQABA.

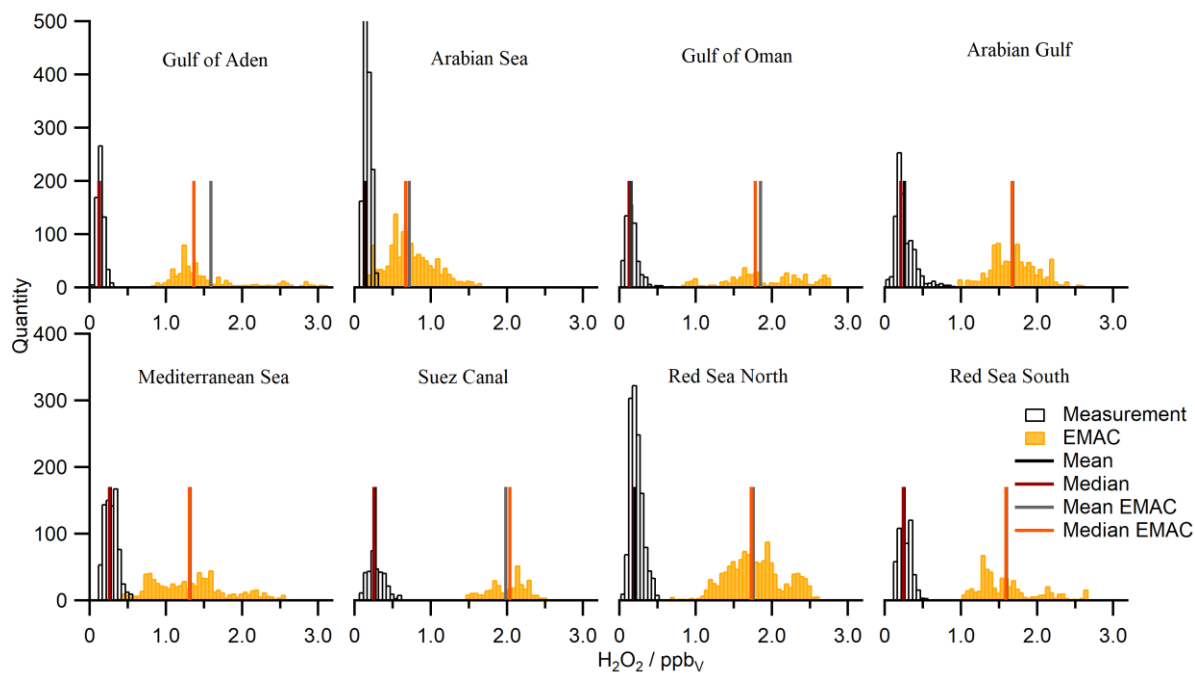


Figure S15: Frequency distributions of the H_2O_2 observations (black) and the EMAC model results (orange) for the eight regions encountered during AQABA.

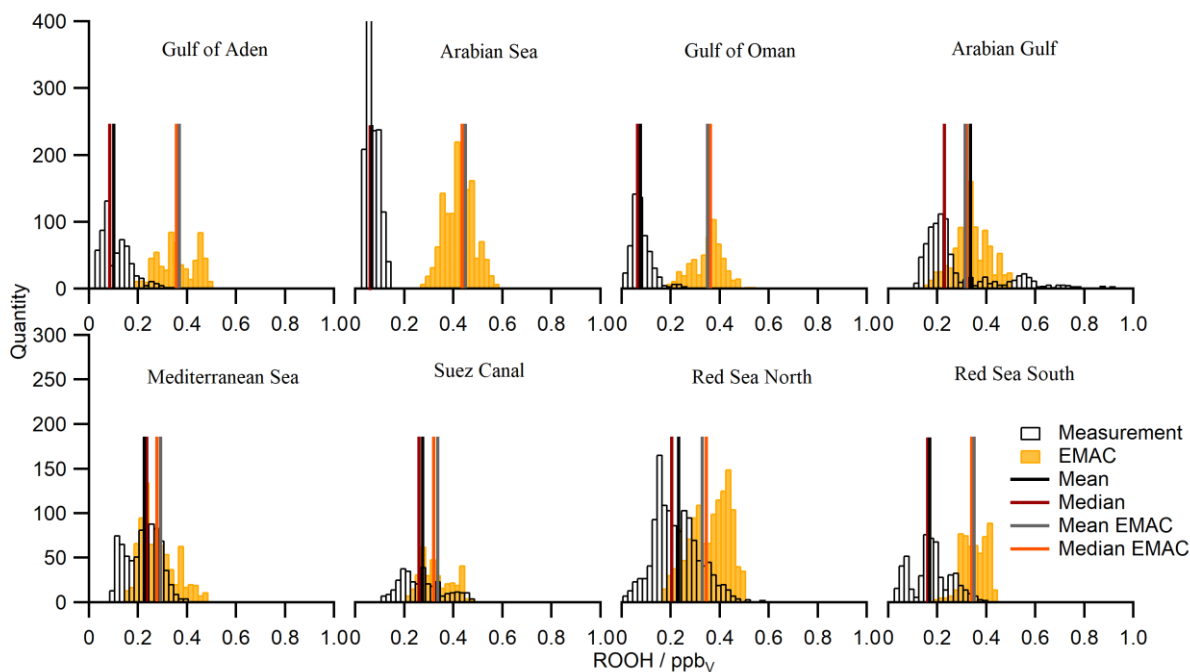


Figure S16: Frequency distributions of the ROOH observations (black) and the EMAC model results (orange) for the eight regions encountered during AQABA.

Table S2: Calculated deposition rates (k_{dep}) of HCHO and H₂O₂ for the Arabian Sea (AS) and the Mediterranean Sea (MS). Values of k_{dep} were determined as the slope of a linear regression (logarithmic decay versus time, Fig. 10) and the corresponding deposition velocities (V_{dep}) are based on Eq. 12 with values for the boundary layer height derived from the ERA5 results for the corresponding timeframe ($\pm 1\sigma$). Errors of k_{dep} and V_{dep} are estimated to be at least $\pm 40\%$.

	k_{dep} HCHO / s ⁻¹	R ²	V_{dep} HCHO / cm s ⁻¹	k_{dep} H ₂ O ₂ / s ⁻¹	R ²	V_{dep} H ₂ O ₂ / cm s ⁻¹	h_{BL} ERA5 / m
07. – 08.08.	$1.75 \pm 0.70 \cdot 10^{-5}$	0.69	0.99 ± 0.40	$1.18 \pm 0.47 \cdot 10^{-5}$	0.65	0.67 ± 0.27	569 ± 12
08. – 09.08.	$1.42 \pm 0.57 \cdot 10^{-5}$	0.47	0.66 ± 0.26	$1.91 \pm 0.76 \cdot 10^{-5}$	0.86	0.89 ± 0.36	465 ± 27
09. – 10.08.	$0.72 \pm 0.29 \cdot 10^{-5}$	0.42	0.37 ± 0.15	$0.42 \pm 0.17 \cdot 10^{-5}$	0.70	0.22 ± 0.09	520 ± 18
10. – 11.08.	$0.91 \pm 0.36 \cdot 10^{-5}$	0.68	0.52 ± 0.21	$1.25 \pm 0.50 \cdot 10^{-5}$	0.96	0.71 ± 0.28	573 ± 19
11. – 12.08.	$2.18 \pm 0.87 \cdot 10^{-5}$	0.64	1.22 ± 0.49	$3.28 \pm 1.31 \cdot 10^{-5}$	0.91	1.83 ± 0.73	559 ± 18
12. – 13.08.	$1.39 \pm 0.56 \cdot 10^{-5}$	0.59	0.82 ± 0.33	$2.72 \pm 1.09 \cdot 10^{-5}$	0.88	1.59 ± 0.64	586 ± 41
13. – 14.08.	$1.18 \pm 0.47 \cdot 10^{-5}$	0.44	0.57 ± 0.23	$2.36 \pm 0.94 \cdot 10^{-5}$	0.82	1.14 ± 0.46	483 ± 93
14. – 15.08.	$1.21 \pm 0.48 \cdot 10^{-5}$	0.52	0.99 ± 0.40	$1.49 \pm 0.60 \cdot 10^{-5}$	0.91	1.22 ± 0.49	822 ± 100
Mean AS ($\pm 1\sigma$)	$1.34 \pm 0.46 \cdot 10^{-5}$	0.56	0.77 ± 0.29	$1.83 \pm 0.93 \cdot 10^{-5}$	0.84	1.03 ± 0.52	572 ± 110
24. – 25.08.	–	–	–	$0.95 \pm 0.38 \cdot 10^{-5}$	0.58	0.86 ± 0.34	906 ± 68
25. – 26.08.	–	–	–	$2.87 \pm 1.15 \cdot 10^{-5}$	0.87	2.34 ± 0.94	814 ± 59
26. – 27.08.	$2.20 \pm 0.88 \cdot 10^{-5}$	0.70	1.76 ± 0.70	$2.30 \pm 0.92 \cdot 10^{-5}$	0.67	1.84 ± 0.74	800 ± 63
27. – 28.08.	$2.74 \pm 1.10 \cdot 10^{-5}$	0.56	2.22 ± 0.89	$1.68 \pm 0.67 \cdot 10^{-5}$	0.82	1.36 ± 0.54	810 ± 70
28. – 29.08.	$2.31 \pm 0.92 \cdot 10^{-5}$	0.39	1.86 ± 0.74	$1.16 \pm 0.46 \cdot 10^{-5}$	0.54	0.94 ± 0.38	808 ± 35
29. – 30.08.	$1.97 \pm 0.79 \cdot 10^{-5}$	0.73	1.39 ± 0.56	$1.22 \pm 0.49 \cdot 10^{-5}$	0.58	0.86 ± 0.34	706 ± 47
30. – 31.08.	$0.33 \pm 0.13 \cdot 10^{-5}$	0.39	0.23 ± 0.09	$0.39 \pm 0.15 \cdot 10^{-5}$	0.45	0.26 ± 0.10	715 ± 68
Mean MS ($\pm 1\sigma$)	$1.91 \pm 0.93 \cdot 10^{-5}$	0.55	1.49 ± 0.76	$1.51 \pm 0.85 \cdot 10^{-5}$	0.66	1.21 ± 0.69	792 ± 74

4.3 Formaldehyde production rates and their relation to OH reactivity

The following chapter presents a study about HCHO production rates, which were calculated based on the photochemical steady-state (PSS) of formaldehyde. I am the first author of this paper, performed the data analysis, the involved PSS calculations and the HCHO measurements during AQABA. The paper was published as a measurement report in ACP on the 01.12.2021.

In PSS, photochemical production and losses of a certain trace gas balance and thus the respective production rate can be estimated via its loss reactions. Formaldehyde production and losses are dominated by reactions of the OH radical: its main production pathway in clean conditions is the oxidation of CH₄ and with increasing amounts of air pollution, the HCHO production pathways get more diverse, as it can be released during the photochemical oxidation of many other VOCs. Further important production pathways are e.g. the oxidation of MHP, methanol, acetaldehyde and unsaturated hydrocarbons like isoprene (Nussbaumer et al., 2021b). The losses of HCHO are dominated by the reaction with OH during the day, besides physical losses due to photolysis and deposition.

The study thereby focuses on the oxidation pathways of OH, since the calculated production rates are in theory related to the measured OH reactivity and the mixing ratios of OH radicals. As the OH reactivity also includes many reactions of OH which do not yield HCHO, the so-called inorganic reactivity was subtracted, which includes reactions of NO₂, NO, CO, SO₂ and HCHO itself. Based on regionally divided scatter plots of HCHO production versus the total reacting OH, the theoretical yield of HCHO (α_{eff}) can be estimated, which reflects the regional yield of HCHO. The intercept of the regression analysis thereby reflects additional sources of HCHO e.g. ozonolysis of unsaturated hydrocarbons.



Measurement report: Observation-based formaldehyde production rates and their relation to OH reactivity around the Arabian Peninsula

Dirk Dienhart¹, John N. Crowley¹, Efstratios Bourtsoukidis², Achim Edtbauer¹, Philipp G. Eger¹, Lisa Ernle¹, Hartwig Harder¹, Bettina Hottmann¹, Monica Martinez¹, Uwe Parchatka¹, Jean-Daniel Paris^{3,2}, Eva Y. Pfannerstill¹, Roland Rohloff¹, Jan Schuladen¹, Christof Stöner¹, Ivan Tadic¹, Sebastian Tauer¹, Nijing Wang¹, Jonathan Williams^{1,2}, Jos Lelieveld^{1,2}, and Horst Fischer¹

¹Department of Atmospheric Chemistry, Max Planck Institute for Chemistry, Mainz, Germany

²Climate and Atmosphere Research Centre, The Cyprus Institute, Nicosia, Cyprus

³Laboratoire des Sciences du Climat et de l'Environnement, CEA-CNRS-UVSQ, UMR8212, IPSL, Gif-sur-Yvette, France

Correspondence: Dirk Dienhart (d.dienhart@mpic.de) and Horst Fischer (horst.fischer@mpic.de)

Received: 8 April 2021 – Discussion started: 29 April 2021

Revised: 4 October 2021 – Accepted: 14 October 2021 – Published: 1 December 2021

Abstract. Formaldehyde (HCHO) is the most abundant aldehyde in the troposphere. While its background mixing ratio is mostly determined by the oxidation of methane, in many environments, especially in the boundary layer, HCHO can have a large variety of precursors, in particular biogenic and anthropogenic volatile organic compounds (VOCs) and their oxidation products. Here we present shipborne observations of HCHO, hydroxyl radical (OH) and OH reactivity ($R(\text{OH})$), which were obtained during the Air Quality and Climate Change in the Arabian Basin (AQABA) campaign in summer 2017. The loss rate of HCHO was inferred from its reaction with OH, measured photolysis rates and dry deposition. In photochemical steady state, the HCHO loss is balanced by production via OH-initiated degradation of VOCs, photolysis of oxygenated VOCs (OVOCs) and the ozonolysis of alkenes. The slope α_{eff} from a scatter plot of the HCHO production rate versus the product of OH and $R(\text{OH})_{\text{eff}}$ (excluding inorganic contribution) yields the fraction of OH reactivity that contributes to HCHO production. Values of α_{eff} varied between less than 2 % in relatively clean air over the Arabian Sea and the southern Red Sea and up to 32 % over the polluted Arabian Gulf (also known as Persian Gulf), signifying that polluted areas harbor a larger variety of HCHO precursors. The separation of $R(\text{OH})_{\text{eff}}$ into individual compound classes revealed that elevated values of α_{eff} coincided with increased contribution of alkanes and

OVOCs, with the highest reactivity of all VOCs over the Arabian Gulf.

1 Introduction

Formaldehyde (HCHO) is a ubiquitous trace gas that can help provide insight into the dynamical and chemical processes controlling atmospheric composition as an important source of hydroperoxyl radicals (HO_2) (Volkamer et al., 2010; Whalley et al., 2010; Anderson et al., 2017). The global atmospheric distribution of HCHO is dominated by in situ production during the oxidation of volatile organic compounds (VOCs) (Fortems-Cheiney et al., 2012; Anderson et al., 2017), although primary emissions from biomass burning (Akagi et al., 2011; Coggon et al., 2019; Kluge et al., 2020), vegetation (DiGangi et al., 2011), the industry sector (Parrish et al., 2012), shipping (Marbach et al., 2009; Celik et al., 2020) and agriculture (Kaiser et al., 2015) can contribute significantly to the local HCHO abundance. HCHO is the most abundant aldehyde in the atmosphere and one of the few oxygenated volatile organic compounds (OVOCs) that can be measured directly from satellites (De Smedt et al., 2008, 2012, 2015, 2018; Marbach et al., 2009; Zhu et al., 2020). In particular, the ability to measure HCHO from satellites has instigated several studies on the relation between HCHO column densities and emissions of isoprene, one of

its dominant biogenic precursors (Palmer et al., 2003; Shim et al., 2005; Millet et al., 2008; Wolfe et al., 2016). In most of the free troposphere and the remote marine boundary layer (MBL), HCHO mixing ratios are determined by methane (CH₄) oxidation (Ayers et al., 1997; Weller et al., 2000; Wagner et al., 2002; Anderson et al., 2017) and degradation of the oxidation products methanol (CH₃OH), methylhydroperoxide (CH₃OOH) and other ubiquitous OVOCs like acetone (Kormann et al., 2003; Reeves and Penkett 2003; Stickler et al., 2006; Anderson et al., 2017). In polluted areas, the oxidation of a large variety of biogenic and anthropogenic precursors contributes to HCHO production (Liu et al., 2007; DiGangi et al., 2012; Wolfe et al., 2016; Wennberg et al., 2018; Kluge et al., 2020). HCHO/NO₂ ratios have been used to differentiate between nitrogen oxide (NO_x = NO + NO₂) and VOC-limited ozone production (Martin et al., 2004; Duncan et al., 2010; Schroeder et al., 2017; Tadic et al., 2020) and to infer global hydroxyl radical (OH) concentrations (Wolfe et al., 2019). If HCHO loss rates are well defined, estimation of the concentrations of OH from HCHO mixing ratios is feasible since HCHO production is dominated by the oxidation of VOCs via OH.

Formaldehyde production in the troposphere results from reactions of VOCs with OH; ozone (O₃) and the nitrate radical (NO₃), with the oxidation processes to be dominated by OH over the day and by NO₃ during nighttime, for many trace gases of biogenic origin. Liebmann et al. (2018) showed that the daytime loss of biogenic compounds via reaction with NO₃ can also be significant in forested areas. Unsaturated hydrocarbons (e.g. ethene, isoprene and terpenes) additionally react with O₃ in the form of a cycloaddition to form energy-rich primary ozonides (Criegee intermediates) that rapidly fragment, releasing HCHO (Cox et al., 2020). This class of reactions is most important in relation to biogenic emissions in forested regions. Many OVOCs (e.g. alcohols, aldehydes, hydroperoxides, alkyl nitrates) also produce HCHO in reactions with OH, chlorine radicals or via photolysis. Alkanes react with OH, forming saturated peroxy radicals (RO₂) that further react with NO to form alkoxy radicals and subsequently carbonyl compounds including HCHO. Since the oxidation of almost every VOC can produce HCHO, some with a yield greater than unity (Luecken et al., 2018), HCHO is an ideal candidate to test our understanding of VOC chemistry using zero-dimensional box models (Wagner et al., 2002; Fried et al., 2011) and three-dimensional general circulation models (Kormann et al., 2003; Liu et al., 2007; Klippel et al., 2011; Anderson et al., 2017).

In addition to the integral of contributions by individual HCHO production pathways, the production rate of HCHO resulting from reactions involving OH chemistry (P_{OH}(HCHO)) can be deduced from the OH concentration ([OH]), the HCHO yield α_{*i*} and the OH reactivity (R(OH)), which represents the summation of trace gases R_{*i*} that react

with OH with the rate coefficient *k_i*; Wolfe et al., 2019):

$$P_{\text{OH}}(\text{HCHO}) = \alpha_i \cdot [\text{OH}] \cdot R(\text{OH})_i, \quad (1)$$

with

$$R(\text{OH}) = \sum k_i \cdot R_i. \quad (2)$$

R(OH) includes reactions of OH with species like carbon monoxide (CO), sulfur dioxide (SO₂), nitrogen dioxide (NO₂) or nitrogen oxide (NO) that do not result in HCHO formation as well as reactions with VOCs like methane, alkanes, alkenes, aromatics or OVOCs (Williams and Brune, 2015). Calculating P_{OH}(HCHO) this way has the advantage that reactions of non-measured VOCs with OH will be included. Not all reactions with OH will produce HCHO, which is accounted for by the yield factor α (Wolfe et al., 2019), which is a summation over the HCHO yield α_{*i*} of each *k_i* · R_{*i*}. For reactants that do not yield HCHO (e.g. NO, NO₂, SO₂, CO, O₃ and HCHO itself), α_{*i*} is zero. Species that yield HCHO have positive α_{*i*} values (e.g. CH₄, isoprene, etc.). Note that the individual α_{*i*} values and thus the overall α can be functions of NO_x (Wolfe et al., 2016). For example, the yield of HCHO from methane oxidation depends on the fate of the initially formed methyl peroxy radical (CH₃O₂). At high NO_x levels, CH₃O₂ will react with NO, subsequently forming HCHO. At low NO_x, CH₃O₂ preferentially reacts with the hydroperoxy radical (HO₂) forming methyl hydroperoxide (CH₃OOH), reducing the yield of HCHO production from CH₄ oxidation (Wagner et al., 2002). Since the production of HCHO is not only controlled by OH chemistry, P_{add}(HCHO) represents additional sources for instance direct emissions, its production due to photolysis (e.g. CH₃OOH, acetaldehyde (CH₃CHO) and further OVOCs) and the ozonolysis of alkenes (Stickler et al., 2006; Parrish et al., 2012; Anderson et al., 2017).

$$P(\text{HCHO}) = P_{\text{OH}}(\text{HCHO}) + P_{\text{add}}(\text{HCHO}) \quad (3)$$

In photochemical steady state (PSS), P(HCHO) is expected to be balanced by HCHO losses (L(HCHO)) and is most likely achieved at midday (*j*_{HCHO} ~ 7 × 10⁻⁵ s⁻¹; R(OH + HCHO) ~ 4 × 10⁻⁵ s⁻¹), when the formaldehyde lifetime is ~ 2.5 h. In this study we used the PSS assumption to calculate P(HCHO) via its loss reactions:

$$\begin{aligned} P(\text{HCHO}) &= L(\text{HCHO}) \\ &= \left(k_{\text{OH}+\text{HCHO}} \cdot [\text{OH}] + j_{\text{HCHO}} + \frac{v_d}{\text{BLH}} \right) \\ &\quad \cdot [\text{HCHO}]. \end{aligned} \quad (4)$$

The first term within brackets in Eq. (4) represents HCHO loss due to reaction with OH radicals, while the second term describes total losses due to photolysis (both the radical and molecular channel). In the boundary layer, additional loss due to dry deposition has to be considered and depends on the

deposition velocity v_d and the boundary layer height (BLH), i.e. its mixing volume. Further loss due to wet deposition has been neglected in this study since we did not encounter significant precipitation during the AQABA campaign. The derived production and loss rates of HCHO can be influenced by direct emissions or by advective transport. Obvious direct emissions from ship plumes or other sources were excluded from the dataset. The potential role of transport is addressed in Sect. 4.

In this study we use in situ observations of HCHO, OH, R(OH) and j_{HCHO} together with the HCHO deposition velocity v_d (calculated for 34 m above the ocean; Stickler et al., 2007) and ERA-5 meteorological data of the BLH (<https://www.ecmwf.int/en/forecasts/datasets/reanalysis-datasets/era5>, last access: 3 December 2020), which were obtained during a ship cruise around the Arabian Peninsula as part of the AQABA (Air Quality and Climate Change in the Arabian Basin) campaign in summer 2017. From this dataset, we calculated the loss rates of HCHO, which represent P(HCHO) during PSS conditions. Scatter plots of $[\text{OH}] \times \text{R}(\text{OH})$ versus P(HCHO) yield the lower estimate of the formaldehyde yield α with respect to total OH chemistry (including NO_x , SO_2 and other non-HCHO-producing reactions; see Fig. S2 in the Supplement), reflecting the transition between rather clean to highly polluted conditions, both with respect to NO_x and VOCs.

$$\alpha = \frac{\text{P}(\text{HCHO}) - \text{P}_{\text{add}}^*(\text{HCHO})}{[\text{OH}] \cdot \text{R}(\text{OH})} \quad (5)$$

For further interpretation, the effective HCHO yield α_{eff} was determined for each region by removal of non-HCHO-yielding reactions (of NO , NO_2 , SO_2 , CO , HCHO and O_3 with OH) from the OH reactivity data ($\text{R}(\text{OH})_{\text{eff}}$, Fig. S1).

$$\alpha_{\text{eff}} = \frac{\text{P}(\text{HCHO}) - \text{P}_{\text{add}}(\text{HCHO})}{[\text{OH}] \cdot \text{R}(\text{OH})_{\text{eff}}} \quad (6)$$

The major questions addressed in this study are the following:

1. Are reactions involving OH the dominant HCHO source in the different regions around the Arabian Peninsula, or do photolysis (e.g. of oxidized organics), reactions (e.g. of unsaturated hydrocarbons) with O_3 or direct emissions contribute significantly to the HCHO distribution?
2. Can this method be used to identify whether the local HCHO distribution can be explained through OH oxidation only?
3. What is the contribution of different VOC compound classes (alkanes, alkenes, aromatics, OVOC) towards HCHO production via reaction with OH?

In Sect. 2, we give a brief outline of the AQABA cruise and the measurements performed. An investigation of the balance between HCHO production via the product of R(OH)

and OH (Eq. 1) and production deduced from HCHO loss assuming PSS (Eq. 3) is given in Sect. 3. Section 4 covers a discussion of the variation of α and α_{eff} in different regions, and a summary of the results obtained is presented in Sect. 5.

2 The AQABA campaign

Measurements during AQABA took place on board the research and survey vessel *Kommandor Iona* from 25 June to 3 September 2017. The first leg from southern France to Kuwait started in La Seyne-sur-Mer (near Toulon, France) and continued via the Mediterranean Sea, the Suez Canal, the Red Sea, the Arabian Sea, the Gulf of Oman and the Arabian Gulf (also known as the Persian Gulf) to Kuwait. During the second leg, the vessel returned via the same route (Fig. 1).

Four laboratory containers with instrumentation for in situ and offline monitoring of a large suite of trace gases, particles and radicals were mounted on the front deck of the ship. With the exception of aerosols and radical measurements (OH and HO_2), air sampling was achieved from a high-flow ($10 \text{ m}^3 \text{ min}^{-1}$) cylindrical stainless-steel inlet (HFI, sampling height: 5.5 m above deck, diameter: 0.2 m), placed between the containers on the front deck of the ship. Air was drawn from the center of the HFI into the air-conditioned laboratory containers using PFA (perfluoroalkoxy alkane) tubing. The inlet for OH and HO_2 measurements was mounted on top of a laboratory container closest to the bow.

Formaldehyde measurements were based on the Hantzsch technique using a commercial instrument (Aero-Laser, model AL4021, Garmisch-Partenkirchen, Germany). The limit of detection (LOD), determined from the reproducibility of on-board zero-air measurements, was between 80 and 128 pptv (influenced by wave-induced rolling of the ship) with a confidence interval of 1σ . The total measurement uncertainty including line losses was 13 % (Dienhart et al., 2021).

Measurements of OH radicals were performed using laser-induced fluorescence (LIF) with the HORUS instrument (Martinez et al., 2010; Hens et al., 2014; Marno et al., 2020). Typical detection limits for OH were between 1×10^5 and 5×10^5 molecules cm^{-3} with the total uncertainty of ~ 30 %. OH measurements below the instrumental LOD were excluded from this study. Note that an inlet pre-injector (IPI) was used to determine the OH background signal via chemical modulation (Novelli et al., 2014).

Total OH reactivity was measured using the comparative reactivity method (Sinha et al., 2008; Fuchs et al., 2017). A detailed description of the measurement technique and the results from the AQABA campaign can be found in Pfannerstill et al. (2019). The 5 min detection limit was 5.4 s^{-1} , derived from the 2σ standard deviation of clean air measurements over the Arabian Sea. Total uncertainty (1σ) of the OH reactivity measurements was between 7 % and 60 % with mean and average of 50 %.

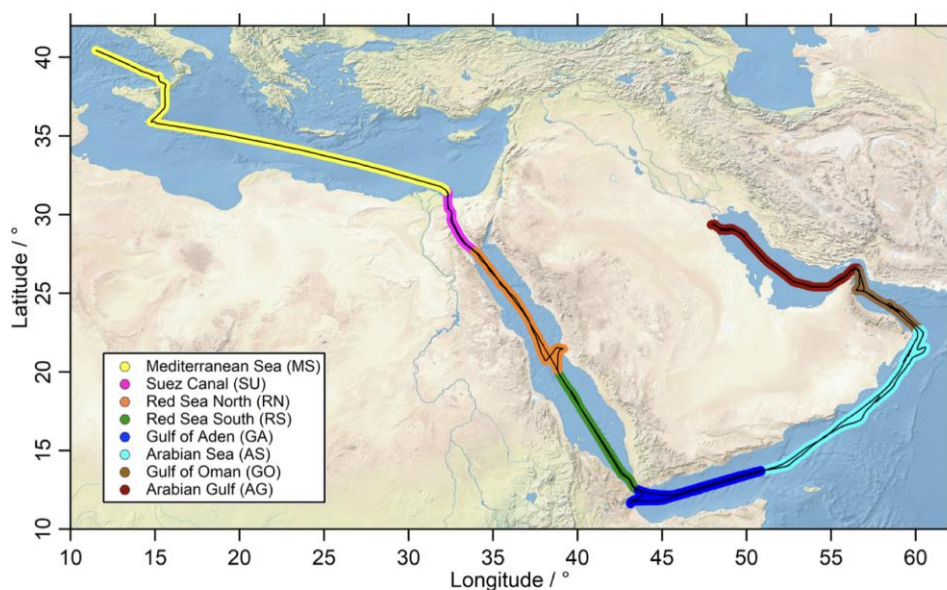


Figure 1. The ship route (black) of the *Kommandor Iona* during the AQABA cruise subdivided into eight regions: Mediterranean Sea (MS: yellow), Suez Canal (SU: pink), Red Sea north (RN: orange), Red Sea south (RS: green), Gulf of Aden (GA: blue), Arabian Sea (AS: turquoise), Gulf of Oman (GO: brown) and Arabian Gulf (AG: red).

Nitrogen oxides ($\text{NO}_x = \text{NO} + \text{NO}_2$) were measured with a two-channel chemiluminescence instrument (CLD 790 SR, ECO Physics AG, Dürnten, Switzerland). A detailed description of the instrument during AQABA can be found in Tadic et al. (2020). The measurement uncertainty of the NO data was calculated to be 6 % at 5 min integration time and a confidence level of 1σ . The LOD for the NO channel was estimated as the full width at half maximum of the frequency distribution of all zero-air measurements obtained during the campaign to be 9 pptv with a confidence level of 1σ . The total uncertainty of the NO_2 data was estimated as a conservative upper limit at 23 % as the average of the relative uncertainties of all data points obtained during the campaign. The absolute detection limit of the NO_2 instrument was estimated at 112 pptv (Tadic et al., 2020).

O_3 measurements were performed with a commercial absorption photometer (model 202 ozone monitor, 2B Technologies, Boulder, Colorado, USA). Water and particle interferences during the expedition were minimized by sampling through a Nafion tube and a Teflon filter; the overall uncertainty of the data was 2 % (Tadic et al., 2020).

CO and CH_4 mixing ratios were determined with a cavity ring-down spectrometer (Picarro G2401; Santa Clara, USA) with a precision of ≤ 8 ppbv for CO and ≤ 0.3 ppbv for CH_4 . The air was not dried prior to analysis, and water vapor effects were corrected. The data were quality-controlled following ICOS (Integrated Carbon Observing System) standards; further details can be found in Paris et al. (2021).

Non-methane hydrocarbons (NMHCs) were measured with two coupled GC-FID systems (GC5000VOC and

GC5000BTX; AMA Instruments GmbH, Germany). The GC5000VOC was used for the quantification of light hydrocarbons (C_2 – C_6), while the GC5000BTX was used for the heavier hydrocarbons and aromatics (C_6 – C_8). The NMHCs have average detection limits in the range of 1–25 pptv and a total uncertainty in the range of 6 %–13 % (Bourtsoukidis et al., 2019).

OVOCs were detected with a proton-transfer-reaction time-of-flight mass spectrometer (PTR-ToF-MS 8000, Ionicon Analytik GmbH, Innsbruck, Austria) with a total measurement uncertainty in the range of 6 %–17 %; an accuracy of ~ 50 %; and 3σ detection limits (derived by background measurements) of 52 ± 26 pptv for acetaldehyde, 22 ± 9 pptv for acetone, and 9 ± 6 pptv for methyl ethyl ketone (Wang et al., 2020).

Sulfur dioxide (SO_2) was detected with a chemical ionization quadrupole mass spectrometer (CI-QMS) using an electrical, radio-frequency discharge ion source with a detection limit of 38 pptv and a total uncertainty of $20\% \pm 23$ pptv. Further details about the instrument and ionization method are described in Eger et al. (2019).

Photolysis rates for a large number of trace gases were calculated from wavelength-resolved actinic flux measurements with a spectral radiometer (Metcon GmbH, Glashütten, Germany) located approximately 10 m a.s.l. (~ 5 m above the front deck). The total uncertainty of the HCHO photolysis rates obtained are ~ 10 %, based on the calibration of the instrument (Bohn et al., 2008), and the data were not corrected for upwelling radiation, which is considered to be insignificant at the sea surface.

As the sampling location was in front of the ship's chimney, contamination of the measurements with the ship's own exhaust occurred when the vessel was sailing ahead of the wind. Thus, a data filter based on relative wind direction and NO, CO and SO₂ observations was used to eliminate contaminated data (including other ship exhaust emissions and the stops in Jeddah and Kuwait). This affected mainly the measurements during the first leg of the cruise (Tadic et al., 2020).

3 Results

The daytime observations of HCHO, OH, R(OH) and the photolysis rate of HCHO (j_{HCHO}) during the AQABA cruise are displayed in Fig. 2. Note that only daytime observations ($j_{\text{NO}_2} \geq 3 \times 10^{-3} \text{ s}^{-1}$) after 20 July 2017 (the start of the OH measurements) were used in this study. Formaldehyde mixing ratios varied between minimum values of approximately 0.1 ppbv over the Arabian Sea during the first leg (AS Leg 1; 20–23 July) and the Red Sea south (RS; 17–19 August) up to more than 10 ppbv over the Arabian Gulf (AG; 28 July to 5 August). The highest values were detected at the center of the gulf, coincident with the highest ozone (O₃) mixing ratios > 150 ppbv during AQABA (Tadic et al., 2020). Simultaneously, elevated ethene (Bourtsoukidis et al., 2019), OVOCs (Wang et al., 2020) and organic peroxides (Dienhart et al., 2021) highlight that this area as a hotspot of photochemical air pollution. Median HCHO concentrations between 1 and 2 ppbv were measured in most of the other regions (Mediterranean Sea (MS); Red Sea north (RN); Gulf of Aden (GA); Arabian Sea leg 2 (AS Leg 2); Gulf of Oman (GO)), while pollution events also occurred in the area around the Suez Canal (SU). In general, diurnal variations of HCHO with maximum values around local noon were observed, while the diurnal variation in clean regions like the Arabian Sea was quite small (Fig. 2).

Strong diurnal variations were observed for OH mixing ratios with noontime maximum values varying between 0.1 and 0.5 pptv in most regions. The highest noontime mixing ratios (~ 0.8 pptv) were observed over the Gulf of Aden (GA; 16 August), while air masses over the Gulf of Oman (GO) and the Mediterranean Sea (MS) also showed elevated concentrations of OH (Fig. 2). Although there is some regional variation, there is no clear trend with respect to the different locations, as, for example, found for HCHO mixing ratios.

Large regional variations were also found for the OH reactivity, with noontime values ranging from close to the detection limit over the Arabian Sea (AS Legs 1 and 2), the Gulf of Aden (GA) and the Red Sea (RS and RN) to values of more than 30 s^{-1} , predominately in the polluted regions of the Arabian Gulf (AG) and the Suez Canal (SU). For a detailed discussion of the OH reactivity in different regions and its relations to VOCs and inorganic compounds, see Pfannerstill et al. (2019).

Noontime maxima of the formaldehyde photolysis rates varied between 4.5×10^{-5} and $7.8 \times 10^{-5} \text{ s}^{-1}$. On most days, clear diurnal profiles were observed under clear-sky conditions. Significant cloud cover was observed only on 20–22 July and 8–10 August.

The boundary layer height varied between 250 and 1400 m (Fig. 2), with least diurnal variation in the Arabian Sea and the Mediterranean Sea with a mean of 566 and 780 m, respectively. The boundary layer height in other regions was more variable, with a mean value ($\pm 1\sigma$) for the entire dataset (excluding the stop in Kuwait) of 750 ± 113 m.

The sink of HCHO was calculated by summing the loss rate coefficients through reaction with OH, photolysis and dry deposition (Eq. 4, Fig. 3). Based on Gaussian error propagation of uncertainty in the HCHO and OH mixing ratios, j_{HCHO} , and in the rate coefficient k_{OH} for reaction of OH with HCHO, the total uncertainties of the loss rates due to OH and j_{HCHO} are 33 % and 15 %, respectively. Loss of HCHO via photolysis and reaction with OH were found to be of the same order of magnitude, with total noontime loss rates varying from 0.01 up to 1 pptv s^{-1} . The formaldehyde sinks due to OH and photolysis were on the order of 0.1 pptv s^{-1} during noon, with the lowest values over the Arabian Sea, the Gulf of Aden (8–15 August) and the southern Red Sea (18–20 August). Significantly enhanced noontime values ($> 0.2 \text{ pptv s}^{-1}$) were found for the loss through photolysis over the Arabian Gulf (28–31 August) due to the elevated HCHO mixing ratios.

The removal of HCHO by dry deposition depends on turbulent transport and also on the wind speed. Since our results for the HCHO mixing ratio are just one dimensional, the dry deposition could not be calculated directly for the AQABA dataset and was thus inferred with the literature value for the HCHO deposition velocity (v_d) over sea and the boundary layer height. In our analysis we used a fixed value of $0.36 \pm 0.18 \text{ cm s}^{-1}$ for v_d based on the findings by Stickler et al. (2007). For the BLH, we used the mean value ($\pm 1\sigma$) of the ERA-5 results (750 ± 113 m). Assuming an uncertainty of 50 % for v_d and 15 % for the BLH as conservative estimate results in an uncertainty of 52 % for the dry deposition term.

Close to local noon, the loss rate due to dry deposition was in general below 0.1 pptv s^{-1} and thus much smaller than HCHO removal by either photolysis or reaction with OH (Fig. 3). Only close to sunrise and sunset was dry deposition of similar magnitude to photochemical loss processes. The lowest panel in Fig. 3 shows the sum of all three loss processes according to Eq. (4). Based on Gaussian error propagation, the estimated uncertainty of $L(\text{HCHO})$ is 62 %.

In photochemical steady state the HCHO loss and production balance each other, and a scatter plot of the product of the OH reactivity $R(\text{OH})$ (s^{-1}) and the OH mixing ratio (pptv) versus the HCHO production rate $P(\text{HCHO})$ ($= L_{\text{HCHO total}}$) yields the slope, i.e. the factor α according to Eq. (5) (Fig. 4). A compact linear relationship is expected un-

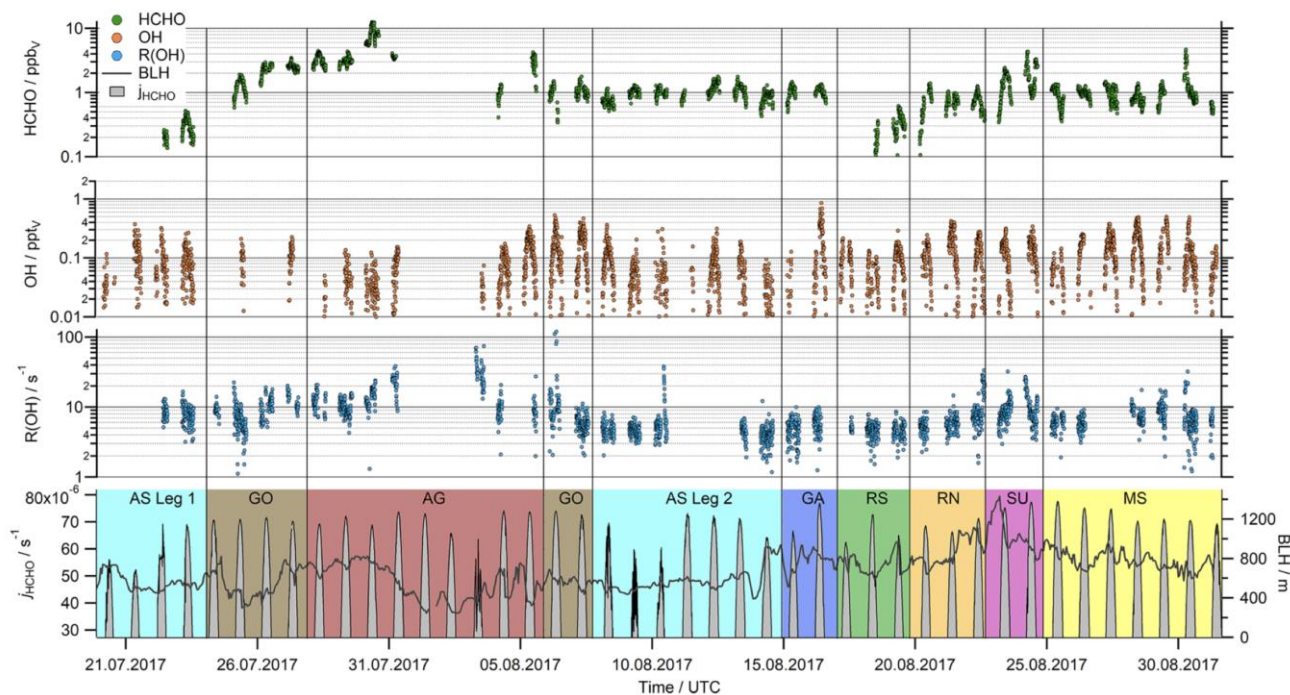


Figure 2. Time series of HCHO, OH, R(OH) and the HCHO photolysis (j_{HCHO} , sum of the molecular and the radical channel) in 5 min resolution. For the boundary layer height (BLH), we used the ERA-5 meteorological reanalysis data in hourly averages, which resolve the earth's atmosphere on a 30 km grid (<https://www.ecmwf.int/en/forecasts/datasets/reanalysis-datasets/era5>, last access: 3 December 2020).

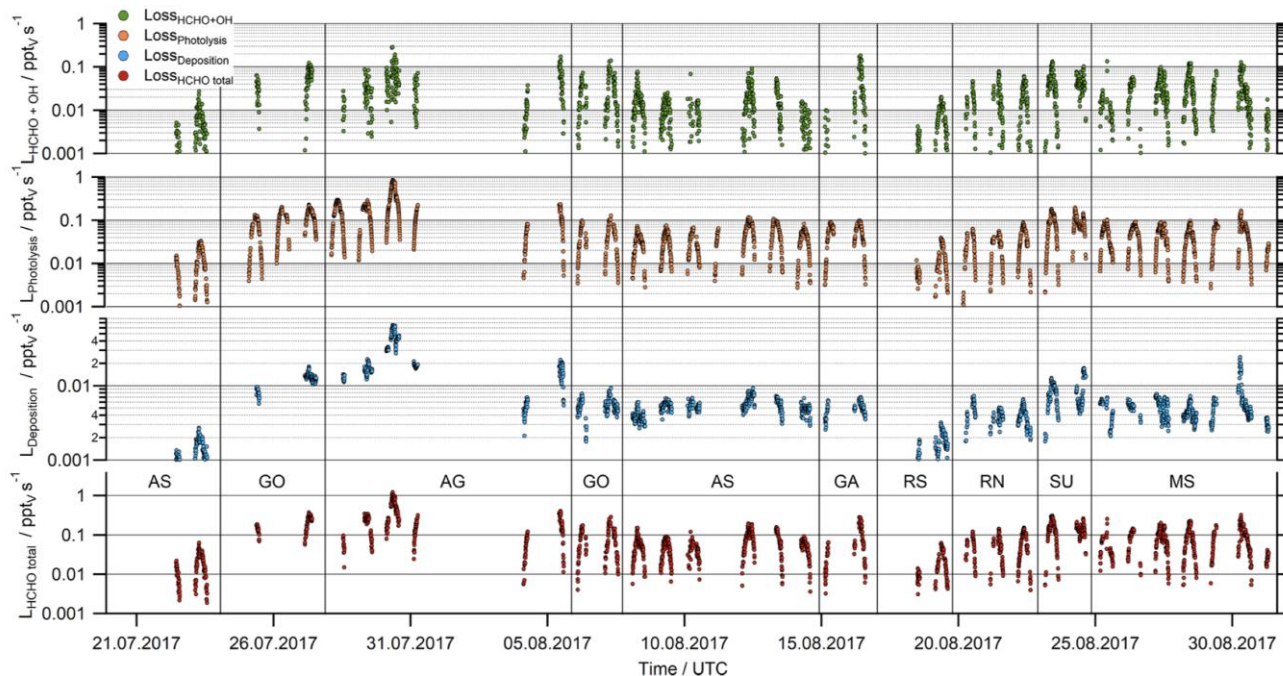


Figure 3. HCHO loss rates due to reaction with OH, photolysis, dry deposition and the total sink as the sum of all three processes.

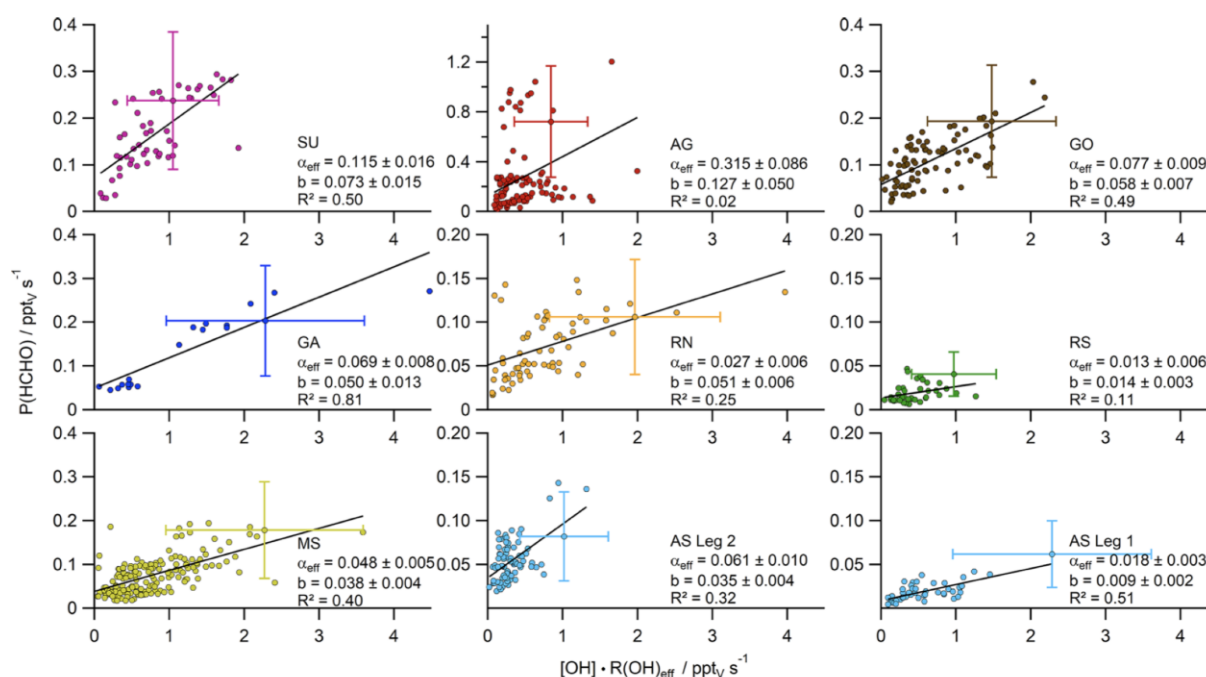


Figure 4. Scatter plots with bivariate fits (York et al., 2004) of the product $[\text{OH}] \times \text{R}(\text{OH})_{\text{eff}}$ ($\pm 58\%$) versus the HCHO production rate $\text{P}(\text{HCHO})$ ($\pm 62\%$), subdivided into the different regions probed during the AQABA cruise. The slope of the respective regression represents the HCHO yield α_{eff} , while the intercept can be interpreted as additional HCHO sources not related to OH chemistry ($\text{P}_{\text{add}}(\text{HCHO})$).

der PSS conditions if chemical conditions do not change and the air mass is not affected by transport, while data points that do not fulfill PSS (e.g. due to direct emissions from point sources or advection of HCHO-enriched or HCHO-depleted air masses) are expected to not follow the regression line, yielding additional scatter. For example, a fresh pollution plume (e.g. containing unsaturated hydrocarbons and no primary HCHO) would result in data shifted below the regression line since a high OH reactivity is expected along with low initial HCHO production, as secondary processes taking place over longer timescales (e.g. photolysis) are involved in the HCHO production from unsaturated hydrocarbons. The dataset covers a highly polluted event in AG (30 July 2017), although the high HCHO/R(OH) ratio, as well as enhanced methanol, acetaldehyde and O_3 mixing ratios (Wang et al., 2020; Tadic et al., 2020), indicates rather processed air masses which could also include primary emissions of HCHO. Primary emission from point sources would likely shift data above the regression line due to the correlation with the HCHO mixing ratio (although this effect can be compensated for depending on the OH concentration in emission plumes). The primary emission of HCHO cannot be accurately identified, but we removed obvious pollution events (e.g. plumes from ships or oil rigs) via covariance with elevated NO_x , CO and SO_2 mixing ratios. Furthermore, rain-out can affect the relationship, because it would result in data points shifted below the regression line, although the impact

can be neglected in this study as only minor precipitation occurred in AS on the 12 August 2017 during the night.

In our analysis, we first subdivided the data into the smaller regions according to Fig. 1 and examined the correlation between $\text{P}(\text{HCHO})$ and $[\text{OH}] \times \text{R}(\text{OH})$ for each subregion (Fig. S2). For the Arabian Sea, the dataset has been further partitioned into the two individual legs heading towards and away from the Gulf of Oman. This is justified by the significant differences in HCHO mixing ratios and $\text{R}(\text{OH})$ during the two legs (AS Legs 1 and 2), reflecting different air-mass origins. For the individual regions, bivariate fits were performed according to York et al. (2004). In general, values of R^2 varied between 0.08 (Arabian Gulf) and 0.82 for the Gulf of Aden, while the slopes (α) varied between less than 0.02 for the Arabian Sea during the first leg and the southern Red Sea and up to 0.26 for the Arabian Gulf. The highly elevated $\text{P}(\text{HCHO})$ values over the Arabian Gulf (Fig. S2) also include data during a pollution event on 30 July 2017 in the center of the gulf (Fig. 2; see also Tadic et al., 2020; Wang et al., 2020; Pfannerstill et al., 2019; Bourtsoukidis et al., 2019) and thus the evaluated α in AG is likely influenced by primary emissions or transport of air pollution from the western coast of the gulf. However, this pollution event seems to be representative for this unique region; thus, we did not exclude the data from the study. Primary emissions of HCHO at low $[\text{OH}] \times \text{R}(\text{OH})$ would result in data shifted towards the y axis and thus may be partially responsible for the positive

intercept on the y axis. This would also bias the regression analysis and impact α . Primary emissions of HCHO at low $[\text{OH}] \times R(\text{OH})$ would tend to increase the intercept, whereas primary emissions at high $[\text{OH}] \times R(\text{OH})$ would bias α to larger values.

In general, the values of α represent lower limits, since the $R(\text{OH})$ data still include reactions with inorganic trace gases and other species that do not yield HCHO (e.g. CO, NO₂ and SO₂). The inorganics and CO account for $\sim 10\%$ of the reactivity, except for the Suez Canal ($\sim 16\%$) (see Table 1 in Pfannerstill et al., 2019). Nonzero $P(\text{HCHO})$ at zero $[\text{OH}] \times R(\text{OH})$, corresponding to the intercept b of the linear regression, can be interpreted as the result of several processes including additional chemical loss and production, dry deposition, and may also be related to partial break-down of the PSS assumption when OH is low (e.g. early morning, late evening). The intercept should thus not be over-interpreted and used to calculate deposition velocities. Values for the intercept b ($P_{\text{add}}(\text{HCHO})$) were less or equal to 0.05 pptv s^{-1} in most regions; the cleanest regions with respect to NO_x and VOCs also showed very low values for $P_{\text{add}}(\text{HCHO})$ with approximately 0.01 pptv s^{-1} over the Arabian Sea during the first leg and the southern Red Sea, indicating that HCHO production was dominated by OH chemistry. Highest values of $P_{\text{add}}(\text{HCHO})$ were found over the Arabian Gulf (0.14 pptv s^{-1}) and the area around the Suez Canal (0.09 pptv s^{-1}), where enhanced mixing ratios of unsaturated hydrocarbons and OVOCs (Wang et al., 2020) as well as elevated O₃ mixing ratios prevailed (Tadic et al., 2020).

For further analysis, we removed the highest contributors to inorganic reactivity (NO, NO₂, SO₂, O₃) and major non-HCHO-yielding reactions (CO, HCHO) from $R(\text{OH})$, which resulted in so-called effective OH reactivity ($R(\text{OH})_{\text{eff}}$). Even though the dataset was already filtered for stack emissions, NO_x showed the highest contribution of these reactants (Fig. S1, Table S1 in the Supplement), especially over the Gulf of Oman and while passing Bab-el-Mandeb (16 August 2017) and the Strait of Messina (30 August 2017). Over the Arabian Gulf the correction was dominated by contributions from CO, O₃ and HCHO. The use of $R(\text{OH})_{\text{eff}}$ resulted in reduced data coverage and an increased slope compared to when using non-adjusted $R(\text{OH})$ (Figs. 4 and S2). The effective HCHO yield α_{eff} increased significantly in five sub-regions (Suez, Arabian Gulf, Gulf of Oman, Gulf of Aden, Arabian Sea Leg 2), and the plots show in general slightly reduced scatter. Values for the intercept b were not substantially affected by choice of $R(\text{OH})$ or $R(\text{OH})_{\text{eff}}$, and both methods yielded similar results within their uncertainties, except for the Arabian Sea during the second leg, where the intercept decreased to similar values of the Mediterranean Sea when $R(\text{OH})_{\text{eff}}$ was used.

4 Discussion

According to Eq. (4), formaldehyde loss $L(\text{HCHO})$ is the product of the HCHO mixing ratio and the loss rates due to reaction with OH, photolysis and dry deposition. In photochemical steady state (typical lifetime of HCHO $\sim 2.5 \text{ h}$), formaldehyde loss is equal to its production $P(\text{HCHO})$ (Eq. 4). $P(\text{HCHO})$ varied between 0 and approximately 1.2 pptv s^{-1} , with values above 0.4 pptv s^{-1} only detected over the Arabian Gulf. Air masses encountered in this region were likely influenced by air pollution, which was mainly transported from the west coast of the gulf and Kuwait, where oil and gas industries are numerous (Pfannerstill et al., 2019). We also detected a biomass burning plume close to the Suez Canal (Wang et al., 2020), which was excluded from this study as it occurred in the early morning and thus a steady state analysis is not appropriate. Additionally, the entire region is well known for its intensive ship transport (Celik et al., 2020); thus, the interference with other primary HCHO sources or, for example, elevated background concentrations are likely. Maximum $P(\text{HCHO})$ was determined at the center of the Arabian Gulf during the first leg, where elevated mixing ratios of unsaturated hydrocarbons, OVOCs and O₃ were observed (Bourtsoukidis et al., 2019; Wang et al., 2020; Tadic et al., 2020). This air mass was characterized by rather low OH, slightly elevated OH reactivity and the highest HCHO mixing ratios during AQABA (30 July 2017, Fig. 2), which resulted in data points shifted towards the y axis (Fig. 4). We nevertheless decided to include the data as they represent highly polluted air within the center of this unique region. Minimum values of $P(\text{HCHO})$ were determined over the southern Red Sea and the Arabian Sea during the first leg ($\leq 0.05 \text{ pptv s}^{-1}$). In general, these results emphasize the limits of the method used in this study, since primary emissions and transport can significantly affect the local HCHO distribution. Furthermore, some HCHO-yielding reactions require oxidation (not only via OH) and subsequent photolysis steps of rather long-lived oxidation products before releasing HCHO and are thus temporarily decoupled from measurements of OH and OH reactivity. Values of $[\text{OH}] \times R(\text{OH})_{\text{eff}}$ varied between practically zero and more than 4 pptv s^{-1} with maximum values over the northern Red Sea, the Mediterranean Sea and the Gulf of Aden, while most data represents values $\leq 3 \text{ pptv s}^{-1}$. Rather compact correlations between $P(\text{HCHO})$ and $[\text{OH}] \times R(\text{OH})_{\text{eff}}$ were observed over the Gulf of Aden, the Arabian Sea during Leg 1, the Suez Canal and the Gulf of Oman as indicated by R^2 values between 0.49 and 0.81 (Fig. 4). Decreased R^2 (less than 0.40) were found for the Mediterranean Sea, the Red Sea, the Arabian Sea during the second leg and the Arabian Gulf. The weak correlation in the Arabian Sea during Leg 2 results from a cluster of data points at low values on both the x and the y axes. In this subregion there was little variation in chemical composition as air masses (during the Indian summer monsoon) originated from the east coast of

Table 1. Average speciated reactivity $R(\text{OH})_x \pm 1\sigma$ standard deviation) of certain compound classes (based on the results of Pfannerstill et al., 2019), $R(\text{OH})_{\text{eff}}$ and α_{eff} (\pm uncertainty of the slope of the bivariate fit). For NO_x , the median values are listed instead of the means.

	$R(\text{OH})_{\text{alkanes}}$ / s^{-1}	$R(\text{OH})_{\text{alkenes}}$ / s^{-1}	$R(\text{OH})_{\text{OVOCs}}$ / s^{-1}	$R(\text{OH})_{\text{aromatics}}$ / s^{-1}	$R(\text{OH})_{\text{eff}}$ / s^{-1}	α_{eff}	NO_x / ppb_v
MS	0.323 ± 0.131	0.117 ± 0.179	0.656 ± 0.283	0.105 ± 0.143	6.412 ± 2.854	0.048 ± 0.005	0.275 ± 2.024
SU	0.683 ± 0.546	0.765 ± 1.025	1.118 ± 0.870	0.699 ± 1.178	10.17 ± 5.174	0.115 ± 0.016	4.806 ± 8.014
RN	0.449 ± 0.187	0.562 ± 0.522	1.110 ± 0.488	0.386 ± 0.410	8.192 ± 3.251	0.027 ± 0.006	0.752 ± 5.648
RS	0.310 ± 0.071	0.781 ± 0.729	1.171 ± 0.444	0.670 ± 0.644	7.840 ± 4.138	0.013 ± 0.006	0.232 ± 1.208
GA	0.290 ± 0.039	0.290 ± 0.372	0.861 ± 0.198	0.262 ± 0.344	7.502 ± 2.999	0.069 ± 0.008	0.604 ± 3.500
AS Leg 1	0.270 ± 0.001	0.174 ± 0.073	0.658 ± 0.046	0.114 ± 0.026	7.881 ± 1.872	0.018 ± 0.003	0.212 ± 0.192
GO	0.366 ± 0.100	0.421 ± 0.309	1.504 ± 0.280	0.427 ± 0.334	7.168 ± 3.548	0.077 ± 0.009	2.596 ± 4.850
AG	1.198 ± 1.195	1.208 ± 1.190	3.853 ± 2.438	0.852 ± 0.843	11.57 ± 5.976	0.315 ± 0.086	1.207 ± 3.997
AS Leg 2	0.274 ± 0.016	0.136 ± 0.075	0.476 ± 0.087	0.092 ± 0.061	4.308 ± 0.711	0.061 ± 0.010	0.155 ± 1.838

Africa (Edtbauer et al., 2020, Tegtmeier et al., 2020). In contrast, the results for the Arabian Gulf cover the highest variation of HCHO and VOCs (Bourtsoukidis et al., 2019; Wang et al., 2020) and are characterized by substantial changes in chemical composition, although obvious point sources (e.g. ship exhaust) with enhanced NO_x , CO and SO_2 mixing ratios were excluded from the entire study.

Based on Eq. (5), the intercept b of the bivariate fit can be interpreted either as an additional loss of HCHO (e.g. washout, dry deposition) or as a region-wide attribution of additional HCHO sources not related to OH chemistry ($P_{\text{add}}(\text{HCHO})$, Fig. 4). The effect of washout should be negligible, since we only experienced a short rain event on the 12 August 2017 during the night. Dry deposition can only account for 8%–19% of the intercept, based on our calculation with literature values for the deposition velocity (Stickler et al., 2007) and the ERA5 boundary layer height. The elevated intercept of the Arabian Gulf is biased by the pollution event encountered at the center of the gulf, although further regions which covered enhanced concentrations of air pollution (SU, GO, RN) also show significantly elevated intercepts within their uncertainties (0.051–0.127 pptv s^{-1}). In the relatively clean regions (AS, MS, RS) we determined smaller intercepts (0.009–0.038 pptv s^{-1}). Additional HCHO production via the ozonolysis of alkenes seems very likely in AG and SU, indicated by elevated levels of O_3 (Tadic et al., 2020) and ethene (Bourtsoukidis et al., 2019). Furthermore, we detected enhanced concentrations of OVOCs (Wang et al., 2020) and CH_3OOH (Dienhart et al., 2021) in these regions. Therefore, it seems more appropriate to evaluate the intercept as an indication of additional HCHO sources ($P_{\text{add}}(\text{HCHO})$), which are not necessarily related to OH chemistry.

Large variability was observed for the slope m of the regression line along the different regions probed. This slope can be equated to the regional HCHO yield α_{eff} (Eq. 6), quantifying the fraction of OH reactivity that results in HCHO production. Inorganic species and CO made up $\sim 10\%$ of the reactivity in most regions and 16% over the Suez Canal (Pfannerstill et al., 2019); thus, subtraction of the inorganic

reactivity reduced the span on the x axis significantly. Removal of non-HCHO-yielding reactions from total OH reactivity indicates that between 1% and 32% of $R(\text{OH})_{\text{eff}}$ contributed to HCHO production, with the largest values determined for the Arabian Gulf (0.315), the Suez Canal (0.115) and the Gulf of Oman (0.077). However, values of α_{eff} show low variability among the other regions and reflect rather comparable chemical regimes. Pfannerstill et al. (2019) compared the $R(\text{OH})$ measurements to the calculated reactivity from all measured species. In summary, accumulation of the measured trace gases resulted in $\sim 20\%$ unattributed OH reactivity over the Arabian Gulf and up to 55% over the Gulf of Aden, which could bias the derived α_{eff} towards lower values.

We expect HCHO to be produced from methane (CH_4), non-methane hydrocarbons such as alkanes and alkenes, OVOCs, and to a lesser extent from aromatic hydrocarbons (Wagner et al., 2002). For further analysis, we have recalculated mean OH reactivities ($\pm 1\sigma$ standard deviation) of the individual substance classes ($R(\text{OH})_x$, e.g. alkanes, alkenes, OVOCs, aromatics) based on the findings by Pfannerstill et al. (2019). We assume that the unmeasured VOCs occurred at levels proportional to the measured compounds of a certain compound class, so these values represent general trends for the VOC oxidation of the subdivided regions. Please note that we removed the reaction of HCHO with OH from the OVOC class, which is usually included when presenting the speciated reactivity (Table S2; see also Table 1 in Pfannerstill et al., 2019). The ratio of $R(\text{OH})_x/R(\text{OH})_{\text{eff}}$ then represents the relative contribution of a certain compound class to the regional OH reactivity, which reflects the measured VOC oxidation plus unattributed reactivity. Alkanes (including CH_4) contributed on average 3%–10%, alkenes 2%–10%, OVOCs 8%–33% and aromatics 1%–9% to regional $R(\text{OH})_{\text{eff}}$ (Table 1, Fig. 5). All sulfur-containing VOCs together contributed less than 1% to the total $R(\text{OH})_{\text{eff}}$ and were thus neglected. Elevated contributions of alkanes to $R(\text{OH})_{\text{eff}}$ were found in SU and AG, while their contribution in the remaining regions was rather constant ($\sim 5\%$)

and dominated by the oxidation of methane. Lowest relative contributions of the other compound classes were generally found over the Mediterranean Sea and the Arabian Sea, where also the lowest total OH reactivity has been detected (Table 1; see also Fig. 1 in Pfannerstill et al., 2019). Highest relative contributions were observed over the Arabian Gulf, with alkanes and alkenes each contributing $\sim 10\%$ and OVOCs $\sim 33\%$ to $R(\text{OH})_{\text{eff}}$. The largest relative contribution of aromatic compounds was found over the area near the Suez Canal with $\sim 9\%$. The sum of alkanes, alkenes, OVOCs and aromatic compounds contributed on average 19% over the Mediterranean Sea, 32% over the Suez Canal, 31% over the northern Red Sea, 37% over the southern Red Sea, 23% over the Gulf of Aden, 16% on the first leg over the Arabian Sea, 38% over the Gulf of Oman, 62% over the Arabian Gulf and 23% on the second leg over the Arabian Sea to $R(\text{OH})_{\text{eff}}$.

In general, the sensitivity of HCHO production to different VOCs results from both the per molecule yield (amount of HCHO produced per VOC molecule lost) and the total abundance (or anthropogenic emissions) of the VOC. Luecken et al. (2018) showed for the continental United States that the per molecule sensitivity of HCHO is highest for anthropogenic emissions of alkenes and comparable within the uncertainties for alkanes, OVOCs and aromatics. Methane oxidation via OH and other oxidants (e.g. chlorine, Cl) is expected to be the main source of HCHO in the remote marine boundary layer, via the production of methyl peroxy radicals (CH_3O_2). The fate of these CH_3O_2 radicals determines the main production pathway of HCHO, as they can react to form other species, e.g. methyl hydroperoxide (CH_3OOH) or methanol (CH_3OH) under low- NO_x conditions (Anderson et al., 2017). The determining step to produce HCHO is the reaction of CH_3O_2 with NO; thus, it can be expected that HCHO production is suppressed in very clean regimes, since these favor the recombination of CH_3O_2 and the reaction with HO_2 . Emission of rather short-lived alkenes (e.g. ethene, isoprene) can significantly enhance HCHO production via reaction with O_3 or OH and the subsequent formation of OVOCs (e.g. acetone, acetaldehyde). The release of HCHO from these secondary products not only depends on their chemical structure but also on additional photolysis steps involved. While methane oxidation dominates the HCHO production in the MBL, isoprene is expected to be the main precursor over continents for near-surface HCHO. The results by Wolfe et al. (2016) also highlight that the HCHO yield from isoprene oxidation is a nonlinear function of NO_x .

As demonstrated above, the yield of HCHO from $\text{OH} \times R(\text{OH})_{\text{eff}}$ is expected to depend on the composition of $R(\text{OH})_{\text{eff}}$ with respect to alkanes, alkenes, OVOCs and aromatic compounds and also on the presence of NO_x . Mixing ratios of biogenic hydrocarbons, in particular isoprene, were very low during AQABA with the exception of dimethylsulfide (Edtbauer et al., 2020). In clean MBL environments, emissions of alkenes and aromatics are less relevant; thus, the distribution of HCHO should be controlled mainly via

variability of HO_x ($= \text{OH} + \text{HO}_2$) and the presence of NO_x (> 0.1 ppbv), while we expect the HCHO budget to be highly complex under more polluted conditions, e.g. for the area around the Suez Canal and over the Arabian Gulf.

In order to investigate if the change in chemical composition along the different regions correlates with the determined HCHO yield, Fig. 5 shows scatter plots of the HCHO yield α_{eff} versus the measured OH reactivity towards certain compound classes (alkanes, alkenes, OVOCs, aromatics). We also color-coded the z axis with the median of measured NO_x as an indicator for air pollution and in order to identify the regions more easily.

The relative contribution of alkanes to $R(\text{OH})_{\text{eff}}$ shows little variation at $\sim 4\%$ – 5% except over the area near the Suez Canal ($\sim 7\%$) and over the Arabian Gulf ($\sim 10\%$), where methane (Paris et al., 2021) and a variety of NMHCs (Bourtsoukidis et al., 2019) showed significantly elevated mixing ratios. Over the Arabian Gulf, these were likely caused by emissions from the oil and gas industry, indicated by the ratio between *i*-pentane and *n*-pentane of 0.93 ± 0.03 ppbv ppbv $^{-1}$. Bourtsoukidis et al. (2019) found a ratio of 1.71 ± 0.06 ppbv ppbv $^{-1}$ over the Suez Canal, which is representative of ship emissions. From visual inspection, a slight increase in the relative reactivity of alkanes leads to a small but significant increase in α_{eff} with simultaneously elevated values of NO_x . Alkenes contributed on average between $\sim 2\%$ – 10% to $R(\text{OH})_{\text{eff}}$, with the highest values over the Arabian Gulf, the southern Red Sea and the Suez Canal. Interestingly, a high reactivity of alkenes was detected over the southern Red Sea, which was similar to the enhanced values over the Suez Canal (Table 1), although with a higher relative contribution. The NO_x measurements indicate rather clean air over the southern Red Sea (median 0.23 ppbv), where we experienced mostly winds coming from the west (Eritrea, Sudan). As a first result, a higher reactivity of alkenes is not necessarily correlated with an increase in α_{eff} , which can be partly explained by the fact that release of HCHO from alkene oxidation depends on photolysis steps and other reactions involved, and our method does not take into account chemical aging. Additionally, the availability of other oxidants (e.g. O_3) was higher over the Suez Canal and the Arabian Gulf, where the highest amounts of O_3 were detected during AQABA (Tadic et al., 2020). This likely interferes with the presented results and could lead to an increase in $P_{\text{add}}(\text{HCHO})$. In general, emissions of alkenes favor HCHO production, which was also mentioned by Luecken et al. (2018), who found a high sensitivity of HCHO to anthropogenic and biogenic emissions of alkenes with isoprene as the main contributor in summer. We therefore emphasize the limits of our method, as it only takes into account the “immediate yield” of HCHO. OVOCs showed overall the highest contribution to $R(\text{OH})_{\text{eff}}$ with $\sim 8\%$ – 33% during AQABA, and elevated $R(\text{OH})_{\text{OVOCs}}$ generally resulted in an increased α_{eff} , with the highest contribution over the Arabian Gulf, the Gulf of Oman and the Suez Canal. The production

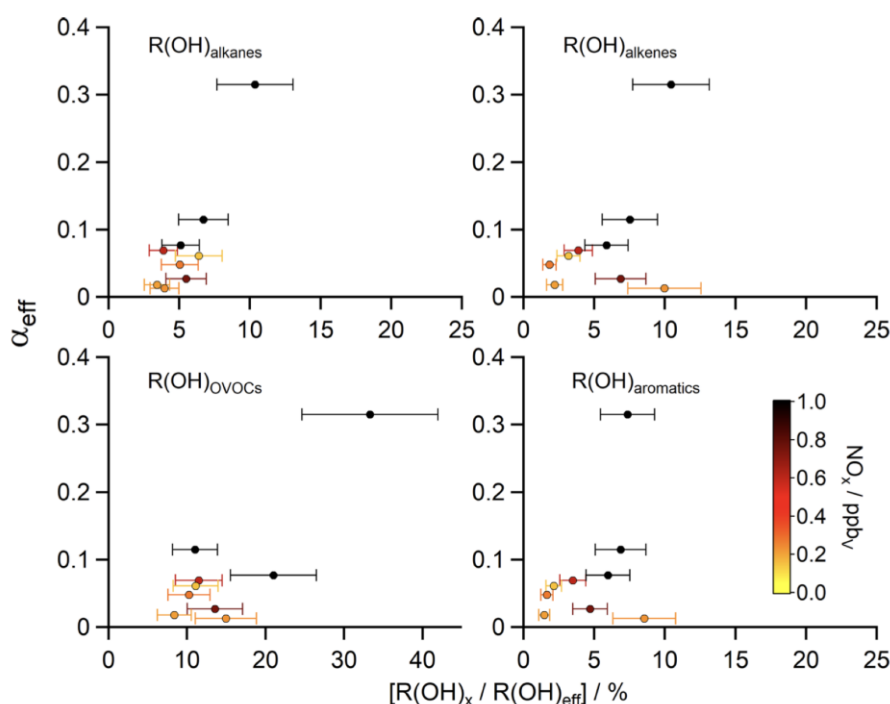


Figure 5. Scatter plots of the contribution of certain substance classes $R(\text{OH})_x$ (e.g. alkanes, alkenes, OVOCs, aromatics) to the total OH reactivity without the contribution of inorganic reactions ($R(\text{OH})_x/R(\text{OH})_{\text{eff}}$) versus the HCHO yield α_{eff} (calculated with $R(\text{OH})_{\text{eff}}$ via Eq. 6). The z axis was color-coded with the measured NO_x median values, representative for the nine different regions during AQABA (Table 1).

of HCHO through OVOCs strongly depends on the composition and amounts of anthropogenic emissions. Some C_1 – C_3 OVOCs (e.g. methanol, acetaldehyde, acetone, glyoxal) are expected to have a strong influence on the local HCHO distribution depending on their mixing ratio, although this effect is minor in remote marine boundary layer conditions with the least amounts of anthropogenic contributions (Anderson et al., 2017). The largest mean mixing ratios of the aliphatic carbonyls acetaldehyde (1.73 ± 1.61 ppbv), acetone (4.50 ± 2.40 ppbv) and HCHO (3.83 ± 2.55 ppbv) were observed over the Arabian Gulf (Wang et al., 2020) and highlight this region as a hotspot of photochemical air pollution, which is reflected in the highest α_{eff} and $R(\text{OH})_{\text{OVOCs}}$. $R(\text{OH})_{\text{aromatics}}$ showed in general the lowest contribution to $R(\text{OH})_{\text{eff}}$ with 1 %–9 % with again highest contribution over the Arabian Gulf, the southern Red Sea and the Suez Canal. Luecken et al. (2018) showed that HCHO concentrations over the United States had about the same sensitivity towards aromatic and alkane emissions. Aromatic compounds do not necessarily release HCHO during their oxidation, but they generally can be useful to identify complex anthropogenic emissions, e.g. from ships or the industry sector. These results overall underscore the elevated levels and complexity of air pollution detected over the Arabian Gulf and the Suez Canal. Also, an absolute increase in $R(\text{OH})_x$ is mostly accompanied by an increase in α_{eff} , although the majority of

data points is scattered at low values of α_{eff} , and there is no clear correlation with $R(\text{OH})_{\text{aromatics}}$ and $R(\text{OH})_{\text{alkenes}}$. Our results are not directly comparable to the findings by Luecken et al. (2018), since in their analysis reactions with O_3 (alkenes) and photolysis of HCHO precursors (OVOCs) were included. These sources of HCHO are not represented by $R(\text{OH})_x$ used in our study and additionally our method would be more valuable by “following” an air mass, to account for air mass aging.

The yield of HCHO can also be interpreted as a function of NO_x levels if there are processes (at low NO) that lead to formation of, for example, peroxides rather than HCHO (Wolfe et al., 2016), as already mentioned above. NO also directly affects the availability of OH, first of all as a sink by the formation of nitrous acid (HONO). HONO rapidly regenerates NO and OH by photolysis during the day, which was identified as a major source of daytime background NO_x during AQABA (Friedrich et al., 2021). Additionally, NO enhances the conversion of HO_2 radicals to OH and thus accelerates VOC oxidation (Wolfe et al., 2016). Valin et al. (2016) found that in isoprene-rich regions, the influence of NO_x on HCHO production is primarily due to its feedback on the production of OH. Wolfe et al. (2016) showed that the chemical link between HCHO and isoprene is a strong, nonlinear function of NO_x . They demonstrated an increase in the prompt yield of HCHO by a factor of 3 (from 0.3

to 0.9 ppbv ppbv⁻¹) over the range of observed NO_x (0.1–2 ppbv), while background HCHO increased by a factor of 2 (from 1.6 to 3.3 ppbv ppbv⁻¹). We found a similar trend, as the increased reactivity of alkenes in the southern Red Sea at rather low NO_x (median 0.23 ppbv) was not accompanied by enhanced HCHO mixing ratios, although high values of α_{eff} coincided with elevated NO_x. In general, the impact of NO_x on HCHO production can be reduced to two factors: radical recycling and the termination of RO₂ radicals (Wolfe et al., 2016). The fact that very clean background MBL air was rarely sampled during AQABA (lowest median NO_x of 0.16 ppbv over AS Leg 2) suggests that we hardly achieved conditions in which the production of peroxides through the reaction of CH₃O₂ with HO₂ would dominate the production of HCHO through CH₃O₂ + NO. Tadic et al. (2020) also showed that most regions were in the O₃ production regime (signaling sufficient NO), which indicates that the production of HCHO was more likely limited by the abundance of oxidants and reactive VOCs rather than NO_x.

5 Conclusions

In situ observations of HCHO and its sinks due to reaction with OH, photolysis and dry deposition to the ocean surface have been compared to its production from the reaction of OH with VOCs by using the total OH reactivity (R(OH)) and measured OH concentrations during the AQABA ship campaign around the Arabian Peninsula. Large variation of HCHO mixing ratios about more than an order of magnitude with maximum values (up to ~12 ppbv) in the center of the Arabian Gulf highlight the region as a hotspot of photochemical air pollution with elevated mixing ratios of several VOCs and high amounts of ozone (≥ 150 ppbv; Tadic et al., 2020). Lowest concentrations of HCHO and its precursors identified the Arabian Sea as the cleanest region of the measurement campaign, related to the stable winds of the Indian summer monsoon, originating near the east coast of Africa (Edtbauer et al., 2020). Rather clean air (from a NO_x perspective) was also detected over the southern Red Sea, which showed enhanced alkene and aromatic compound concentrations. In photochemical steady state, compact relationships between HCHO production and loss were found for some regions along the ship route. Excluding inorganic reactivity and non-HCHO-yielding reactions from total R(OH) slightly improved the correlation between production and loss of HCHO. The region-wide yield of HCHO per reacting OH (α_{eff}) differs along the various chemical regimes encountered with lowest values (less than 2%) deduced over the Arabian Sea during the first leg and the southern Red Sea and with highest values (~32%) over the Arabian Gulf. In most regions less than 10% of R(OH)_{eff} contributed to HCHO production. The separation of R(OH)_{eff} into certain compound classes showed that OVOCs had the highest overall contribution to OH reactivity and were most variable.

In general, elevated values of α_{eff} coincided with elevated contributions of alkanes and OVOCs, with highest reactivity of all compound classes over the Arabian Gulf. The increased reactivity of alkenes and aromatic compounds over the southern Red Sea at rather low NO_x (median 0.23 ppbv) was not accompanied by an elevated α_{eff} . A clear dependence of α_{eff} on NO_x could not be identified, although highest values of α_{eff} coincided with elevated NO_x. Future studies on the HCHO budget around the Arabian Peninsula would likely benefit from longer stationary measurements, e.g. to identify the regularity of highly polluted events over the Arabian Gulf and to evaluate diurnal variation.

Data availability. The data used in this study can be accessed for all scientists agreeing to the AQABA protocol at <https://doi.org/10.5281/zenodo.3354117> (Pfanterstill et al., 2019) and through the KEEPER service of the Max Planck Digital Library via the person responsible on request.

Supplement. The supplement related to this article is available online at: <https://doi.org/10.5194/acp-21-17373-2021-supplement>.

Author contributions. HF and DD designed the study. DD and BH performed the HCHO measurements. IT and UP provided the NO_x measurements. RR, ST, MM and HH performed the LIF OH and HO₂ measurements during AQABA. EP and NW provided the OH reactivity measurements. NW, AE and CS were responsible for the OVOC measurements. EB and LE carried out the VOC measurements during AQABA, which were used together with the OVOCs by EP to calculate speciated OH reactivity. JW supervised the VOC, OVOC and OH reactivity measurements. PE and JNC performed the O₃ and SO₂ measurements during AQABA. JS and JNC provided the actinic flux measurements and calculated photolysis rates. JL designed and supervised the AQABA project.

Competing interests. The authors declare that they have no conflict of interest.

Disclaimer. Publisher's note: Copernicus Publications remains neutral with regard to jurisdictional claims in published maps and institutional affiliations.

Acknowledgements. We thankfully acknowledge the cooperation with The Cyprus Institute (CyI), King Abdullah University of Science and Technology (KAUST) and Kuwait Institute for Scientific Research (KISR). We thank Hays Ships Ltd., captain Pavel Kirzner and the *Kommandor Iona's* ship crew for the great support during all weather or wavy conditions and for an unforgettable time on board. We would like to especially thank Marcel Dorf and Claus Koepfel for the organization of the campaign and Hartwig Harder for the management on board. Last but not least we are grateful

for the whole AQABA community for a successful campaign. Efstratios Bourtsoukidis, Jonathan Williams and Jos Lelieveld additionally acknowledge the European Union's Horizon 2020 Research and Innovation Programme, as well as matching co-funding by the government of the Republic of Cyprus.

Financial support. The AQABA campaign was funded by the Max Planck Society. Efstratios Bourtsoukidis, Jonathan Williams and Jos Lelieveld were supported by the EMME-CARE project from the European Union's Horizon 2020 Research and Innovation Programme (grant agreement no. 856612), as well as matching co-funding by the government of the Republic of Cyprus.

The article processing charges for this open-access publication were covered by the Max Planck Society.

Review statement. This paper was edited by John Orlando and reviewed by two anonymous referees.

References

- Akagi, S. K., Yokelson, R. J., Wiedinmyer, C., Alvarado, M. J., Reid, J. S., Karl, T., Crouse, J. D., and Wennberg, P. O.: Emission factors for open and domestic biomass burning for use in atmospheric models, *Atmos. Chem. Phys.*, 11, 4039–4072, <https://doi.org/10.5194/acp-11-4039-2011>, 2011.
- Anderson, D. C., Nicely, J. M., Wolfe, G. M., Hanisco, T. F., Salawitch, R. J., Canty, T. P., Dickerson, R. R., Apel, E. C., Baidar, S., Bannan, T. J., Blake, N. J., Chen, D., Dix, B., Fernandez, R. P., Hall, S. R., Hornbrook, R. S., Huey, L. G., Josse, B., Jöckel, P., Kinnison, D. E., Koenig, T. K., Le Breton, M., Maréchal, V., Morgenstern, O., Oman, L. D., Pan, L. L., Percival, C., Plummer, D., Revell, L. E., Rozanow, E., Saiz-Lopez, A., Stenke, A., Sudo, K., Tilmes, S., Ullmann, K., Volkamer, R., Weinheimer, A. J. and Zeng, G.: Formaldehyde in the tropical western Pacific: Chemical sources and sinks, convective transport, and representation in CAM-Chem and the CCM1 models, *J. Geophys. Res.-Atmos.*, 122, 11, 201–11, 226, <https://doi.org/10.1002/2016JD026121>, 2017.
- Ayers, G. P., Gillet, R. W., Granek, H., de Sreves, C., and Cox, R. A.: Formaldehyde production in clean marine air, *Geophys. Res. Lett.*, 24, 401–404, <https://doi.org/10.1029/97GL00123>, 1997.
- Bohn, B., Corlett, G. K., Gillmann, M., Sanghavi, S., Stange, G., Tensing, E., Vrekoussis, M., Bloss, W. J., Clapp, L. J., Kortner, M., Dorn, H.-P., Monks, P. S., Platt, U., Plass-Dülmer, C., Mihalopoulos, N., Heard, D. E., Clemitshaw, K. C., Meixner, F. X., Prevot, A. S. H., and Schmitt, R.: Photolysis frequency measurement techniques: results of a comparison within the ACCENT project, *Atmos. Chem. Phys.*, 8, 5373–5391, <https://doi.org/10.5194/acp-8-5373-2008>, 2008.
- Bourtsoukidis, E., Ernle, L., Crowley, J. N., Lelieveld, J., Paris, J.-D., Pozzer, A., Walter, D., and Williams, J.: Non-methane hydrocarbon (C₂–C₈) sources and sinks around the Arabian Peninsula, *Atmos. Chem. Phys.*, 19, 7209–7232, <https://doi.org/10.5194/acp-19-7209-2019>, 2019.
- Celik, S., Drewnick, F., Fachinger, F., Brooks, J., Darbyshire, E., Coe, H., Paris, J.-D., Eger, P. G., Schuladen, J., Tadic, I., Friedrich, N., Dienhart, D., Hottmann, B., Fischer, H., Crowley, J. N., Harder, H., and Borrmann, S.: Influence of vessel characteristics and atmospheric processes on the gas and particle phase of ship emission plumes: in situ measurements in the Mediterranean Sea and around the Arabian Peninsula, *Atmos. Chem. Phys.*, 20, 4713–4734, <https://doi.org/10.5194/acp-20-4713-2020>, 2020.
- Coggon, M. M., Lim, C. Y., Koss, A. R., Sekimoto, K., Yuan, B., Gilman, J. B., Hagan, D. H., Selimovic, V., Zarzana, K. J., Brown, S. S., Roberts, J. M., Müller, M., Yokelson, R., Wisthaler, A., Krechmer, J. E., Jimenez, J. L., Cappa, C., Kroll, J. H., de Gouw, J., and Warneke, C.: OH chemistry of non-methane organic gases (NMOGs) emitted from laboratory and ambient biomass burning smoke: evaluating the influence of furans and oxygenated aromatics on ozone and secondary NMOG formation, *Atmos. Chem. Phys.*, 19, 14875–14899, <https://doi.org/10.5194/acp-19-14875-2019>, 2019.
- Cox, R. A., Ammann, M., Crowley, J. N., Herrmann, H., Jenkin, M. E., McNeill, V. F., Mellouki, A., Troe, J., and Wallington, T. J.: Evaluated kinetic and photochemical data for atmospheric chemistry: Volume VII – Criegee intermediates, *Atmos. Chem. Phys.*, 20, 13497–13519, <https://doi.org/10.5194/acp-20-13497-2020>, 2020.
- De Smedt, I., Müller, J.-F., Stavrou, T., van der A, R., Eskes, H., and Van Roozendaal, M.: Twelve years of global observations of formaldehyde in the troposphere using GOME and SCIAMACHY sensors, *Atmos. Chem. Phys.*, 8, 4947–4963, <https://doi.org/10.5194/acp-8-4947-2008>, 2008.
- De Smedt, I., Van Roozendaal, M., Stavrou, T., Müller, J.-F., Lerot, C., Theys, N., Valks, P., Hao, N., and van der A, R.: Improved retrieval of global tropospheric formaldehyde columns from GOME-2/MetOp-A addressing noise reduction and instrumental degradation issues, *Atmos. Meas. Tech.*, 5, 2933–2949, <https://doi.org/10.5194/amt-5-2933-2012>, 2012.
- De Smedt, I., Stavrou, T., Hendrick, F., Danckaert, T., Vlemmix, T., Pinardi, G., Theys, N., Lerot, C., Gielen, C., Vigouroux, C., Hermans, C., Fayt, C., Veefkind, P., Müller, J.-F., and Van Roozendaal, M.: Diurnal, seasonal and long-term variations of global formaldehyde columns inferred from combined OMI and GOME-2 observations, *Atmos. Chem. Phys.*, 15, 12519–12545, <https://doi.org/10.5194/acp-15-12519-2015>, 2015.
- De Smedt, I., Theys, N., Yu, H., Danckaert, T., Lerot, C., Compernelle, S., Van Roozendaal, M., Richter, A., Hilboll, A., Peters, E., Pedergnana, M., Loyola, D., Beirle, S., Wagner, T., Eskes, H., van Geffen, J., Boersma, K. F., and Veefkind, P.: Algorithm theoretical baseline for formaldehyde retrievals from S5P TROPOMI and from the QA4ECV project, *Atmos. Meas. Tech.*, 11, 2395–2426, <https://doi.org/10.5194/amt-11-2395-2018>, 2018.
- Dienhart, D., Hottmann, B., Crowley, J. N., Eger, P. G., Hafermann, S., Harder, H., Röder, L., Martinez, M., Parchatka, U., Pozzer, A., Rohloff, R., Schuladen, J., Tadic, I., Tauer, S., Walter, D., Lelieveld, J., and Fischer, H.: Formaldehyde (HCHO) and Hydroperoxide distribution around the Arabian Peninsula – A comparison of ship-based measurements with the general circulation model EMAC, *Atmos. Chem. Phys.*, in preparation, 2021.
- DiGangi, J. P., Boyle, E. S., Karl, T., Harley, P., Turnipseed, A., Kim, S., Cantrell, C., Maudlin III, R. L., Zheng, W.,

- Flocke, F., Hall, S. R., Ullmann, K., Nakashima, Y., Paul, J. B., Wolfe, G. M., Desai, A. R., Kajii, Y., Guenther, A., and Keutsch, F. N.: First direct measurements of formaldehyde flux via eddy covariance: implications for missing in-canopy formaldehyde sources, *Atmos. Chem. Phys.*, 11, 10565–10578, <https://doi.org/10.5194/acp-11-10565-2011>, 2011.
- DiGangi, J. P., Henry, S. B., Kammrath, A., Boyle, E. S., Kaser, L., Schnitzhofer, R., Graus, M., Turnipseed, A., Park, J.-H., Weber, R. J., Hornbrook, R. S., Cantrell, C. A., Maudlin III, R. L., Kim, S., Nakashima, Y., Wolfe, G. M., Kajii, Y., Apel, E. C., Goldstein, A. H., Guenther, A., Karl, T., Hansel, A., and Keutsch, F. N.: Observations of glyoxal and formaldehyde as metrics for the anthropogenic impact on rural photochemistry, *Atmos. Chem. Phys.*, 12, 9529–9543, <https://doi.org/10.5194/acp-12-9529-2012>, 2012.
- Duncan, B. N., Yoshida, Y., Olson, J. R., Sillman, S., Martin, R. V., Lamsal, L., Hu, Y., Pickering, K. E., Retscher, C., Allen, D. J., and Crawford, J. H.: Application of OMI observations to a space-based indicator of NO_x and VOC controls on surface ozone formation, *J. Atmos. Env.*, 44, 2213–2223, <https://doi.org/10.1016/j.atmosenv.2010.03.010>, 2010.
- Edtbauer, A., Stöner, C., Pfannerstill, E. Y., Berasategui, M., Walter, D., Crowley, J. N., Lelieveld, J., and Williams, J.: A new marine biogenic emission: methane sulfonamide (MSAM), dimethyl sulfide (DMS), and dimethyl sulfone (DMSO₂) measured in air over the Arabian Sea, *Atmos. Chem. Phys.*, 20, 6081–6094, <https://doi.org/10.5194/acp-20-6081-2020>, 2020.
- Eger, P. G., Friedrich, N., Schuladen, J., Shenolikar, J., Fischer, H., Tadic, I., Harder, H., Martinez, M., Rohloff, R., Tauer, S., Drewnick, F., Fachinger, F., Brooks, J., Darbyshire, E., Sciare, J., Pikridas, M., Lelieveld, J., and Crowley, J. N.: Shipborne measurements of ClNO₂ in the Mediterranean Sea and around the Arabian Peninsula during summer, *Atmos. Chem. Phys.*, 19, 12121–12140, <https://doi.org/10.5194/acp-19-12121-2019>, 2019.
- Fortems-Cheiney, A., Chevallier, F., Pison, I., Bousquet, P., Saunio, M., Szopa, S., Cressot, C., Kurosu, T. P., Chance, K., and Fried, A.: The formaldehyde budget as seen by a global-scale multi-constraint and multi-species inversion system, *Atmos. Chem. Phys.*, 12, 6699–6721, <https://doi.org/10.5194/acp-12-6699-2012>, 2012.
- Fried, A., Cantrell, C., Olson, J., Crawford, J. H., Weibring, P., Walega, J., Richter, D., Junkermann, W., Volkamer, R., Sinreich, R., Heikes, B. G., O'Sullivan, D., Blake, D. R., Blake, N., Meinardi, S., Apel, E., Weinheimer, A., Knapp, D., Perrin, A., Cohen, R. C., Fuelberg, H., Shetter, R. E., Hall, S. R., Ullmann, K., Brune, W. H., Mao, J., Ren, X., Huey, L. G., Singh, H. B., Hair, J. W., Riemer, D., Diskin, G., and Sachse, G.: Detailed comparisons of airborne formaldehyde measurements with box models during the 2006 INTEX-B and MILAGRO campaigns: potential evidence for significant impacts of unmeasured and multi-generation volatile organic carbon compounds, *Atmos. Chem. Phys.*, 11, 11867–11894, <https://doi.org/10.5194/acp-11-11867-2011>, 2011.
- Friedrich, N., Eger, P., Shenolikar, J., Sobanski, N., Schuladen, J., Dienhart, D., Hottmann, B., Tadic, I., Fischer, H., Martinez, M., Rohloff, R., Tauer, S., Harder, H., Pfannerstill, E. Y., Wang, N., Williams, J., Brooks, J., Drewnick, F., Su, H., Li, G., Cheng, Y., Lelieveld, J., and Crowley, J. N.: Reactive nitrogen around the Arabian Peninsula and in the Mediterranean Sea during the 2017 AQABA ship campaign, *Atmos. Chem. Phys.*, 21, 7473–7498, <https://doi.org/10.5194/acp-21-7473-2021>, 2021.
- Fuchs, H., Novelli, A., Rolletter, M., Hofzumahaus, A., Pfannerstill, E. Y., Kessel, S., Edtbauer, A., Williams, J., Michoud, V., Dusanter, S., Locoge, N., Zannoni, N., Gros, V., Truong, F., Sarda-Esteve, R., Cryer, D. R., Brumby, C. A., Whalley, L. K., Stone, D., Seakins, P. W., Heard, D. E., Schoemaeker, C., Blocquet, M., Coudert, S., Batut, S., Fittschen, C., Thames, A. B., Brune, W. H., Ernest, C., Harder, H., Müller, J. B. A., Elste, T., Kubistin, D., Andres, S., Bohn, B., Hohaus, T., Holland, F., Li, X., Rohrer, F., Kiendler-Scharr, A., Tillmann, R., Wegener, R., Yu, Z., Zou, Q., and Wahner, A.: Comparison of OH reactivity measurements in the atmospheric simulation chamber SAPHIR, *Atmos. Meas. Tech.*, 10, 4023–4053, <https://doi.org/10.5194/amt-10-4023-2017>, 2017.
- Hens, K., Novelli, A., Martinez, M., Auld, J., Axinte, R., Bohn, B., Fischer, H., Keronen, P., Kubistin, D., Nölscher, A. C., Oswald, R., Paasonen, P., Petäjä, T., Regelin, E., Sander, R., Sinha, V., Sipilä, M., Taraborrelli, D., Tatum Ernest, C., Williams, J., Lelieveld, J., and Harder, H.: Observation and modelling of HO_x radicals in a boreal forest, *Atmos. Chem. Phys.*, 14, 8723–8747, <https://doi.org/10.5194/acp-14-8723-2014>, 2014.
- Kaiser, J., Wolfe, G. M., Bohn, B., Broch, S., Fuchs, H., Ganzeveld, L. N., Gomm, S., Häsel, R., Hofzumahaus, A., Holland, F., Jäger, J., Li, X., Lohse, I., Lu, K., Prévôt, A. S. H., Rohrer, F., Wegener, R., Wolf, R., Mentel, T. F., Kiendler-Scharr, A., Wahner, A., and Keutsch, F. N.: Evidence for an unidentified non-photochemical ground-level source of formaldehyde in the Po Valley with potential implications for ozone production, *Atmos. Chem. Phys.*, 15, 1289–1298, <https://doi.org/10.5194/acp-15-1289-2015>, 2015.
- Klippel, T., Fischer, H., Bozem, H., Lawrence, M. G., Butler, T., Jöckel, P., Tost, H., Martinez, M., Harder, H., Regelin, E., Sander, R., Schiller, C. L., Stickler, A., and Lelieveld, J.: Distribution of hydrogen peroxide and formaldehyde over Central Europe during the HOOVER project, *Atmos. Chem. Phys.*, 11, 4391–4410, <https://doi.org/10.5194/acp-11-4391-2011>, 2011.
- Kluge, F., Hüneke, T., Knecht, M., Lichtenstern, M., Rotermund, M., Schlager, H., Schreiner, B., and Pfeilsticker, K.: Profiling of formaldehyde, glyoxal, methylglyoxal, and CO over the Amazon: normalized excess mixing ratios and related emission factors in biomass burning plumes, *Atmos. Chem. Phys.*, 20, 12363–12389, <https://doi.org/10.5194/acp-20-12363-2020>, 2020.
- Kormann, R., Fischer, H., de Reus, M., Lawrence, M., Brühl, Ch., von Kuhlmann, R., Holzinger, R., Williams, J., Lelieveld, J., Warneke, C., de Gouw, J., Heland, J., Ziereis, H., and Schlager, H.: Formaldehyde over the eastern Mediterranean during MINOS: Comparison of airborne in-situ measurements with 3D-model results, *Atmos. Chem. Phys.*, 3, 851–861, <https://doi.org/10.5194/acp-3-851-2003>, 2003.
- Liebmann, J. M., Müller, J. B. A., Kubistin, D., Claude, A., Holla, R., Plass-Dülmer, C., Lelieveld, J., and Crowley, J. N.: Direct measurements of NO₃ reactivity in and above the boundary layer of a mountaintop site: identification of reactive trace gases and comparison with OH reactivity, *Atmos. Chem. Phys.*, 18, 12045–12059, <https://doi.org/10.5194/acp-18-12045-2018>, 2018.
- Liu, L., Flatøy, F., Ordóñez, C., Braathen, G. O., Hak, C., Junkermann, W., Andreani-Aksoyoglu, S., Mellqvist, J., Galle, B.,

- Prévôt, A. S. H., and Isaksen, I. S. A.: Photochemical modelling in the Po basin with focus on formaldehyde and ozone, *Atmos. Chem. Phys.*, 7, 121–137, <https://doi.org/10.5194/acp-7-121-2007>, 2007.
- Luecken, D. J., Napelenok, S. L., Strum, M., Scheffe, R., and Phillips, S.: Sensitivity of ambient atmospheric formaldehyde and ozone to precursor species and source types across the United States, *Environ. Sci. Technol.*, 52, 4668–4675, <https://doi.org/10.1021/acs.est.7b05509>, 2018.
- Marbach, T., Beirle, S., Platt, U., Hoor, P., Wittrock, F., Richter, A., Vrekoussis, M., Grzegorski, M., Burrows, J. P., and Wagner, T.: Satellite measurements of formaldehyde linked to shipping emissions, *Atmos. Chem. Phys.*, 9, 8223–8234, <https://doi.org/10.5194/acp-9-8223-2009>, 2009.
- Marno, D., Ernest, C., Hens, K., Javed, U., Klimach, T., Martinez, M., Rudolf, M., Lelieveld, J., and Harder, H.: Calibration of an airborne HO_x instrument using the All Pressure Altitude-based Calibrator for HO_x Experimentation (APACHE), *Atmos. Meas. Tech.*, 13, 2711–2731, <https://doi.org/10.5194/amt-13-2711-2020>, 2020.
- Martin, R. V., Fiore, A. M., and Van Donkelaar, A.: Space-based diagnosis of surface ozone sensitivity to anthropogenic emissions, *Geophys. Res. Lett.*, 31, L06120, <https://doi.org/10.1029/2004GL019416>, 2004.
- Martinez, M., Harder, H., Kubistin, D., Rudolf, M., Bozem, H., Eerdeken, G., Fischer, H., Klüpfel, T., Gurk, C., Königstedt, R., Parchatka, U., Schiller, C. L., Stickler, A., Williams, J., and Lelieveld, J.: Hydroxyl radicals in the tropical troposphere over the Suriname rainforest: airborne measurements, *Atmos. Chem. Phys.*, 10, 3759–3773, <https://doi.org/10.5194/acp-10-3759-2010>, 2010.
- Millet, D. B., Jacob, D. J., Boersma, K. F., Fu, T. M., Kurosu, T. P., Chance, K., Heald, C. L., and Guenther, A.: Spatial distribution of isoprene emissions from North America derived from formaldehyde column measurements by the OMI satellite sensor, *J. Geophys. Res.*, 113, D02307, <https://doi.org/10.1029/2007JD008950>, 2008.
- Novelli, A., Hens, K., Tatum Ernest, C., Kubistin, D., Regelin, E., Elste, T., Plass-Dülmer, C., Martinez, M., Lelieveld, J., and Harder, H.: Characterisation of an inlet pre-injector laser-induced fluorescence instrument for the measurement of atmospheric hydroxyl radicals, *Atmos. Meas. Tech.*, 7, 3413–3430, <https://doi.org/10.5194/amt-7-3413-2014>, 2014.
- Palmer, P. I., Jacob, D. J., Fiore, A. M., Martin, R. V., Chance, K., and Kurosu, T. P.: Mapping isoprene emissions over North America using formaldehyde column observations from space, *J. Geophys. Res.*, 108, 4180, <https://doi.org/10.1029/2002JD002153>, 2003.
- Paris, J.-D., Riandet, A., Bourtsoukidis, E., Delmotte, M., Berchet, A., Williams, J., Ernle, L., Tadic, I., Harder, H., and Lelieveld, J.: Shipborne measurements of methane and carbon dioxide in the Middle East and Mediterranean areas and the contribution from oil and gas emissions, *Atmos. Chem. Phys.*, 21, 12443–12462, <https://doi.org/10.5194/acp-21-12443-2021>, 2021.
- Parrish, D. D., Ryerson, T. B., Mellqvist, J., Johansson, J., Fried, A., Richter, D., Walega, J. G., Washenfelder, R. A., de Gouw, J. A., Peischl, J., Aikin, K. C., McKeen, S. A., Frost, G. J., Fehsenfeld, F. C., and Herndon, S. C.: Primary and secondary sources of formaldehyde in urban atmospheres: Houston Texas region, *Atmos. Chem. Phys.*, 12, 3273–3288, <https://doi.org/10.5194/acp-12-3273-2012>, 2012.
- Pfannerstill, E. Y., Wang, N., Edtbauer, A., Bourtsoukidis, E., Crowley, J. N., Dienhart, D., Eger, P. G., Ernle, L., Fischer, H., Hottmann, B., Paris, J.-D., Stönnner, C., Tadic, I., Walter, D., Lelieveld, J., and Williams, J.: Shipborne measurements of total OH reactivity around the Arabian Peninsula and its role in ozone chemistry, *Atmos. Chem. Phys.*, 19, 11501–11523, <https://doi.org/10.5194/acp-19-11501-2019>, 2019.
- Pfannerstill, E. Y., Wang, N., and Williams, J.: Total OH reactivity measured around the Arabian Peninsula July–August 2017, 3.2, Zenodo [data set], <https://doi.org/10.5281/zenodo.3354117>, 2019.
- Reeves, C. E. and Penkett, S. A.: Measurements of peroxides and what they tell us, *Chem. Rev.*, 103, 5199–5218, <https://doi.org/10.1021/cr0205053>, 2003.
- Schroeder, J. R., Crawford, J. H., Fried, A., Walega, J., Weinheimer, A., Wisthaler, A., Müller, M., Mikoviny, T., Chen, G., Shook, M., Blake, D. R., and Tonnesen, G. S.: New insights into the column CH₂O/NO₂ ratio as an indicator of near-surface ozone sensitivity, *J. Geophys. Res.-Atmos.*, 122, 8885–8907, <https://doi.org/10.1002/2017JD026781>, 2017.
- Shim, C., Wang, Y., Choi, Y., Palmer, P. I., Abbot, D. S., and Chance, K.: Constraining global isoprene emissions with Global Ozone Monitoring Experiment (GOME) formaldehyde column measurements, *J. Geophys. Res.*, 110, D24301, <https://doi.org/10.1029/2004JD005629>, 2005.
- Sinha, V., Williams, J., Crowley, J. N., and Lelieveld, J.: The Comparative Reactivity Method – a new tool to measure total OH Reactivity in ambient air, *Atmos. Chem. Phys.*, 8, 2213–2227, <https://doi.org/10.5194/acp-8-2213-2008>, 2008.
- Stickler, A., Fischer, H., Williams, J., de Reus, M., Sander, R., Lawrence, M. G., Crowley, J. N., and Lelieveld, J.: Influence of summertime deep convection on formaldehyde in the middle and upper troposphere over Europe, *J. Geophys. Res.*, 111, D14308, <https://doi.org/10.1029/2005JD007001>, 2006.
- Stickler, A., Fischer, H., Bozem, H., Gurk, C., Schiller, C., Martinez-Harder, M., Kubistin, D., Harder, H., Williams, J., Eerdeken, G., Yassaa, N., Ganzeveld, L., Sander, R., and Lelieveld, J.: Chemistry, transport and dry deposition of trace gases in the boundary layer over the tropical Atlantic Ocean and the Guyanas during the GABRIEL field campaign, *Atmos. Chem. Phys.*, 7, 3933–3956, <https://doi.org/10.5194/acp-7-3933-2007>, 2007.
- Tadic, I., Crowley, J. N., Dienhart, D., Eger, P., Harder, H., Hottmann, B., Martinez, M., Parchatka, U., Paris, J.-D., Pozzer, A., Rohloff, R., Schuladen, J., Shenolikar, J., Tauer, S., Lelieveld, J., and Fischer, H.: Net ozone production and its relationship to nitrogen oxides and volatile organic compounds in the marine boundary layer around the Arabian Peninsula, *Atmos. Chem. Phys.*, 20, 6769–6787, <https://doi.org/10.5194/acp-20-6769-2020>, 2020.
- Tegtmeier, S., Marandino, C., Jia, Y., Quack, B., and Mahajan, A. S.: Atmospheric gas-phase composition over the Indian Ocean, *Atmos. Chem. Phys. Discuss.* [preprint], <https://doi.org/10.5194/acp-2020-718>, in review, 2020.
- Valin, L. C., Fiore, A. M., Chance, K., and González Abad, G.: The role of OH production in interpreting the variability of CH₂O

- columns in the southeast U.S., *J. Geophys. Res.-Atmos.*, 121, 478–493, <https://doi.org/10.1002/2015JD024012>, 2016.
- Volkamer, R., Sheehy, P., Molina, L. T., and Molina, M. J.: Oxidative capacity of the Mexico City atmosphere – Part 1: A radical source perspective, *Atmos. Chem. Phys.*, 10, 6969–6991, <https://doi.org/10.5194/acp-10-6969-2010>, 2010.
- Wagner, V., von Glasow, R., Fischer, H., and Crutzen, P. J.: Are CH₂O measurements in the marine boundary layer suitable for testing the current understanding of CH₄ photooxidation?: A model study, *J. Geophys. Res.*, 107, ACH 3-1–ACH 3-14, <https://doi.org/10.1029/2001JD000722>, 2002.
- Wang, N., Edtbauer, A., Stöner, C., Pozzer, A., Bourtsoukidis, E., Ernle, L., Dienhart, D., Hottmann, B., Fischer, H., Schuladen, J., Crowley, J. N., Paris, J.-D., Lelieveld, J., and Williams, J.: Measurements of carbonyl compounds around the Arabian Peninsula: overview and model comparison, *Atmos. Chem. Phys.*, 20, 10807–10829, <https://doi.org/10.5194/acp-20-10807-2020>, 2020.
- Weller, R., Schrems, O., Boddenberg, A., Gäb, S., and Gautrois, M.: Meridional distribution of hydroperoxides and formaldehyde in the marine boundary layer of the Atlantic (48° N–35° S) measured during the Albatross campaign, *J. Geophys. Res.*, 105, 14401–14412, <https://doi.org/10.1029/1999JD901145>, 2000.
- Wennberg, P. O., Bates, K. H., Crounse, J. D., Dodson, L. G., McVay, R. C., Mertens, L. A., Nguyen, T. B., Praske, E., Schwantes, R. H., Smarte, M. D., St Clair, J. M., Teng, A. P., Zhang, X., and Seinfeld, J. H.: Gas-Phase Reactions of Isoprene and Its Major Oxidation Products, *Chem. Rev.*, 118, 3337–3390, <https://doi.org/10.1021/acs.chemrev.7b00439>, 2018.
- Williams, J. and Brune, W.: A roadmap for OH reactivity research, *Atmos. Environ.*, 106, 371–372, <https://doi.org/10.1016/j.atmosenv.2015.02.017>, 2015.
- Whalley, L. K., Furneaux, K. L., Goddard, A., Lee, J. D., Mahajan, A., Oetjen, H., Read, K. A., Kaaden, N., Carpenter, L. J., Lewis, A. C., Plane, J. M. C., Saltzman, E. S., Wiedensohler, A., and Heard, D. E.: The chemistry of OH and HO₂ radicals in the boundary layer over the tropical Atlantic Ocean, *Atmos. Chem. Phys.*, 10, 1555–1576, <https://doi.org/10.5194/acp-10-1555-2010>, 2010.
- Wolfe, G. M., Kaiser, J., Hanisco, T. F., Keutsch, F. N., de Gouw, J. A., Gilman, J. B., Graus, M., Hatch, C. D., Holloway, J., Horowitz, L. W., Lee, B. H., Lerner, B. M., Lopez-Hilfiker, F., Mao, J., Marvin, M. R., Peischl, J., Pollack, I. B., Roberts, J. M., Ryerson, T. B., Thornton, J. A., Veres, P. R., and Warneke, C.: Formaldehyde production from isoprene oxidation across NO_x regimes, *Atmos. Chem. Phys.*, 16, 2597–2610, <https://doi.org/10.5194/acp-16-2597-2016>, 2016.
- Wolfe, G. M., Nicely, J. M., St. Clair, J. M., Hanisco, T. F., Liao, J., Oman, L. D., Brune, W. B., Miller, D., Thames, A., Gonzalez Abad, G., Ryerson, T. B., Thompson, C. R., Peischl, J., McCain, K., Sweeney, C., Wennberg, P. O., Kim, M., Crounse, J. D., Hall, S. R., Ullmann, K., Diskin, G., Bui, P., Chang, C., and Dean-Day, J.: Mapping hydroxyl variability throughout the global remote troposphere via synthesis of airborne and satellite formaldehyde observations, *P. Natl. Acad. Sci. USA*, 116, 11171–11180, <https://doi.org/10.1073/pnas.1821661116>, 2019.
- York, D., Evensen, N. M., Lopez Martinez, M., and De Basabe Delgado, J.: Unified equations for the slope, intercept, and standard errors of the best straight line, *Am. J. Phys.*, 72, 367–375, <https://doi.org/10.1119/1.1632486>, 2004.
- Zhu, L., González Abad, G., Nowlan, C. R., Chan Miller, C., Chance, K., Apel, E. C., DiGangi, J. P., Fried, A., Hanisco, T. F., Hornbrook, R. S., Hu, L., Kaiser, J., Keutsch, F. N., Permar, W., St. Clair, J. M., and Wolfe, G. M.: Validation of satellite formaldehyde (HCHO) retrievals using observations from 12 aircraft campaigns, *Atmos. Chem. Phys.*, 20, 12329–12345, <https://doi.org/10.5194/acp-20-12329-2020>, 2020.

4.4 Case Study: The Arabian Gulf

As already addressed in section 4.2, the air masses encountered in the center of the Arabian Gulf during the first leg showed the highest mixing ratios of HCHO and ROOH during AQABA, with up to 12.3 ppb_v HCHO and 2.3 ppb_v ROOH, while only a slight increase of H₂O₂ was detected (0.4 ppb_v). Severe air pollution was encountered in these air masses with more than 100 ppb_v of O₃ for about 24 h, reaching maximum values of up to 167.4 ppb_v of O₃ during night with a mean ($\pm 1\sigma$) of 74.0 ± 9.2 ppb_v. Besides HCHO and ROOH, simultaneously elevated mixing ratios of several other VOCs, such as acetaldehyde, acetone, methanol, ethene and isoprene were detected. This air pollution plume during the first leg can be subdivided into two major events on the basis of maximum O₃ mixing ratios (Fig. 32, 1. & 2. event), with the highest HCHO, ROOH and OVOC mixing ratios during the second event. A further, less pronounced O₃ event was encountered while passing Dubai with up to 103 ppb_v of O₃, but no significant increases of HCHO, ROOH and OVOCs were detected in this air mass. The change of the chemical composition during the first leg is display in Fig. 33.

The HYSPLIT trajectories indicate that these air masses were mainly transported from Iraq, passing the corridor between Kuwait and Iran, with some winds originating from the coastline of Iran. The height profiles of the trajectories did not indicate significant convection, so that they can be used to identify local sources through horizontal transport. Most oil refineries in the region are operating on the west coast of the Arabian Gulf (section 3.1, Fig. 23), but strong contributions of flaring emissions have been detected all around the coastline of the Gulf on the basis of satellite observations (Fig. 36).

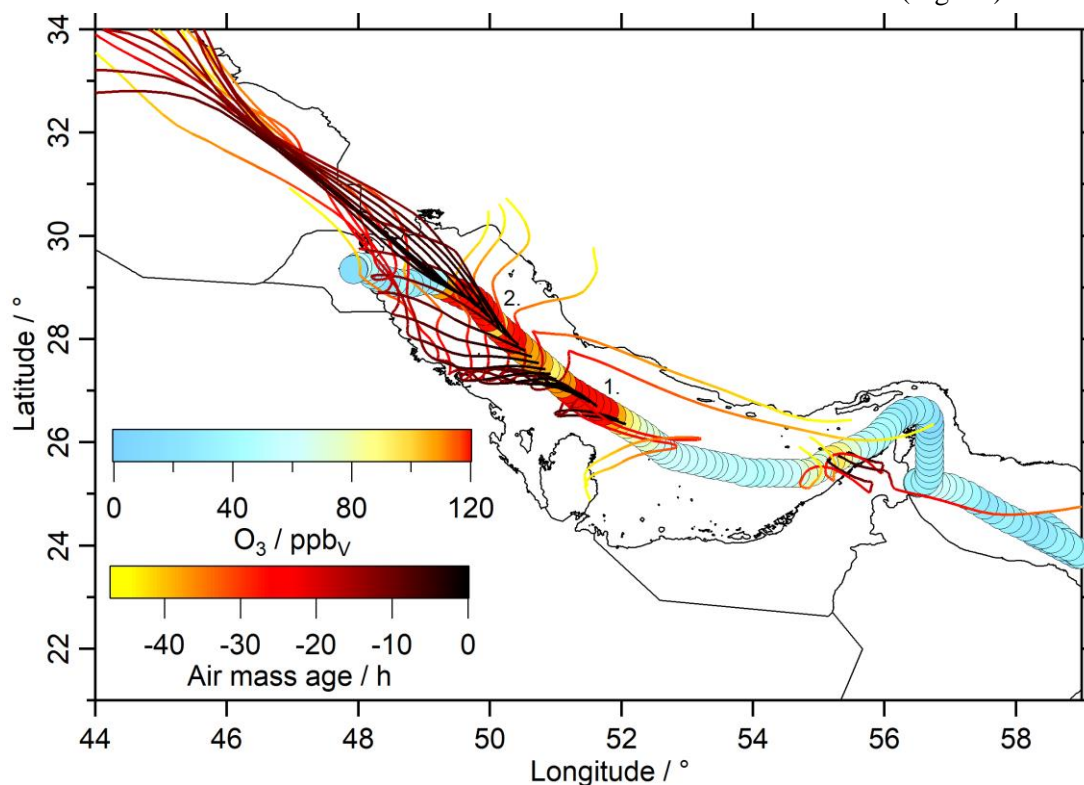


Figure 32: O₃ observations highlight two air pollution maxima (1. & 2. event) in the center of the Arabian Gulf during the first leg. HYSPLIT trajectories indicate mainly transport from Iraq during the high O₃ conditions with less influence of the Iranian coastline.

Just before the high O₃ event, a sharp increase of ROOH (~1 ppb_v), acetaldehyde (~4 ppb_v) and acetone (~8 ppb_v) was detected, with no significant increase of NO_x, HCHO or O₃. According to HYSPLIT, this air mass was transported from Qatar (Fig. 32), and likely contained emissions of a strong local source. The first O₃ event (Fig. 32, 1.) was observed during night and contained heavily elevated O₃ (~167 ppb_v), ethene (~3 ppb_v) and HCHO (~8 ppb_v) and originated from Iraq, Kuwait and the Saudi Arabian

coastline. Mixing ratios of acetone, acetaldehyde and ROOH were slightly decreased in this air mass, but still elevated compared to the other regions during AQABA. O₃, ethene and HCHO then declined again to a local minimum (90 ppb_v of O₃) in air masses which were influenced by the Iranian coast on the morning of the 30.07.2017. Subsequently, the highest mixing ratios of HCHO (~12 ppb_v), ROOH (~2 ppb_v), ethene (~4 ppb_v), isoprene (~0.8 ppb_v), acetaldehyde (~6 ppb_v), methanol (~4 ppb_v) and methane (~2 ppm_v) were detected in highly contaminated winds from Iraq (Fig. 32, 2.), with relatively low levels of NO_x compared to other pollution events (≤ 5 ppb_v). These air masses also contained high levels of HO₂ (~11 ppt_v), but simultaneously decreased OH compared to the other days of the Arabian Gulf.

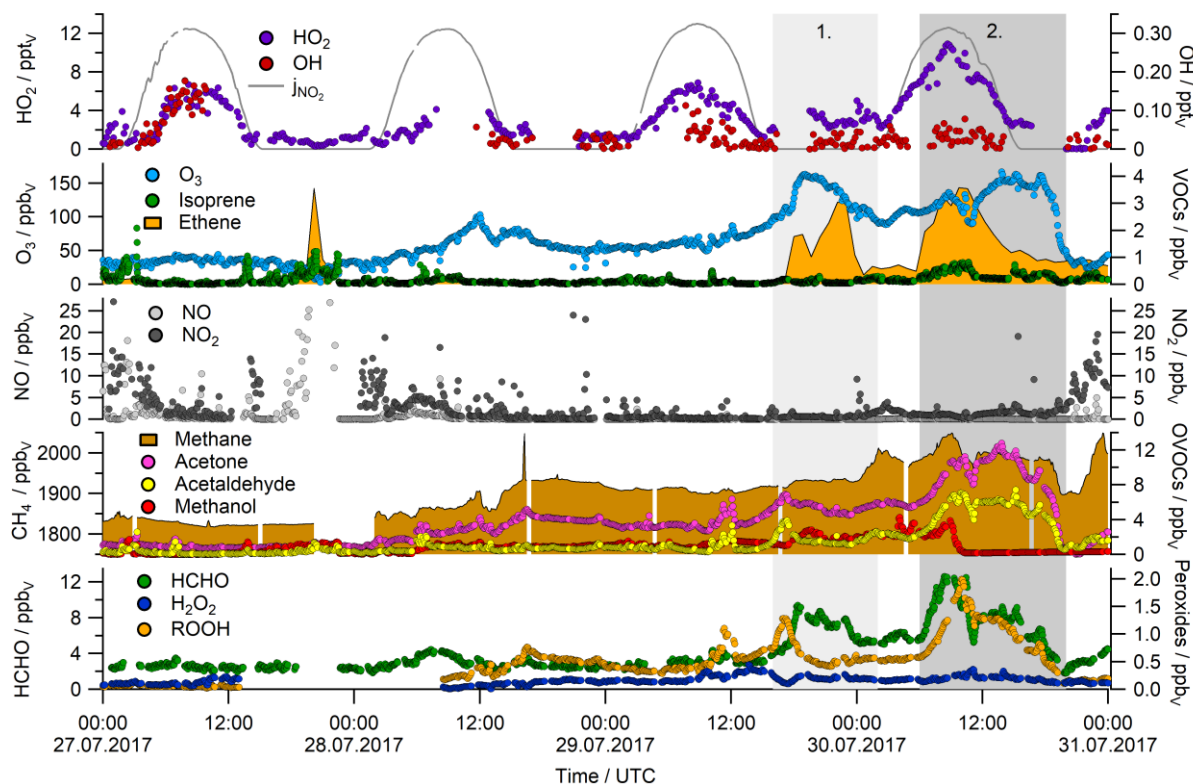


Figure 33: Trace gas observations during the first leg highlight the complexity and variability of air pollution over the Arabian Gulf, with two major air pollution events and the highest O₃ mixing ratios during AQABA.

Enhanced organic peroxides reflect the abundance of RO₂, which was also shown by Tadic et al. (2020), who calculated the highest values of RO₂ + HO₂ over the Arabian Gulf. Pfannerstill et al. (2019) also determined immense OH reactivity in this air mass ($22.1 \pm 7.2 \text{ s}^{-1}$). The complex mixture of elevated CH₄, unsaturated VOCs, OVOCs and O₃ could be an indication for emissions related to combustion processes of the oil and gas industry, e.g. due to gas flaring on the extraction sites. The suppressed OH with simultaneously high levels of HO₂, O₃ and VOCs, but rather low NO (mean of 83 ppt_v on the 30.07.) shows, that even though highly efficient primary production and photochemical recycling of OH (due to reactions of NO + HO₂, NO + RO₂ or O₃ + HO₂) are expected, the OH production could not compete for the elevated consumption of OH. This leads to the assumption that OH recycling was inefficient, which could be the case when radical self-reactions compete with NO_x recycling, e.g. high reactivity of HO₂ + RO₂, which is supported by the elevated mixing ratios of ROOH.

The second leg of AQABA started on the 03.08. and shortly after leaving the harbor of Kuwait, we detected drastically enhanced O₃ with maximum mixing ratios of up to 170 ppb_v, similar to the air pollution event of the first leg. This event had similar characteristics with highly elevated mixing ratios of HCHO, ROOH, acetone, acetaldehyde and ethene (Fig 34). The determination of the air mass origin with HYSPLIT revealed, that we again detected winds from Iraq and the western coastline of the Gulf

(Fig. 35, 3. event). This area seems to be a hotspot of VOC emission, as e.g. ethene and HCHO have rather short lifetimes during the day (~several hours) due to oxidation by OH and O₃. This event was only detected for a few hours, then the air mass origin changed to easterly winds coming from the Iranian Zagros Mountains (Fig. 35, 4. event), which were in general less polluted, but still contained elevated O₃ compared to clean regions (in the range of 70 – 100 ppb_v). O₃ mixing ratios then increased again in air masses originating from the border between Iraq and Iran (Fig. 35, 5. event), with up to 144 ppb_v of O₃. This air mass was detected during night and it contained high levels of OVOCs (HCHO, acetaldehyde, acetone) but decreased amounts of unsaturated hydrocarbons compared to the other events (1. – 3.). This leads to the assumption that we detected aged pollution and / or influence of combustion e.g. due to natural gas flaring. This is supported by elevated mixing ratios of CH₄ with more than 2 ppm_v during these events (2., 3., 5. event). Air masses over the Arabian Gulf were in general influenced by elevated amounts of CH₄, with more than 1.9 ppm_v for both legs, which then decreased after leaving the Gulf.

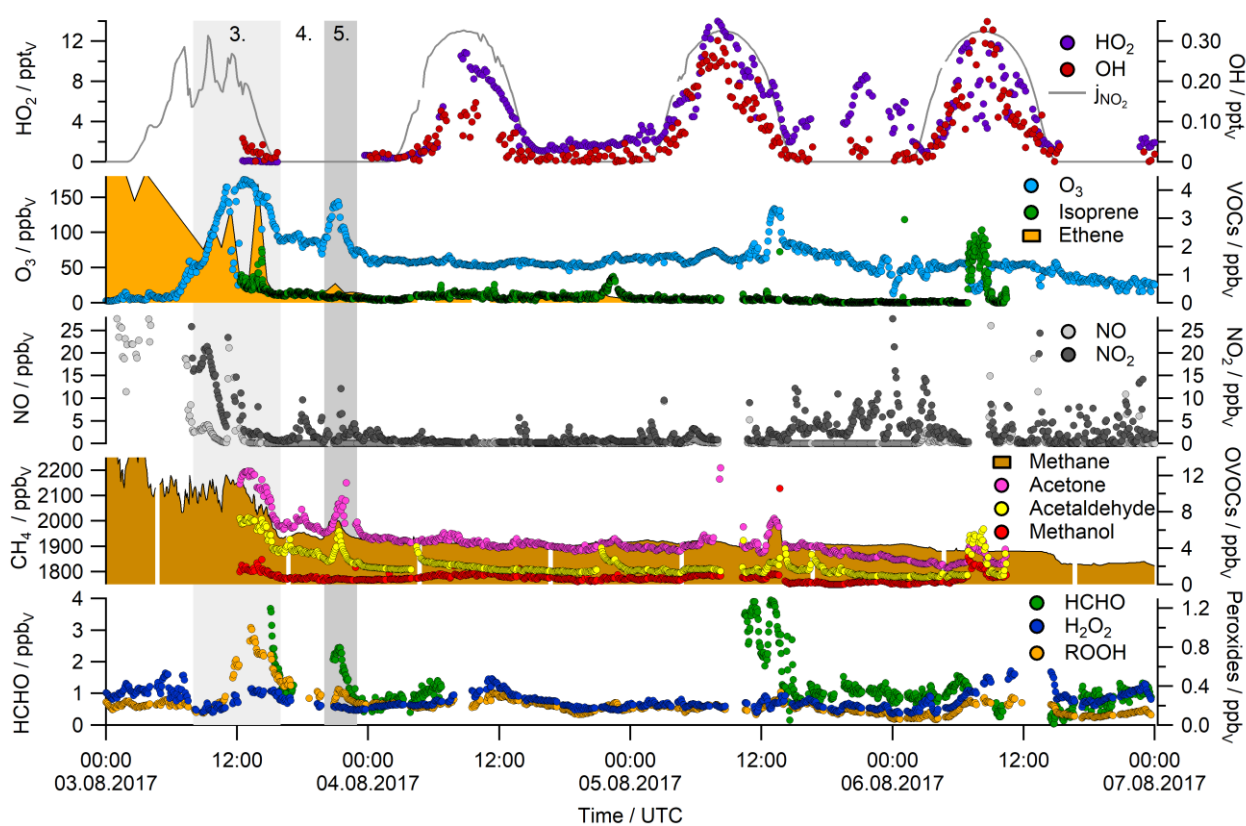


Figure 34: Trace gas observations over the Arabian Gulf during the second leg. Further air pollution events were encountered after leaving the harbor of Kuwait, with elevated O₃, HCHO, ROOH and several other VOCs.

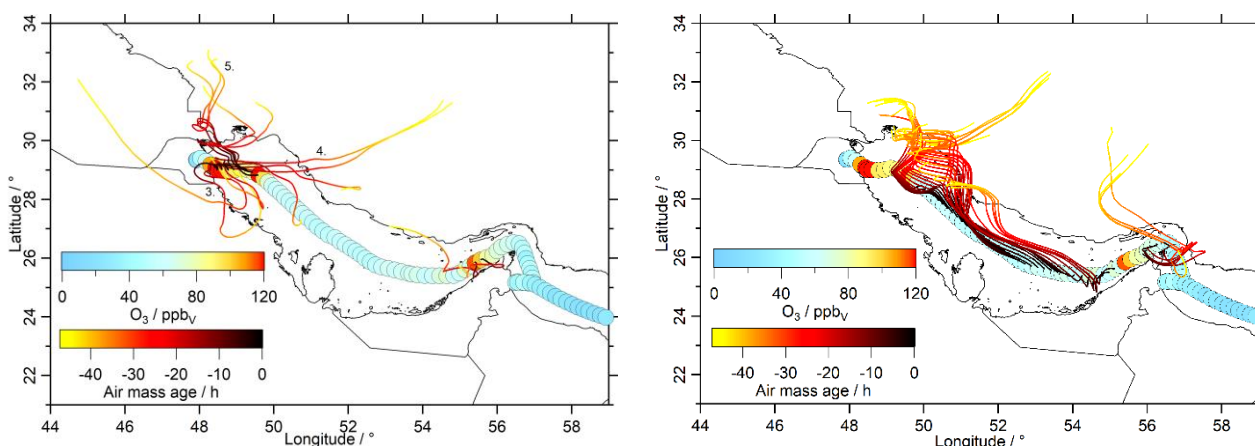


Figure 35: O₃ measurements and HYSPLIT air mass trajectories for the Arabian Gulf during the second leg. Further pollution events were encountered after leaving the harbor of Kuwait (left), while the center of the Gulf was characterized by cleaner conditions compared to the first leg, with air masses mostly originating from Iran and the Zagros Mountains (right). Elevated O₃ was again detected while sailing close to Dubai.

After these events we mainly experienced air masses with slow wind speeds coming from the Zagros Mountains and the more rural coastline of Iran during the second leg (Fig. 35, right). These were characterized by decreased O₃ mixing ratios in the range of 45 – 74 ppb_v with a mean of 59 ppb_v and still elevated, but less variable OVOCs. Stronger diurnal variations of OH and HO₂ were observed, also reflected by a regional maximum of H₂O₂ on the 04.08. with up to 0.5 ppb_v. Additionally, the H₂O₂ / ROOH ratio increased to values ≥ 1 , an indication for decreased abundance of RO₂ radicals. To put this into perspective, the first leg was continuously dominated by ROOH (28. – 30.07.). O₃ mixing ratios then increased another time while passing Dubai, which was accompanied by elevated levels of HCHO, acetone, acetaldehyde and CH₄. These short, but very pronounced air pollution events highlight the air pollution potential of local sources in the Arabian Gulf.

Tadic et al. (2020) also derived the highest net ozone production rates during AQABA for the Arabian Gulf with a median of 32 ppb_v d⁻¹, followed by 16 ppb_v d⁻¹ for both the Gulf of Oman and the northern Red Sea including the Suez Canal. Highest values were derived during the air pollution event of the first leg with a median of 83 ppb_v d⁻¹. Additionally, they estimated highest amounts of RO₂ + HO₂ during this event with median values of 180 – 210 ppt_v. Paris et al. (2021) showed flaring sources detected by the NASA / NOAA Visible Infrared Imaging Radiometer Suite during 2017. The here presented air mass origin analysis shows a strong overlap with these flaring sources, with major air pollution transported from Iraq (1. & 2. event), Kuwait and the eastern coast of Saudi Arabia (3. event), and the north-western coastline of Iran (5. event), demonstrating the immense air pollution potential of gas flaring around the Arabian Gulf (Fig. 36).

DeSmedt et al. (2021) presented multi-annual regional maps of HCHO based on TROPOMI satellite observations, which overlap well with the identified gas flaring sources. It thus seems very likely that a majority of the encountered air pollution was caused by natural gas flaring of both on- and offshore platforms (Fig. SU14).

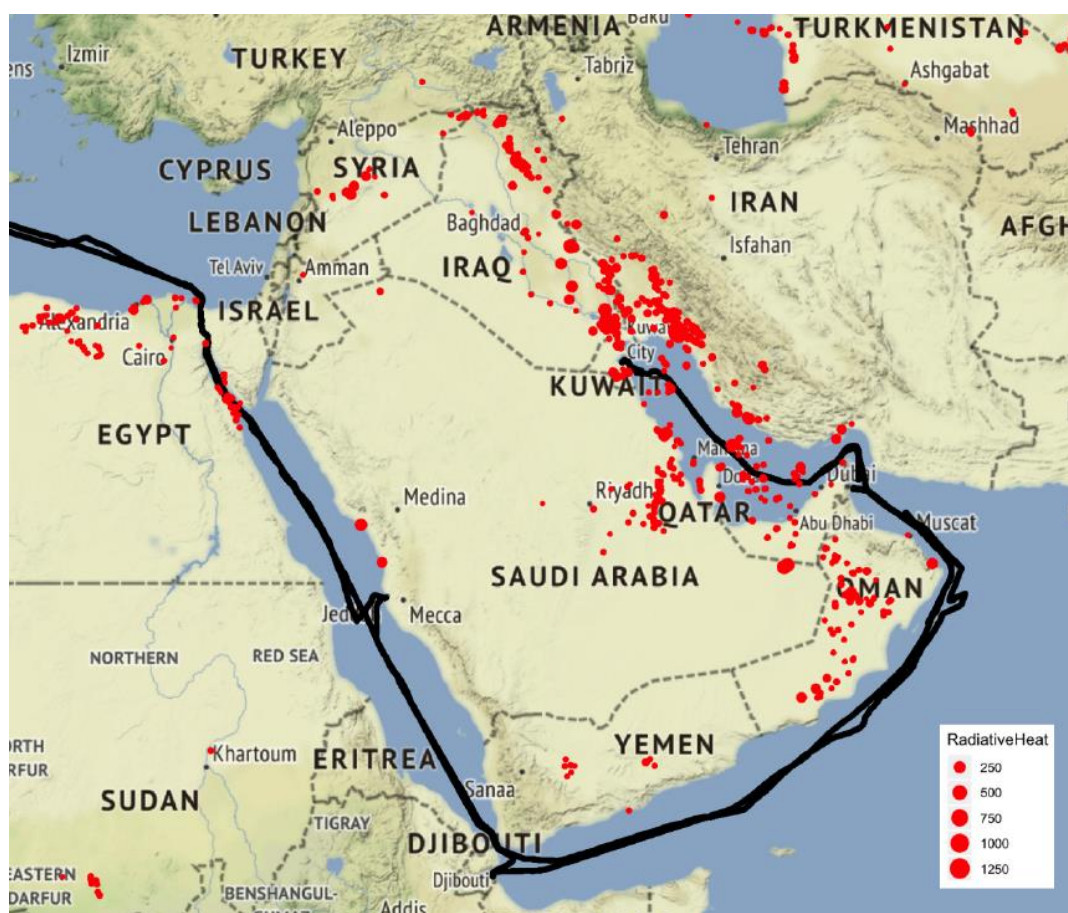


Figure 36: Flaring sources detected by the NASA/NOAA Visible Infrared Imaging Radiometer Suite during 2017 based on Paris et al. (2021). The dot size is proportional to the highest observed radiative heat (in MW), which is related to the total volume of gas flared (Elvidge et al., 2016). Flaring occurs mostly at the upstream production sites and is therefore a proxy for the presence of extraction and production sites. Flaring spots were retrieved from <http://skytruth.org> (last access: 16 April 2019), the background map by ©OpenStreetMap. Distributed under the Open Data Commons Open Database License (ODbL) v1.0.

Photochemical production of O_3 is determined by the reaction of peroxy radicals ($HO_2 + RO_2$) and NO , whereby OH radicals and NO_2 are produced. Photolysis of the generated NO_2 then produces O_3 , so that production of O_3 can either be NO_x or VOC limited. The VOC limit thereby describes that the production of O_3 is controlled by the abundance of peroxy radicals. As a tracer for VOC oxidation, $HCHO$ can here be used as a proxy for the abundance of RO_2 . The $HCHO / NO_2$ – ratio can thus be used to estimate whether net ozone production (NOPR) is VOC or NO_x limited (Tadic et al., 2020; Duncan et al., 2010). Duncan et al. (2010) derived a NO_x limited regime for $HCHO / NO_2 \geq 2$ and a VOC limited regime for $HCHO / NO_2 \leq 1$; in the transition between both of these regimes, both the reduction of VOC or NO_x emissions may lead to a reduction of ozone (Tadic et al., 2020).

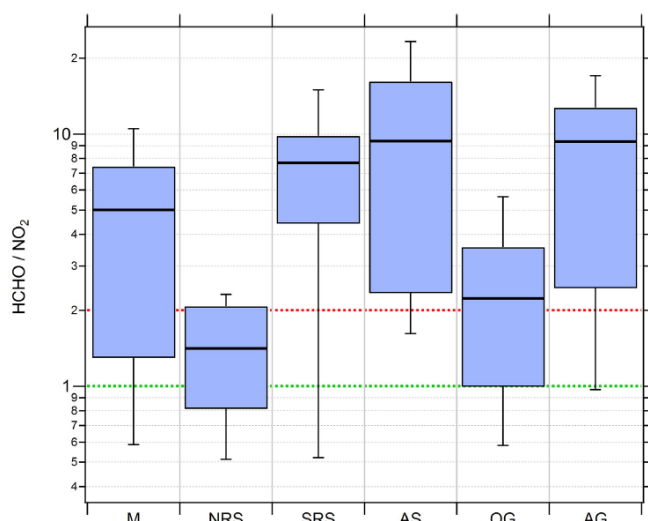


Figure 37: Box and whisker plot of the HCHO / NO₂ ratio as indicator for NO_x (≥ 2 , red line) and VOC (≤ 1 , green line) limitation of ozone production (Duncan et al. 2010) based on Tadic et al. (2020). The black line represents median values, the box 25 – 75 % and the whiskers 10 – 90 % of the data.

The measurements during AQABA show that we rarely encountered air masses in the VOC-limit, with most median HCHO / NO₂ ratios ≥ 2 , only the air masses over the northern Red Sea and the Gulf of Oman classified to be in the transition regime between NO_x and VOC limited ozone production, while none of the medians of the six regions fall below the VOC limit derived by Duncan et al. (2010). NO_x limitation is also observed for the highly polluted Arabian Gulf, where enhanced contribution of NO_x emissions by ships and other combustion processes may lead to more efficient O₃ production (Tadic et al., 2020). Besides HCHO, enhanced ROOH mixing ratios confirmed the abundance of elevated RO₂ radicals.

Furthermore, an additional proxy for the presence of RO₂ was the specification of ROOH with the dual-enzyme HPLC (section 2.2.4). Unfortunately, the instrument only provided qualitative results during AQABA due to a strong interference of the ship movement with the baseline of the chromatograms. Even though no quantification was possible, the chromatograms proved the presence of three organic peroxides besides H₂O₂. These were identified by means of their retention times as methyl hydroperoxide (MHP), peracetic acid (PAA), and ethyl hydroperoxide (EHP) during the third pollution event after leaving the harbor of Kuwait (Fig. 38, 3. event), and indicate that at least three different RO₂ species have been present as ROOH precursors in these air masses.

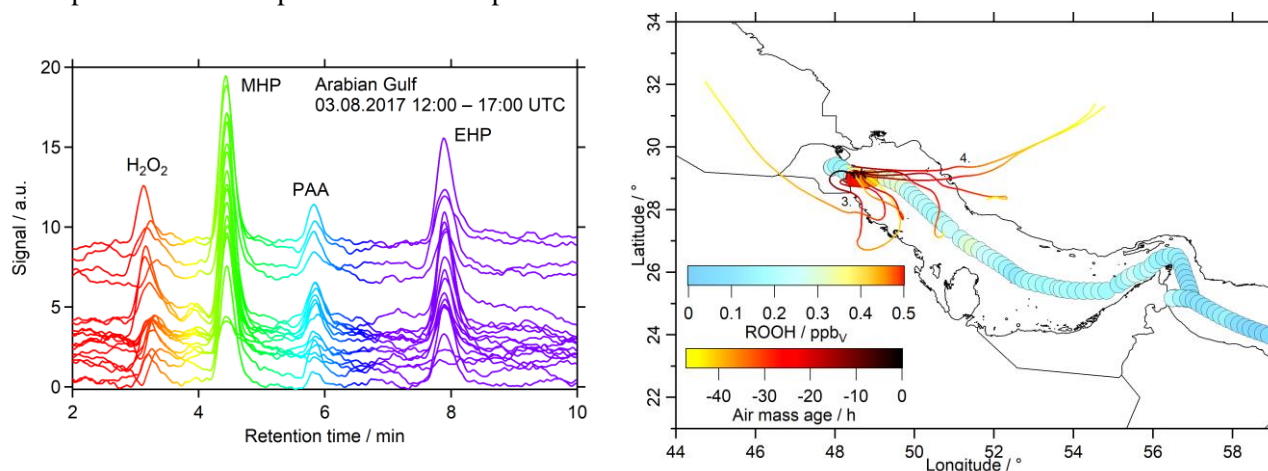


Figure 38: Chromatograms of the HPLC prove the abundance of methyl hydroperoxide (MHP), peracetic acid (PAA) and ethyl hydroperoxide (EHP) in polluted encountered over the Arabian Gulf during the second leg (04.08.17), when we observed winds coming from Iraq and Kuwait (3.). The air masses originating from Iran (4.) did not contain elevated ROOH.

4.4.1 Simulation of the Arabian Gulf with EMAC and WRF-Chem

EMAC results were already compared to the measurements in section 4.2.1, with overall satisfactory results for HCHO (within a factor of 2) and an overestimation of H₂O₂ (more than factor of 5) by EMAC. ROOH were also overestimated on average, even though the model underestimated the organic peroxides over the Arabian Gulf during the high pollution events. EMAC did not simulate significantly elevated ROOH with a mean of 0.33 ± 0.07 ppb_v compared to rest of the dataset (0.28 – 0.35 ppb_v), while the model simulated significantly higher levels of HCHO with 2.26 ± 0.76 ppb_v compared to mean values of 0.59 – 1.53 ppb_v during AQABA. Figure 39 displays that the model did not reproduce the elevated levels of HCHO during the high pollution events of the first leg, which may be due to the coarse resolution of roughly 100 km grids. Therefore, I evaluated a model run of the high resolution model WRF-Chem (Weather Research and Forecasting-Chemistry), which includes atmospheric chemistry, aerosol processes and meteorology. Osipov et al. 2022 configured WRF-Chem to simulate tropospheric chemistry in the Middle East for the domain $6.67^\circ - 45.56^\circ\text{N}$ and $22.92^\circ - 69.66^\circ\text{E}$ at a spatial resolution of 10 km. Gas phase chemistry was based on the Earth System Research Laboratory (ESRL) version of the Regional Atmospheric Chemistry Mechanism (RACM). CH₄ was prescribed with a mixing ratio of 1.8 ppm_v for the domain, while O₃, SO₂, CO and other trace gases were prescribed from the Modern-Era Retrospective analysis for Research and Applications, Version 2 (MERRA-2). Anthropogenic emissions were included with several emission inventories: CAMS-GLOB-SHIPv2.1 (shipping emissions, VOCs), HTAPv2 (VOCs), OMI-HTAPv2 (SO₂) and EDGARv5 (all air pollutants excluding shipping emissions, VOC and industrial SO₂ from the energy industry, combustion, oil refineries etc.), further details are described in Osipov et al. (2022).

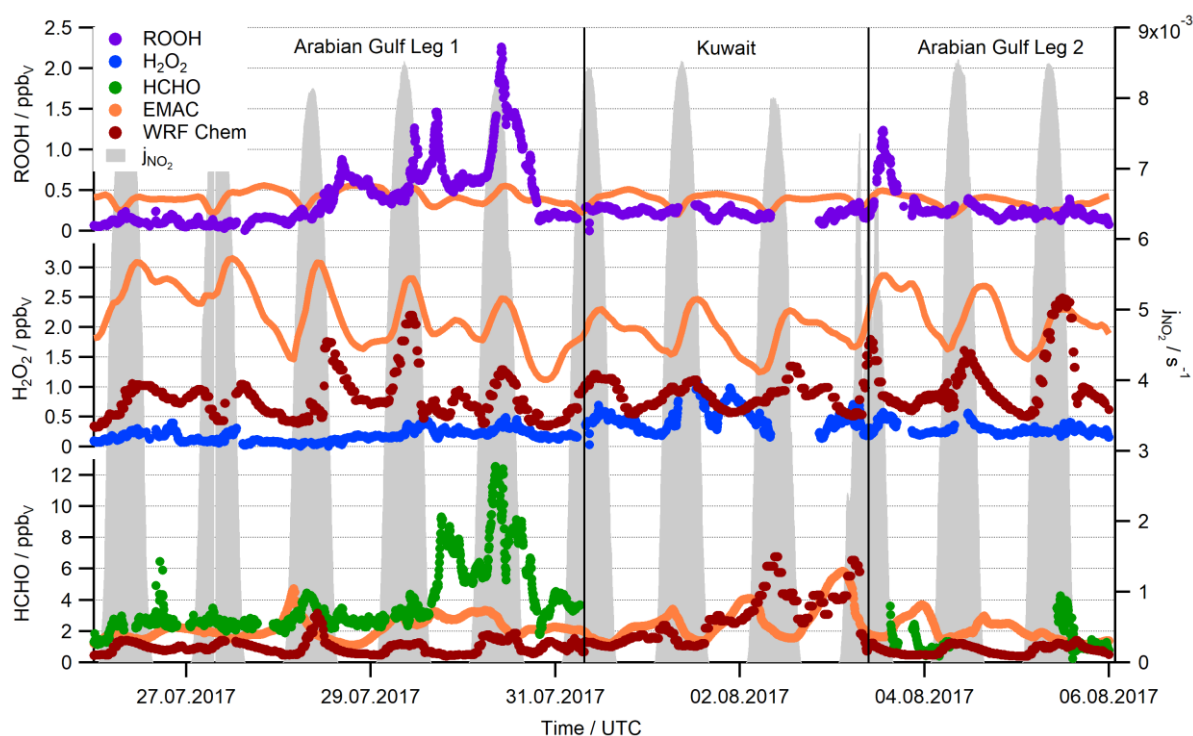


Figure 39: Observations of HCHO (green), H₂O₂ (blue) and ROOH (violet) compared to the EMAC (orange) and WRF-Chem (red) results in 10 minute averages. No ROOH results were available based on WRF-Chem.

WRF-Chem simulated significantly decreased levels of both HCHO and H₂O₂ compared to EMAC, so that the model matches the observations of H₂O₂ mostly within a factor of 4, while it drastically underestimates HCHO (more than a factor of 4). For the merged datasets (only the datapoints when measured data was available), this resulted in mean HCHO ($\pm 1\sigma$) of 0.89 ± 0.36 ppb_v for WRF-Chem,

3.77 ± 2.44 ppb_v for the measurement and 2.26 ± 0.76 ppb_v for EMAC. On average, WRF-Chem thus simulated roughly a factor of 2.5 lower levels of HCHO over the Arabian Gulf compared to EMAC. A similar trend was found for H₂O₂ with 0.93 ± 0.44 ppb_v for WRF-Chem, 0.26 ± 0.15 ppb_v for the measurement and 1.68 ± 0.33 ppb_v for EMAC. Both models overestimated H₂O₂, while the WRF-Chem results were more accurate and matched the observations on average within a factor of 4, while EMAC simulated H₂O₂ almost a factor of 2 higher. Unfortunately, there was no WRF-Chem output available for ROOH.

Despite a ten times higher spatial resolution than EMAC, WRF-Chem was not able to reproduce the air pollution encountered over the Arabian Gulf. The model does not reproduce the enhanced air pollution during the first leg (29. – 30.07.), but it simulated elevated HCHO mixing ratios during the short event while passing Dubai (28.07.). Additionally, WRF-Chem shows an improved agreement with the measurements for the less polluted air masses during the second leg. Simulations of H₂O₂ in WRF-Chem showed strong diurnal cycles with average variations of roughly 0.5 ppb_v. Such strong variations were not observed, but this is a great improvement compared to the extreme daily variations in EMAC (≥ 1.0 ppb_v).

Furthermore, WRF-Chem simulated strong enhancements of O₃ around the Arabian Peninsula, with the highest levels of O₃ over the Arabian Gulf (Fig. 40). The model simulated mean O₃ of 66.3 ± 8.9 ppb_v for the Arabian Gulf, compared to a mean of 74.0 ± 35.7 ppb_v for the measurement and 76.8 ± 12.8 ppb_v for EMAC. Figure 40 shows that WRF-Chem simulated daily maxima of O₃ in the center of the Arabian Gulf and also above Iran and the Zagros Mountains with more than 70 ppb_v. Our observations indicate that air masses from the Zagros Mountains were cleaner than the winds coming from Iraq and Kuwait, but still contained elevated mixing ratios of O₃ in the range of 45 – 74 ppb_v with a mean of 59 ppb_v. Osipov et al. (2022) emphasize the extent of the long-term exposure to O₃ and also NO₂ in the region. The results top the World Health Organization (WHO) seasonal guideline of ~ 30 ppb_v and the daily maxima also exceed the 50 ppb_v limit (<https://www.who.int/news-room/questions-and-answers/item/who-global-air-quality-guidelines>).

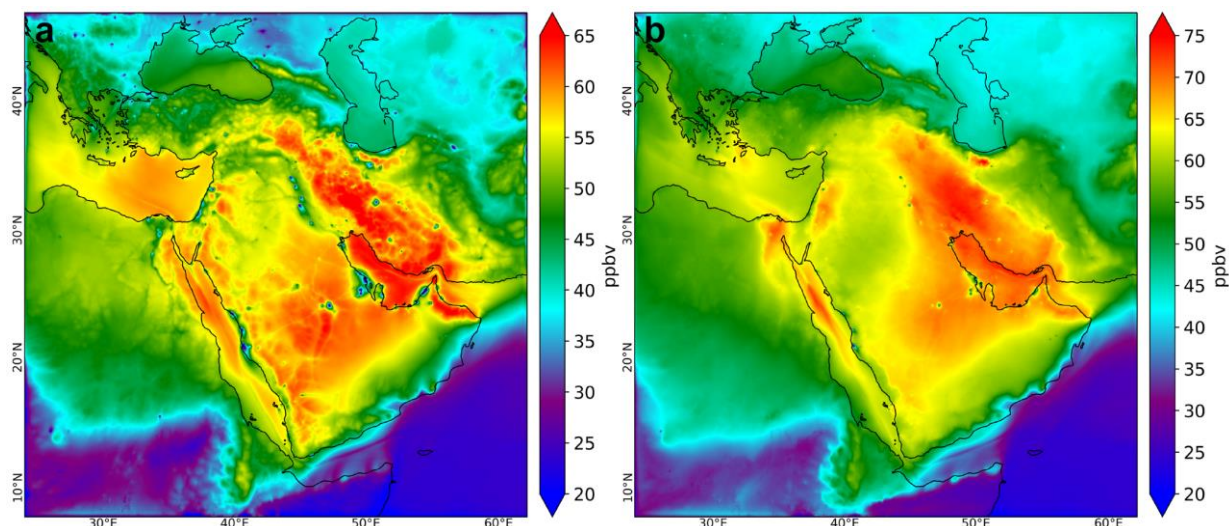


Figure 40: WRF-Chem results for mean O₃ at the surface (a, left) and daily maximum 8-hourly O₃ (b, right) based on Osipov et al. (2022).

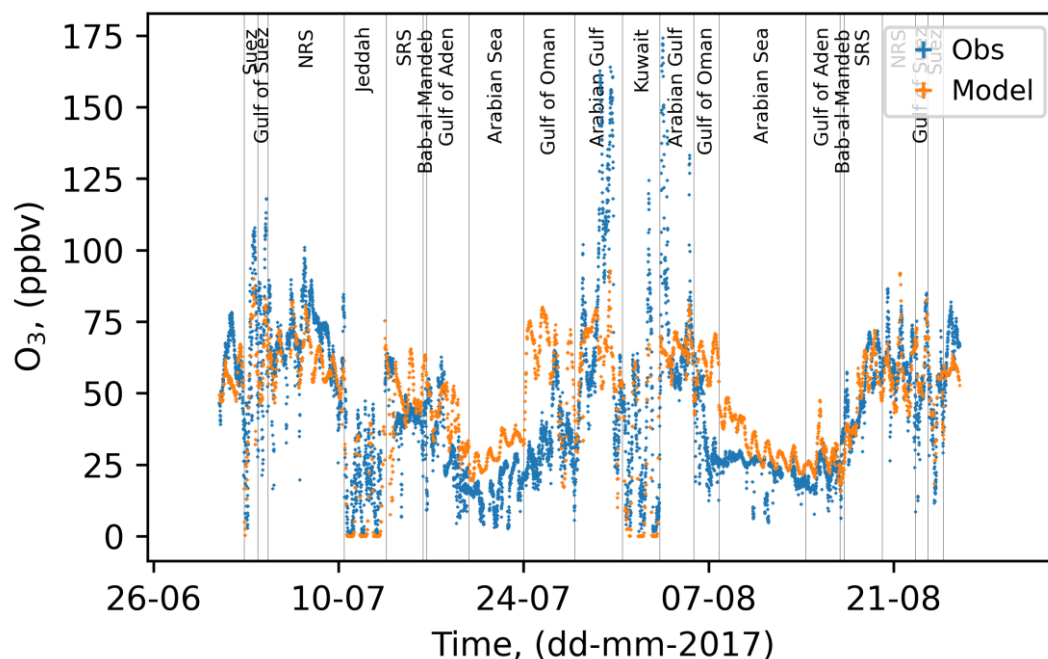


Figure 41: Timeline of the O₃ results based on WRF-Chem (orange, Osipov et al. 2022) compared to the observations (blue).

The timeline in Fig. 41 shows a comparison between WRF-Chem and the O₃ observations and highlights missing sources of O₃ over the Arabian Gulf and the Suez Canal in the model, while it simultaneously overestimated O₃ over the Gulf of Oman and the eastern part of the Arabian Sea. Altogether, WRF-Chem achieved more accurate results than EMAC for rather clean conditions, mainly due to EMAC's overestimation of O₃ over the Arabian Sea (Fig. SU2), while it underperformed EMAC in polluted conditions. This may be related to missing anthropogenic emissions in emission databases or due to missing reactions in the atmospheric chemistry reaction scheme. Similar trends are shown for further trace gases (e.g. HCHO, CO) in the supplement (SU15 – SU21). Another similarity for both atmospheric chemistry models is the overestimation of both OH and HO₂, even though WRF-Chem simulated on average less HO₂ compared to EMAC, which may be related to its missing VOCs (e.g. the underestimated HCHO). Overall the improved resolution of WRF-Chem did not lead to significantly improved results over the Arabian Gulf or the Suez Canal. I recommend an increase of anthropogenic VOC emissions in the emission databases used. Despite the missing air pollution, WRF-Chem simulated more accurate results for H₂O₂ and HCHO in less polluted MBL conditions.

4.5 Cleaner regimes around the Arabian Peninsula

In contrast to the highly polluted air masses over the Arabian Gulf, cleaner MBL conditions were encountered over the Arabian Sea, the southern Red Sea and the Mediterranean Sea. The following chapter describes the abundance of the major trace gases in these regions, evaluates diurnal variation profiles and examines the influence of heterogeneous uptake on dust particles.

4.5.1 Diurnal variation of trace gases

Diurnal variation of trace gases is expected when the respective production and loss terms do not balance, e.g. during noon when the maximum radiation reaches the MBL and OH production rapidly increases. H_2O_2 and HCHO, which are strongly coupled to the abundance of HO_x in clean environments, can then undergo a diurnal variation according to the variability of OH and HO_2 . In particular, H_2O_2 reflects the diurnal variation of HO_x , as its production depends quadratic on HO_2 but its loss only linearly on OH (with the assumption that other processes, e.g. deposition and transport, are constant or do not affect the mixing ratio drastically in the observed air mass). Since we operated on a moving platform, the situation is even more complex due to variability of the air mass origin and generally changing conditions. The best chances for studies of diurnal variation profiles therefore enabled the observations during the stable winds over the Arabian Sea, which had a similar origin for a couple of days, with a longer period during the second leg (08.08. – 12.08.2017) while sailing against the wind. The observed diurnal variations of H_2O_2 , ROOH and HCHO over the Arabian Sea are compared to results of the Mediterranean Sea in Fig. 42.

Only a slight diurnal variation of H_2O_2 was observed over the Arabian Sea, with a maximum of ~ 200 ppt_v around 11 – 12 UTC, resulting in a diurnal variation of only 50 ppt_v, while we observed an average variation of 200 ppt_v over the Mediterranean Sea. Air masses detected over the Mediterranean Sea generally showed higher variability and also a broader maximum during noon. For the organic hydroperoxides we did not observe a diurnal variation over the Arabian Sea with rather stable mean values of ~ 70 ppt_v (± 30 ppt_v), while mixing ratios were mostly in the range of 180 – 300 ppt_v over the Mediterranean Sea. The local maximum at 12 UTC is in line with highest H_2O_2 , although we observed decreased noontime ROOH mean values compared to H_2O_2 , with maxima of ~ 300 ppt_v and ~ 400 ppt_v, respectively. Furthermore, the H_2O_2 observations reflect a higher variability (2σ) of roughly 200 ppt_v compared to ~ 100 ppt_v for ROOH. Preconcentrated injections into the HPLC also proved the abundance of PAA over the Mediterranean Sea (chapter 4.2.2, p. 83).

For HCHO, the observations demonstrate similar mixing ratios over both regions, with a larger variability (2σ) over the Arabian Sea with roughly 600 ppt_v during noon, compared to ~ 400 ppt_v over the Mediterranean Sea. Mean and median values are in the range of 0.6 – 1.2 ppb_v for the Arabian Sea with a less pronounced decline of HCHO compared to the results of the Mediterranean Sea, where mean values decreased to 0.4 ppb_v during night. The increasing mean values during night (23 UTC) were caused by enhanced HCHO while sailing close to the Italian coastline, without this event the 2σ -variability agrees well with the other nights of the Mediterranean Sea. Highest HCHO mixing ratios were observed around 6 – 9 UTC, which is in line with the maximum levels of OH (Fig. 43). Note that the graphs are presented in UTC time, and thus the maxima over the Arabian Sea are shifted by about two hours compared to the results of the Mediterranean Sea (maximum HO_x between 9 – 12 UTC).

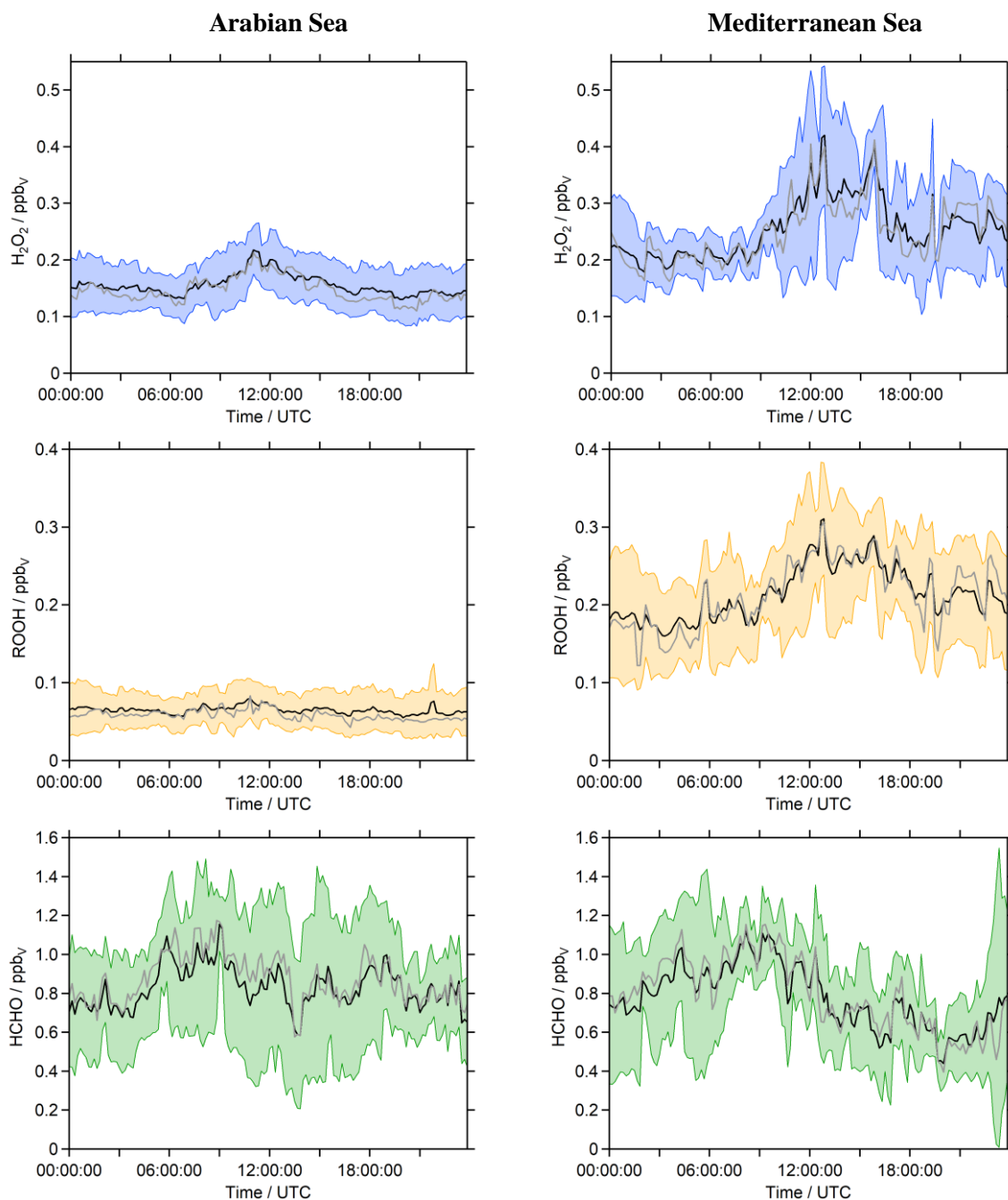


Figure 42: Diurnal variation of H_2O_2 , ROOH and HCHO over the Arabian Sea (08.08. – 13.08.2017) and the Mediterranean Sea (25.08. – 31.08.2017) on the basis of the respective mean (black) and median (grey) values and the general variability within the region ($\pm 1\sigma$) as 10 minute averages.

Mean OH mixing ratios during noon only reached $\sim 0.1 \text{ ppt}_v$ over the Arabian Sea, while OH radicals increased to $\sim 0.3 \text{ ppt}_v$ over the Mediterranean Sea. The same trend is shown by the HO_2 radicals, with mean noontime maxima of $\sim 10 \text{ ppt}_v$ and $\sim 30 \text{ ppt}_v$, respectively. The diurnal variation of HO_2 shows a distinct drop between 7 – 9 UTC on a few days. The significantly elevated HO_x over the Mediterranean Sea reached similar levels compared to the Arabian Sea already by about 6 UTC, and thus the Mediterranean Sea generally represented a more photochemically active regime.

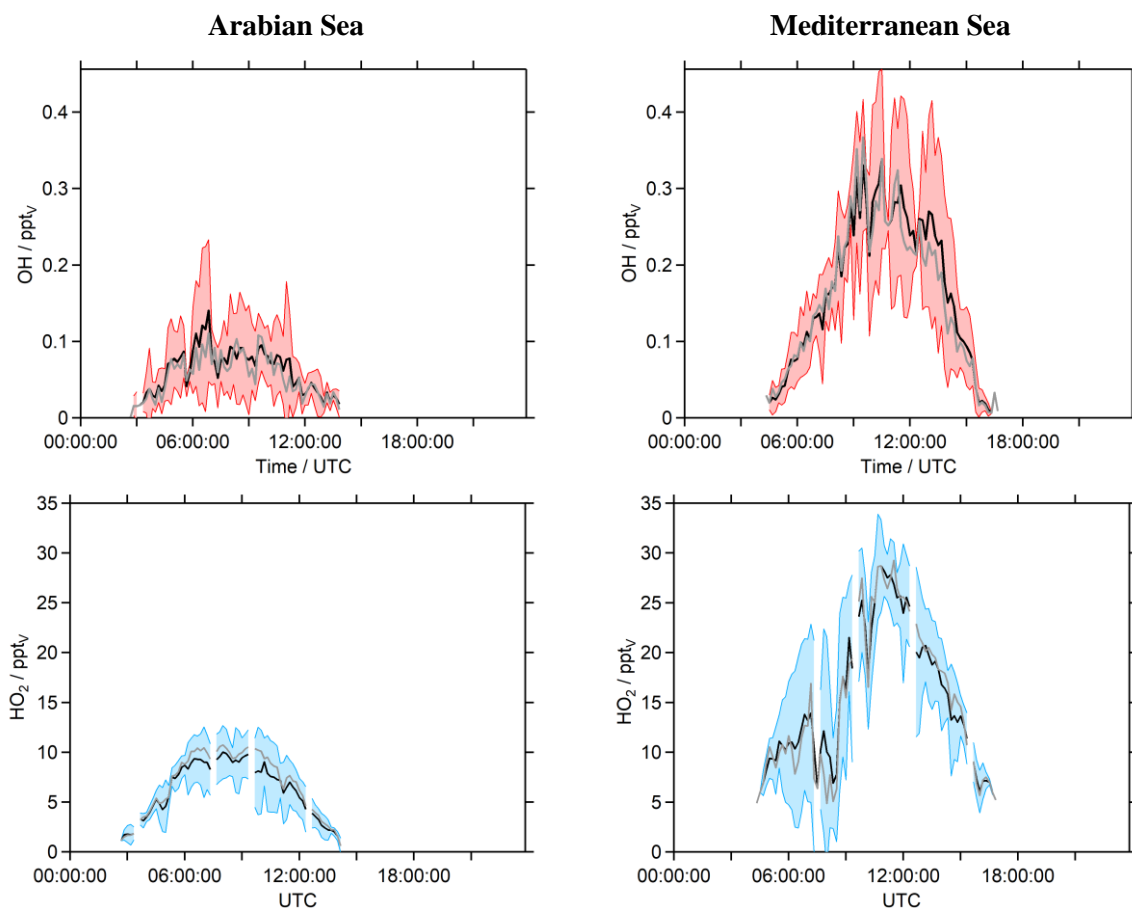


Figure 43: Diurnal variation of OH and HO₂ over the Arabian Sea (08.08. – 13.08.2017) and the Mediterranean Sea (25.08. – 31.08.2017) on the basis of the respective mean (black) and median (grey) values and the general variability within the region ($\pm 1\sigma$) as 10 minute averages.

This trend is also reflected by the NO_x measurements, although to a lesser extent. Tadic et al. (2020) determined a NO_x median of 190 ppt_v for the Arabian Sea and 250 ppt_v for the Mediterranean Sea. As a comparison, Fischer et al. (2015) detected less than 20 ppt_v of NO_x in pristine MBL conditions over the South Atlantic. We rarely encountered such clean MBL conditions, as NO only sparsely declined below 100 ppt_v while sailing through the Arabian Sea (Fig. 44). These enhanced levels of NO were most likely caused by ship emissions. To a lesser extent the transport of aged emissions from the eastern coast of Somalia could have also affected these air masses. Due to the elevated NO, secondary OH production (NO_x recycling) is expected to be enhanced by the reaction of HO₂ with NO. Enhanced NO_x also favors HCHO production instead that of ROOH (section 1.3.2).

Altogether, only a small diurnal variation of H₂O₂, ROOH and HCHO was observed over the Arabian Sea. This trend can be explained by the generally low levels of OH and HO₂ radicals, about a factor of three smaller than the observed levels over the Mediterranean Sea. A stronger diurnal variation of H₂O₂ was observed compared to ROOH and HCHO, as its production depends quadratic on HO₂ while the production of ROOH only scales linearly with HO₂. NO_x observations showed that we only rarely encountered pristine conditions, and thus the observed area of the MBL of the Arabian Sea can be described as a transition regime, which is analyzed more detailed in the next section.

4.5.2 The Arabian Sea during the South Asian Summer Monsoon

Ozone mixing ratios confirm rather clean conditions over the Arabian Sea with a mean ($\pm 1\sigma$) of 24.2 ± 4.6 ppb_v, although not as pristine as the remote MBL observed by Fischer et al. (2015) over the South Atlantic during OOMPH with 20.3 ± 1.8 ppb_v O₃. Wagner et al. (2002) also observed pristine MBL background conditions over the Indian Ocean during INDOEX, which originated from the southern hemisphere with mean values of 10.3 ppb_v O₃, 56 ppb_v CO and 2 ppt_v NO (daytime). HCHO mixing ratios were mostly in the range of 0.20 – 0.50 ppb_v (Wagner et al., 2001; Wagner et al., 2002), with mean values ($\pm 1\sigma$) of 0.20 ± 0.04 ppb_v for the pristine southern hemisphere and 0.31 ± 0.10 ppb_v for the pristine northern hemisphere. Contrary to these results, we observed 0.83 ± 0.33 ppb_v over the Arabian Sea during AQABA. Mean H₂O₂ levels are with 0.16 ± 0.05 ppb_v lower than the observations by Fischer et al. (2015), who measured 0.35 ± 0.22 ppb_v H₂O₂ with mixing ratios mostly in the range of 0.20 to 0.30 ppb_v during the first part of the cruise, far away from the African coastline. Even lower mean mixing ratios of ROOH were detected over the Arabian Sea with 0.07 ± 0.03 ppb_v compared to 0.28 ± 0.25 ppb_v MHP by Fischer et al. (2015).

As already shown, we observed elevated NO_x over the Arabian Sea (median 0.19 ± 3.15 ppb_v) compared to the pristine conditions during OOMPH and INDOEX (≤ 0.05 ppb_v). Additionally, elevated acrolein was identified as a main contributor to OH reactivity over the Arabian Sea and the Gulf of Aden (Pfannerstill et al., 2019), which is an indicator for combustion processes. We also detected slightly elevated ethene (up to ~200 ppt_v, Fig. 44), isoprene (up to ~100 ppt_v) and further biogenic emissions (Edtbauer et al., 2020; Bourtsoukidis et al., 2019). The first days in the eastern part of the AS also show elevated methanol and acetone compared to the western part of AS (12. – 14.08.2017).

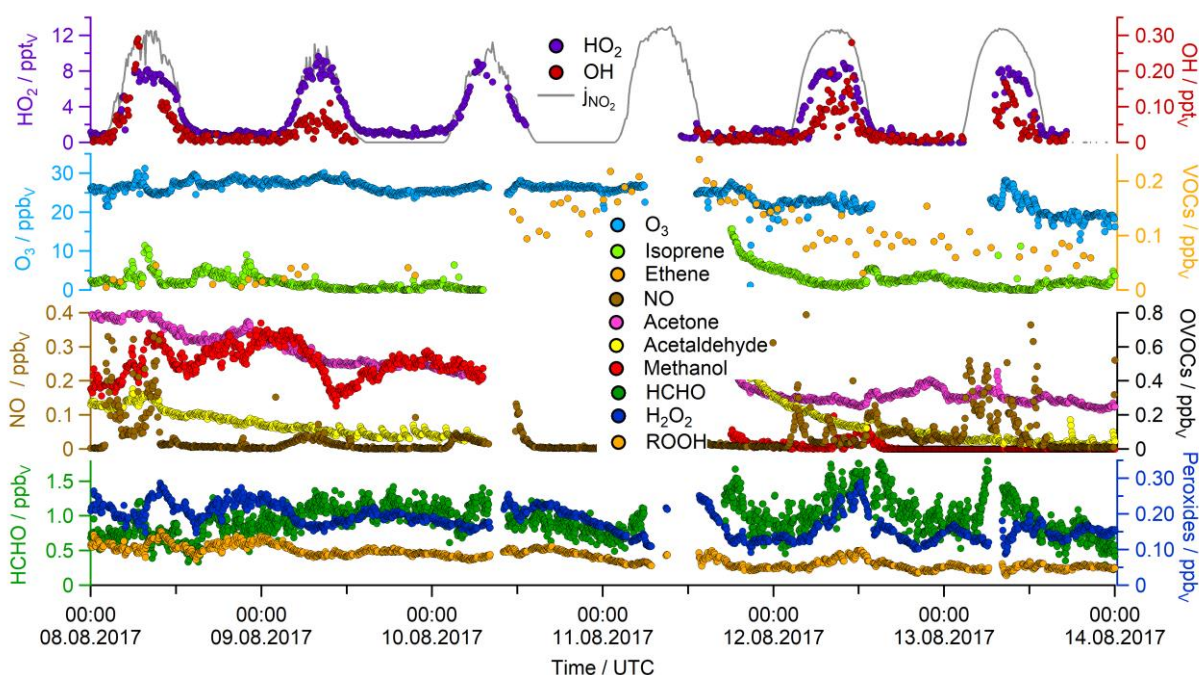


Figure 44: Timelines of trace gas measurements for the Arabian Sea during the second leg.

Tripathi et al. (2020) also highlight the sea-to-air emission potential of the Indian Ocean as a global source of VOCs. They observed high mean mixing ratios of e.g. ethene and propene with 8.9 ± 3.5 ppb_v and 3.4 ± 1.3 ppb_v, respectively. The abiotic production of carbonyl compounds and isoprene in the sea-surface micro layer (SML) by photo-degradation of dissolved organic matter has recently been discussed as a global source of VOCs in the MBL besides the known emissions from marine biology (Brüggemann et al., 2018; Brüggemann et al., 2017; Ciuraru et al., 2015). Brüggemann et al. (2018) emphasize the wind speed dependence of the calculated VOC emission potential. With an upper limit of 13 m s^{-1} , the

Arabian Sea shows a high VOC emission potential from July to September. Gopikrishnan and Kuttippurath (2021) also highlighted the significant increase of formaldehyde due to shipping emissions on the basis of satellite measurements. Large amounts of HCHO were detected close to the major routes through the Indian Ocean with up to $8 \cdot 10^{15}$ molec cm^{-3} , which is about twice the ambient background of formaldehyde of the northern Indian Ocean when there are no shipping emissions. The HCHO results during AQABA confirm these findings with HCHO about a factor of 2 higher than during INDOEX, although partially enhanced unsaturated hydrocarbons related to SML emissions likely also contributed to the enhanced HCHO.

Another highlight of the observations over the Arabian Sea is the generally suppressed ROOH, with the lowest mixing ratios of the AQABA data set (≤ 0.1 ppb_v). Similar ROOH levels were only detected during some events over the southern Red Sea. According to Fig. 45, the H₂O₂ / ROOH – ratio reflects mostly values close to 1 for AQABA (Hottmann, 2019), with the exception of the observations over the Arabian Sea (H₂O₂ dominated), the southern Red Sea (H₂O₂ dominated during the first leg) and the Arabian Gulf (ROOH dominated during the first leg). In pristine MBL conditions, the sum of organic peroxides is expected to be dominated by MHP, based on the photochemical oxidation of methane. Methyl hydroperoxide production thereby competes with formaldehyde production via the reaction of methyl peroxy radicals with NO, which releases HCHO, while their self-reaction releases MHP (1.3.2). Since we only rarely detected air masses with least amounts of NO, HCHO production was favored, which explains the suppressed ROOH compared to H₂O₂ over the Arabian Sea. Furthermore, we observed decreased HO_x compared to the Mediterranean Sea (Fig. 43) leading to generally less photochemical production. A stronger pronounced diurnal variation of HCHO was observed during the enhanced NO while sailing closer to the Gulf of Aden (12. – 13.08.2017), most likely related to accelerated OH recycling compared to the eastern part of the Arabian Sea (Fig. 44). Air masses further south are likely to be cleaner from a NO_x perspective, as most of the shipping traffic follows a route close to the coastline around the Arabian Peninsula.

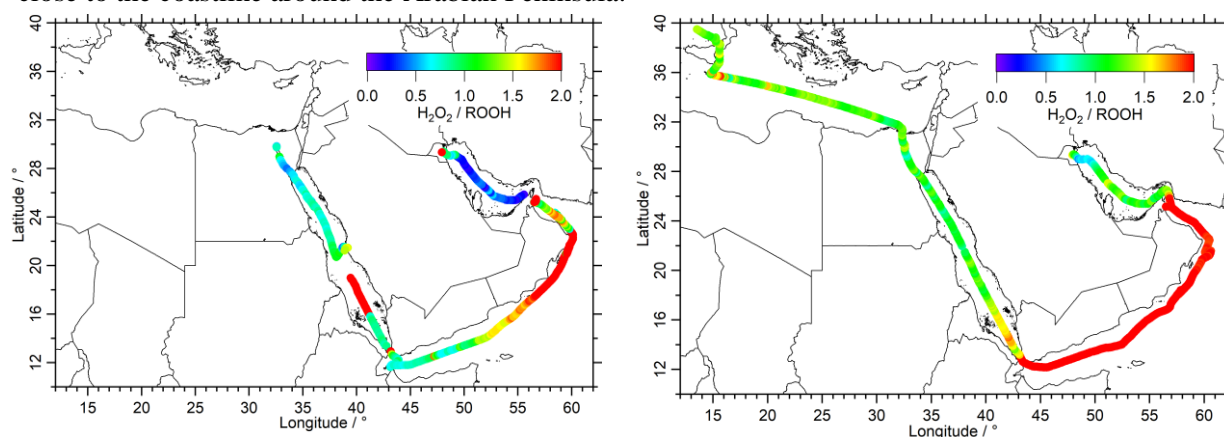


Figure 45: GPS Plot of the hydrogen peroxide / organic peroxide – ratio for the first (left) and second leg (right) of the AQABA campaign. The Arabian Sea and the southern Red Sea (first leg) were dominated by H₂O₂, while ROOH excess was detected over the Arabian Gulf and parts of the Suez Canal during the first leg.

4.5.3 Dust events over the southern Red Sea and the Gulf of Aden

A dust storm occurred between the 14. – 15.07. during the first leg of the campaign, when we were sailing through the southern Red Sea. These winds coming from Eritrea and central Sudan (Fig. 30) transported large amounts of Saharan dust. No diurnal variation of HCHO, H₂O₂ or ROOH was observed in this air mass, which contained very low NO mixing ratios on the 15.07. (mostly below 100 ppt_v). Very low mixing ratios of ROOH in the range of 20 – 75 ppt_v were observed, while HCHO levels were also decreased to ~50 – 700 ppt_v. The particle surface area concentration (PS) of PS₁₀ (all particles ≤ 10 μm) and PS₁ (all particles ≤ 1 μm) was used to estimate the abundance of dust particles, which represent the main component of large particles when subtracting PS₁ from PS₁₀. Largest values were detected during the night of the 15.07. from 0 – 4 UTC with a local maximum of 350 μm² cm⁻³ (Fig. 46). This event constitutes a distinct anti-correlation with observed H₂O₂ and ROOH mixing ratios, which dropped by ~80 ppt_v and ~20 ppt_v, respectively. Unfortunately, there are no HCHO, HO₂ or OH data points available during this event. Particle surface concentrations remained high for the whole day (≥ 150 μm² cm⁻³) and then halved on the way to the Gulf of Aden through the strait of Bab-el-Mandeb, where we detected a local maximum of HCHO (2.33 ppb_v) and H₂O₂ (0.37 ppb_v). Air masses over the Gulf of Aden also contained elevated amounts of dust particles with several explicit events on the 17. and 18. July. Most of these events coincide with decreased mixing ratios of HCHO, H₂O₂ and ROOH (e.g. 17.07. 0 – 5 UTC; 18.07. 0 – 4 UTC; 18.07. 10 – 16 UTC). Additionally, higher levels of organic peroxides compared to H₂O₂ were detected in these air masses, which was otherwise only found for the Suez Canal and the Arabian Gulf (Fig. 45). In the eastern part of the Gulf, the mixing ratios of H₂O₂ and ROOH decreased and were almost equal. The transition into waters of the Arabian Sea was defined by a change of the air mass origin with winds coming from the East African coastline and the western Indian Ocean (Fig. 30), where declined ROOH has been detected (Fig. 44).

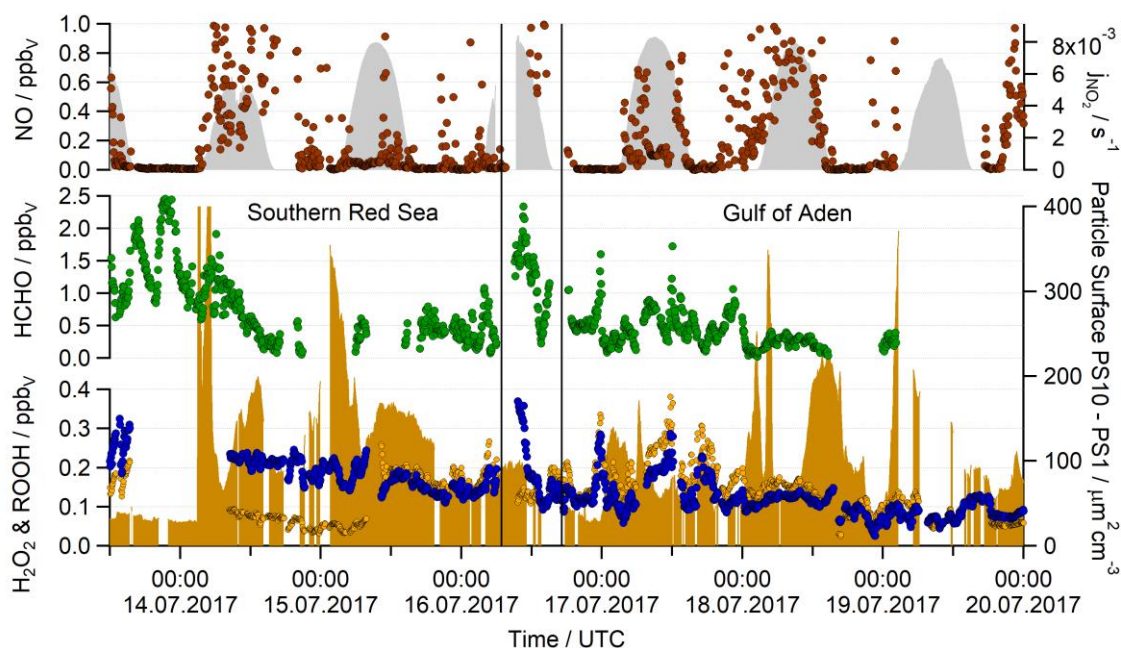


Figure 46: Timelines of NO, HCHO, H₂O₂, ROOH and j_{NO_2} during dust storm events over the southern Red Sea and the Gulf of Aden, indicated by the particle surface area concentrations of PS₁₀ – PS₁ (all particles between 1 – 10 μm), which represents mostly large dust particles. Passing the strait of Bab-el-Mandeb is indicated by the black lines.

The second leg did not show the same levels of enhanced dust particles, with mean PS over the Gulf of Aden below 50 μm² cm⁻³, although elevated abundance of dust was detected during the night of the 17.08. when we were approaching the Strait of Bab-el-Mandeb, with PS of up to 150 μm² cm⁻³ (Fig. 47). During this rather short event, H₂O₂ mixing ratios dropped from ~350 ppt_v to ~180 ppt_v, even though

highest levels of H_2O_2 were also accompanied by elevated dust particles. PS then decreased to values below $100 \mu\text{m}^2 \text{cm}^{-3}$ over the southern Red Sea.

The air masses encountered during the second leg had a similar origin with winds coming from Ethiopia and Somalia over the Gulf of Aden, although these contained decreased levels of organic peroxides compared to the first leg with a mean ($\pm 1\sigma$) of $58 \pm 16 \text{ ppt}_v$ and $144 \pm 61 \text{ ppt}_v$ during the first leg. Less H_2O_2 was abundant during the enhanced presence of dust on the first leg with $115 \pm 43 \text{ ppt}_v$ compared to $149 \pm 45 \text{ ppt}_v$ for the second leg. Formaldehyde data coverage is overall lower during the second leg due to instrumental issues, even though the HCHO measurements indicate elevated mixing ratios during the second leg with $892 \pm 241 \text{ ppt}_v$ compared to mean HCHO of $407 \pm 243 \text{ ppt}_v$ during the first leg. Additionally, stronger diurnal variations of HCHO and H_2O_2 were detected when there was less dust.

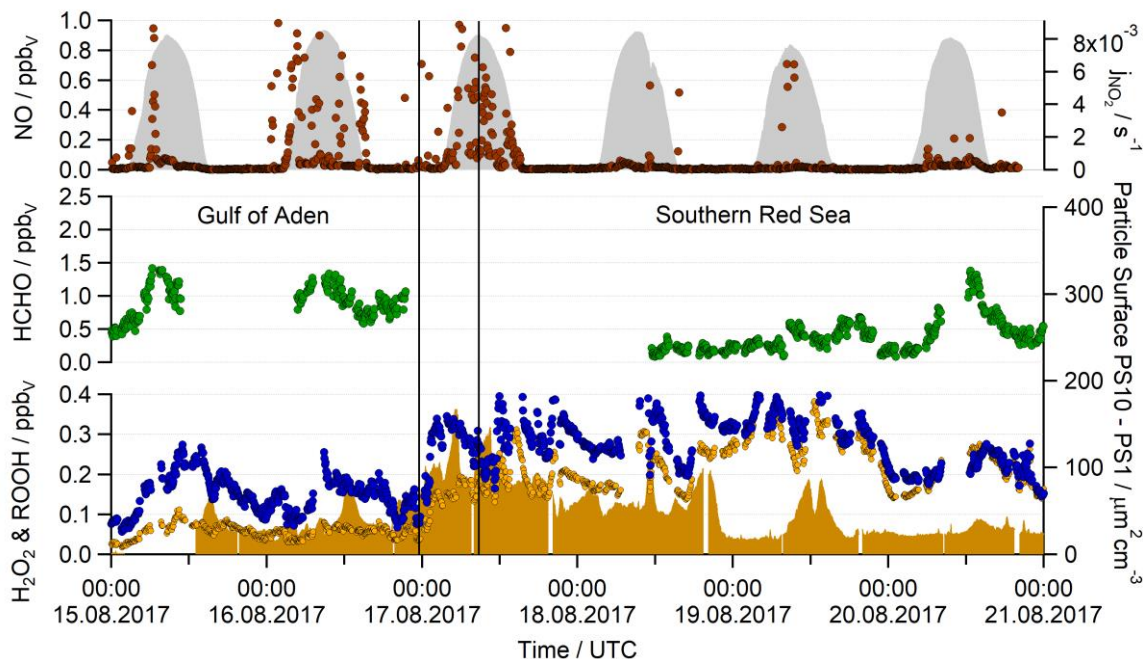


Figure 47: Timelines of NO, HCHO, H_2O_2 , ROOH and j_{NO_2} over the southern Red Sea and the Gulf of Aden during the less dusty conditions of the second leg, indicated by the particle surface area concentrations of $\text{PS}_{10} - \text{PS}_1$ (all particles between 1 – 10 μm), which represents mostly large dust particles. Passing the strait of Bab-el-Mandeb is indicated by the black lines.

Air masses over the southern Red Sea were one of the cleanest during AQABA from a NO_x perspective, with a median of less than 50 ppt_v for the 18. – 19. August. These low NO_x conditions were accompanied by the lowest HCHO mixing ratios during AQABA with a mean of $283 \pm 142 \text{ ppt}_v$ compared to $407 \pm 182 \text{ ppt}_v$ during the first leg. Enhanced peroxide mixing ratios were detected in this air mass compared to the first leg with $307 \pm 69 \text{ ppt}_v$ H_2O_2 and $229 \pm 64 \text{ ppt}_v$ ROOH compared to $180 \pm 34 \text{ ppt}_v$ H_2O_2 and $113 \pm 61 \text{ ppt}_v$ ROOH during the first leg. The very low NO during the second leg ($22 \pm 97 \text{ ppt}_v$) defined this air mass as almost pristine, so that methane oxidation primarily produced MHP instead of HCHO via recombination of peroxy radicals, which is confirmed by elevated ROOH and decreased HCHO in this air mass. Altogether, higher levels of hydroperoxides were detected with decreased abundance of dust particles ($\text{PS}_{10} - \text{PS}_1$) for both legs and an anti-correlation of H_2O_2 and to a lesser extent also ROOH and HCHO was observed. The observations highlight a potentially irreversible loss of these trace gases due to heterogeneous uptake and / or chemical interaction with the particles. The quantification of this loss mechanism was not possible due to fast changing chemical conditions between both legs related to changes of the air mass origin. Further studies are needed to quantify the interaction with dust, which might have a large effect on the global budget of HO_x reservoirs.

5. Summary and Conclusion

This doctoral thesis presents studies about production and loss processes of the main HO_x reservoir species in the marine boundary layer around the Arabian Peninsula and the Mediterranean Sea. To achieve these investigations, measurements of formaldehyde, hydrogen peroxide and organic hydroperoxides were conducted with three separate instruments based on fluorescence spectroscopy (AL4021, AL2021, Dual-Enzyme-HPLC) onboard the *Kommandor Iona* during summer 2017.

Both instrumental techniques for the detection of HCHO and H₂O₂ were successful and showed instrumental characteristics comparable to previous expeditions and lab studies. Only the results of the HPLC could not be used for quantification of separated organic peroxides due to an interference of the instrumental background with the movement of the ship. Generally, the AL4021 data has to be corrected for primary emissions of HCHO and other combustion processes, which was done with a filter based on NO_x, CO, SO₂ and wind direction data, mainly to remove ship exhaust plumes from the dataset. Nevertheless, data coverage during AQABA was still $\geq 60\%$, with major data gaps during the first leg while sailing with the wind direction. Detection limits (2σ) of 128 ppt_v HCHO, 13 ppt_v H₂O₂ and 8 ppt_v ROOH were derived for the AQABA dataset. Temporal resolution of the instruments was higher than 180 s, but the analysis was mainly performed with 5 minute averages. The AL4021 and the AL2021 have some known cross sensitivities to other trace gases, e.g. O₃ and NO_x, which were corrected in post. In addition to the formaldehyde and hydroperoxide measurements, in situ observations of several VOCs, O₃, NO_x, OH reactivity, OH and HO₂ radicals, absolute humidity, temperature and actinic flux were used to determine photochemical production and loss processes of the HO_x reservoirs and to evaluate the air quality around the Arabian Peninsula.

Various air pollution events were encountered in the area around the Suez Canal and the Arabian Gulf, whereas the MBL of the Arabian Gulf proved to be a unique hotspot of photochemical air pollution with the highest mean of O₃ (74.06 ± 9.23 ppb_v). Extreme amounts of air pollution were encountered with air masses originating from Iraq / Kuwait and the western coastline, while winds from the Iranian Zagros Mountains were less polluted. In the polluted air masses tropospheric O₃ reached values which are usually detected close to highly populated urban areas in summer with mixing ratios of up to 166.90 ppb_v during night. These events also contained the highest HCHO and ROOH mixing ratios during AQABA, which reached mixing ratios of up to 12.44 ppb_v HCHO and 2.32 ppb_v ROOH, respectively. Formaldehyde mean values ($\pm 1\sigma$) were almost twice as high compared to the Suez Canal with 3.77 ± 2.44 and 2.07 ± 1.61 ppb_v, while the whole dataset demonstrates a mean of 1.33 ± 1.43 ppb_v. A less pronounced trend was found for the organic peroxides with a mean of 0.35 ± 0.28 ppb_v for the Arabian Gulf, 0.27 ± 0.09 ppb_v for the Suez Canal and 0.18 ± 0.16 ppb_v for the whole dataset. Organic peroxide mixing ratios ≥ 1 ppb_v were only detected over the Arabian Gulf, leading to the assumption of highly elevated organic peroxy radicals in this area. No drastic enhancements of H₂O₂ were detected in these air masses, with means of 0.26 ± 0.15 ppb_v for the Arabian Gulf, 0.27 ± 0.11 ppb_v for the Suez Canal and 0.20 ± 0.10 ppb_v for the AQABA dataset. Hydrogen peroxide mixing ratios were overall the least variable, with highest values in the harbor of Kuwait with up to 0.92 ppb_v. Large diurnal variations were also determined over the Mediterranean Sea with daily variations occasionally rising up to ~ 300 ppt_v.

Cleaner regimes were encountered with aged air masses over the Arabian Sea, with the lowest mean mixing ratios of O₃ (24.23 ± 4.62 ppb_v) and NO_x (0.95 ± 3.15 ppb_v). Mean HCHO mixing ratios were elevated with 0.83 ± 0.33 ppb_v compared to pristine Indian Ocean conditions of 0.31 ± 0.10 ppb_v (Wagner et al., 2001), while we observed the lowest levels of H₂O₂ and ROOH during AQABA over the Arabian Sea with 0.16 ± 0.05 ppb_v and 0.07 ± 0.03 ppb_v, respectively. Both the elevated NO_x and

HCHO compared to pristine MBL conditions confirm that the air masses over the Arabian Sea contained significant amounts of ship emissions, which may have additionally suppressed hydroperoxide production during the already low HO_x conditions. Air masses over the southern Red Sea during the first leg were influenced by a dust storm originating from the Sahara. Enhanced abundance of dust particles (PS₁₀ – PS₁) revealed a slight anti-correlation with H₂O₂, ROOH and to a lesser extent also with HCHO mixing ratios, which could be related to uptake or heterogeneous chemistry on the particle surface. Furthermore, these winds were rather clean with mean NO of 268 ± 853 ppt_v, however the lowest NO values were detected in the same area during the second leg with 22 ± 97 ppt_v. Simultaneously, the lowest levels of HCHO (0.28 ± 0.14 ppb_v), but slightly enhanced ROOH (0.23 ± 0.06 ppb_v) and H₂O₂ (0.31 ± 0.07 ppb_v) highlight this continental air mass as one of the cleanest encountered during AQABA.

These observations were used to evaluate EMAC model results based on the complex oxidation mechanism MOM, which includes the chemistry of all main organics (e.g. alkanes, alkenes, aromatics, terpenes) and inorganics. On average, EMAC reproduced the observations of HCHO quite well, with most data matching within a factor of 2. However, the model did not resolve the high pollution events as clearly, which may be due to its coarse resolution of ~110 km grids. Organic peroxide mixing ratios were matched in regions where we observed elevated HO₂, mainly over the Suez Canal and the Mediterranean, while regions with decreased HO_x (Arabian Sea, Gulf of Oman) were overestimated by more than a factor of 3 on average. Furthermore, EMAC did not simulate significantly enhanced ROOH over the Arabian Gulf, only a slight increase of PAA and EHP. In contrast to HCHO and ROOH, H₂O₂ mixing ratios were overestimated for the whole AQABA campaign and only some data points over the Arabian Sea during night match the observations. The model simulated a very strong diurnal variation of H₂O₂ with daily variations of more than 1 ppb_v in some regions, while maximum daily variations of ~300 ppt_v were detected. Calculation of the photochemical budget of H₂O₂ revealed an overestimation of HO_x, as production of H₂O₂ scales quadratic with HO₂, but its loss only linearly with OH. Deposition velocities showed that EMAC underestimates deposition loss over the Mediterranean Sea by about a factor of 2 during night. V_{dep} over the Arabian Sea matched the observations on average, while the model generally constitutes less variation. In this context, the AQABA results lead to the recommendation of a missing or underestimated loss of HO_x radicals and simultaneously missing HCHO sources not related to OH chemistry. Further investigation of the Arabian Gulf with HYSPLIT trajectories revealed high contributions of oil- and gas-refinery emissions e.g. related to gas flaring, which highlight the emission potential of this region not only for local air quality. A short comparison with the WRF-Chem model revealed that a higher model resolution did not improve the accuracy of the simulated HCHO over the Arabian Gulf and the Suez Canal, even though the high resolution model achieved improved results for HCHO, H₂O₂ and O₃ for less polluted MBL conditions (e.g. the Arabian Sea) compared to EMAC. Therefore, an update of the anthropogenic VOC emissions in emission inventories (e.g. the EDGAR database) is recommended.

HCHO production rates were calculated on basis of the photochemical steady-state assumption and were used together with OH reactivity and OH radical observations to determine the HCHO yield factor α_{eff} , which represents the theoretical yield of HCHO per OH radical consumed. This technique has the advantage, that non-observed species are accounted for by measurements of the total OH reactivity and the disadvantage that further sources of HCHO, like primary emissions or ozonolysis of alkenes, are just identified as an elevated intercept of the regression analysis. Highest α_{eff} were determined for the Arabian Gulf (0.315), the Suez Canal (0.115) and the Gulf of Oman (0.077), where significantly elevated VOCs have been observed. On the other side, the lowest values were derived for the air masses over the southern Red Sea (0.013), where also the lowest HCHO / ROOH – ratios were detected. This air mass was the cleanest continental air mass from a NO_x perspective, so that MHP production was favored

instead of HCHO, which explains the small α_{eff} . In sum, this technique confirmed to be valuable to estimate regional HCHO production efficiencies without the determination of the photochemical budget of HCHO. But it has high uncertainties due to observational errors and, especially during AQABA, due to fast air mass changes and elevated contributions of additional oxidants (e.g. O_3 , NO_3 , Cl). Further studies are necessary to evaluate the technique with datasets based on a fixed platform and ideally also with a more stable air mass origin.

The AQABA datasets of HCHO, ROOH and H_2O_2 confirmed the Arabian Gulf and the Suez Canal as major hotspots of photochemical air pollution, not only to be a threat for health of the local population, but also for climate change. Increased air quality controls are necessary in these regions to monitor the extent and transport of the enhanced tropospheric O_3 , NO_x and VOCs. Fossil fuel related emissions could be reduced e.g. by a reduction of gas flaring around the Arabian Gulf. Recently developed satellite instruments proved to be useful for identification of these emission sources and could be useful for updated emission factors in atmospheric chemistry models. Additionally, the measurements of H_2O_2 were highly valuable to identify an overestimation of HO_x in EMAC and lead together with a slight underestimation of the deposition velocity to a missing sink of HO_x . In air masses over the Arabian Gulf this could also be related to the radical recycling mechanism, since EMAC did not match the observations of ROOH while overestimating HO_2 . These observations lead to an underestimation of RO_2 in the model, which may also be related to the missing anthropogenic emissions (e.g. gas flaring) around the Arabian Gulf.

6. Supplement

6.1 List of Tables

Table 1: Brief comparison of analytical techniques for the detection of gaseous HCHO.....	17
Table 2: Determination of the AL4021 temporal resolution by the signal increase of the liquid HCHO standards..	22
Table 3: Trace gas interferences of the AL4021 measurements during AQABA.....	26
Table 4: Comparison of the AL4021 characteristics during AQABA with further measurement expeditions.....	27
Table 5: Brief comparison of measurement techniques used for the detection of gaseous H ₂ O ₂	28
Table 6: Henry's law constants (at 25 °C) of the most abundant hydroperoxides in Earth's atmosphere based on the determinations of O'Sullivan et al. (1996).....	29
Table 7: Instrumental characteristics of the AL2021 and the HYPHOP during the recent measurement expedition.....	34
Table 8: Summary of instrumentation installed during AQABA 2017.....	45

Dienhart et al., 2022:

Table 1: Instrument characteristics of the HCHO and hydroperoxide measurements during the AQABA campaign.....	60
Table S1: Mean, median, 25- and 75-percentile values of the HCHO, H ₂ O ₂ and organic peroxide measurements (black) and the corresponding EMAC simulations (orange) for the eight different regions encountered during AQABA: Mediterranean Sea (MS), Suez Canal (SU), Red Sea North (RN), Red Sea South (RS), Gulf of Aden (GA), Arabian Sea (AS), Gulf of Oman (GO) and Arabian Gulf (AG).....	81
Table S2: Calculated deposition rates (k_{dep}) of HCHO and H ₂ O ₂ for the Arabian Sea (AS) and the Mediterranean Sea (MS). Values of k_{dep} were determined as the slope of a linear regression (logarithmic decay versus time, Fig. 10) and the corresponding deposition velocities (V_{dep}) are based on Eq. 12 with values for the boundary layer height derived from the ERA5 results for the corresponding timeframe ($\pm 1\sigma$). Errors of k_{dep} and V_{dep} are estimated to be at least $\pm 40\%$	87

Dienhart et al. 2021:

Table 1: Average speciated reactivity ($R(\text{OH})_x \pm 1\sigma$ standard deviation) of certain compound classes (based on the results of Pfannerstill et al., 2019), $R(\text{OH})_{\text{eff}}$ and α_{eff} (\pm uncertainty of the slope of the bivariate fit). For NO _x the median values are listed instead of the means.....	96
--	----

6.2 List of Figures

Figure 1: Vertical structure of the earth's atmosphere with its temperature profile.....	2
Figure 2: Temporal and spatial scales of variability for atmospheric constituents (Seinfeld and Pandis, 2016).....	4
Figure 3: HO _x cycling and the thereby involved reservoir species on the basis of the methane oxidation in clean conditions, i.e. simplified by exclusion of NO _x and halogen chemistry (adopted from Reeves and Penkett, 2003).....	8
Figure 4: VOC oxidation in on the basis of the methane oxidation, simplified by exclusion halogen chemistry (adopted from Reeves and Penkett, 2003).....	9
Figure 5: Reactions and products following the ozonolysis of isoprene. Many of the Criegee decomposition products remain unidentified (adopted from Wennberg et al., 2018).....	10
Figure 6: Reactions and products following the ozonolysis of isoprene. Many of the Criegee decomposition products remain unidentified (adopted from Wennberg et al., 2018).....	11

Figure 7: Reactions and products following the oxidation of isoprene by the nitrate radical (adopted from Wennberg et al., 2018).....	13
Figure 8: Hantzsch reaction of formaldehyde and acetylacetone in ammoniac solution, the product DDL (3,5-diacetyl-1,4-dihydrolutidine) is a fluorescent dye which is excited at 410 nm followed by fluorescence detection at 510 nm.....	18
Figure 9: Scheme of the AL4021 instrumental design.....	18
Figure 10: Schematic for the injection of liquid HCHO standards (AL4021 manual v2.2, Aero-Laser GmbH, 2019).....	20
Figure 11: Example of ambient HCHO measurements during AQABA including the calibration of the instrument. The calibration includes the injection of 0.1 M HCl (4 min), followed by injection of a HCHO standard solution (26 min) and zero gas (24 min), the lines in black are used for the determination of the sensitivity, LOD and temporal resolution while the red parts were excluded from the dataset.....	21
Figure 12: Timeline of the zero gas measurements during the AQABA ship campaign, elevated noise levels were detected between the 08.08. to 14.08.2017 during wavy conditions in the Arabian Sea and the Gulf of Aden.....	23
Figure 13: Frequency distribution and Gauss fit of the zero gas measurements AQABA, the Gauss fit confirms normal distribution of the measured background noise, so that the 2σ deviation represents 95 % of the data. The detection limit of the AL4021 was determined as 128 ppt.....	23
Figure 14: Frequency distribution liquid standard injections during AQABA (green) and with the exclusion of the Arabian Gulf and the Arabian Sea (grey), which demonstrate higher variability compared to the rest of the dataset.....	24
Figure 15: Reaction scheme of the detection of gaseous HCHO with chromotropic acid in sulfuric acid. The released carbenium ion is a strong chromophore and ideal for the quantification with UV/Vis spectroscopy.....	25
Figure 16: Determination of the O ₃ interference of the AL4021 during AQABA, no significant increase of the HCHO signal was detected with increasing amounts of O ₃	26
Figure 17: Reaction scheme of the dual-enzyme technique. HRP catalyzes the reaction of POPHA and H ₂ O ₂ to the corresponding dimer. The addition of Catalase in channel B selectively breaks down H ₂ O ₂ , so that only ROOH are detected in this channel.....	30
Figure 18: Flow chart of the AL2021 and the respective solutions. Please note that PMT A and B represent both the respective flow cells and photomultiplier tubes. The Cadmium lamp in the instrument is set up in 90° light angle to the corresponding photomultiplier tubes.....	30
Figure 19: External calibration of the AL2021 with a 4-point calibration by the injection of liquid H ₂ O ₂ standards.....	31
Figure 20: Reaction of titanium tetrachloride and H ₂ O ₂ to the octahedral η^2 -peroxo titanium tetrachloride.....	32
Figure 21: Flow chart of the data processing steps involved with the AL2021 and the AL4021 to convert raw signals (V) into ambient mixing ratios (ppb.).....	35
Figure 22: Overview of both legs during AQABA and color-coded regional structuring. The following acronyms are used for the different regions encountered during AQABA: MS for Mediterranean Sea (yellow), SU for Suez Canal and Gulf of Suez (magenta), RN for Red Sea North (orange), RS for Red Sea South (green), GA for Gulf of Aden (blue), AS for Arabian Sea (cyan), GO for Gulf of Oman (brown) and AG for Arabian Gulf (red).....	38

Figure 23: Oil (red) and gas field locations (blue) around the Arabian Peninsula with the oil refineries as red circles. The image was processed with Harvard WorldMap (<https://worldmap.harvard.edu/maps/6718/dJT>).....39

Figure 24: Examples of anthropogenic emissions around the Arabian Peninsula: Oil rig with a gas flare close to the Suez Canal (photo: Steffen Dörner during the first leg) and heavy ship emissions close to Fujairah (western part of the Gulf of Oman just after leaving the Arabian Gulf during the second leg).....40

Figure 25: Mean sea(surface)-level pressure and surface wind for the summer monsoon from June – August 2018 based on Fig. 1 of Tegtmeier et al. (2022).....40

Figure 26: Instrumental setup on the *Kommandor Iona*. The HCHO, H₂O₂, ROOH, CO and NO_x instruments were set up in the highlighted lab container and connected to the trace gas sampling inlet via bypass tubing with high flow rates. The HO_x and aerosol instruments had separated sampling inlets, specialized with regards to the needs of the respective instrumentation.....42

Figure 27: Timeline of the final HCHO dataset (blue) the filtered HCHO data (green) and the NO measurements (black) which were used with the addition of CO, SO₂ and wind direction data to set up a filter, mainly to remove ship exhaust emissions.....46

Figure 28: Qualitative overview of the observed ship exhaust plume characteristics and their dependency on ship parameters, combustion conditions and the atmospheric processing / ageing after release into the atmosphere based on Celik et al. (2020).....47

Figure 29: Meteorological observations during the AQABA campaign: Mediterranean Sea (MS), Suez Canal (SU), Red Sea North (RN), Red Sea South (RS), Gulf of Aden (GA), Arabian Sea (AS), Gulf of Oman (GO), Arabian Gulf (AG).....49

Figure 30: HYSPLIT trajectories for of the Mediterranean Sea (MS), the Suez Canal (SU), the northern Red Sea (RN) and the southern Red Sea (RS) for the first (left) and the second leg (right) of AQABA. Trajectories were calculated with a sampling time of 48 hours and a temporal resolution of one hour.....50

Figure 31: HYSPLIT trajectories for of the Gulf of Aden (GA), the Arabian Sea (AS), the Gulf of Oman (GO) and the Arabian Gulf (AG) for the first (left) and the second leg (right) of AQABA. Trajectories were calculated with a sampling time of 48 hours and a temporal resolution of one hour.....51

Dienhart et al., 2022:

Figure 1: The shiptrack (black) of the Kommandor Iona during the AQABA cruise subdivided into eight regions: Mediterranean sea (MS: yellow), Suez Canal (SU: pink), Red Sea North (RN: orange), Red Sea South (RS: green), Gulf of Aden (GA: blue), Arabian Sea (AS: turquoise), Gulf of Oman (GO: brown) and Arabian Gulf (AG: red). The map was created with data provided by the Natural Earth website (<http://www.naturalearthdata.com>).....62

Figure 2: Overview and data coverage of HCHO, H₂O₂ and organic hydroperoxide measurements during both legs of the AQABA ship campaign (graphs on the left represent the first leg). Contaminated HCHO data (e.g. by ship exhausts) were removed from the dataset with a stack filter (based on the NO, CO and SO₂ observations), therefore there is less HCHO data coverage during the first leg in the Arabian Sea.....63

Figure 3: Formaldehyde observations (green) and EMAC simulations (yellow) divided into the eight regions during AQABA: Mediterranean sea (MS), Suez Canal (SU), Red Sea North (RN), Red Sea South (RS), Gulf of Aden (GA), Arabian Sea (AS), Gulf of Oman (GO) and Arabian Gulf (AG). We used the lowermost model results (~30 m) for the comparison in 10 min averages (left). The box represents 25 to 75 % of the data and the whiskers 10 to 90 % with the median as the black line. The right panel shows the ratio between the observations and the model simulations.....65

Figure 4: H₂O₂ (blue) and organic hydroperoxide (ROOH, orange) observations compared to the EMAC simulations (yellow), we used the lowermost model results (~30 m) for the comparison. The box represents 25 to

75 % of the data and the whiskers 10 to 90 % with the median as the black line. The right panel shows the ratio between the observations and the simulations.....	67
Figure 5: OH and HO ₂ daytime values ($j_{\text{NO}_2} \geq 10^{-3} \text{ s}^{-1}$) of the observations (grey) and the EMAC simulations (yellow). The box represents 25 to 75 % of the data and the whiskers 10 to 90 % with the median as the black line. The EMAC data was adapted to the measurements with a time resolution of 10 minutes, so that the diurnal variations are reflected accurately.....	69
Figure 6: Box plots of H ₂ O ₂ production rates ($\text{ppt}_v \text{ h}^{-1}$) for the observations (grey) and the EMAC model (yellow) during daytime ($j_{\text{NO}_2} \geq 10^{-3} \text{ s}^{-1}$) and the corresponding loss rate constants (s^{-1}) for photolysis (observations in grey and EMAC in yellow) and reaction with OH (green, orange). The boxes represent 25 to 75 % of the data and the whisker intervals 10 to 90 % with the median values as the black lines. The corresponding timelines are presented in Fig. S11.....	70
Figure 7: Box Plot of the net photochemical production of H ₂ O ₂ ($\text{P}(\text{H}_2\text{O}_2) - \text{L}(\text{H}_2\text{O}_2)$) of the observations and the EMAC model results (yellow) during noon ($j_{\text{NO}_2} \geq 10^{-3} \text{ s}^{-1}$) without the dry deposition. The boxes represent 25 to 75 % of the data and the whisker intervals 10 to 90 % with the median values as the black lines. The corresponding timelines are presented in Fig. S11.....	71
Figure 8: Diurnal variation of the net photochemical production of H ₂ O ₂ ($\text{P}(\text{H}_2\text{O}_2) - \text{L}(\text{H}_2\text{O}_2)$) of the observations (grey) and the EMAC model results (orange) during noon ($j_{\text{NO}_2} \geq 10^{-3} \text{ s}^{-1}$) without the dry deposition. The corresponding timelines are presented in Fig. S11.....	72
Figure 9: Comparison of the simulated BLH in EMAC with ERA5 (ECMWF ReAnalysis 5 th generation) data at a four times higher resolution (31 km grid) than EMAC (~110 km grid) and hourly averaged data. EMACs BLH indicates continental influence by the strong diurnal variation while cruising close to the coast (SU, RN, GA, GO and AG, with the highest values determined for the ports of Jeddah (10. – 13.07.), Djibouti (16.07.) and Kuwait (01. – 03.08.). The measured photolysis frequency j_{NO_2} serves as a reference of sunlight intensity during AQABA.....	73
Figure 10: Determination of the deposition rates k_{dep} for H ₂ O ₂ and HCHO over the Arabian and the Mediterranean Sea in 10 min averages during night ($j_{\text{NO}_2} < 10^{-3} \text{ s}^{-1}$).....	74
Figure 11: Comparison of the calculated deposition velocity V_{dep} for HCHO and H ₂ O ₂ in the Arabian (AS) and the Mediterranean Sea (MS).....	75
Figure S1: Timelines of the HCHO measurements and the EMAC simulation, averaged along the ship track.....	78
Figure S2: Scatter plot of the HCHO measurements versus the simulated data (EMAC) in hourly averages.....	78
Figure S3: Timelines of the H ₂ O ₂ measurements and the EMAC simulation, averaged along the ship track.....	79
Figure S4: Scatter plot of the H ₂ O ₂ measurements versus the simulated data (EMAC) in hourly averages.....	79
Figure S5: Timelines of the organic peroxide (ROOH) measurements and the EMAC simulations along the ship the track. The simulated dataset consists of the most prominent species methyl hydroperoxide (MHP), peracetic acid (PAA) and ethyl hydroperoxide (EHP).....	80
Figure S6: Scatter plot of the organic peroxide measurements versus the simulated data (EMAC) in hourly averages.....	80
Figure S7: Timelines of the OH measurements and the EMAC simulation, averaged along the ship track.....	81
Figure S8: Timelines of the HO ₂ measurements and the EMAC simulation, averaged along the ship track.....	82
Figure S9: Case study of the Arabian Gulf during the first leg for the observations and the corresponding EMAC simulations. Highly polluted air masses were detected during the night of the 29.07.17, when we measured 170 ppbv of O ₃ in the center of the Arabian Gulf.....	82
Figure S10: Identification of H ₂ O ₂ and three separated organic peroxides based on the qualitative HPLC measurements. MHP (methyl hydroperoxide), PAA (peracetic acid) and EHP (ethyl hydroperoxide) were	

identified with their respective retention times and gaseous injections of PAA with a diffusion source. The lower panel shows the continuous results in AG, the upper panel the injection of enriched samples in MS.....83

Figure S11: Timelines of the production and loss terms of H₂O₂ for the observations (black) and the EMAC model results (orange). Note that the loss terms were not multiplied with the H₂O₂ mixing ratio.....84

Figure S12: Scatter plot of $k_{\text{HO}_2+\text{HO}_2}$ for the measurements and EMAC. The water dependence causes a maximum deviation of about factor 2, as EMAC slightly underestimated water vapor.....84

Figure S13: Diurnal variation of H₂O₂ ($\pm 1\sigma$) over the Mediterranean Sea (MS) for the observations (green) and EMAC (orange).....85

Figure S14: Frequency distributions of the HCHO observations (black) and the EMAC model results (orange) for the eight regions encountered during AQABA.....85

Figure S15: Frequency distributions of the H₂O₂ observations (black) and the EMAC model results (orange) for the eight regions encountered during AQABA.....86

Figure S16: Frequency distributions of the ROOH observations (black) and the EMAC model results (orange) for the eight regions encountered during AQABA.....86

Dienhart et al. 2021:

Figure 1: The shiptrack (black) of the Kommandor Iona during the AQABA cruise subdivided into eight regions: Mediterranean sea (MS: yellow), Suez Canal (SU: pink), Red Sea North (RN: orange), Red Sea South (RS: green), Gulf of Aden (GA: blue), Arabian Sea (AS: turquoise), Gulf of Oman (GO: brown) and Arabian Gulf (AG: red).....91

Figure 2: Time series of HCHO, OH, R(OH) and the HCHO photolysis (j_{HCHO} , sum of the molecular and the radical channel) in 5 min resolution. For the boundary layer height (BLH) we used the ERA-5 meteorological reanalysis data in hourly averages, which resolves the earth's atmosphere on a 30 km grid (<https://www.ecmwf.int/en/forecasts/datasets/reanalysis-datasets/era5>).....93

Figure 3: HCHO loss rates due to reaction with OH, photolysis, dry deposition and the total sink as the sum of all three processes.....93

Figure 4: Scatter plots with bivariate fits (York et al., 2004) of the product $[\text{OH}] \times \text{R}(\text{OH})_{\text{eff}}$ ($\pm 58\%$) versus the HCHO production rate $\text{P}(\text{HCHO})$ ($\pm 62\%$), subdivided into the different regions probed during the AQABA cruise. The slope of the respective regression represents the HCHO yield α_{eff} , while the intercept can be interpreted as additional HCHO sources not related to OH chemistry ($\text{P}_{\text{add}}(\text{HCHO})$).....94

Figure 5: Scatter plots of the contribution of certain substance classes $\text{R}(\text{OH})_x$ (e.g. alkanes, alkenes, OVOCs, aromatics) to the total OH reactivity without the contribution of inorganic reactions ($[\text{R}(\text{OH})_x/\text{R}(\text{OH})_{\text{eff}}]$) versus the HCHO yield α_{eff} (calculated with $\text{R}(\text{OH})_{\text{eff}}$ via Eq. 6). The z-axis was color-coded with the measured NO_x median values, representative for the nine different regions during AQABA (Table 1).....98

Figure 32: O₃ observations highlight two air pollution maxima (1. & 2. event) in the center of the Arabian Gulf during the first leg. HYSPLIT trajectories indicate mainly transport from Iraq during the high O₃ conditions with less influence of the Iranian coastline.....104

Figure 33: Trace gas observations during the first leg highlight the complexity and variability of air pollution over the Arabian Gulf, with two major air pollution events and the highest O₃ mixing ratios during AQABA.....105

Figure 34: Trace gas observations over the Arabian Gulf during the second leg. Further air pollution events were encountered after leaving the harbor of Kuwait, with elevated O₃, HCHO, ROOH and several other VOCs.....106

Figure 35: O₃ measurements and HYSPLIT air mass trajectories for the Arabian Gulf during the second leg. Further pollution events were encountered after leaving the harbor of Kuwait (left), while the center of the Gulf was characterized by cleaner conditions compared to the first leg, with air masses mostly originating from Iran and the Zagros Mountains (right). Elevated O₃ was again detected while sailing close to Dubai.....107

Figure 36: Flaring sources detected by the NASA/NOAA Visible Infrared Imaging Radiometer Suite during 2017 based on Paris et al. (2021). The dot size is proportional to the highest observed radiative heat (in MW), which is related to the total volume of gas flared (Elvidge et al., 2016). Flaring occurs mostly at the upstream production sites and is therefore a proxy for the presence of extraction and production sites. Flaring spots were retrieved from http://skytruth.org (last access: 16 April 2019), the background map by ©OpenStreetMap. Distributed under the Open Data Commons Open Database License (ODbL) v1.0.....	108
Figure 37: Box and whisker plot of the HCHO / NO ₂ ratio as indicator for NO _x (≥ 2, red line) and VOC (≤ 1, green line) limitation of ozone production (Duncan et al. 2010) based on Tadic et al. (2020). The black line represents median values, the box 25 – 75 % and the whiskers 10 – 90 % of the data.....	109
Figure 38: Chromatograms of the HPLC prove the abundance of methyl hydroperoxide (MHP), peracetic acid (PAA) and ethyl hydroperoxide (EHP) in polluted encountered over the Arabian Gulf during the second leg (04.08.17), when we observed winds coming from Iraq and Kuwait (3.). The air masses originating from Iran (4.) did not contain elevated ROOH.....	109
Figure 39: Observations of HCHO (green), H ₂ O ₂ (blue) and ROOH (violet) compared to the EMAC (orange) and WRF-Chem (red) results in 10 minute averages. No ROOH results were available based on WRF-Chem.....	110
Figure 40: WRF-Chem results for mean O ₃ at the surface (a, left) and daily maximum 8-hourly O ₃ (b, right) based on Osipov et al. (2022).....	111
Figure 41: Timeline of the O ₃ results based on WRF-Chem (orange, Osipov et al. 2022) compared to the observations (blue).....	112
Figure 42: Diurnal variation of H ₂ O ₂ , ROOH and HCHO over the Arabian Sea (08.08. – 13.08.2017) and the Mediterranean Sea (25.08. – 31.08.2017) on the basis of the respective mean (black) and median (grey) values and the general variability within the region (± 1σ) as 10 minute averages.....	113
Figure 43: Diurnal variation of OH and HO ₂ over the Arabian Sea (08.08. – 13.08.2017) and the Mediterranean Sea (25.08. – 31.08.2017) on the basis of the respective mean (black) and median (grey) values and the general variability within the region (± 1σ) as 10 minute averages.....	115
Figure 44: Timelines of trace gas measurements for the Arabian Sea during the second leg.....	116
Figure 45: GPS Plot of the hydrogen peroxide / organic peroxide – ratio for the first (left) and second leg (right) of the AQABA campaign. The Arabian Sea and the southern Red Sea (first leg) were dominated by H ₂ O ₂ , while ROOH excess was detected over the Arabian Gulf and parts of the Suez Canal during the first leg.....	117
Figure 46: Timelines of NO, HCHO, H ₂ O ₂ , ROOH and j _{NO2} during dust storm events over the southern Red Sea and the Gulf of Aden, indicated by the particle surface area concentrations of PS ₁₀ – PS ₁ (all particles between 1 – 10 μm), which represents mostly large dust particles. Passing the strait of Bab-el-Mandeb is indicated by the black lines.....	118
Figure 47: Timelines of NO, HCHO, H ₂ O ₂ , ROOH and j _{NO2} over the southern Red Sea and the Gulf of Aden during the less dusty conditions of the second leg, indicated by the particle surface area concentrations of PS ₁₀ – PS ₁ (all particles between 1 – 10 μm), which represents mostly large dust particles. Passing the strait of Bab-el-Mandeb is indicated by the black lines.....	119
Figure SU1: GPS plots of the O ₃ measurements during AQABA, separated into the first (left) and the second leg (right) in hourly averages. Highest O ₃ was observed in the polluted air masses over the Arabian Gulf with up to ~167 ppb _v O ₃ during the first leg. Cleanest conditions were observed the Arabian Sea (≤ 35 ppb _v).....	130
Figure SU2: Timelines of the O ₃ measurements (blue) and EMAC model results (orange) during AQABA.....	130
Figure SU3: GPS plots of the CO measurements based on Cavity Ring-Down Spectroscopy (CRDS) during AQABA, separated into the first (left) and the second leg (right) in hourly averages. Similar to the observed O ₃ , highly elevated CO was detected over the Arabian Gulf during the first leg with winds from Iraq / Kuwait (up to 307 ppb _v). Less CO was abundant over the center of the Gulf in air masses originating from the Zagros Mountains	

(Iran) during the second leg (~120 ppb _v). Cleanest conditions were observed over the Arabian Sea with (~55 ppb _v CO).....	131
Figure SU4: Timelines of the CO EMAC results (orange) and measurements based on Cavity Ring-Down Spectroscopy (CRDS, brown) and Tunable Diode Laser Absorption Spectroscopy (blue) during AQABA. Sharp increases of CO were observed in ship exhausts and further anthropogenic emission sources, which were used to set up the ship exhaust filter.....	131
Figure SU5: Timelines of the CH ₄ measurements based on Cavity Ring-Down Spectroscopy (blue) and EMAC results (orange) during AQABA.....	132
Figure SU6: GPS plot of the HCHO / CO ratio based on the measurements during AQABA, separated into the first (left) and the second leg (right) in hourly averages.....	132
Figure SU7: GPS plot of the HCHO / ROOH ratio based on the measurements during AQABA, separated into the first (left) and the second leg (right) in hourly averages.....	132
Figure SU8. Overview of mixing ratios for aliphatic, aromatic and unsaturated carbonyl compounds (C _x H _y O) measured during AQABA based on Wang et al. (2020). The box represents 25% to 75% of the data with the central line and square indicating the median value and the mean value respectively. The whiskers show data from 5% to 95% and stars were drawn for the minimum and maximum data points within 1% to 99% of the dataset. The bracket under the region acronym indicates the main characters of the air mass in the region, which was determined based on variability-lifetime results (b factor) from Bourtsoukidis et al. (2019) and acetone mixing ratios (Wang et al 2020).....	133
Figure SU9: Timelines of the major VOCs used in this thesis acetone (orange), methyl ethyl ketone (MEK, blue), acetaldehyde (light green), methanol (violet) and formaldehyde (dark green).....	133
Figure SU10: Scatter plot of acetone, acetaldehyde, methyl ethyl ketone (MEK) and methanol versus the formaldehyde observations for the Arabian Gulf (27.07. – 04.08.2017).....	134
Figure SU11: Timelines of the NO observations in comparison with EMAC model results during AQABA. Please note that this graph only presents NO data up to 5 ppb _v to compare rather clean conditions. NO reached mixing of more than 300 ppb _v in ship exhausts, further details can be found in Tadic et al. (2020).....	134
Figure SU12: Timelines of the OH production according to measurements (blue) and EMAC results (orange). Reaction rate for the primary OH production through O ¹ D + H ₂ O, production of O ¹ D by O ₃ photolysis and secondary OH production through HO ₂ + NO and photolysis of H ₂ O ₂ . The secondary production through does not match the observations, due to overestimated HO ₂ and low accuracy of NO in clean conditions. OH production through H ₂ O ₂ photolysis is overestimated, but it anyway only accounts for a few percent of OH production in total.....	135
Figure SU13: Timelines of the particle surface area concentrations of all particles ≤ 10 μm (PS ₁₀), particles ≤ 1 μm (PS ₁) and the calculated large particles (PS ₁₀ – PS ₁) which mainly represented dust particles around the Arabian Peninsula. Highest amounts of dust were observed during the dust storm events (RS, GA).....	135
Figure SU14: Flaring sources detected by the NASA/NOAA Visible Infrared Imaging Radiometer Suite during 2017 (left) based on Paris et al. (2021) and multi-annual map of HCHO based on TROPOMI satellite observations of DeSmedt et al. (2021).....	136
Figure SU15: Timelines of the HCHO measurements (blue) and the WRF Chem model results (orange, Osipov et al., 2022) during AQABA.....	136
Figure SU16: Timelines of the H ₂ O ₂ measurements (blue) and the WRF Chem model results (orange, Osipov et al., 2022) during AQABA.....	137
Figure SU17: Timelines of the sum of measured H ₂ O ₂ + ROOH (blue) and the H ₂ O ₂ WRF Chem model results (orange, Osipov et al., 2022) during AQABA.....	137

Figure SU18: Timelines of the OH measurements (blue) and the WRF Chem model results (orange, Osipov et al., 2022) during AQABA.....	138
Figure SU19: Timelines of the HO ₂ measurements (blue) and the WRF Chem model results (orange, Osipov et al., 2022) during AQABA.....	138
Figure SU20: Timelines of the CO measurements (blue) and the WRF Chem model results (orange, Osipov et al., 2022) during AQABA.....	139
Figure SU21: Timelines of the NO ₂ measurements (blue) and the WRF Chem model results (orange, Osipov et al., 2022) during AQABA.....	139
Figure SU22: Sampling of the H ₂ O ₂ gas standard in impinger flasks, which are stored in a refrigerator.....	143

6.3 Figures

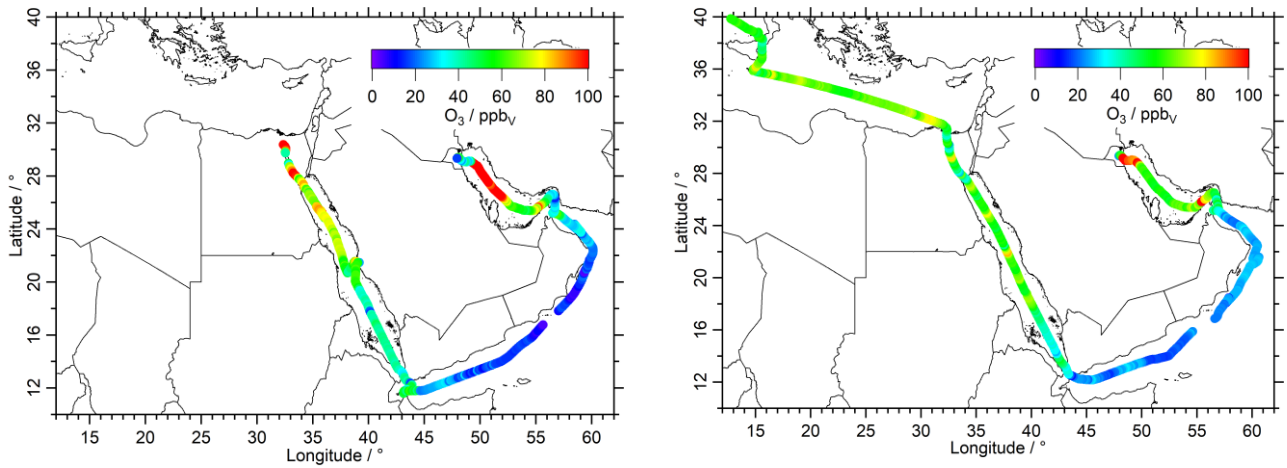


Figure SU1: GPS plots of the O₃ measurements during AQABA, separated into the first (left) and the second leg (right) in hourly averages. Highest O₃ was observed in the polluted air masses over the Arabian Gulf with up to ~167 ppbv O₃ during the first leg. Cleanest conditions were observed the Arabian Sea (≤ 35 ppbv).

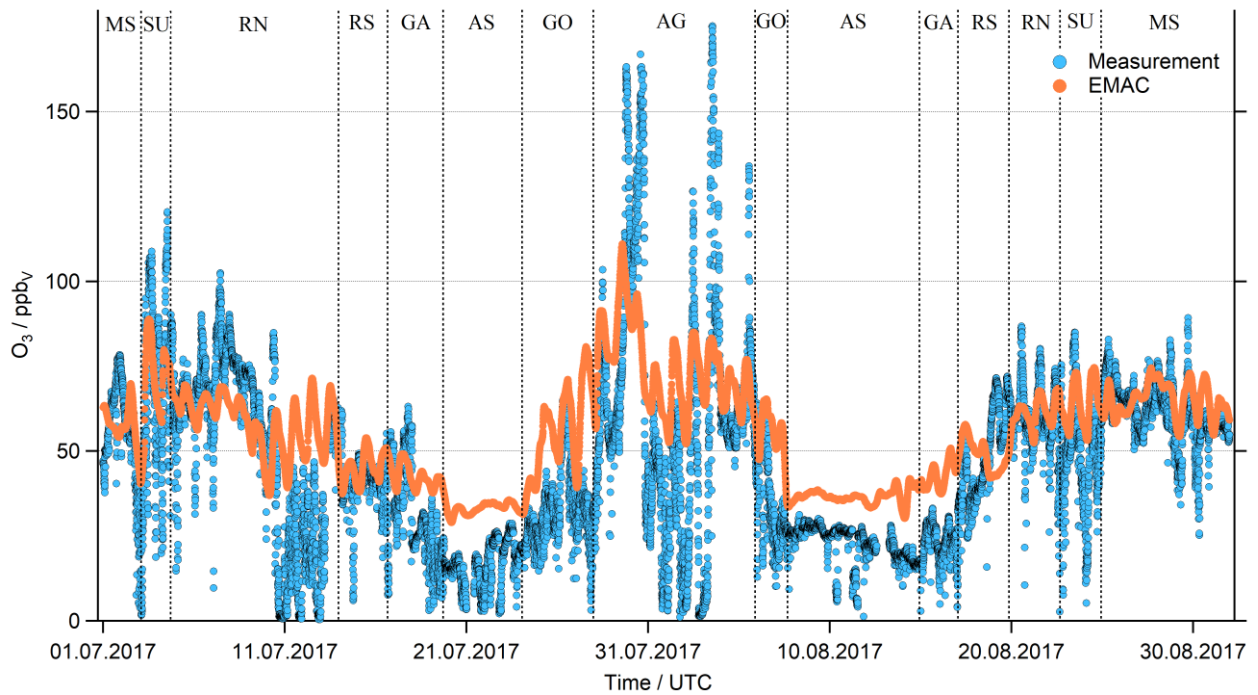


Figure SU2: Timelines of the O₃ measurements (blue) and EMAC model results (orange) during AQABA.

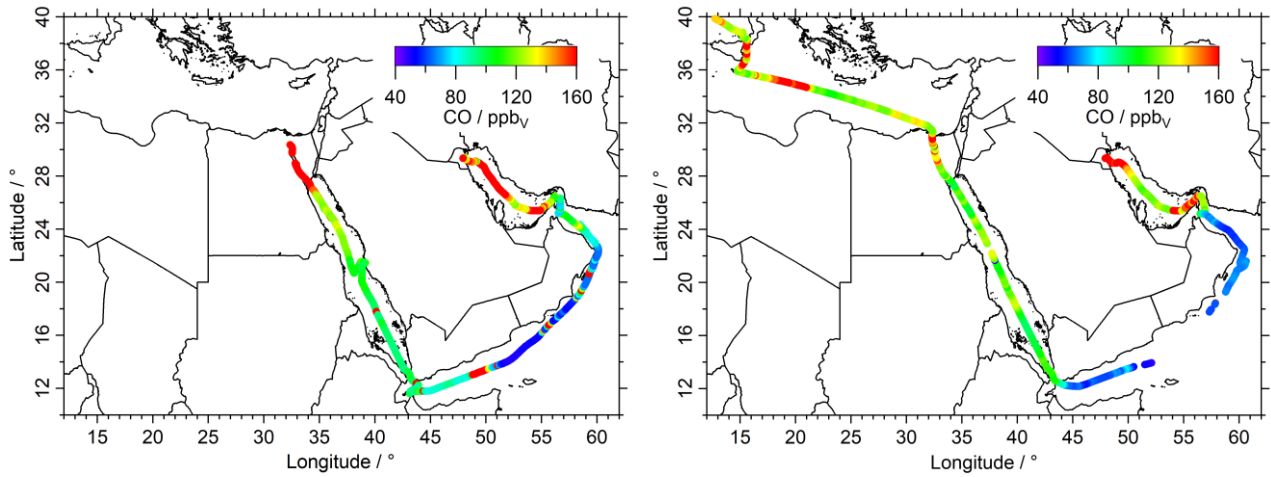


Figure SU3: GPS plots of the CO measurements based on Cavity Ring-Down Spectroscopy (CRDS) during AQABA, separated into the first (left) and the second leg (right) in hourly averages. Similar to the observed O₃, highly elevated CO was detected over the Arabian Gulf during the first leg with winds from Iraq / Kuwait (up to 307 ppb_v). Less CO was abundant over the center of the Gulf in air masses originating from the Zagros Mountains (Iran) during the second leg (~120 ppb_v). Cleanest conditions were observed over the Arabian Sea with (~55 ppb_v CO).

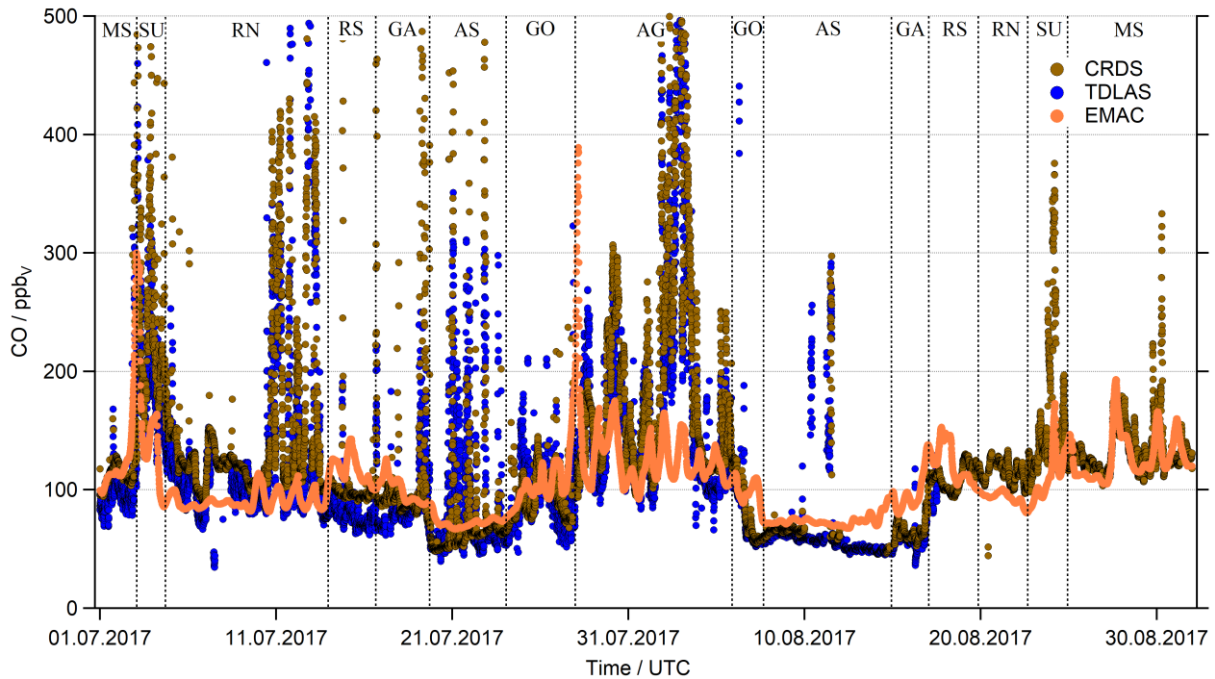


Figure SU4: Timelines of the CO EMAC results (orange) and measurements based on Cavity Ring-Down Spectroscopy (CRDS, brown) and Tunable Diode Laser Absorption Spectroscopy (blue) during AQABA. Sharp increases of CO were observed in ship exhausts and further anthropogenic emission sources, which were used to set up the ship exhaust filter.

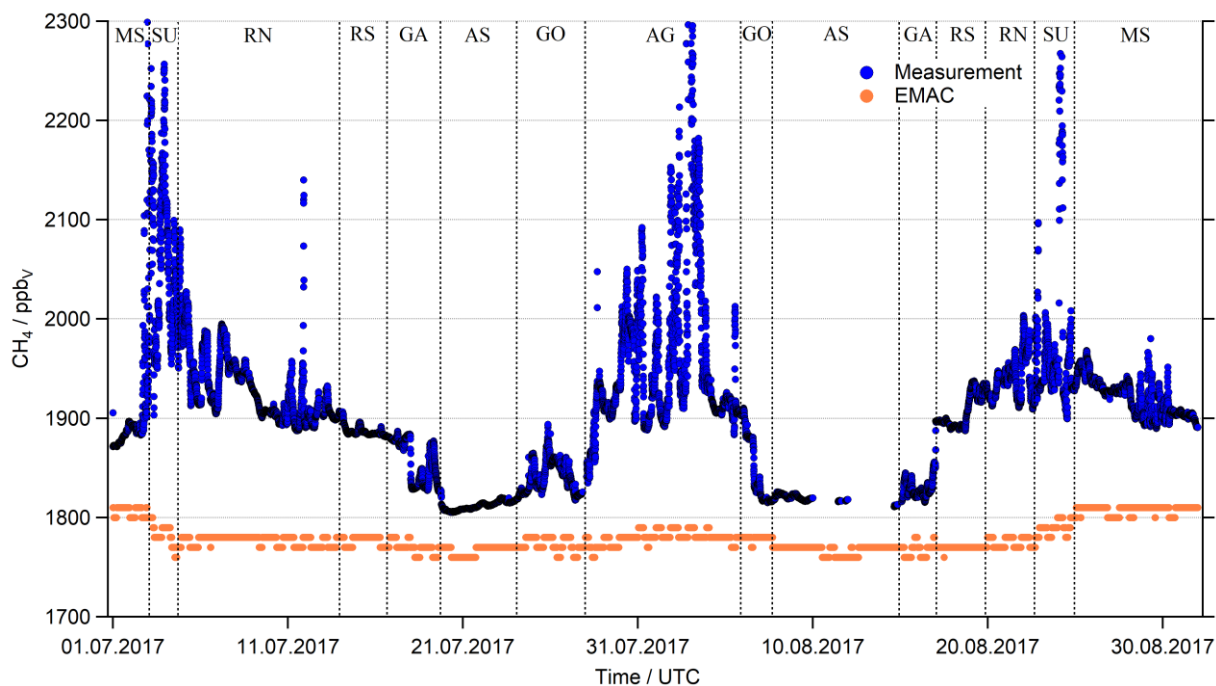


Figure SU5: Timelines of the CH₄ measurements based on Cavity Ring-Down Spectroscopy (blue) and EMAC results (orange) during AQABA.

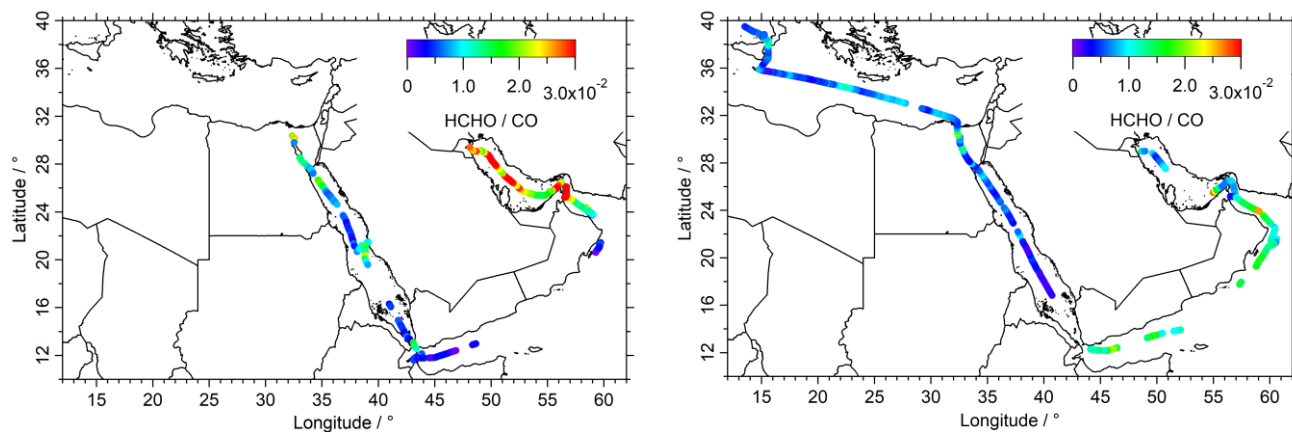


Figure SU6: GPS plot of the HCHO / CO ratio based on the measurements during AQABA, separated into the first (left) and the second leg (right) in hourly averages.

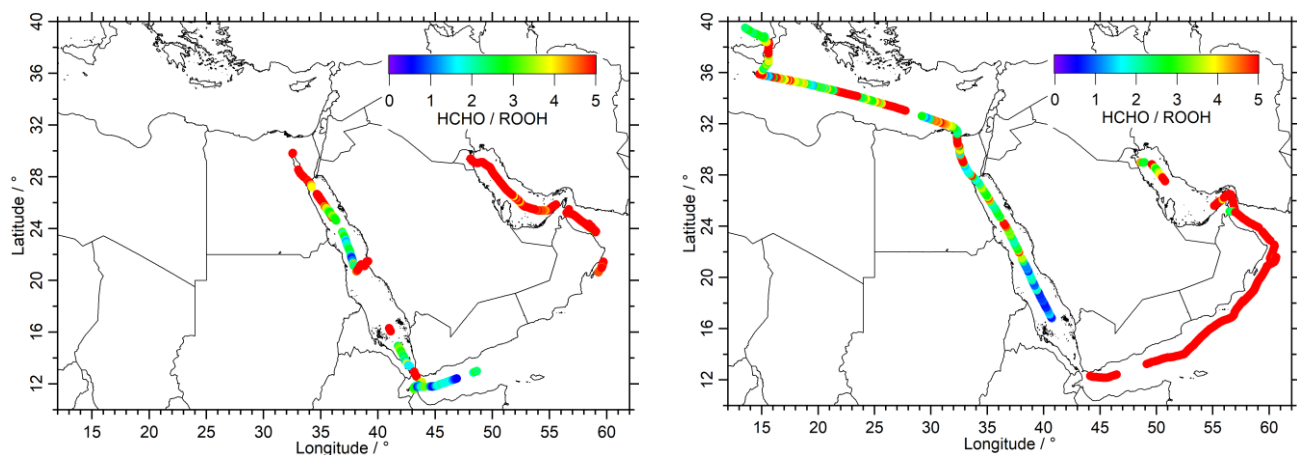


Figure SU7: GPS plot of the HCHO / ROOH ratio based on the measurements during AQABA, separated into the first (left) and the second leg (right) in hourly averages.

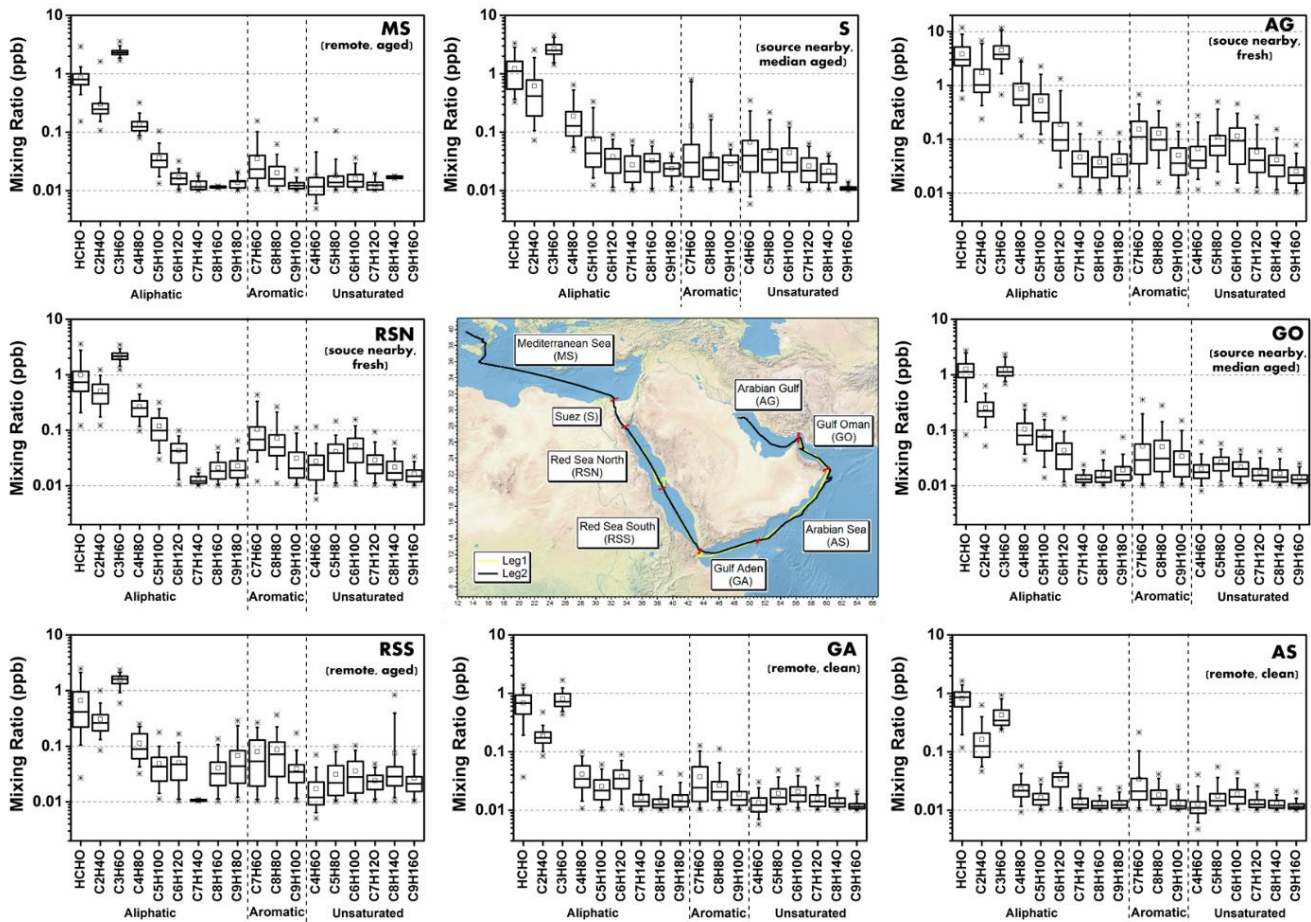


Figure SU8. Overview of mixing ratios for aliphatic, aromatic and unsaturated carbonyl compounds (C_xH_yO) measured during AQABA based on Wang et al. (2020). The box represents 25% to 75% of the data with the central line and square indicating the median value and the mean value respectively. The whiskers show data from 5% to 95% and stars were drawn for the minimum and maximum data points within 1% to 99% of the dataset. The bracket under the region acronym indicates the main characters of the air mass in the region, which was determined based on variability-lifetime results (b factor) from Bourtsoukidis et al. (2019) and acetone mixing ratios (Wang et al 2020).

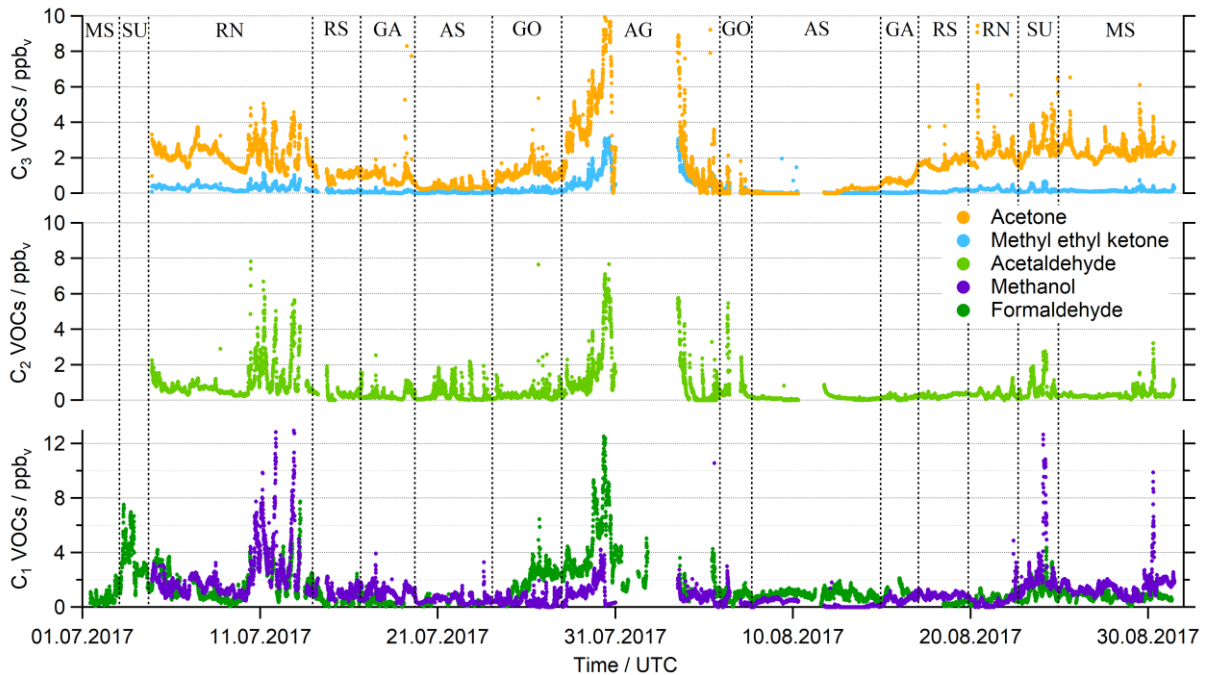


Figure SU9: Timelines of the major VOCs used in this thesis acetone (orange), methyl ethyl ketone (MEK, blue), acetaldehyde (light green), methanol (violet) and formaldehyde (dark green).

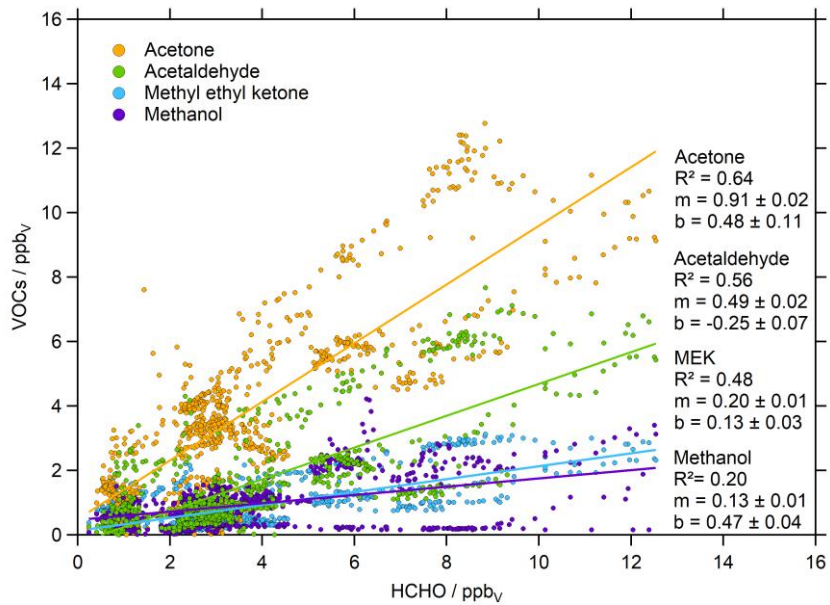


Figure SU10: Scatter plot of acetone, acetaldehyde, methyl ethyl ketone (MEK) and methanol versus the formaldehyde observations for the Arabian Gulf (27.07. – 04.08.2017)

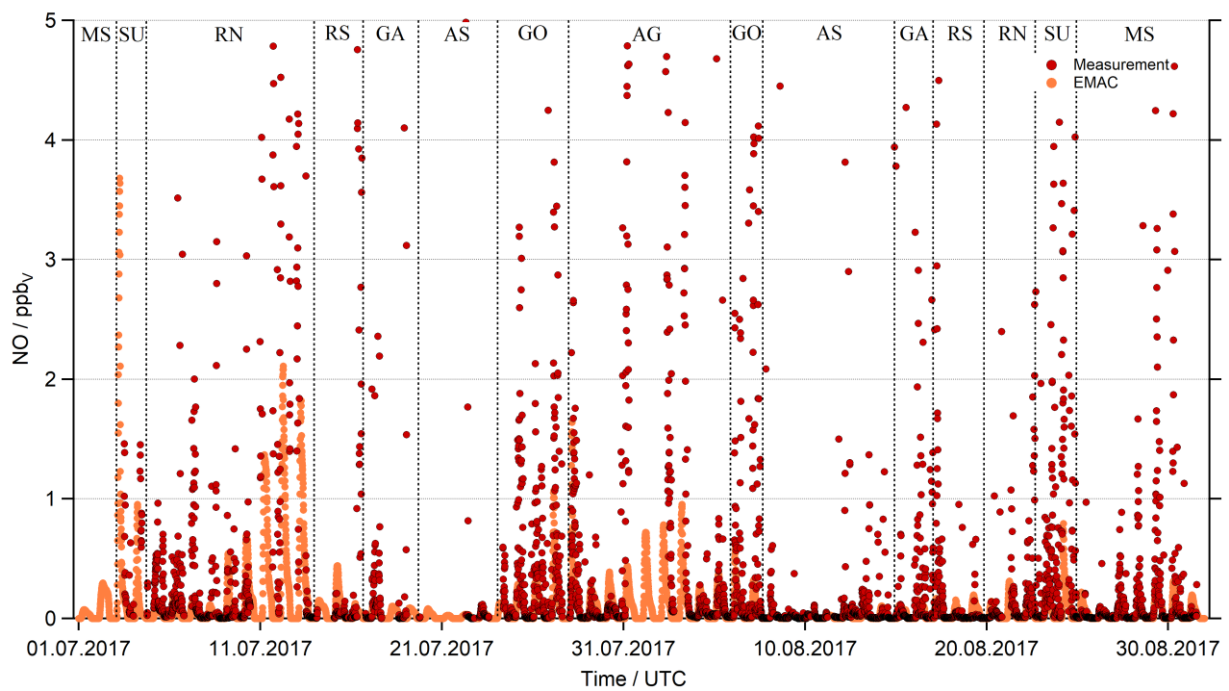


Figure SU11: Timelines of the NO observations in comparison with EMAC model results during AQABA. Please note that this graph only presents NO data up to 5 ppbv to compare rather clean conditions. NO reached mixing of more than 300 ppbv in ship exhausts, further details can be found in Tadic et al. (2020).

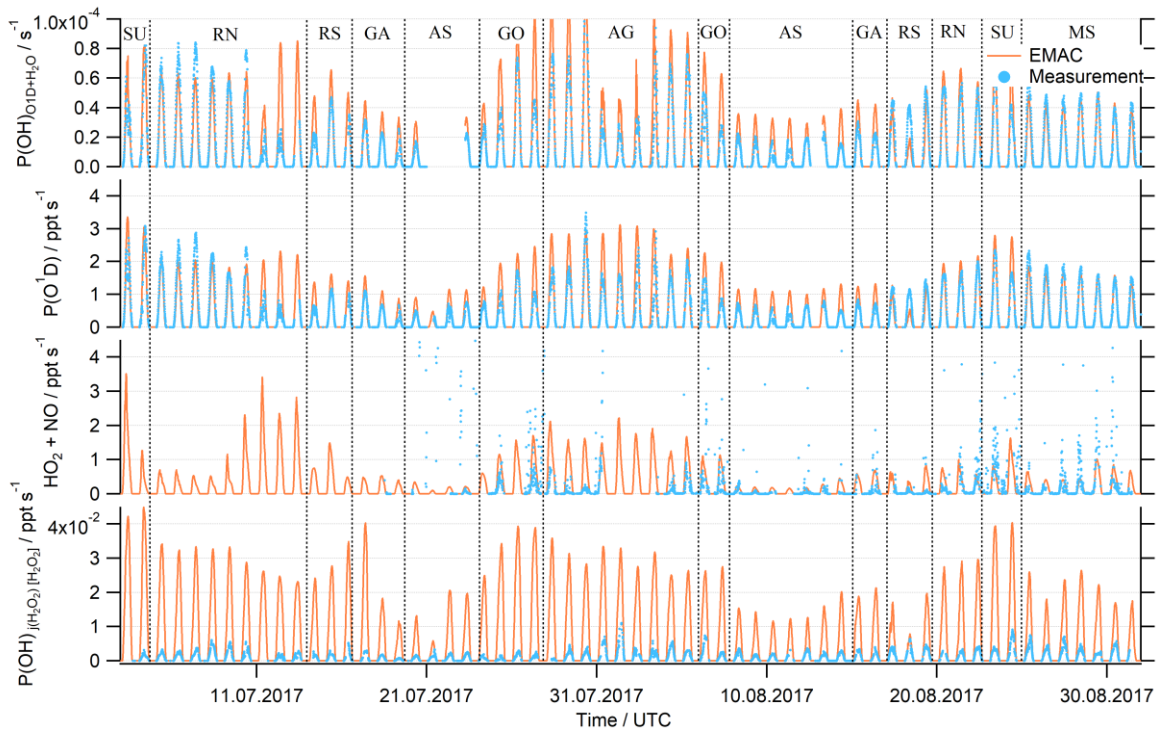


Figure SU12: Timelines of the OH production according to measurements (blue) and EMAC results (orange). Reaction rate for the primary OH production through $O^1D + H_2O$, production of O^1D by O_3 photolysis and secondary OH production through $HO_2 + NO$ and photolysis of H_2O_2 . The secondary production through does not match the observations, due to overestimated HO_2 and low accuracy of NO in clean conditions. OH production through H_2O_2 photolysis is overestimated, but it anyway only accounts for a few percent of OH production in total.

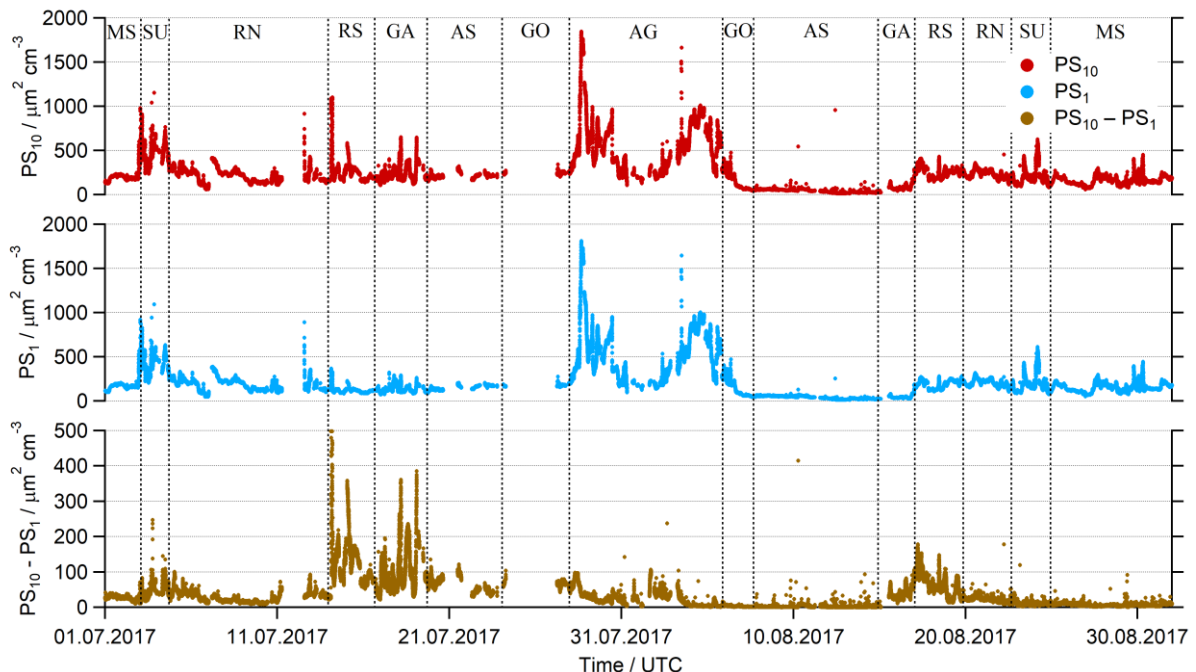
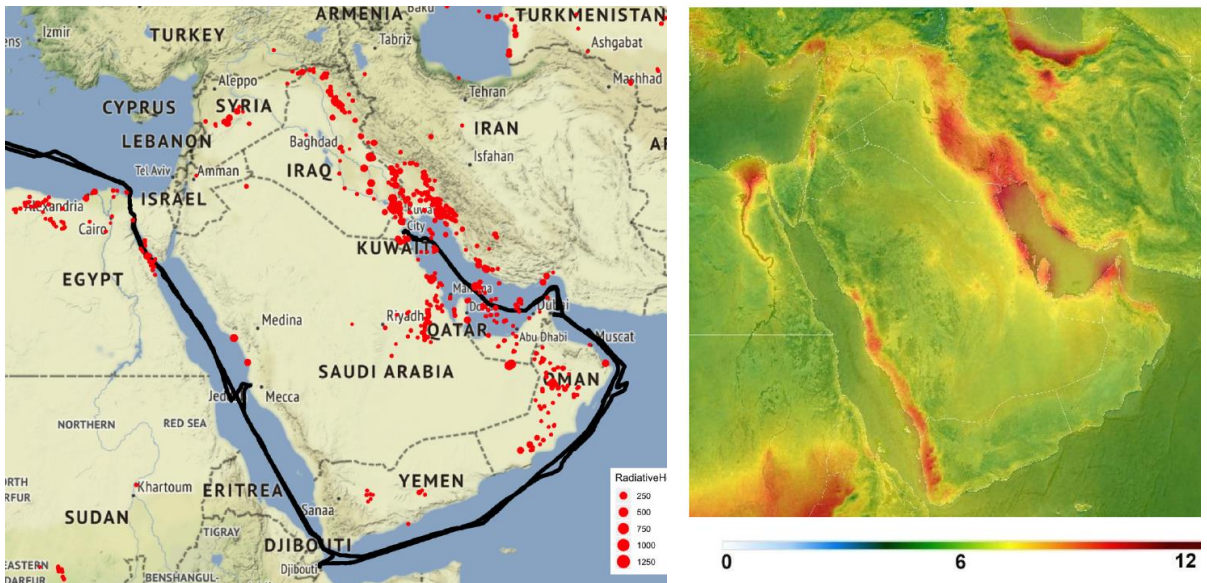


Figure SU13: Timelines of the particle surface area concentrations of all particles $\leq 10 \mu m$ (PS_{10}), particles $\leq 1 \mu m$ (PS_1) and the calculated large particles ($PS_{10} - PS_1$) which mainly represented dust particles around the Arabian Peninsula. Highest amounts of dust were observed during the dust storm events (RS, GA).



Arabic Peninsula (max.scale: 12×10^{15} molec.cm)

Figure SU14: Flaring sources detected by the NASA/NOAA Visible Infrared Imaging Radiometer Suite during 2017 (left) based on Paris et al. (2021) and multi-annual map of HCHO based on TROPOMI satellite observations of DeSmedt et al. (2021).

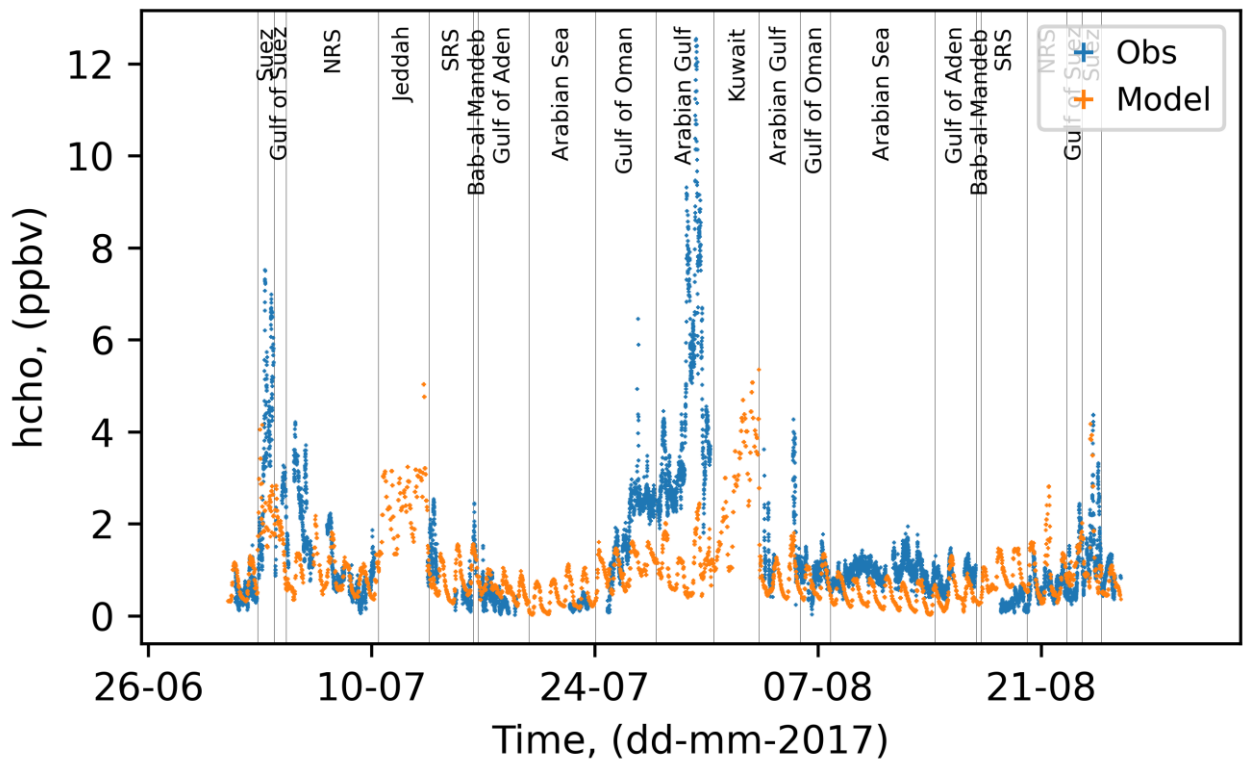


Figure SU15: Timelines of the HCHO measurements (blue) and the WRF Chem model results (orange, Osipov et al., 2022) during AQABA.

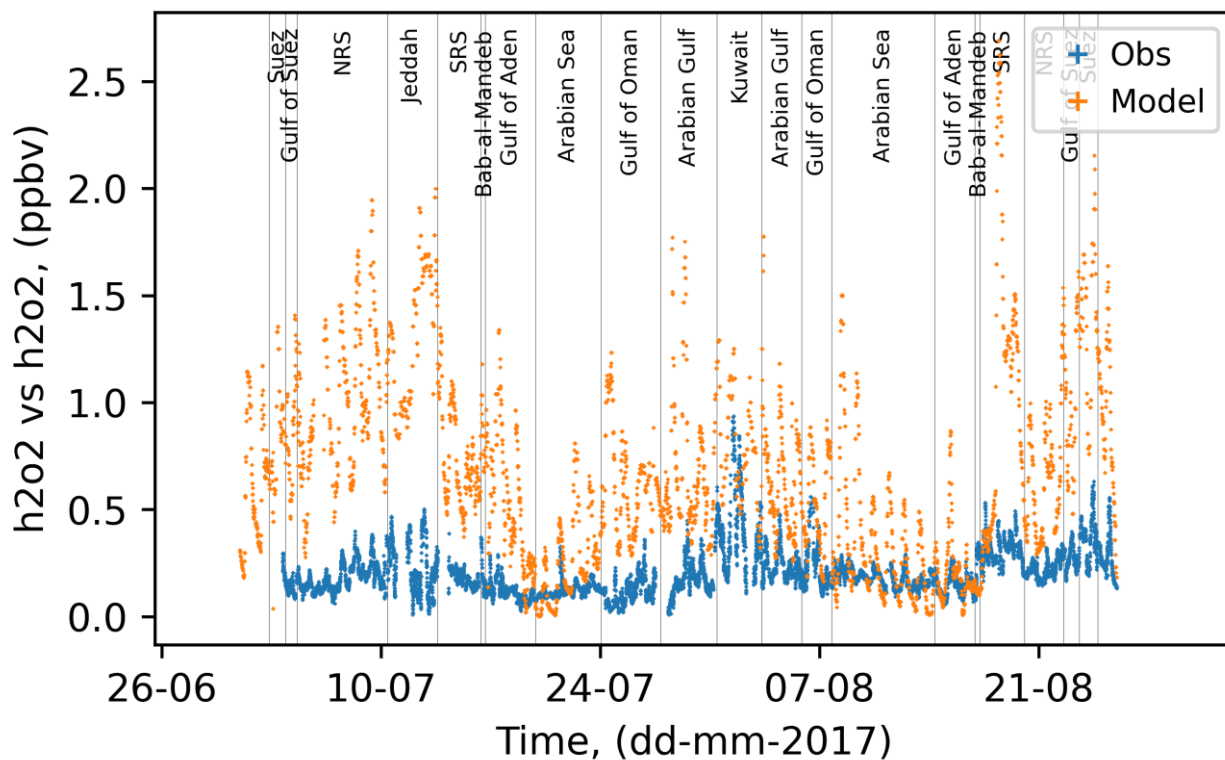


Figure SU16: Timelines of the H_2O_2 measurements (blue) and the WRF Chem model results (orange, Osipov et al., 2022) during AQABA.

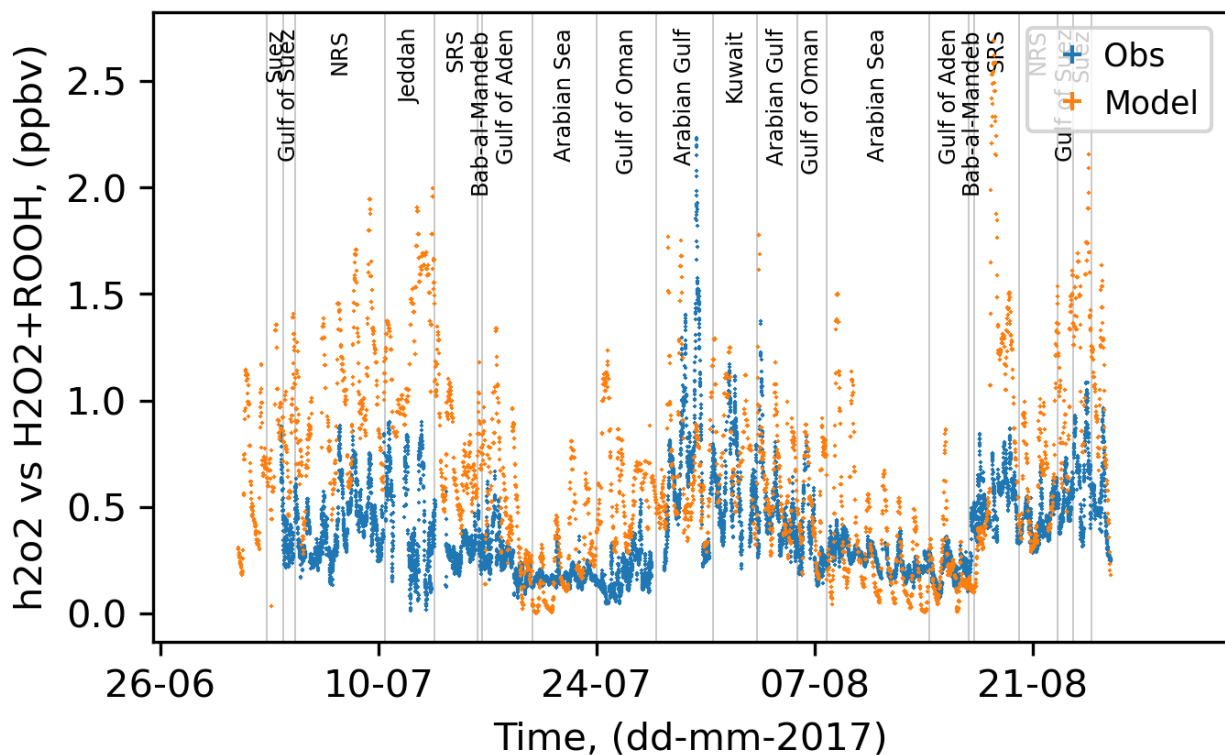


Figure SU17: Timelines of the sum of measured $\text{H}_2\text{O}_2 + \text{ROOH}$ (blue) and the H_2O_2 WRF Chem model results (orange, Osipov et al., 2022) during AQABA.

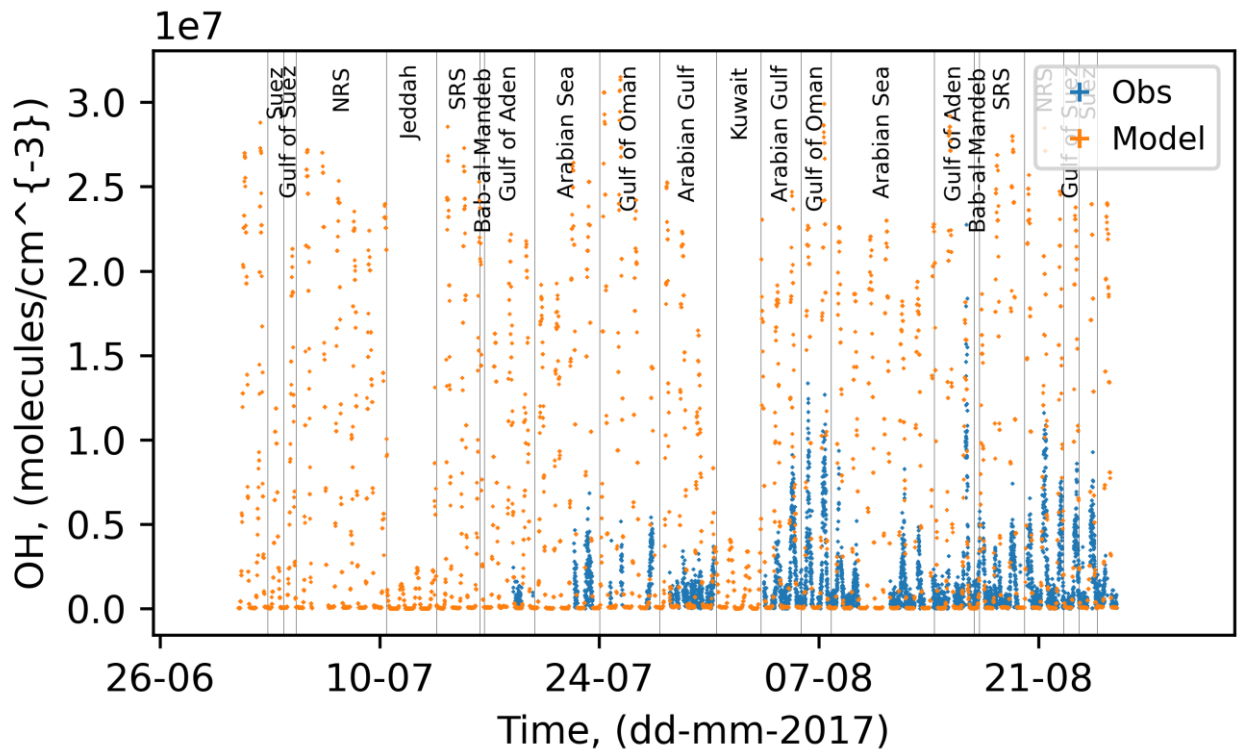


Figure SU18: Timelines of the OH measurements (blue) and the WRF Chem model results (orange, Osipov et al., 2022) during AQABA.

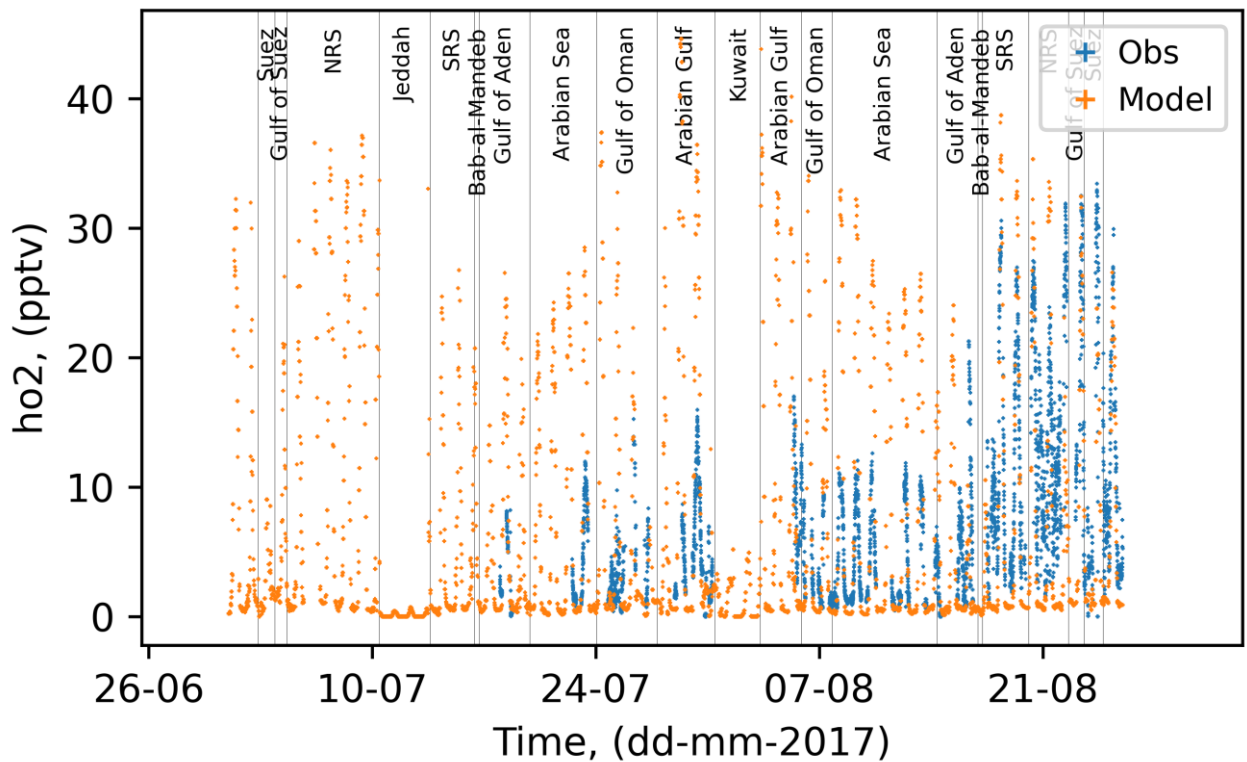


Figure SU19: Timelines of the HO₂ measurements (blue) and the WRF Chem model results (orange, Osipov et al., 2022) during AQABA.

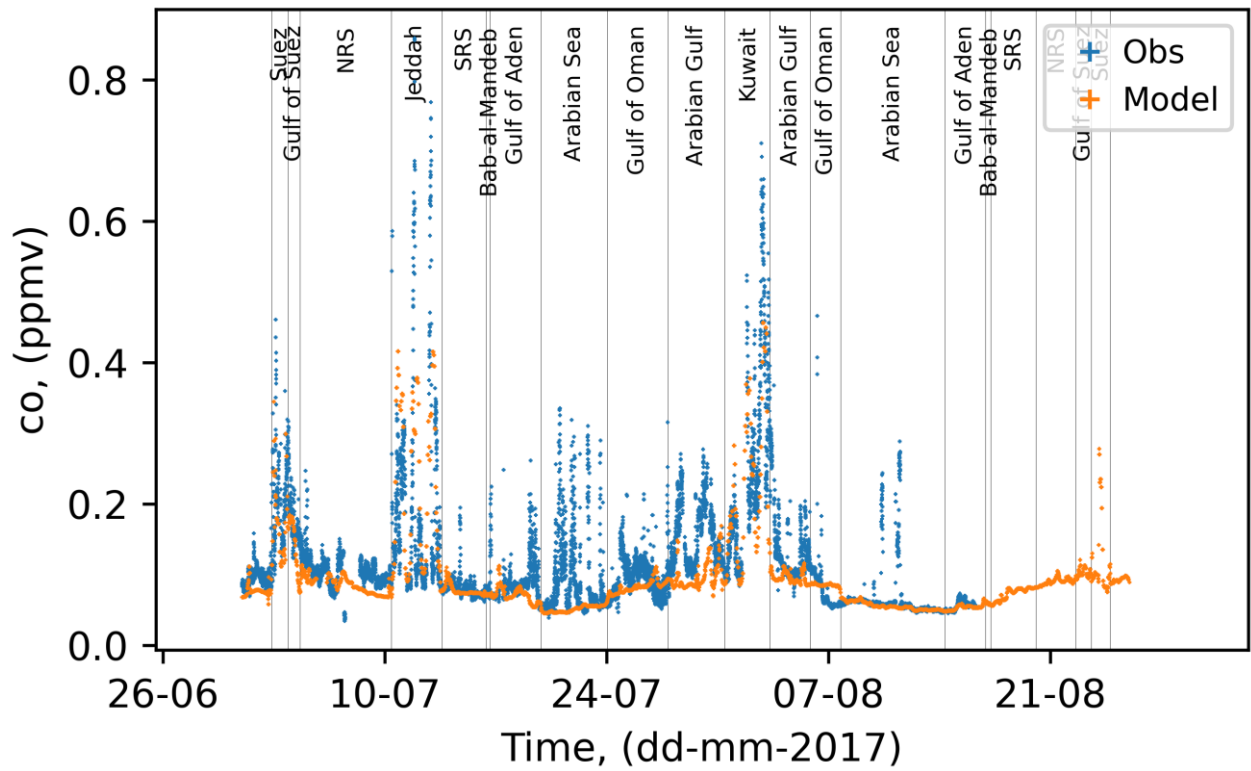


Figure SU20: Timelines of the CO measurements (blue) and the WRF Chem model results (orange, Osipov et al., 2022) during AQABA.

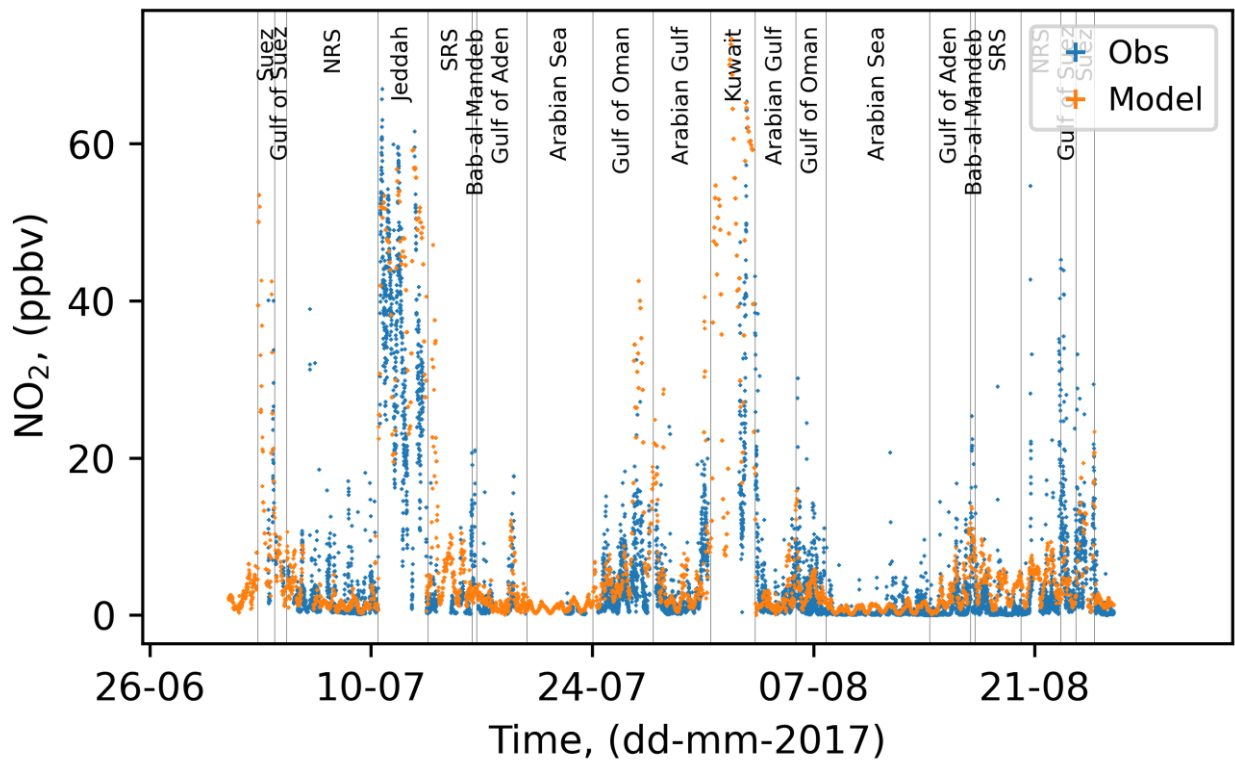


Figure SU21: Timelines of the NO₂ measurements (blue) and the WRF Chem model results (orange, Osipov et al., 2022) during AQABA.

6.4 Experimental Procedures

Formaldehyde measurements:

Basics for the operation of the AL4021:

Sampling solution:

15 mL H₂SO₄ (97 %) are diluted with 5 L of ultrapure water (H₂O) in a glass bottle and stored in a dark container, prevent HCHO from entering into the bottle (set up a pressure compensation with Hopcalite®).

Hantzsch reagent:

Fill 800 mL of cold ultrapure H₂O into a 5 L glass bottle, then add 385 g Ammonium Acetate and stir the solution until the salt is dissolved. Add 12.5 mL Acetic Acid and 10 mL Acetyl Acetone and fill up with cold ultrapure H₂O to 5 L. Store the Hantzsch reagent in a refrigerator and prevent HCHO from entering into the bottle (set up a pressure compensation with Hopcalite®).

HCHO liquid standards:

First, a HCHO stock solution is prepared by diluting 3 mL HCHO (37 %) with cooled ultrapure H₂O in a 1 L brown glass volumetric flask. After proper mixing, HCHO standards were prepared based on this solution which has a stable HCHO concentration for several weeks when stored properly in a refrigerator.

HCHO standards were prepared just before use by the dilution of 1:250 in duplicate with two 250 mL brown glass volumetric flasks. Shortly before the liquid calibration, 1 mL of HCHO stock solution was pipetted with a precision pipette (Eppendorf AG, Germany) and diluted with 249 mL cooled ultrapure water. Then the solution is mixed and the same dilution step is performed again with a new pipette tip and a cleaned and baked out 250 mL volumetric flask. These standards cannot be stored and have to be prepared freshly.

Titration of the HCHO stock solution:

First, prepare stock solutions ideally with ultrapure water and store them dark and cooled in a refrigerator:

1. Na₂SO₃ 0.25 M (0.63 g in 20 mL H₂O)
2. Acetic Acid 1 M (ampoule + fill up with H₂O in 500 mL volumetric flask)
3. Boric acid buffer (12.37 g H₃BO₃ + 100 mL 1 M NaOH, fill up with H₂O in 1000 mL volumetric flask, pH 9.2 @ 20 °C)
4. Na₂CO₃ 1 M (10.6 g in 100 mL H₂O)
5. I₂ 0.025 M (ampoule + fill up with H₂O in 2000 mL brown glass volumetric flask)
6. Starch solution (at least 1 g in 100 mL H₂O, I recommend to use a bit more and heat up to dissolve)

Cool all solutions in refrigerator to ~2 °C before the titration.

Use 300 mL Erlenmeyer flask and add 25 mL cooled H₂O, 25 mL H₃BO₃, 4 mL Na₂SO₃ and 10 mL HCHO stock solution. Cool the solution with ice or ideally ice/salt mixture to 0 – 2 °C and let it stir for at least 7 minutes. This step is crucial, as it is the derivatization step. Then add 5 mL acetic acid and 1 mL starch solution slowly while cooling. Do not increase the temperature of the solution by adding warmed up solutions. Excess SO₃²⁻ is then titrated with I₂, turnover is indicated by the grey-black Iodine-starch complex. Afterwards add 30 mL Na₂CO₃ solution, this will increase the pH and release the masked HCHO with the equimolar fraction of SO₃²⁻-ions. Titration of the released SO₃²⁻ with I₂ yields the HCHO in 10 mL stock solution.

$$[\text{HCHO}] = \frac{[\text{I}_2] \cdot V(\text{I}_2)}{V(\text{HCHO})}$$

HCHO gas standards:

Gaseous HCHO standards were set up with a paraformaldehyde permeation tube (VICI® AG, Switzerland) which was placed in a glass impinger flask heated to 60 °C and flushed constantly with synthetic air at a flow rate of 80 mL min⁻¹. The gaseous HCHO standard was diluted with ~3 L min⁻¹ zero gas just in front of the AL4021 inlet.

Determination of the HCHO gas phase concentration is achieved based on the chromotropic acid reaction (2.1.9). Therefore, 20 mg of chromotropic acid are dissolved in 10 mL H₂O and carefully mixed with 90 mL of H₂SO₄ (97 %) while simultaneously cooling the glass flask. Preheat the oven for the impinger flasks to 70 °C and use 10 mL of the chromotropic acid mixture in each flask. Connect two of these flasks with PFA tubing and seal them carefully. Start the measurement by placing the HCHO gas standard outlet (1/8" PFA tubing) into the liquid of the first impinger flask and determine the injection time with a stopwatch. After roughly 4 hours the sampling flask should have turned violet. The second flask (breakthrough of HCHO) and the third flask as blank should still be transparent and will be used to determine the background signal. Seal the flasks and cool down the solutions in a water bath.

Determination of the HCHO concentration is then performed by spectrophotometric analysis of the synthesized dye at $\lambda = 580 \text{ nm}$ (Thermo Fisher Genesys™ 10S UV-Vis) via the Lambert-Beer-law.

$$A = c \cdot d \cdot \varepsilon$$

With A as the absorbance, c as the concentration, d as the diameter of the cuvette (1 cm) and ε as the molar absorption coefficient (17620 L mol⁻¹ cm⁻¹). The background signal of the absorbance was subtracted with the blank vial. The permeation rate p(HCHO) was then calculated with the pipetted volume (0.01 L) and the reaction time, which was afterwards converted into the respective mixing ratio with the flow rate (Q) and the molar volume of an ideal gas (V_m).

$$p(\text{HCHO}) = c \cdot V \cdot \frac{1}{t}$$
$$\text{HCHO} = \frac{p(\text{HCHO}) \cdot V_m}{Q}$$

The inlet efficiency can then be determined by injection of gaseous HCHO standards once into the sampling inlet and another injection near the AL4021 inlet.

Hydrogen peroxide and organic peroxide measurements:

Basic solvents for the operation of the AL2021:

Sodium hydroxide:

50 mL of NaOH (1 M) are diluted with ultrapure H₂O to 2 L in a glass bottle.

Potassium hydrogen phthalate (KHP) buffer:

41 g KHP and 185 mL of NaOH (1 M) are diluted to 5 L with ultrapure water. The pH-value of this solution should ideally be between 5.8 and 6.0 at room temperature and can be adjusted by the addition of HCl or NaOH solutions. Subsequently, 100 mg of Ethylenediaminetetraacetic acid (EDTA) and 1 mL of HCHO (37 %) are added to the solution and stirred for a few minutes.

Fluorescence reagent:

Dissolve 500 mg of *p*-Hydroxyphenylacetic acid (POPHA) and 30 mg of horseradish peroxidase (HRP) in 2 L of KHP buffer.

Sampling / stripping solution:

Dilute 500 mL of KHP buffer with 4.5 L of ultrapure H₂O.

Sample conditioner without Catalase:

2 L of KHP buffer are used as the sample conditioner.

Sample conditioner with Catalase:

Dilute 1 mL of Catalase (from bovine liver) with 99 mL of KHP buffer in a volumetric flask two or three days before use and store the Catalase stock in a refrigerator.

Depending on the activity of the Catalase stock, approximately 20 mL of it are diluted to 2 L with KHP buffer. If the destruction efficiency of H₂O₂ is not satisfying add more Catalase stock to the Conditioner. The Catalase efficiency starts to increase after a few days after preparing the stock solution.

2 L of KHP buffer are used as the sample conditioner.

H₂O₂ liquid standards:

A stock solution of H₂O₂ is prepared by the dilution of 1 mL H₂O₂ (30 %) with cooled ultrapure water in a brown glass volumetric flask. This stock solution is kept at all times in the refrigerator and just taken out shortly for the preparation of H₂O₂ standards. When stored properly, the H₂O₂ concentration is stable for several weeks.

H₂O₂ standards were prepared just before use by the dilution of 1:100 in duplicates with two 100 mL brown glass volumetric flasks. Shortly before the liquid calibration, 1 mL of H₂O₂ stock solution was pipetted with a precision pipette (Eppendorf AG, Germany) and diluted with 99 mL cooled ultrapure water. Then the solution is mixed and the same dilution step is performed again with a new pipette tip and a cleaned and baked out 100 mL volumetric flask.

Titration of the H₂O₂ stock solution:

Prepare the KMnO₄ solution (0.002 M) with ultrapure water and store it in a brown glass flask in a refrigerator. The titration of the H₂O₂ stock is performed by adding 2 droplets of concentrated H₂SO₄ into 10 mL H₂O₂ stock solution and the titration against MnO₄⁻. Use a bright background for a better identification of the turnover, so that excess of MnO₄⁻ is easy to identify.

$$[\text{H}_2\text{O}_2] = \frac{5 [\text{KMnO}_4] \cdot V(\text{KMnO}_4)}{2 V(\text{H}_2\text{O}_2)}$$

Gaseous H₂O₂ standards:

Several different permeation devices have been tested for validation of gaseous H₂O₂ standards during the recent measurement expeditions and lab studies. Hamryszczak (2020) found the best results with permeation tubes made out of low-density polyethylene (LDPE) and polyvinyl chloride (PVC). During AQABA gaseous H₂O₂ standards were also produced with a permeation source made out of LDPE. Approximately 15 cm of 1/8" LDPE tubing were cut and filled with H₂O₂ (30 %) by using a syringe. This tubing was subsequently sealed with polytetrafluoroethylene (PTFE) caps (Swagelok®) and placed into a tempered glass impinger flask (35 °C) which was flushed constantly with 80 mL min⁻¹ of synthetic air.

Determination of the H₂O₂ gas phase concentration is achieved based on the photometric technique of Pilz and Johann (1974), which utilizes the fast reaction of H₂O₂ and TiCl₄ to the octahedral η²-peroxo titanium tetrachloride (2.2.3). Therefore, three impinger flasks are filled with 20 mL cooled ultrapure H₂O to dissolve the H₂O₂. Two of these are connected to each other (Fig. SU22) and put into a refrigerator. The second flask determines breakthrough of H₂O₂ while the third flask is used to determine the background signal. Start the measurement by placing the H₂O₂ gas standard outlet (1/8" PFA tubing) into the liquid of the first impinger flask and determine the injection time with a stopwatch. Sampling times between 10 – 24 hours are sufficient, depending on the temperature of the oven and the permeation source used.

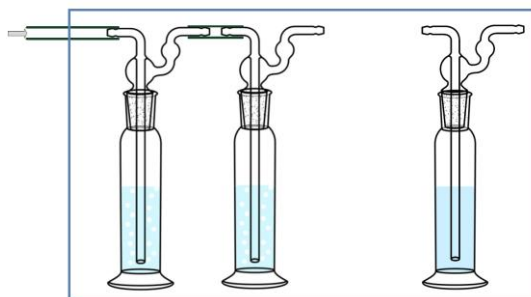


Figure SU22: Sampling of the H₂O₂ gas standard in impinger flasks, which are stored in a refrigerator.

For the TiCl₄ stock solution, dilute 200 g (= 116 mL) TiCl₄ drop by drop in 500 mL HCl (37 %) under slight cooling and stirring. Stored in brown glass under dark conditions, this solution is stable for several years (precipitation of TiO₂ indicates that a new solution should be prepared).

For the photometric analysis, pipette 5 mL of the sampling solution and 1 mL of TiCl₄ stock into a 10 mL volumetric flask and fill up with ultrapure H₂O. After mixing, the probes can be analyzed with the spectrophotometer at $\lambda = 415$ nm (Thermo Fisher Genesys™ 10S UV-Vis). The H₂O₂ concentration is then determined with the Lambert-Beer-law.

$$A = c \cdot d \cdot \varepsilon$$

With A as the absorbance, c as the concentration, d as the diameter of the cuvette (1 cm) and ε as the molar absorption coefficient (735 L mol⁻¹ cm⁻¹). The background signal of the absorbance was subtracted with the blank vial. The permeation rate p(H₂O₂) was then calculated with the pipetted volume (0.005 L), the dilution steps and the reaction time. p(H₂O₂) was afterwards converted into the respective H₂O₂ mixing ratio with the flow rate (Q) and the molar volume of an ideal gas (V_m).

$$p(\text{H}_2\text{O}_2) = c \cdot V \cdot \frac{1}{t}$$

$$\text{H}_2\text{O}_2 = \frac{p(\text{H}_2\text{O}_2) \cdot V_m}{Q}$$

The inlet efficiency can then be determined by injection of gaseous H₂O₂ once right at the start of the sampling inlet and another injection near the AL2021 inlet. Stable H₂O₂ mixing ratios were detected in lab tests, although gaseous injections of H₂O₂ showed a saturation profile, so that it took at least one hour to determine a stable signal of H₂O₂. It seems likely that this was due to the sticky nature of H₂O₂, so that it took some time to saturate the inlet tubing and the instrument walls. Flushing with dry zero gas right after the injection did not show a significant increase in H₂O₂ mixing ratios, although this effect may be different during humid conditions. Similar saturation effects of the gaseous H₂O₂ injections were observed during AQABA, although liquid injections did not show this effect. Additionally, the observed signals were similar for injections of gaseous H₂O₂ right at the start of the sampling chimney compared to injections close to the inlet of the AL2021. It thus seems likely that these effects occur mainly within the instrument and not in the inlet tubing. High flow rates within the bypass tubing during AQABA also secured low residence times of a few seconds. The inlet efficiency was determined to be 100 % based on these results, even though the saturation effects of H₂O₂ when using permeation sources need further studies. I highly recommend further lab studies with H₂O₂ permeation sources, e.g. a comparison study of the AL2021, the HYPHOP and the dual-enzyme HPLC with a variation of the humidity. Further nebulizing techniques could lead to faster and more accurate gas calibration. Currently, the vaporization of H₂O₂ based on a printer cartridge is in development.

Basic solvents for the operation of the dual-enzyme HPLC:

Sampling solution:

The sampling solution is based on a phosphoric acid buffer. Dilute 0.9 mL H₃PO₄ (90 %, HPLC grade) with 5 L of ultrapure H₂O and adjust the pH to 3.2 with NaOH if necessary. The better the quality of the ultrapure H₂O, the lower the instrumental background of the HPLC will be. Additionally, be sure not to store the H₂O for a longer period in direct sunlight.

Fluorescence reagent:

2.16 g of K₂HPO₄ and 0.32 g POPHA are dissolved in 1 L ultrapure H₂O.

Peroxidase reagent:

30 mg of HRP are dissolved in 1.5 L ultrapure H₂O.

H₂O₂ liquid standards:

H₂O₂ standards are prepared from the same H₂O₂ stock solution but in a linear concentration range with the use of a high precision pipette (e.g. Eppendorf 10 – 1000 µL).

Flow rates used during AQABA:

Air flow	2000 mL min ⁻¹
Sampling solution	0.12 mL min ⁻¹
Eluent	0.55 mL min ⁻¹
Fluorescence reagent	0.20 mL min ⁻¹
Peroxidase reagent	0.30 mL min ⁻¹

7. Literature

Akagi, S. K., Yokelson, R. J., Wiedinmyer, C., Alvarado, M. J., Reid, J. S., Karl, T., Crounse, J. D., and Wennberg, P. O.: Emission factors for open and domestic biomass burning for use in atmospheric models, *Atmos. Chem. Phys.*, 11, 4039–4072, <https://doi.org/10.5194/acp-11-4039-2011>, 2011.

Andreae, M. O., and Merlet, P.: Emission of trace gases and aerosols from biomass burning, *Global Biogeochem. Cycles*, 15, 4, 955–966, <https://doi.org/10.1029/2000GB001382>, 2001.

Allen, H. M., Crounse, J. D., Kim, M. J., Teng, A. P., Ray, E. A., McKain, K., Sweeney, C., Wennberg P. O.: H₂O₂ and CH₃OOH (MHP) in the remote atmosphere: 1. Global distribution and regional influences, *Journal of Geophysical Research: Atmospheres*, 127, e2021JD035701, <https://doi.org/10.1029/2021JD035701>, 2022a.

Allen, H. M., Bates, K. H., Crounse, J. D., Kim, M. J., Teng, A. P., Ray, E. A., Wennberg, P. O.: H₂O₂ and CH₃OOH (MHP) in the remote atmosphere: 2. Physical and chemical controls, *Journal of Geophysical Research: Atmospheres*, 127, e2021JD035702, <https://doi.org/10.1029/2021JD035702>, 2022b.

Altshuller, A. P., Miller, D. L., Sleva, S. F.: Determination of Formaldehyde in Gas Mixtures by the Chromotropic Acid Method., *Anal. Chem.*, 33, 621–625, <https://doi.org/10.1021/ac60172a043>, 1961.

Anderson, D. C., Nicely, J. M., Wolfe, G. M., Hanisco, T. F., Salawitch, R. J., Canty, T. P., Dickerson, R. R., Apel, E. C., Baidar, S., Bannan, T. J., Blake, N. J., Chen, D., Dix, B., Fernandez, R. P., Hall, S. R., Hornbrook R. S., Huey, L. G., Josse, B., Jöckel, P., Kinnison, D. E., Koenig, T. K., Le Breton, M., Marécal, V., Morgenstern, O., Oman, L. D., Pan, L. L., Percival, C., Plummer, D., Revell, L. E., Rozanow, E., Saiz-Lopez, A., Stenke, A., Sudo, K., Tilmes S., Ullmann, K., Volkamer, R., Weinheimer, A. J. and Zeng, G.: Formaldehyde in the tropical western Pacific: Chemical sources and sinks, convective transport, and representation in CAM-Chem and the CCMI models, *J. Geophys. Res.: Atmospheres*, 122, 11201–11226, <https://doi.org/10.1002/2016JD026121>, 2017.

Anderson, D. C., Duncan, B. N., Fiore, A. M., Baublitz, C. B., Follette-Cook, M. B., Nicely, J. M., and Wolfe, G. M.: Spatial and temporal variability in the hydroxyl (OH) radical: understanding the role of large-scale climate features and their influence on OH through its dynamical and photochemical drivers, *Atmos. Chem. Phys.*, 21, 6481–6508, <https://doi.org/10.5194/acp-21-6481-2021>, 2021.

Aero-Laser AL2021 manual, Aero-Laser GmbH, v2.2, 21.11.2006.

Aero-Laser AL4021 manual, Aero-Laser GmbH, v2.2, 25.06.2019.

Axinte, R.: The oxidation photochemistry and transport of hydrogen peroxide and formaldehyde at three sites in Europe: trends, budgets and 3-D model simulations, Johannes Gutenberg-Universität, 2016.

Ayers, G.P., Gillet, R.W., Granek, H., de Sreves, C., and Cox, R.A.: Formaldehyde production in clean marine air, *Geophys. Res. Lett.*, 24, 401-404, <https://doi.org/10.1029/97GL00123>, 1997.

Bourtsoukidis, E., Ernle, L., Crowley, J. N., Lelieveld, J., Paris, J.-D., Pozzer, A., Walter, D., and Williams, J.: Non-methane hydrocarbon (C₂–C₈) sources and sinks around the Arabian Peninsula, *Atmos. Chem. Phys.*, 19, 7209–7232, <https://doi.org/10.5194/acp-19-7209-2019>, 2019.

Berasategui, M., Amedro, D., Vereecken, L., Lelieveld, J., Crowley, J. N.: Reaction between $\text{CH}_3\text{C}(\text{O})\text{OOH}$ (peracetic acid) and OH in the gas phase. A combined experimental and theoretical study of the kinetics and mechanism. *Atmos. Chem. Phys.*, 20, 13541–13555, <https://doi.org/10.5194/acp-20-13541-2020>, 2020.

Berrisford, P., Dee, D., Poli, P., Brugge, R., Fielding, M., Fuentes, M., Källberg, P., Kobayashi, S., Uppala, S., and Simmons, A.: The ERA-Interim archive version 2.0, p. 23, <https://www.ecmwf.int/node/8174> (last access: 02.03.2022), 2011.

Bohn, B., Lohse, I.: Calibration and evaluation of CCD spectroradiometers for ground-based and airborne measurements of spectral actinic flux densities, *Atmos. Meas. Tech.*, 10, 3151–3174, <https://doi.org/10.5194/amt-10-3151-2017>, 2017.

Bourtsoukidis, E., Ernle, L., Crowley, J. N., Lelieveld, J., Paris, J.-D., Pozzer, A., Walter, D., and Williams, J.: Non-methane hydrocarbon ($\text{C}_2\text{--C}_8$) sources and sinks around the Arabian Peninsula, *Atmos. Chem. Phys.*, 19, 7209–7232, <https://doi.org/10.5194/acp-19-7209-2019>, 2019.

Bozem, H., Pozzer, A., Harder, H., Martinez, M., Williams, J., Lelieveld, J., Fischer, H.: The influence of deep convection on HCHO and H_2O_2 in the upper troposphere over Europe, *Atmos. Chem. Phys.*, 17, 11835–11848, <https://doi.org/10.5194/acp-17-11835-2017>, 2017.

Brüggemann, M., Hayeck, N. and George, C.: Interfacial photochemistry at the ocean surface is a global source of organic vapors and aerosols, *Nat. Commun.*, 9, 2101, <https://doi.org/10.1038/s41467-018-04528-7>, 2018.

Campos, T. L., Kok, G. L.: Evaluation of Horibe traps for cryogenic collection of hydrogen peroxide and methyl hydroperoxide, *Atmos. Environm.*, 30, 14, 2575–2582, [https://doi.org/10.1016/1352-2310\(95\)00446-7](https://doi.org/10.1016/1352-2310(95)00446-7), 1996.

Cazorla, M., Wolfe, G. M., Bailey, S. A., Swanson, A. K., Arkinson, H. L., and Hanisco, T. F.: A new airborne laser-induced fluorescence instrument for in situ detection of formaldehyde throughout the troposphere and lower stratosphere, *Atmos. Meas. Tech.*, 8, 541–552, <https://doi.org/10.5194/amt-8-541-2015>, 2015.

Celik, S., Drewnick, F., Fachinger, F., Brooks, J., Darbyshire, E., Coe, H., Paris, J.-D., Eger, P. G., Schuladen, J., Tadic, I., Friedrich, N., Dienhart, D., Hottmann, B., Fischer, H., Crowley, J. N., Harder, H., and Borrmann, S.: Influence of vessel characteristics and atmospheric processes on the gas and particle phase of ship emission plumes: in situ measurements in the Mediterranean Sea and around the Arabian Peninsula, *Atmos. Chem. Phys.*, 20, 4713–4734, <https://doi.org/10.5194/acp-20-4713-2020>, 2020.

Chang, W., Lee, M., Heikes, B. G.: One-dimensional photochemical study of H_2O_2 , CH_3OOH , and HCHO in the marine boundary layer during Pacific Exploratory Mission in the Tropics (PEM-Tropics) B, *J. Geophys. Res.*, 109, D06307, <https://doi.org/10.1029/2003JD004256>, 2004.

Christian, N.: Charakterisierung des Peroxidmonitors HYPHOP im Hinblick auf flugzeuggetragene Messungen, Johannes Gutenberg-Universität, 2019.

Coggon, M. M., Lim, C. Y., Koss, A. R., Sekimoto, K., Yuan, B., Gilman, J. B., Hagan, D. H., Selimovic, V., Zarzana, K. J., Brown, S. S., Roberts, J. M., Müller, M., Yokelson, R., Wisthaler, A., Krechmer, J. E., Jimenez, J. L., Cappa, C., Kroll, J. H., de Gouw, J., and Warneke, C.: OH chemistry of non-methane organic gases (NMOGs) emitted from laboratory and ambient biomass burning smoke: evaluating the influence of furans and oxygenated

aromatics on ozone and secondary NMOG formation, *Atmos. Chem. Phys.*, 19, 14875–14899, <https://doi.org/10.5194/acp-19-14875-2019>, 2019.

Cox, R. A., Ammann, M., Crowley, J. N., Herrmann, H., Jenkin, M. E., McNeill, V. F., Mellouki, A., Troe, J., and Wallington, T. J.: Evaluated kinetic and photochemical data for atmospheric chemistry: Volume VII – Criegee intermediates, *Atmos. Chem. Phys.*, 20, 13497–13519, <https://doi.org/10.5194/acp-20-13497-2020>, 2020.

Crowley, J. N., Pouvesle, N., Phillips, G. J., Axinte, R., Fischer, H., Petäjä, T.: Insights into HO_x and RO_x chemistry in the boreal forest via measurement of peroxyacetic acid, peroxyacetic nitric anhydride (PAN) and hydrogen peroxide, *Atmos. Chem. Phys.*, 18, 13457–13479, <https://doi.org/10.5194/acp-18-13457-2018>, 2018.

Crutzen, P.J.: The influence of nitrogen oxides on the atmospheric ozone content, *Q.J.R. Meteorol. Soc.*, 96, 320–325, <https://doi.org/10.1002/qj.49709640815>, 1970.

Dasgupta, P. K., Dong, S., Hwang, H., Yang, H.-C., Genfa, Z.: Continuous liquid-phase fluorometry coupled to a diffusion scrubber for the real-time determination of atmospheric formaldehyde, hydrogen peroxide and sulfur dioxide. *Atmos. Environ.*, 22, 949–963, [https://doi.org/10.1016/0004-6981\(88\)90273-9](https://doi.org/10.1016/0004-6981(88)90273-9), 1988.

De Smedt, I., Müller, J.-F., Stavrou, T., van der A, R., Eskes, H., and Van Roozendaal, M.: Twelve years of global observations of formaldehyde in the troposphere using GOME and SCIAMACHY sensors, *Atmos. Chem. Phys.*, 8, 4947–4963, <https://doi.org/10.5194/acp-8-4947-2008>, 2008.

De Smedt, I., Van Roozendaal, M., Stavrou, T., Müller, J.-F., Lerot, C., Theys, N., Valks, P., Hao, N., and van der A, R.: Improved retrieval of global tropospheric formaldehyde columns from GOME-2/MetOp-A addressing noise reduction and instrumental degradation issues, *Atmos. Meas. Tech.*, 5, 2933–2949, <https://doi.org/10.5194/amt-5-2933-2012>, 2012.

De Smedt, I., Stavrou, T., Hendrick, F., Danckaert, T., Vlemmix, T., Pinardi, G., Theys, N., Lerot, C., Gielen, C., Vigouroux, C., Hermans, C., Fayt, C., Veefkind, P., Müller, J.-F., and Van Roozendaal, M.: Diurnal, seasonal and long-term variations of global formaldehyde columns inferred from combined OMI and GOME-2 observations, *Atmos. Chem. Phys.*, 15, 12519–12545, <https://doi.org/10.5194/acp-15-12519-2015>, 2015.

De Smedt, I., Theys, N., Yu, H., Danckaert, T., Lerot, C., Compernelle, S., Van Roozendaal, M., Richter, A., Hilboll, A., Peters, E., Pedergnana, M., Loyola, D., Beirle, S., Wagner, T., Eskes, H., van Geffen, J., Boersma, K. F., and Veefkind, P.: Algorithm theoretical baseline for formaldehyde retrievals from S5P TROPOMI and from the QA4ECV project, *Atmos. Meas. Tech.*, 11, 2395–2426, <https://doi.org/10.5194/amt-11-2395-2018>, 2018.

De Smedt, I., Pinardi, G., Vigouroux, C., Compernelle, S., Bais, A., Benavent, N., Boersma, F., Chan, K.-L., Donner, S., Eichmann, K.-U., Hedelt, P., Hendrick, F., Irie, H., Kumar, V., Lambert, J.-C., Langerock, B., Lerot, C., Liu, C., Loyola, D., Piders, A., Richter, A., Rivera Cárdenas, C., Romahn, F., Ryan, R. G., Sinha, V., Theys, N., Vlietinck, J., Wagner, T., Wang, T., Yu, H., and Van Roozendaal, M.: Comparative assessment of TROPOMI and OMI formaldehyde observations and validation against MAX-DOAS network column measurements, *Atmos. Chem. Phys.*, 21, 12561–12593, <https://doi.org/10.5194/acp-21-12561-2021>, 2021.

Dienhart, D., Crowley, J. N., Bourtsoukidis, E., Edtbauer, A., Eger, P. G., Ernle, L., Harder, H., Hottmann, B., Martinez, M., Parchatka, U., Paris, J.-D., Pfannerstill, E. Y., Rohloff, R., Schuladen, J., Stöner, C., Tadic, I., Tauer, S., Wang, N., Williams, J., Lelieveld, J., and Fischer, H.: Measurement report: Observation-based

formaldehyde production rates and their relation to OH reactivity around the Arabian Peninsula, *Atmos. Chem. Phys.*, 21, 17373–17388, <https://doi.org/10.5194/acp-21-17373-2021>, 2021.

Dienhart, D., Brendel, B., Crowley, J. N., Eger, P. G., Harder, H., Martinez, M., Pozzer, A., Rohloff, R., Schuladen, J., Tauer, S., Lelieveld, J., and Fischer, H.: Formaldehyde and hydroperoxide distribution around the Arabian Peninsula – evaluation of EMAC model results with ship-based measurements, *Atmos. Chem. Phys. Discuss.* [preprint], <https://doi.org/10.5194/acp-2022-580>, in review, 2022.

DiGangi, J. P., Boyle, E. S., Karl, T., Harley, P., Turnipseed, A., Kim, S., Cantrell, C., Maudlin III, R. L., Zheng, W., Flocke, F., Hall, S. R., Ullmann, K., Nakashima, Y., Paul, J. B., Wolfe, G. M., Desai, A. R., Kajii, Y., Guenther, A., and Keutsch, F. N.: First direct measurements of formaldehyde flux via eddy covariance: implications for missing in-canopy formaldehyde sources, *Atmos. Chem. Phys.*, 11, 10565–10578, <https://doi.org/10.5194/acp-11-10565-2011>, 2011.

DiGangi, J. P., Henry, S. B., Kamrath, A., Boyle, E. S., Kaser, L., Schnitzhofer, R., Graus, M., Turnipseed, A., Park, J.-H., Weber, R. J., Hornbrook, R. S., Cantrell, C. A., Maudlin III, R. L., Kim, S., Nakashima, Y., Wolfe, G. M., Kajii, Y., Apel, E. C., Goldstein, A. H., Guenther, A., Karl, T., Hansel, A., and Keutsch, F. N.: Observations of glyoxal and formaldehyde as metrics for the anthropogenic impact on rural photochemistry, *Atmos. Chem. Phys.*, 12, 9529–9543, <https://doi.org/10.5194/acp-12-9529-2012>, 2012.

Dovrou, E., Rivera-Rios, J. C., Bates, K. H., and Keutsch, F. N.: Sulfate Formation via Cloud Processing from Isoprene Hydroxyl Hydroperoxides (ISOPOOH), *Environ. Sci. Technol.*, 53, 12476–12484, <https://doi.org/10.1021/acs.est.9b04645>, 2019.

Dovrou, E., Bates, K. H., Rivera-Rios, J. C., Cox, J. L., Shutter, J. D., and Keutsch, F. N.: Towards a chemical mechanism of the oxidation of aqueous sulfur dioxide via isoprene hydroxyl hydroperoxides (ISOPOOH), *Atmos. Chem. Phys.*, 21, 8999–9008, <https://doi.org/10.5194/acp-21-8999-2021>, 2021.

Dovrou, E., Bates, K. H., Moch, J. M., Mickley, L. J., Jacob, D. J., and Keutsch, F. N.: Catalytic role of formaldehyde in particulate matter formation, *Proceedings of the National Academy of Sciences of the United States of America*, 119, 6, e2113265119, <https://doi.org/10.1073/pnas.2113265119>, 2022.

Draxler, R. R., and Hess, G. D.: An overview of the HYSPLIT4 modelling system for trajectories, dispersion and deposition, *Australian meteorological magazine*, 47, 295–308, 1998.

Drewnick, F., Böttger, T., von der Weiden-Reinmüller, S.-L., Zorn, S. R., Klimach, T., Schneider, J., and Borrmann, S.: Design of a mobile aerosol research laboratory and data processing tools for effective stationary and mobile field measurements, *Atmos. Meas. Tech.*, 5, 1443–1457, <https://doi.org/10.5194/amt-5-1443-2012>, 2012.

Duncan, B. N., Yoshida, Y., Olson, J. R., Sillman, S., Martin, R. V., Lamsal, L., Hu, Y., Pickering, K. E., Retscher, C., Allen, D. J., Crawford, J. H.: Application of OMI observations to a space-based indicator of NO_x and VOC controls on surface ozone formation, *J. Atmos. Env.*, 44, 2213–2223, <https://doi.org/10.1016/j.atmosenv.2010.03.010>, 2010.

Edtbauer, A., Stöner, C., Pfannerstill, E. Y., Berasategui, M., Walter, D., Crowley, J. N., Lelieveld, J., and Williams, J.: A new marine biogenic emission: methane sulfonamide (MSAM), dimethyl sulfide (DMS), and

dimethyl sulfone (DMSO₂) measured in air over the Arabian Sea, *Atmos. Chem. Phys.*, 20, 6081–6094, <https://doi.org/10.5194/acp-20-6081-2020>, 2020.

Eger, P. G., Friedrich, N., Schuladen, J., Shenolikar, J., Fischer, H., Tadic, I., Harder, H., Martinez, M., Rohloff, R., Tauer, S., Drewnick, F., Fachinger, F., Brooks, J., Darbyshire, E., Sciare, J., Pikridas, M., Lelieveld, J., and Crowley, J. N.: Shipborne measurements of ClNO₂ in the Mediterranean Sea and around the Arabian Peninsula during summer, *Atmos. Chem. Phys.*, 19, 12121–12140, <https://doi.org/10.5194/acp-19-12121-2019>, 2019.

Emmerichs, T., Kerkweg, A., Ouwersloot, H., Fares, S., Mammarella, I., and Taraborrelli, D.: A revised dry deposition scheme for land–atmosphere exchange of trace gases in ECHAM/MESSy v2.54, *Geosci. Model Dev.*, 14, 495–519, <https://doi.org/10.5194/gmd-14-495-2021>, 2021.

Fischer, H., Kormann, R., Klüpfel, T., Gurk, Ch., Königstedt, R., Parchatka, U., Mühle, J., Rhee, T. S., Brenninkmeijer, C. A. M., Bonasoni, P., and Stohl, A.: Ozone production and trace gas correlations during the June 2000 MINATROC intensive measurement campaign at Mt. Cimone, *Atmos. Chem. Phys.*, 3, 725–738, <https://doi.org/10.5194/acp-3-725-2003>, 2003.

Fischer, H., Pozzer, A., Schmitt, T., Jöckel, P., Klippel, T., Taraborrelli, D., Lelieveld, J.: Hydrogen peroxide in the marine boundary layer over the South Atlantic during the OOMPH cruise in March 2007, *Atmos. Chem. Phys.*, 15, 6971–6980, <https://doi.org/10.5194/acp-15-6971-2015>, 2015.

Fischer, H., Axinte, R., Bozem, H., Crowley, J. N., Ernest, C., Gilge, S.: Diurnal variability, photochemical production and loss processes of hydrogen peroxide in the boundary layer over Europe, *Atmos. Chem. Phys.*, 19, 11953–11968, <https://doi.org/10.5194/acp-19-11953-2019>, 2019.

Fittschen, C., Whalley, L. K., Heard, D. E.: The reaction of CH₃O₂ radicals with OH radicals. A neglected sink for CH₃O₂ in the remote atmosphere, *Environ. Sci. Technol.*, 48, 7700–7701, <https://doi.org/10.1021/es502481q>, 2014.

Fortems-Cheiney, A., Chevallier, F., Pison, I., Bousquet, P., Saunois, M., Szopa, S., Cressot, C., Kurosu, T. P., Chance, K., and Fried, A.: The formaldehyde budget as seen by a global-scale multi-constraint and multi-species inversion system, *Atmos. Chem. Phys.*, 12, 6699–6721, <https://doi.org/10.5194/acp-12-6699-2012>, 2012.

Fried, A., Cantrell, C., Olson, J., Crawford, J. H., Weibring, P., Walega, J., Richter, D., Junkermann, W., Volkamer, R., Sinreich, R., Heikes, B. G., O'Sullivan, D., Blake, D. R., Blake, N., Meinardi, S., Apel, E., Weinheimer, A., Knapp, D., Perring, A., Cohen, R. C., Fuelberg, H., Shetter, R. E., Hall, S. R., Ullmann, K., Brune, W. H., Mao, J., Ren, X., Huey, L. G., Singh, H. B., Hair, J. W., Riemer, D., Diskin, G., and Sachse, G.: Detailed comparisons of airborne formaldehyde measurements with box models during the 2006 INTEX-B and MILAGRO campaigns: potential evidence for significant impacts of unmeasured and multi-generation volatile organic carbon compounds, *Atmos. Chem. Phys.*, 11, 11867–11894, <https://doi.org/10.5194/acp-11-11867-2011>, 2011.

Friedrich, N., Eger, P., Shenolikar, J., Sobanski, N., Schuladen, J., Dienhart, D., Hottmann, B., Tadic, I., Fischer, H., Martinez, M., Rohloff, R., Tauer, S., Harder, H., Pfannerstill, E. Y., Wang, N., Williams, J., Brooks, J., Drewnick, F., Su, H., Li, G., Cheng, Y., Lelieveld, J., and Crowley, J. N.: Reactive nitrogen around the Arabian Peninsula and in the Mediterranean Sea during the 2017 AQABA ship campaign, *Atmos. Chem. Phys.*, 21, 7473–7498, <https://doi.org/10.5194/acp-21-7473-2021>, 2021.

Fuchs, H., Novelli, A., Rolletter, M., Hofzumahaus, A., Pfannerstill, E. Y., Kessel, S., Edtbauer, A., Williams, J., Michoud, V., Dusanter, S., Locoge, N., Zannoni, N., Gros, V., Truong, F., Sarda-Esteve, R., Cryer, D. R., Brumby, C. A., Whalley, L. K., Stone, D., Seakins, P. W., Heard, D. E., Schoemaeker, C., Blocquet, M., Coudert, S., Batut, S., Fittschen, C., Thames, A. B., Brune, W. H., Ernest, C., Harder, H., Muller, J. B. A., Elste, T., Kubistin, D., Andres, S., Bohn, B., Hohaus, T., Holland, F., Li, X., Rohrer, F., Kiendler-Scharr, A., Tillmann, R., Wegener, R., Yu, Z., Zou, Q., and Wahner, A.: Comparison of OH reactivity measurements in the atmospheric simulation chamber SAPHIR, *Atmos. Meas. Tech.*, 10, 4023–4053, <https://doi.org/10.5194/amt-10-4023-2017>, 2017.

Glowania, M., Rohrer, F., Dorn, H.-P., Hofzumahaus, A., Holland, F., Kiendler-Scharr, A., Wahner, A., and Fuchs, H.: Comparison of formaldehyde measurements by Hantzsch, CRDS and DOAS in the SAPHIR chamber, *Atmos. Meas. Tech.*, 14, 4239–4253, <https://doi.org/10.5194/amt-14-4239-2021>, 2021.

Gopikrishnan, G. S. and Kuttippurath, J.: A decade of satellite observations reveal significant increase in atmospheric formaldehyde from shipping in Indian Ocean, *Atmos. Environ.*, 246, 118095, <https://doi.org/10.1016/j.atmosenv.2020.118095>, 2021.

Hafermann, S.: Entwicklung und Anwendung von Messinstrumenten für spezifische Hydroperoxid-Messungen in der Troposphäre, Johannes Gutenberg-Universität, 2016.

Hak, C., Pundt, I., Trick, S., Kern, C., Platt, U., Dommen, J., Ordóñez, C., Prévôt, A. S. H., Junkermann, W., Astorga-Lloréns, C., Larsen, B. R., Mellqvist, J., Strandberg, A., Yu, Y., Galle, B., Kleffmann, J., Lörzer, J. C., Braathen, G. O., and Volkamer, R.: Intercomparison of four different in-situ techniques for ambient formaldehyde measurements in urban air, *Atmos. Chem. Phys.*, 5, 2881–2900, <https://doi.org/10.5194/acp-5-2881-2005>, 2005.

Hamryszczak, Z.: CAFE-EU: Photochemie und Verteilung von Hydroperoxiden in der Troposphäre, Johannes Gutenberg-Universität, 2020.

Hamryszczak, Z. T., Pozzer, A., Obersteiner, F., Bohn, B., Steil, B., Lelieveld, J., and Fischer, H.: Distribution of hydrogen peroxide over Europe during the BLUESKY aircraft campaign, *Atmos. Chem. Phys.*, 22, 9483–9497, <https://doi.org/10.5194/acp-22-9483-2022>, 2022a.

Hamryszczak, Z., Dienhart, D., Brendel, B., Rohloff, R., Marno, D., Martinez, M., Harder, H., Pozzer, A., Bohn, B., Zöger, M., Lelieveld, J., and Fischer, H.: Hydrogen peroxide in the upper tropical troposphere over the Atlantic Ocean and western Africa during the CAFE-Africa aircraft campaign, *Atmos. Chem. Phys. Discuss.* [preprint], <https://doi.org/10.5194/acp-2022-693>, in review, 2022b.

Harris, G.W., Klemp, D., Zenker, T. and Burrows, J. P.: Tunable diode laser measurements of trace gases during the 1988 Polarstern cruise and intercomparisons with other methods. *J. Atmos. Chem.*, 15, 315–326, <https://doi.org/10.1007/BF00115401>, 1992.

Heikes, B. G., Lee, M., Bradshaw, J., Sandholm, S., Davis, D. D., Crawford, J., Rodriguez, J., Liu, S., McKeen, S., Thornton, D., Bandy, A., Gregory, G., Talbot, R., and Blake, D.: Hydrogen peroxide and methylhydrogenperoxide distributions related to ozone and odd hydrogen over the North Pacific in the fall of 1991, *J. Geophys. Res.*, 101, 1891–1905, <https://doi.org/10.1029/95JD01364>, 1996.

Heikes, B., Snow, J., Egli, P., O'Sullivan, D., Crawford, J., Olson, J.: Formaldehyde over the central Pacific during PEM-Tropics B, *J. Geophys. Res.*, 106, 32717–32731, <https://doi.org/10.1029/2001JD900012>, 2001.

- Hens, K., Novelli, A., Martinez, M., Auld, J., Axinte, R., Bohn, B., Fischer, H., Keronen, P., Kubistin, D., Nölscher, A. C., Oswald, R., Paasonen, P., Petäjä, T., Regelin, E., Sander, R., Sinha, V., Sipilä, M., Taraborrelli, D., Tatum Ernest, C., Williams, J., Lelieveld, J., and Harder, H.: Observation and modelling of HO_x radicals in a boreal forest, *Atmos. Chem. Phys.*, 14, 8723–8747, <https://doi.org/10.5194/acp-14-8723-2014>, 2014.
- Hladová, M., Martinka, J., Rantuch, P., and Nečas, A.: Review of spectrophotometric methods for determination of formaldehyde, *Research Papers Faculty of Materials Science and Technology in Trnava Slovak University of Technology in Bratislava*, 27, 44, 105–120, <https://doi.org/10.2478/rput-2019-0012>, 2019.
- Holton, J. R., Haynes, P. H., McIntyre, M. E., Douglass, A. R., Rood, R. B., and Pfister, L.: Stratosphere-troposphere exchange, *Rev. Geophys.*, 33 (4), 403–439, <https://doi.org/10.1029/95RG02097>, 1995.
- Hosaynali Beygi, Z., Fischer, H., Harder, H., Martinez, M., Sander, R., Williams, J.: Oxidation photochemistry in the Southern Atlantic boundary layer. Unexpected deviations of photochemical steady state, *Atmos. Chem. Phys.*, 11, 8497–8513, <https://doi.org/10.5194/acp-11-8497-2011>, 2011.
- Hottmann, B., Hafermann, S., Tomsche, L., Marno, D., Martinez, M., Harder, H., Pozzer, A., Neumaier, M., Zahn, A., Bohn, B., Stratmann, G., Ziereis, H., Lelieveld, J., and Fischer, H.: Impact of the South Asian monsoon outflow on atmospheric hydroperoxides in the upper troposphere, *Atmos. Chem. Phys.*, 20, 12655–12673, <https://doi.org/10.5194/acp-20-12655-2020>, 2020.
- Hottmann, B.: Photochemie und Verteilung von Hydroperoxiden im Bereich der Arabischen Halbinsel, Johannes Gutenberg-Universität, 2019.
- Jeuken, A., Siegmund, P., Heijboer, L., Feichter, J., and Bengtsson, L.: On the potential assimilating meteorological analyses in a global model for the purpose of model validation, *J. Geophys. Res.-Atmos.*, 101, 16939–16950, 1996.
- Joeckel, P., Kerkweg, A., Pozzer, A., Sander, R., Tost, H., Riede, H.: Development cycle 2 of the Modular Earth Submodel System (MESSy2), *Geosci. Model Dev.*, 3, 717–752, <https://doi.org/10.5194/gmd-3-717-2010>, 2010.
- Junkerman, W. and Stockwell, W.: On the budget of photooxidants in the marine boundary layer of the tropical South Atlantic, *J. Geophys. Res.*, 104, 8039–8046, <https://doi.org/10.1029/1998JD100060>, 1999.
- Kaiser, J., Wolfe, G. M., Bohn, B., Broch, S., Fuchs, H., Ganzeveld, L. N., Gomm, S., Häsel, R., Hofzumahaus, A., Holland, F., Jäger, J., Li, X., Lohse, I., Lu, K., Prévôt, A. S. H., Rohrer, F., Wegener, R., Wolf, R., Mentel, T. F., Kiendler-Scharr, A., Wahner, A., and Keutsch, F. N.: Evidence for an unidentified non-photochemical ground-level source of formaldehyde in the Po Valley with potential implications for ozone production, *Atmos. Chem. Phys.*, 15, 1289–1298, <https://doi.org/10.5194/acp-15-1289-2015>, 2015.
- Kelly, T. J., Fortune, C. R.: Continuous Monitoring of Gaseous Formaldehyde Using an Improved Fluorescence Approach., *International journal of environmental analytical chemistry*, 54, 249–263. <https://doi.org/10.1080/03067319408034093>, 1994.
- Kieber, R. J., Cooper, W. J., Willey, J. D., and Avery Jr., G. B.: Hydrogen peroxide at the Bermuda Atlantic Time Series Station. Part 1: Temporal variability of atmospheric hydrogen peroxide and its influence on seawater concentrations, *J. Atmos. Chem.*, 39, 1–13, 2001.

Klippel, T., Fischer, H., Bozem, H., Lawrence, M. G., Butler, T., Jöckel, P., Tost, H., Martinez, M., Harder, H., Regelin, E., Sander, R., Schiller, C. L., Stickler, A., and Lelieveld, J.: Distribution of hydrogen peroxide and formaldehyde over Central Europe during the HOOVER project, *Atmos. Chem. Phys.*, 11, 4391–4410, <https://doi.org/10.5194/acp-11-4391-2011>, 2011.

Kluge, F., Hüneke, T., Knecht, M., Lichtenstern, M., Rotermund, M., Schlager, H., Schreiner, B., and Pfeilsticker, K.: Profiling of formaldehyde, glyoxal, methylglyoxal, and CO over the Amazon: normalized excess mixing ratios and related emission factors in biomass burning plumes, *Atmos. Chem. Phys.*, 20, 12363–12389, <https://doi.org/10.5194/acp-20-12363-2020>, 2020.

Kok, G. L., McLaren, S. E., and Stafflbach, T. A.: HPLC Determination of Atmospheric Organic Hydroperoxides. *Journal of Atmospheric and Oceanic Technology*, 12, 2, 282–289, [https://doi.org/10.1175/1520-0426\(1995\)012<0282:HDOAOH>2.0.CO;2](https://doi.org/10.1175/1520-0426(1995)012<0282:HDOAOH>2.0.CO;2), 1995.

Kormann, R., Fischer, H., de Reus, M., Lawrence, M., Brühl, Ch., von Kuhlmann, R., Holzinger, R., Williams, J., Lelieveld, J., Warneke, C., de Gouw, J., Heland, J., Ziereis, H., and Schlager, H.: Formaldehyde over the eastern Mediterranean during MINOS: Comparison of airborne in-situ measurements with 3D-model results, *Atmos. Chem. Phys.*, 3, 851–861, <https://doi.org/10.5194/acp-3-851-2003>, 2003.

Lawrence, M. G. and Lelieveld, J.: Atmospheric pollutant outflow from southern Asia: a review, *Atmos. Chem. Phys.*, 10, 11017–11096, <https://doi.org/10.5194/acp-10-11017-2010>, 2010.

Lazrus, A. L., Kok, G. L., Gitlin, S. N., Lind, J. A., McLaren, S. E.: Automated fluorimetric method for hydrogen peroxide in atmospheric precipitation, *Anal. Chem.*, 57, 917–922, <https://doi.org/10.1021/ac00281a031>, 1986.

Leahey, D. M., Preston, K., and Strosher, M.: Theoretical and Observational Assessments of Flare Efficiencies, *J. Air & Waste Manage. Assoc.*, 51, 12, 1610–1616, <https://doi.org/10.1080/10473289.2001.10464390>, 2001.

Lee, M., Noone, B. C., O'Sullivan, D. and Heikes, B. G.: Method for the Collection and HPLC Analysis of Hydrogen Peroxide and C1 and C2 Hydroperoxides in the Atmosphere, *Journal of Atmospheric and Oceanic Technology*, 12, 5, 1060–1070, [https://doi.org/10.1175/1520-0426\(1995\)012<1060:MFTCAH>2.0.CO;2](https://doi.org/10.1175/1520-0426(1995)012<1060:MFTCAH>2.0.CO;2), 1995.

Lee, M., Heikes, B. G., Jacob, D. J., Sachse, G., Anderson, B.: Hydrogen peroxide, organic hydroperoxide, and formaldehyde as primary pollutants from biomass burning, *J. Geophys. Res.*, 102, 1301–1309, <https://doi.org/10.1029/96JD01709>, 1997.

Lee, M., Heikes, B. G., O'Sullivan, D. W.: Hydrogen peroxide and organic hydroperoxide in the troposphere: A review, *Atmos. Environm.*, 34, 3475–3494, [https://doi.org/10.1016/S1352-2310\(99\)00432-X](https://doi.org/10.1016/S1352-2310(99)00432-X), 2000.

Lelieveld, J., Crutzen, P. J., Ramanathan, V., Andreae, M. O., Brenninkmeijer, C. A. M., Campos, T., Cass, G. R., Dickerson, R. R., Fischer, H., de Gouw, J. A., Hansel, A., Jefferson, A., Kley, D., de Laat, A. T. J., Lal, S., Lawrence, M. G., Lobert, J. M., Mayol-Bracero, O. L., Mitra, A. P., Novakov, T., Oltmans, S. J., Prather, K. A., Reiner, T., Rodhe, H., Scheeren, H. A., Sikka, D., Williams, J.: The Indian Ocean experiment: widespread air pollution from South and Southeast Asia, *Science*, 291, 5506, 1031–1036, <https://doi.org/10.1126/science.1057103>, 2001

- Lelieveld, J., Hoor, P., Jöckel, P., Pozzer, A., Hadjinicolaou, P., Cammas, J.-P., Beirle, S.: Severe ozone air pollution in the Persian Gulf region, *Atmos. Chem. Phys.*, 9, 1393–1406, <https://doi.org/10.5194/acp-9-1393-2009>, 2009.
- Lelieveld, J., Gromov, S., Pozzer, A., Taraborrelli, D.: Global tropospheric hydroxyl distribution, budget and reactivity, *Atmos. Chem. Phys.*, 16, 12477–12493, <https://doi.org/10.5194/acp-16-12477-2016>, 2016.
- Lelieveld, J., Bourtsoukidis, E., Brühl, C., Fischer, H., Fuchs, H., Harder, H., Hofzumahaus, A., Holland, F., Marno, D., Neumaier, M., Pozzer, A., Schlager, H., Williams, J., Zahn, A., Ziereis, H.: The South Asian monsoon–pollution pump and purifier, *Science*, 361, 6399, 270-273, <https://doi.org/10.1126/science.aar2501>, 2018.
- Lelieveld, J., Klingmüller, K., Pozzer, A., Burnett, R. T., Haines, A., Ramanathan, V.: Effects of fossil fuel and total anthropogenic emission removal on public health and climate, *Proceedings of the National Academy of Sciences of the United States of America*, 116, 7192–7197, <https://doi.org/10.1073/pnas.1819989116>, 2019.
- Lelieveld, S., Wilson, J., Dovrou, E., Mishra, A., Lakey, P. S. J., Shiraiwa, M., Poeschl, U., Berkemeier, T.: Hydroxyl Radical Production by Air Pollutants in Epithelial Lining Fluid Governed by Interconversion and Scavenging of Reactive Oxygen Species, *Environ. Sci. Technol.*, 2021, 55, 14069-14079 <https://doi.org/10.1021/acs.est.1c03875>, 2021.
- Liao, J., Wolfe, G. M., Hannun, R. A., St. Clair, J. M., Hanisco, T. F., Gilman, J. B., Lamplugh, A., Selimovic, V., Diskin, G. S., Nowak, J. B., Halliday, H. S., DiGangi, J. P., Hall, S. R., Ullmann, K., Holmes, C. D., Fite, C. H., Agastra, A., Ryerson, T. B., Peischl, J., Bourgeois, I., Warneke, C., Coggon, M. M., Gkatzelis, G. I., Sekimoto, K., Fried, A., Richter, D., Weibring, P., Apel, E. C., Hornbrook, R. S., Brown, S. S., Womack, C. C., Robinson, M. A., Washenfelder, R. A., Veres, P. R., and Neuman, J. A.: Formaldehyde evolution in US wildfire plumes during the Fire Influence on Regional to Global Environments and Air Quality experiment (FIREX-AQ), *Atmos. Chem. Phys.*, 21, 18319–18331, <https://doi.org/10.5194/acp-21-18319-2021>, 2021.
- Liebmann, J., Karu, E., Sobanski, N., Schuladen, J., Ehn, M., Schallhart, S., Quéléver, L., Hellen, H., Hakola, H., Hoffmann, T., Williams, J., Fischer, H., Lelieveld, J., and Crowley, J. N.: Direct measurement of NO₃ radical reactivity in a boreal forest, *Atmos. Chem. Phys.*, 18, 3799–3815, <https://doi.org/10.5194/acp-18-3799-2018>, 2018a.
- Liebmann, J. M., Muller, J. B. A., Kubistin, D., Claude, A., Holla, R., Plass-Dülmer, C., Lelieveld, J., and Crowley, J. N.: Direct measurements of NO₃ reactivity in and above the boundary layer of a mountaintop site: identification of reactive trace gases and comparison with OH reactivity, *Atmos. Chem. Phys.*, 18, 12045–12059, <https://doi.org/10.5194/acp-18-12045-2018>, 2018b.
- Lindinger, W., Hansel, A. and Jordan, A.: Proton-transfer-reaction mass spectrometry (PTR-MS): on-line monitoring of volatile organic compounds at pptv levels, *Chem. Soc. Rev.*, 27, 347-375, <https://doi.org/10.1039/A827347Z>, 1998.
- Liss, P. S. and Johnson, M. T.: *Ocean-Atmosphere Interactions of Gases and Particles*, Springer Earth System Sciences, ISBN 978-3-642-25643-1 (eBook), <https://doi.org/10.1007/978-3-642-25643-1>, 2014.
- Liu, L., Flatøy, F., Ordóñez, C., Braathen, G. O., Hak, C., Junkermann, W., Andreani-Aksoyoglu, S., Mellqvist, J., Galle, B., Prévôt, A. S. H., and Isaksen, I. S. A.: Photochemical modelling in the Po basin with focus on formaldehyde and ozone, *Atmos. Chem. Phys.*, 7, 121–137, <https://doi.org/10.5194/acp-7-121-2007>, 2007.

- Luecken, D. J., Napelenok, S. L., Strum, M., Scheffe, R., and Phillips, S.: Sensitivity of ambient atmospheric formaldehyde and ozone to precursor species and source types across the United States, *Environ. Sci. Technol.*, **52**, 4668–4675, <https://doi.org/10.1021/acs.est.7b05509>, 2018.
- Marbach, T., Beirle, S., Platt, U., Hoor, P., Wittrock, F., Richter, A., Vrekoussis, M., Grzegorski, M., Burrows, J. P., and Wagner, T.: Satellite measurements of formaldehyde linked to shipping emissions, *Atmos. Chem. Phys.*, **9**, 8223–8234, <https://doi.org/10.5194/acp-9-8223-2009>, 2009.
- Marioni, A., Parazols, M., Brigante, M., Deguillaume, L., Amato, P., Delort, A.-M., Laj, P. and Mailhot, G.: Hydrogen peroxide in natural cloud water: Sources and photoreactivity, *101*, 256–263, <https://doi.org/10.1016/j.atmosres.2011.02.013>, 2011.
- Marno, D., Ernest, C., Hens, K., Javed, U., Klimach, T., Martinez, M., Rudolf, M., Lelieveld, J., and Harder, H.: Calibration of an airborne HO_x instrument using the All Pressure Altitude-based Calibrator for HO_x Experimentation (APACHE), *Atmos. Meas. Tech.*, **13**, 2711–2731, <https://doi.org/10.5194/amt-13-2711-2020>, 2020.
- Martin, R. V., Fiore, A. M., and Van Donkelaar, A.: Space-based diagnosis of surface ozone sensitivity to anthropogenic emissions, *Geophys. Res. Lett.*, **31**, L06120, doi:10.1029/2004GL019416, 2004.
- Martinez, M., Harder, H., Kubistin, D., Rudolf, M., Bozem, H., Eerdeken, G., Fischer, H., Klüpfel, T., Gurk, C., Königstedt, R., Parchatka, U., Schiller, C. L., Stickler, A., Williams, J., and Lelieveld, J.: Hydroxyl radicals in the tropical troposphere over the Suriname rainforest: airborne measurements, *Atmos. Chem. Phys.*, **10**, 3759–3773, <https://doi.org/10.5194/acp-10-3759-2010>, 2010.
- Millet, D. B., Jacob, D. J., Boersma, K. F., Fu, T. M., Kurosu, T. P., Chance, K., Heald, C. L., and Guenther, A.: Spatial distribution of isoprene emissions from North America derived from formaldehyde column measurements by the OMI satellite sensor, *J. Geophys. Res.*, **113**, D02307, <https://doi.org/10.1029/2007JD008950>, 2008.
- Molina, M., Rowland, F. Stratospheric sink for chlorofluoromethanes: chlorine atom-catalysed destruction of ozone. *Nature*, **249**, 810–812, <https://doi.org/10.1038/249810a0>, 1974.
- Nguyen, T. B., Crouse, J. D., Teng, A. P., St Clair, J. M., Paulot, F., Wolfe, G. M., Wennberg, P. O.: Rapid deposition of oxidized biogenic compounds to a temperate forest, *Proceedings of the National Academy of Sciences of the United States of America*, **112**, E392–401, <https://doi.org/10.1073/pnas.1418702112>, 2015.
- Novelli, A., Hens, K., Tatum Ernest, C., Kubistin, D., Regelin, E., Elste, T., Plass-Dülmer, C., Martinez, M., Lelieveld, J., and Harder, H.: Characterisation of an inlet pre-injector laser-induced fluorescence instrument for the measurement of atmospheric hydroxyl radicals, *Atmos. Meas. Tech.*, **7**, 3413–3430, <https://doi.org/10.5194/amt-7-3413-2014>, 2014.
- Nussbaumer, C. M., Tadic, I., Dienhart, D., Wang, N., Edtbauer, A., Ernle, L., Williams, J., Obersteiner, F., Gutiérrez-Álvarez, I., Harder, H., Lelieveld, J., and Fischer, H.: Measurement report: In situ observations of deep convection without lightning during the tropical cyclone Florence 2018, *Atmos. Chem. Phys.*, **21**, 7933–7945, <https://doi.org/10.5194/acp-21-7933-2021>, 2021a.
- Nussbaumer, C. M., Crowley, J. N., Schuladen, J., Williams, J., Hafermann, S., Reiffs, A., Axinte, R., Harder, H., Ernest, C., Novelli, A., Sala, K., Martinez, M., Mallik, C., Tomsche, L., Plass-Dülmer, C., Bohn, B., Lelieveld, J.,

and Fischer, H.: Measurement report: Photochemical production and loss rates of formaldehyde and ozone across Europe, *Atmos. Chem. Phys.*, 21, 18413–18432, <https://doi.org/10.5194/acp-21-18413-2021>, 2021b.

Nussbaumer, C. M., Pozzer, A., Tadic, I., Röder, L., Obersteiner, F., Harder, H., Lelieveld, J., and Fischer, H.: Tropospheric ozone production and chemical regime analysis during the COVID-19 lockdown over Europe, *Atmos. Chem. Phys.*, 22, 6151–6165, <https://doi.org/10.5194/acp-22-6151-2022>, 2022.

Osipov, S., Chowdhury, S., Crowley, J.N., Tadic, I., Drewnick, F., Borrmann, S., Eger, P., Fachinger, F., Fischer, H., Predybaylo, E., Fnais, M., Harder, H., Pikridas, M., Vouterakos, P., Pozzer, A., Sciare, J., Ukhov, A., Stenchikov, G. L., Williams, J., and Lelieveld, J.: Severe atmospheric pollution in the Middle East is attributable to anthropogenic sources. *Commun Earth Environ*, 3, 203, <https://doi.org/10.1038/s43247-022-00514-6>, 2022.

O'Sullivan, D. W., Lee, M., Noone, B. C., and Heikes, B. G.: Henry's Law Constant Determinations for Hydrogen Peroxide, Methyl Hydroperoxide, Hydroxymethyl Hydroperoxide, Ethyl Hydroperoxide, and Peroxyacetic Acid, *J. Phys. Chem.*, 100, 3241–3247, <https://doi.org/10.1021/jp951168n>, 1996.

O'Sullivan, D. W., Heikes, B. G., Lee, M., Chang, W., Gregory, G. L., Blake, D. R., and Sachse, G. W.: Distribution of hydrogen peroxide and methylhydroperoxide over the Pacific and South Atlantic Oceans, *J. Geophys. Res.*, 104, 5635–5646, <https://doi.org/10.1029/98JD01250>, 1999.

O'Sullivan, D. W., Heikes, B. G., Snow, J., Burrow, P., Avery, M., Blake, D. R., Sachse, G. W., Talbot, R. W., Thornton, D. C., and Bandy, A. R.: Long-term and seasonal variations in the levels of hydrogen peroxide, methylhydroperoxide, and selected compounds over the Pacific Ocean, *J. Geophys. Res.*, 109, 13, <https://doi.org/10.1029/2003JD003689>, 2004.

Palmer, P. I., Jacob, D. J., Fiore, A. M., Martin, R. V., Chance, K., and Kurosu, T. P.: Mapping isoprene emissions over North America using formaldehyde column observations from space, *J. Geophys. Res.*, 108, 4180, [doi:10.1029/2002JD002153](https://doi.org/10.1029/2002JD002153), 2003.

Paris, J.-D., Riandet, A., Bourtsoukidis, E., Delmotte, M., Berchet, A., Williams, J., Ernle, L., Tadic, I., Harder, H., and Lelieveld, J.: Shipborne measurements of methane and carbon dioxide in the Middle East and Mediterranean areas and the contribution from oil and gas emissions, *Atmos. Chem. Phys.*, 21, 12443–12462, <https://doi.org/10.5194/acp-21-12443-2021>, 2021.

Parrish, D. D., Ryerson, T. B., Mellqvist, J., Johansson, J., Fried, A., Richter, D., Walega, J. G., Washenfelder, R. A., de Gouw, J. A., Peischl, J., Aikin, K. C., McKeen, S. A., Frost, G. J., Fehsenfeld, F. C., and Herndon, S. C.: Primary and secondary sources of formaldehyde in urban atmospheres: Houston Texas region, *Atmos. Chem. Phys.*, 12, 3273–3288, <https://doi.org/10.5194/acp-12-3273-2012>, 2012.

Penkett, S.A., Jones, B.M.R., Brich, K.A. and Eggleton, A.E.J.: The importance of atmospheric ozone and hydrogen peroxide in oxidising sulphur dioxide in cloud and rainwater, *Atmos. Environ.*, 13, 1, 123-137, [https://doi.org/10.1016/0004-6981\(79\)90251-8](https://doi.org/10.1016/0004-6981(79)90251-8), 1979.

Pfannerstill, E. Y., Wang, N., Edtbauer, A., Bourtsoukidis, E., Crowley, J. N., Dienhart, D., Eger, P. G., Ernle, L., Fischer, H., Hottmann, B., Paris, J.-D., Stöner, C., Tadic, I., Walter, D., Lelieveld, J., and Williams, J.: Shipborne measurements of total OH reactivity around the Arabian Peninsula and its role in ozone chemistry, *Atmos. Chem. Phys.*, 19, 11501–11523, <https://doi.org/10.5194/acp-19-11501-2019>, 2019.

Phillips, G. J., Pouvesle, N., Thieser, J., Schuster, G., Axinte, R., Fischer, H., Williams, J., Lelieveld, J., and Crowley, J. N.: Peroxyacetyl nitrate (PAN) and peroxyacetic acid (PAA) measurements by iodide chemical ionisation mass spectrometry: first analysis of results in the boreal forest and implications for the measurement of PAN fluxes, *Atmos. Chem. Phys.*, 13, 1129–1139, <https://doi.org/10.5194/acp-13-1129-2013>, 2013.

Pilz, W., Johann, I.: Die Bestimmung Kleinster Mengen von Wasserstoffperoxyd in Luft, *International journal of environmental analytical chemistry*, 3, 257–270, <https://doi.org/10.1080/03067317408071087>, 1974.

Pozzer, A., Reifenberg, S. F., Kumar, V., Franco, B., Kohl, M., Taraborrelli, D., Gromov, S., Ehrhart, S., Jöckel, P., Sander, R., Fall, V., Rosanka, S., Karydis, V., Akritidis, D., Emmerichs, T., Crippa, M., Guizzardi, D., Kaiser, J. W., Clarisse, L., Kiendler-Scharr, A., Tost, H., and Tsimpidi, A.: Simulation of organics in the atmosphere: evaluation of EMACv2.54 with the Mainz Organic Mechanism (MOM) coupled to the ORACLE (v1.0) submodel, *Geosci. Model Dev.*, 15, 2673–2710, <https://doi.org/10.5194/gmd-15-2673-2022>, 2022.

Reeves, C. E. and Penkett, S. A.: Measurements of peroxides and what they tell us, *Chem. Rev.*, 103, 12, 5199–5218, <https://doi.org/10.1021/cr0205053>, 2003.

Roeckner, E., Brokopf, R., Esch, M., Giorgetta, M., Hagemann, S., Kornbluh, L.: Sensitivity of Simulated Climate to Horizontal and Vertical Resolution in the ECHAM5 Atmosphere Model, *J. Climate*, 19, 3771–3791, <https://doi.org/10.1175/JCLI3824.1>, 2006.

Rosenfeld, D., Lahav, R., Khain, A. and Pinsky, M.: The role of sea spray in cleansing air pollution over ocean via cloud processes, *Science*, 297, 1667–1670, <https://doi.org/10.1126/science.1073869>, 2002.

Salthammer, T.: Formaldehyde in the Ambient Atmosphere: From an Indoor Pollutant to an Outdoor Pollutant?, *Angew. Chem. Int. Ed.*, 52, 3320–3327, <https://doi.org/10.1002/anie.201205984>, 2013.

Sander, R., Baumgaertner, A., Cabrera-Perez, D., Frank, F., Gromov, S., Groöß, J.-U.: The community atmospheric chemistry box model CAABA/MECCA-4.0, *Geosci. Model Dev.*, 12, 1365–1385, <https://doi.org/10.5194/gmd-12-1365-2019>, 2019.

Sauer, F., Limbach, S., Moortgat, G. K.: Measurements of hydrogen peroxide and individual organic peroxides in the marine troposphere, *Atmos. Environ.*, 31, 1173–1184, [https://doi.org/10.1016/S1352-2310\(96\)00289-0](https://doi.org/10.1016/S1352-2310(96)00289-0), 1997.

Sauer, F., Schaefer, C., Neeb, P., Horie, O., Moortgat, G. K.: Formation of hydrogen peroxide in the ozonolysis of isoprene and simple alkenes under humid conditions, *Atmos. Environ.*, 33, 229–241, [https://doi.org/10.1016/S1352-2310\(98\)00152-6](https://doi.org/10.1016/S1352-2310(98)00152-6), 1999.

Sauer, F., Beck, J., Schuster, G. and Moortgat, G. K.: Hydrogen peroxide, organic peroxides and organic acids in a forested area during FIELDVOC'94, *Chemosphere - Global Change Science*, 3, 3, 309–326, [https://doi.org/10.1016/S1465-9972\(01\)00013-7](https://doi.org/10.1016/S1465-9972(01)00013-7), 2001.

Schroeder, J. R., Crawford, J. H., Fried, A., Walega, J., Weinheimer, A., Wisthaler, A., Müller, M., Mikoviny, T., Chen, G., Shook, M., Blake, D. R., Tonnesen, G. S.: New insights into the column CH₂O/NO₂ ratio as an indicator of near-surface ozone sensitivity, *J. Geophys. Res. Atmos.*, 122, 8885–8907, <https://doi.org/10.1002/2017JD026781>, 2017.

Seinfeld, J. H., Pandis, S. N.: *Atmospheric Chemistry and Physics. From Air Pollution to Climate Change*, 3rd ed., Wiley, 2016.

Seyfioglu, R., Odabasi, M. Determination of Henry's Law Constant of Formaldehyde as a Function of Temperature: Application to Air–Water Exchange in Tahtali Lake in Izmir, Turkey, *Environ Monit Assess*, 128, 343–349, <https://doi.org/10.1007/s10661-006-9317-3>, 2007.

Shepson, P. B., Bottenheim, J. W., Hastie, D. R., Venkatram, A.: Determination of the relative ozone and PAN deposition velocities at night, *Geophys. Res. Lett.*, 19, 1121–1124, <https://doi.org/10.1029/92GL01118>, 1992.

Shim, C., Wang, Y., Choi, Y., Palmer, P. I., Abbot, D. S., and Chance, K.: Constraining global isoprene emissions with Global Ozone Monitoring Experiment (GOME) formaldehyde column measurements, *J. Geophys. Res.*, 110, D24301, <https://doi.org/10.1029/2004JD005629>, 2005.

Sinha, V., Williams, J., Crowley, J. N., and Lelieveld, J.: The Comparative Reactivity Method – a new tool to measure total OH Reactivity in ambient air, *Atmos. Chem. Phys.*, 8, 2213–2227, <https://doi.org/10.5194/acp-8-2213-2008>, 2008.

Snow, J. A., Heikes, B. G., Shen, H., O'Sullivan, D. W., Fried, A., Walega, J.: Hydrogen peroxide, methyl hydroperoxide, and formaldehyde over North America and the North Atlantic, *J. Geophys. Res.*, 112, 8353, <https://doi.org/10.1029/2006JD007746>, 2007.

Slemr, F. and Tremmel, H. G.: Hydroperoxides in the marine troposphere over the Atlantic Ocean, *J. Atmos. Chem.*, 19, 71–404, <https://doi.org/10.1007/BF00694493>, 1994.

Sobanski, N., Schuladen, J., Schuster, G., Lelieveld, J., Crowley, J. N.: A five-channel cavity ring-down spectrometer for the detection of NO₂, NO₃, N₂O₅, total peroxy nitrates and total alkyl nitrates, *Atmos. Meas. Tech.*, 9, 5103–5118, <https://doi.org/10.5194/amt-9-5103-2016>, 2016.

Soltanieh, M., Zohrabian, A., Gholipour, M. J., and Kalnay, E.: A review of global gas flaring and venting and impact on the environment: Case study of Iran, *International Journal of Greenhouse Gas Control*, 49, 488–509, <https://doi.org/10.1016/j.ijggc.2016.02.010>, 2016.

St. Clair, J. M., Rivera-Rios, J. C., Crouse, J. D., Knap, H. C., Bates, K. H., Teng, A. P.: Kinetics and Products of the Reaction of the First-Generation Isoprene Hydroxy Hydroperoxide (ISOPOOH) with OH, *The journal of physical chemistry*, 120, 1441–1451. <https://doi.org/10.1021/acs.jpca.5b06532>, 2016.

Stein, A. F., Draxler, R. R., Rolph, G. D., Stunder, B. J. B., Cohen, M. D., Ngan, F.: NOAA's HYSPLIT Atmospheric Transport and Dispersion Modeling System, *Bull. Amer. Meteor. Soc.*, 96, 2059–2077, <https://doi.org/10.1175/BAMS-D-14-00110.1>, 2015.

Stickler, A., Fischer, H., Williams, J., Reus, M. de, Sander, R., Lawrence, M. G.: Influence of summertime deep convection on formaldehyde in the middle and upper troposphere over Europe, *J. Geophys. Res.*, 111, 955, <https://doi.org/10.1029/2005JD007001>, 2006.

Stickler, A., Fischer, H., Bozem, H., Gurk, C., Schiller, C., Martinez-Harder, M., Kubistin, D., Harder, H., Williams, J., Eerdeken, G., Yassaa, N., Ganzeveld, L., Sander, R., and Lelieveld, J.: Chemistry, transport and dry deposition of trace gases in the boundary layer over the tropical Atlantic Ocean and the Guyanas during the GABRIEL field campaign, *Atmos. Chem. Phys.*, 7, 3933–3956, <https://doi.org/10.5194/acp-7-3933-2007>, 2007.

Stone, D., Whalley, L. K., and Heard, D. E.: Tropospheric OH and HO₂ radicals: field measurements and model comparisons. *Chemical Society Reviews*, 41, 19, 6348–6404, <https://doi.org/10.1039/c2cs35140d>, 2012.

- Tadic, I., Crowley, J. N., Dienhart, D., Eger, P., Harder, H., Hottmann, B., Martinez, M., Parchatka, U., Paris, J.-D., Pozzer, A., Rohloff, R., Schuladen, J., Shenolikar, J., Tauer, S., Lelieveld, J., and Fischer, H.: Net ozone production and its relationship to nitrogen oxides and volatile organic compounds in the marine boundary layer around the Arabian Peninsula, *Atmos. Chem. Phys.*, 20, 6769–6787, <https://doi.org/10.5194/acp-20-6769-2020>, 2020.
- Tadic, I., Nussbaumer, C. M., Bohn, B., Harder, H., Marno, D., Martinez, M., Obersteiner, F., Parchatka, U., Pozzer, A., Rohloff, R., Zöger, M., Lelieveld, J., and Fischer, H.: Central role of nitric oxide in ozone production in the upper tropical troposphere over the Atlantic Ocean and western Africa, *Atmos. Chem. Phys.*, 21, 8195–8211, <https://doi.org/10.5194/acp-21-8195-2021>, 2021.
- Tanner, R. L., and Shen, J.: Measurement of hydrogen peroxide in ambient air by impinger and diffusion scrubber. *Aerosol science and technology*, 12, 1, 86-97, 1990.
- Tegtmeier, S., Marandino, C., Jia, Y., Quack, B., and Mahajan, A. S.: Atmospheric gas-phase composition over the Indian Ocean, *Atmos. Chem. Phys.*, 22, 6625–6676, <https://doi.org/10.5194/acp-22-6625-2022>, 2022.
- Tripathi, N., Sahu, L. K., Singh, A., Yadav, R., Patel, A., Patel, K., and Meenu, P.: Elevated levels of biogenic nonmethane hydrocarbons in the marine boundary layer of the Arabian Sea during the intermonsoon, *J. Geophys. Res. Atmos.*, 125, <https://doi.org/10.1029/2020JD032869>, 2020.
- Tyndall, G. S., Cox, R. A., Granier, C., Lesclaux, R., Moortgat, G. K., Pilling, M. J.: Atmospheric chemistry of small organic peroxy radicals, *J. Geophys. Res.*, 106, 12157–12182, <https://doi.org/10.1029/2000jd900746>, 2001.
- Vairavamurthy, A., Roberts, J. M., and Newman, L.: Methods for determination of low molecular weight carbonyl compounds in the atmosphere: A review, *Atmos. Environ.*, 26, 11, 1965–1993, [https://doi.org/10.1016/0960-1686\(92\)90083-W](https://doi.org/10.1016/0960-1686(92)90083-W), 1992.
- Valin, L. C., Fiore, A. M., Chance, K., and González Abad, G.: The role of OH production in interpreting the variability of CH₂O columns in the southeast U.S., *J. Geophys. Res. Atmos.*, 121, 478–493, [doi:10.1002/2015JD024012](https://doi.org/10.1002/2015JD024012), 2016.
- Volkamer, R., Sheehy, P., Molina, L. T., and Molina, M. J.: Oxidative capacity of the Mexico City atmosphere – Part 1: A radical source perspective, *Atmos. Chem. Phys.*, 10, 6969–6991, <https://doi.org/10.5194/acp-10-6969-2010>, 2010.
- Wagner, V., Schiller, C., Fischer, H.: Formaldehyde measurements in the marine boundary layer of the Indian Ocean during the 1999 INDOEX cruise of the R/V Ronald H. Brown, *J. Geophys. Res.*, 106, 28529–28538, <https://doi.org/10.1029/2000JD900825>, 2001.
- Wagner, V., von Glasow, R., Fischer, H., and Crutzen, P. J.: Are CH₂O measurements in the marine boundary layer suitable for testing the current understanding of CH₄ photooxidation? : A model study, *J. Geophys. Res.*, 107 (D3), [doi:10.1029/2001JD000722](https://doi.org/10.1029/2001JD000722), 2002.
- Wang, N., Edtbauer, A., Stöner, C., Pozzer, A., Bourtsoukidis, E., Ernle, L., Dienhart, D., Hottmann, B., Fischer, H., Schuladen, J., Crowley, J. N., Paris, J.-D., Lelieveld, J., and Williams, J.: Measurements of carbonyl compounds around the Arabian Peninsula: overview and model comparison, *Atmos. Chem. Phys.*, 20, 10807–10829, <https://doi.org/10.5194/acp-20-10807-2020>, 2020.

- Wang, S., Hornbrook, R. S., Hills, A., Emmons, L. K., Tilmes, S., Lamarque, J.-F.: Atmospheric Acetaldehyde: Importance of Air-Sea Exchange and a Missing Source in the Remote Troposphere, *Geophys. Res. Lett.*, 46, 5601–5613, <https://doi.org/10.1029/2019gl082034>, 2019.
- Weller, R., Schrems, O., Boddenberg, A., Gäb, S., and Gautrois, M.: Meridional distribution of hydroperoxides and formaldehyde in the marine boundary layer of the Atlantic (48°N-35°S) measured during the Albatross campaign, *J. Geophys. Res.*, 105 (D11), 14401–14412, <https://doi.org/10.1029/1999JD901145>, 2000.
- Wennberg, P. O., Bates, K. H., Crounse, J. D., Dodson, L. G., McVay, R. C., Mertens, L. A., Nguyen, T. B., Praske, E., Schwantes, R. H., Smarte, M. D., St Clair, J. M., Teng, A. P., Zhang, X., Seinfeld, J. H.: Gas-Phase Reactions of Isoprene and Its Major Oxidation Products, *Chem. Rev.*, 118, 3337–3390, <https://doi.org/10.1021/acs.chemrev.7b00439>, 2018.
- Wert, B. P., Trainer, M., Fried, A., Ryerson, T. B., Henry, B., Potter, W. et al.: Signatures of terminal alkene oxidation in airborne formaldehyde measurements during TexAQS 2000, *J. Geophys. Res.*, 108, <https://doi.org/10.1029/2002JD002502>, 2003.
- Whalley, L. K., Furneaux, K. L., Goddard, A., Lee, J. D., Mahajan, A., Oetjen, H., Read, K. A., Kaaden, N., Carpenter, L. J., Lewis, A. C., Plane, J. M. C., Saltzman, E. S., Wiedensohler, A., and Heard, D. E.: The chemistry of OH and HO₂ radicals in the boundary layer over the tropical Atlantic Ocean, *Atmos. Chem. Phys.*, 10, 1555–1576, <https://doi.org/10.5194/acp-10-1555-2010>, 2010.
- Williams, E. J., Lerner, B. M., Murphy, P. C., Herndon, S. C., Zahniser, M. S.: Emissions of NO_x, SO₂, CO, and HCHO from commercial marine shipping during Texas Air Quality Study (TexAQS) 2006, *J. Geophys. Res.*, 114, 3944, <https://doi.org/10.1029/2009JD012094>, 2009.
- Wietzoreck, M., Kyprianou, M., Musa Bandowe, B. A., Celik, S., Crowley, J. N., Drewnick, F., Eger, P., Friedrich, N., Iakovides, M., Kukučka, P., Kuta, J., Nežiková, B., Pokorná, P., Příbylová, P., Prokeš, R., Rohloff, R., Tadic, I., Tauer, S., Wilson, J., Harder, H., Lelieveld, J., Pöschl, U., Stephanou, E. G., and Lammel, G.: Polycyclic aromatic hydrocarbons (PAHs) and their alkylated, nitrated and oxygenated derivatives in the atmosphere over the Mediterranean and Middle East seas, *Atmos. Chem. Phys.*, 22, 8739–8766, <https://doi.org/10.5194/acp-22-8739-2022>, 2022.
- Williams, J. and Brune, W.: A roadmap for OH reactivity research, *Atmos. Environ.*, 106, 371–372, <https://doi.org/10.1016/j.atmosenv.2015.02.017>, 2015.
- Wisthaler, A., Apel, E. C., Bossmeyer, J., Hansel, A., Junkermann, W., Koppmann, R., Meier, R., Müller, K., Solomon, S. J., Steinbrecher, R., Tillmann, R., and Brauers, T.: Technical Note: Intercomparison of formaldehyde measurements at the atmosphere simulation chamber SAPHIR, *Atmos. Chem. Phys.*, 8, 2189–2200, <https://doi.org/10.5194/acp-8-2189-2008>, 2008.
- Wolfe, G. M., Kaiser, J., Hanisco, T. F., Keutsch, F. N., de Gouw, J. A., Gilman, J. B., Graus, M., Hatch, C. D., Holloway, J., Horowitz, L. W., Lee, B. H., Lerner, B. M., Lopez-Hilifiker, F., Mao, J., Marvin, M. R., Peischl, J., Pollack, I. B., Roberts, J. M., Ryerson, T. B., Thornton, J. A., Veres, P. R., and Warneke, C.: Formaldehyde production from isoprene oxidation across NO_x regimes, *Atmos. Chem. Phys.*, 16, 2597–2610, <https://doi.org/10.5194/acp-16-2597-2016>, 2016.

Wolfe, G.M., Nicely, J.M., St. Clair, J.M., Hanisco, T.F., Liao, J., Oman, L.D., Brune, W.B., Miller, D., Thames, A., Gonzalez Abad, G., Ryerson, T.B., Thompson, C.R., Peischl, J., McCain, K., Sweeney, C., Wennberg, P.O., Kim, M., Crouse, J.D., Hall, S.R., Ullmann, K., Diskin, G., Bui, P., Chang, C., and Dean-Day, J.: Mapping hydroxyl variability throughout the global remote troposphere via synthesis of airborne and satellite formaldehyde observations. *PNAS*, 116, 11171-11180, <https://doi.org/10.1073/pnas.1821661116>, 2019.

Yin, Y., Chevallier, F., Ciais, P., Broquet, G., Fortems-Cheiney, A., Pison, I., and Saunois, M.: Decadal trends in global CO emissions as seen by MOPITT, *Atmos. Chem. Phys.*, 15, 13433–13451, <https://doi.org/10.5194/acp-15-13433-2015>, 2015.

Yokouchi, Y., Fujii, T., Ambe, Y. and Fuwa, K.: Gas chromatographic-mass spectrometric analysis of formaldehyde in ambient air using a sampling tube, *Journal of Chromatography*, 180, 1, 133-138, [https://doi.org/10.1016/S0021-9673\(00\)80182-X](https://doi.org/10.1016/S0021-9673(00)80182-X), 1979.

York, D., Evensen, N. M., Martínez, M. L., Basabe Delgado, J. de: Unified equations for the slope, intercept, and standard errors of the best straight line, *American Journal of Physics*, 72, 367–375, <https://doi.org/10.1119/1.1632486>, 2004.

Zhou, X., Mopper, K.: Photochemical production of low-molecular-weight carbonyl compounds in seawater and surface microlayer and their air-sea exchange, *Marine Chemistry*, 56, 201–213, [https://doi.org/10.1016/S0304-4203\(96\)00076-X](https://doi.org/10.1016/S0304-4203(96)00076-X), 1997.

Zhu, L., González Abad, G., Nowlan, C. R., Chan Miller, C., Chance, K., Apel, E. C., DiGangi, J. P., Fried, A., Hanisco, T. F., Hornbrook, R. S., Hu, L., Kaiser, J., Keutsch, F. N., Permar, W., St. Clair, J. M., and Wolfe, G. M.: Validation of satellite formaldehyde (HCHO) retrievals using observations from 12 aircraft campaigns, *Atmos. Chem. Phys.*, 20, 12329–12345, <https://doi.org/10.5194/acp-20-12329-2020>, 2020.



Dirk Dienhart – Curriculum Vitae

Career & Education

MAX PLANCK INSTITUTE FOR CHEMISTRY, MAINZ – PHD STUDENT, 2017-TODAY

Doctoral Thesis (Atmospheric Chemistry Department – Prof. Dr. Jos Lelieveld):
'Atmospheric oxidation precursors in the marine boundary layer around the Arabian Peninsula'

JOHANNES GUTENBERG-UNIVERSITY, MAINZ – MASTER OF SCIENCE, 2014–2017

Master Thesis (Research group – Prof. Dr. T. Hoffmann):
'Characterization and optimization of a flowing atmospheric pressure afterglow (FAPA) ion source for the detection of halogens and interhalogens by mass spectrometry'

MAX PLANCK INSTITUTE FOR CHEMISTRY, MAINZ – 2015–2016

Research assistant (Multiphase Chemistry Department – Prof. Dr. U. Pöschl):
HPLC-MS, UV-Vis spectroscopy

UNIVERSITY OF ABERDEEN, ABERDEEN – ERASMUS, 2014–2015

ERASMUS project in Analytical Chemistry (Research group – Prof. Dr. J. Feldmann):
'Removal of arsenic from gas condensate'

JOHANNES GUTENBERG-UNIVERSITY, MAINZ – BACHELOR OF SCIENCE, 2010–2014

Bachelor Thesis (Research group – Prof. Dr. T. Hoffmann):
'Development of a paperspray ion source for the analysis of secondary organic aerosol filters by mass spectrometry'

Elective modules: 'Analytical Chemistry' & 'Nuclear Chemistry'

PETER-WUST-GYMNASIUM, WITTLICH – ABITUR, 2000–2009

Social Service

VOLUNTEER MILITARY SERVICE, LUFTWAFFE BUNDESWEHR 01/2010–10/2010

Supplies & Organization, Flugbetriebsstaffel, Airport Büchel

BASIC MILITARY SERVICE, LUFTWAFFE BUNDESWEHR 04/2009–12/2009

Skills & Interests

LANGUAGES

German (native), English (fluent), French (basic), Spanish (basic)

INTERESTS & HOBBIES

Wildlife & Nature Photography, Hiking, Yoga, Music